ESO / ALMA Development Study

Improved and tested atmospheric model above 300 GHz

Contract CFP/ESO/19/25417/HNE
Final report

Juan R. Pardo

June 17th 2024

Collaborators: D. Muders, C. de Breuck, J. González, F. M. Montenegro-Montes, J. P. Pérez-Beaupuits, J. Cernicharo, C. Prigent, and E. Serabyn

1 Introduction

Observations of cold dark clouds, star-forming regions, evolved stars, galaxies, and other objects in space, through millimeter and submillimeter wavelength observations have broadened our vision of the Universe over the last few decades. Those observations are usually performed from high and dry sites, where conditions allowing some sky transparency for them are found, as [Hills et al. (1978)] revealed with pioneering site testing observations from Tenerife at ∼2400 meters above sea level. Even so, the atmospheric millimeter and submillimeter spectrum is rather complicated and fast changing, both in space and time. Site testing for ground-based submillimeter observatories and field spectroscopy and radiometry experiments continued over the years in Mauna Kea (Hawai'i), the Atacama desert (Chile), Hanle (India), the Tibet Plateau, Greenland, the South Pole and a few other sites. See a review in [Tremblin et al. (2012)] and several relevant publications such as [Matsushita et al. (1999)], [Paine et al. (2000)], [Pardo et al. (2001a)], [Chamberlin et al. (2003)], [Ji et al. (2004)], [Pardo et al. (2005)], [Matsushita et al. (2017)], [Mlawer et al. (2019)], [Ningombam et al. (2020)], and [Pardo et al. (2022)].

Besides astronomy, the atmospheric millimeter and submillimeter spectrum is also important for Earth observations. Current operational meteorological applications are limited to 200 GHz. The upcoming European organization for the Exploitation of METeorological SATellites (EUMETSAT) Polar System-Second Generation (MetOp-SG), to be launched in 2025, will carry an instrument, the Ice Cloud Imager (ICI), with frequencies up to 664 GHz. The main objective of ICI is to provide data on humidity and ice hydrometeors, particularly the bulk ice mass that can be uniquely quantified with millimeter wave observations from satellites. Furthermore, the deployment of the EUMETSAT Polar System Sterna (EPS-Sterna) constellation, consisting of 6 micro-satellites for launch around 2030, will enhance Numerical Weather Prediction (NWP) accuracy. Each micro-satellite will carry a sounder, including channels around the H2O line at 325 GHz, providing global temperature and water vapor profiles with unparalleled coverage and revisit time. A prototype to EPS-Sterna, the Arctic Weather Satellite (AWS) by the European Space Agency (ESA), is set for launch in June 2024.

The contributors to the millimeter and submillimeter atmospheric spectrum are O_2 through magnetic dipolar (M1) rotational transitions, H_2O through electric dipolar (E1) rotational transitions, weaker E1 features from other "minor" atmospheric gases, such as O_3, N_2O, CO. HCN, HCl..., isotopologues and vibrationally excited states of some of these molecules, and, finally, non-resonant collision-induced absorption (CIA) due to several mechanisms: N_2-N_2, O_2-O_2 and O_2-N_2 collisions (dry CIA), and H_2O-N_2 + H_2O-O_2 collisions (foreign wet CIA), as well as H_2O-H_2O collisions (self wet CIA), although the last one as it involves collisions between water molecules, H_2O-H_2O, is almost two orders of magnitude lower than the foreign CIA at the dry conditions of submillimeter observatories.

The importance of a reference atmospheric radiative transfer model for both planning and helping in the calibration of ground-based observations at millimeter and submillimeter wavelengths is the main motivation of this study. From 2006 to 2011 the C++ implementation of [Pardo et al. (2001b)] atmospheric transmission model ATM was achieved, under European Southern Observatory (ESO) contract 14977/ESO/07/15694/YWE, to the Telescope Calibration subsystem (TelCal) of the official ALMA software. ATM includes the spectroscopy and reference vertical profiles for all relevant molecular species contributing to the millimeter and submillimeter atmospheric spectrum as seen from ground-based observatories, along with empirical and theoretical descriptions of the CIA mechanisms. The software was delivered on schedule and has been used within ALMA since then. Figure 1 shows a reference calculation of the different opacity terms in ATM under typical conditions at the Chajnantor site.

Most site testing and model validation campaigns at millimeter and submillimeter wavelengths have been carried out with broadband (several hundreds of GHz) Fourier Transform Spectrometers (FTSs), with frequency resolutions ranging from ∼0.2 to 10 GHz, and tipping radiometers using "window" frequencies such as 220, 225, 492 or 850 GHz (see previous references in this section). The study summarized in this final report is the first one to be based on broadband coverage (several hundred of GHz) and very high spectral resolution (better than 1 MHz). The atmospheric spectra have been acquired from October 2020 to September 2022 under different weather conditions, in different diurnal moments and seasons, with the Atacama Pathfinder EXperiment (APEX) and has resulted in a data set

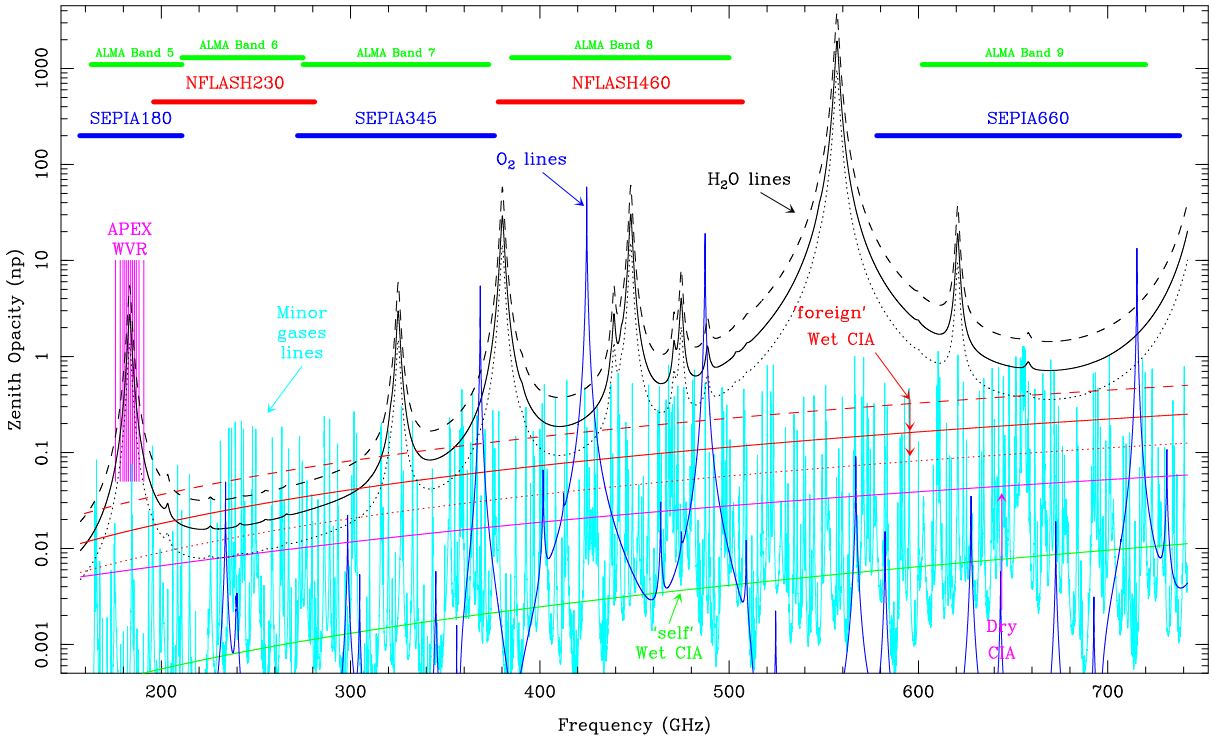

Figure 1: Reference ATM model for the APEX site, considering 555 mb and 273 K as physical parameters at the ground, and 0.5 (dotted black and red lines), 1.0 (solid black and red lines) and 2.0 mm (dashed black and red lines) of precipitable water vapor column. The wet CIA does not include the "self" H_2O-H_2O collisions as they are negligible at these very dry conditions. The frequency ranges covered by the SEPIA and nFLASH receivers used in this work are plotted for reference. The central frequencies of the 6 double side-band channels of the APEX Water Vapor Radiometer, on both sides of the 183.31 GHz H_2O line are also plotted.

of more than 50 spectra within the 157.3-742.1 frequency range, at kHz resolution. The data span one order of magnitude ($\sim$ 0.35-3.5 mm) in precipitable water vapor columns and are unique for their quality and completeness. Due to the proximity of APEX to the Atacama Large Millimeter Array (ALMA), they provide an excellent opportunity to validate and improve the absorption part (imaginary component of the refractivity) in the ATM model. Since the experimental part of this study only concerns a single antenna, no checks can be done on the real part of the refractivity responsible for phase fluctuations. There is scarce literature on this issue [Bendall et al. (2015)] and it remains an open item for further investigation.

This study of this data set is also of interest for the remote sensing community since quantitative use of millimeter wave observations in Numerical Weather Prediction models requires an accurate understanding of atmospheric gas absorption and emission. The meteorological community does not have yet experience in this wavelength range, and following a meeting in 2019 at EUMETSAT [Mattioli et al.(2019)], it was decided to compare different radiative transfer models and to evaluate them with available observations. The APEX observations are particularly suited for this exercise, covering a large frequency range with exceptional accuracy. The fast radiative transfer models used for satellite data assimilation in the NWP models (e.g., RTTOV, CRTM) are often based on HITRAN spectroscopy and on the so-called MT-CKD (Mlawer-Tobin-Clough-Kneizys-Davies) water vapor continuum ([Mlawer et al. (2019)], [Mlawer et al. (2023)]). The MT-CKD is primarily tuned for Earth energy budget, and as a consequence focuses mainly on frequencies higher than 3 THz (as frequencies below are

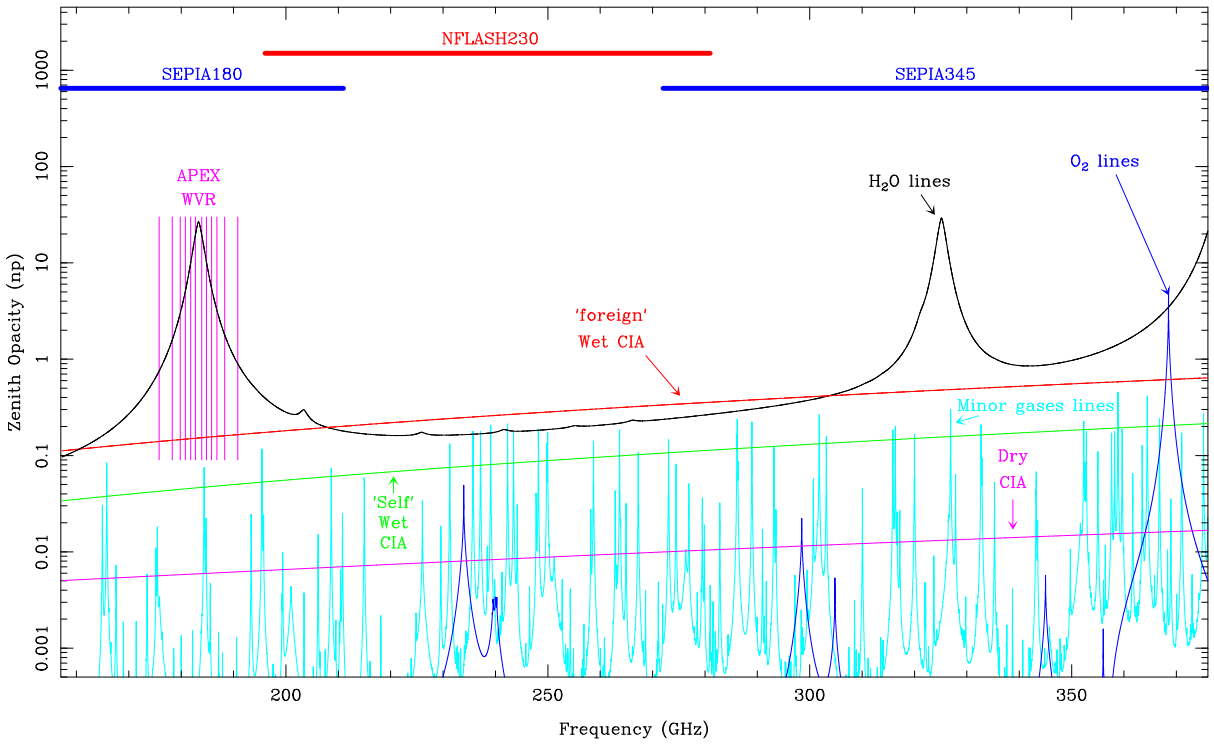

Figure 2: Same as previous figure but for PWVC=10.0 mm and low frequencies. Note that in this case the "self" H_2O-H_2O CIA is not negligible and the the lowest CIA term is the "dry" one.

only weakly contributing to the surface or topofatmosphere energy budgets, [Mlawer et al. (2019)]). The carefully calibrated APEX observations provide additional constraint to the water vapor continuum, to refine the fast radiative transfer models in the millimeter wave range.

In addition to the absorption/emissivity (imaginary part of the atmosphere's complex refractivity) calculations, ATM also incorporates the possibility to make absolute phase/pathlength calculations via the real part of the atmosphere's complex refractivity. This part of the refractivity also has a "resonant" part that is described by the complex line shape for all lines that are present in the atmosphere in our target frequency range, but also beyond it due to large width of H_2O lines beyond ~750 GHz (see equations 27 and 28 in [Pardo et al. (2001b)] for the complex line shape used in ATM. In that respect, the line-by-line validation performed in this work also indirectly serves as a validation for the "resonant" phase calculations. A direct validation is not possible since we have only atmospheric emission spectra from a single antenna, and no differential phase measurements involving two antennas.

2 Instrumental set-up

The Atacama Pathfinder EXperiment [Gusten et al. (2006)] is a world-class millimeter and sub-millimeter observatory operating at a distance of roughly 2 km to the center of ALMA, at the Chajnantor plateau, on the Chilean Andes, 5105 meters above sea level. It hosts a large variety of instruments, from several European partners, due to the experimental nature of this observatory. The APEX antenna has a diameter of 12 meters and is made of 264 aluminum panels. The full surface accuracy is better than 15 μm r.m.s.

The instrumentation program at APEX satisfies both the need of having a test-bed for the development of state-of-the-art equipment, as well as providing general use instruments to cover a broad range of scientific needs. The facility instruments try to fill this need of providing multiple capabilities, while

the PI instrumentation is usually focused on testing new technologies or challenging regimes.

Among the different instruments available, there are five side band separating (2SB) heterodyne (Het) superconductor - insulator - superconductor (SIS) tunnel junction receivers that have been used for this study, connected to Fast Fourier Transform Spectrometers (FFTSs). The kHz resolution provided by the spectrometers plus the good performance of the receivers in terms of stability and, in addition, the use of two loads at very different temperatures for the calibration, have all been crucial for the high resolution absolutely calibrated atmospheric scans that this study requires.

A first set of receivers, called SEPIA (see figure 3) for Swedish ESO PI Instrument at APEX, are in a cryostat that can accommodate 3 ALMA-like receiver cartridges with tertiary optics to illuminate them inside the Nasmyth cabin A of the APEX telescope. They were designed, constructed, and installed by the Group for Advanced Receiver Development (GARD) at Onsala Space Observatory (OSO) in Sweden. The SEPIA cryostat was also manufactured by the GARD team. A complete technical description can be found in [Belitsky et al. (2018)], for SEPIA180 and SEPIA660, and [Meledin et al. (2022)] for SEPIA345. Only one of the three receivers can be used at a given time, but the switch between receivers is very fast, taking only a few minutes to switch between bands. Under relatively stable atmospheric conditions this allows to scan all frequencies covered by the three receivers in just about one hour for a single air mass.

- **SEPIA180 (159-211 GHz)** is a dual polarization 2SB receiver built to the specifications of ALMA Band 5 (it is based on the pre-production version of such receiver). It has two intermediate frequency (IF) outputs per polarization, upper/lower sideband (USB/LSB), each covering 4-8 GHz, adding up a total of 16 GHz instantaneous IF bandwidth. The central frequencies of the two sidebands are separated by 12 GHz. The sideband rejection ratio is by design >10 dB and 18.5 dB on average. The single-sideband noise temperature is below 55 K at all frequencies within the band.

- **SEPIA345 (272376 GHz)** is a dual polarization 2SB receiver delivered in 2020. It has two IF outputs per polarization, USB and LSB, each covering 4-12 GHz, adding up a total of 32 GHz instantaneous IF bandwidth. The central frequencies of the two sidebands are separated by 16 GHz. Each sideband (and polarization) is recorded by two FFTS units, each of them sampling 4 GHz in the following configuration: FFTS1: 4.17 8.17 GHz IF bandwidth, FFTS2: 8.07 12.07 GHz IF bandwidth. Therefore, both units overlap in the middle for about 100 MHz and the full coverage is slightly smaller than 8 GHz (7.9 GHz). The sideband rejection ratio is by design >10 dB over 90% of the band. Typical values of receiver temperatures are <100 K below 320 GHz, approach 150 K at 340 GHz and then rise toward the high-frequency end of the receiver band.

- **SEPIA660 (597725 GHz)** is a dual polarization 2SB receiver that was installed and commissioned during the second half of 2018. The rest of the characteristics are as for SEPIA345 with the exception of the receiver temperature that is below 350 K at all frequencies within the band, and below 250 K in the central part of it.

  The first incarnation of the SEPIA660 receiver was an identical copy of the ALMA band 9 receiver, implementing a double sideband [Baryshev et al. (2015)]. This was later upgraded to a sideband-separating (2SB) version with increased RF coverage. Both versions share the same warm optics of the SEPIA receiver, only the internal cryogenic structure of the receiver cartridge was different to enable the sideband separation optics. Another modification of SEPIA660 compared to the ALMA Band 9 receiver is the extended RF frequency coverage obtained by a modification of the Yttrium iron garnet (YIG) oscillator. The atmospheric spectral scan in this report benefited maximally from this extended frequency coverage, reaching frequencies where the Earth's atmosphere becomes opaque even in very good PWVC conditions. All observations presented in this report were obtained using this 2SB version of the SEPIA660 receiver.

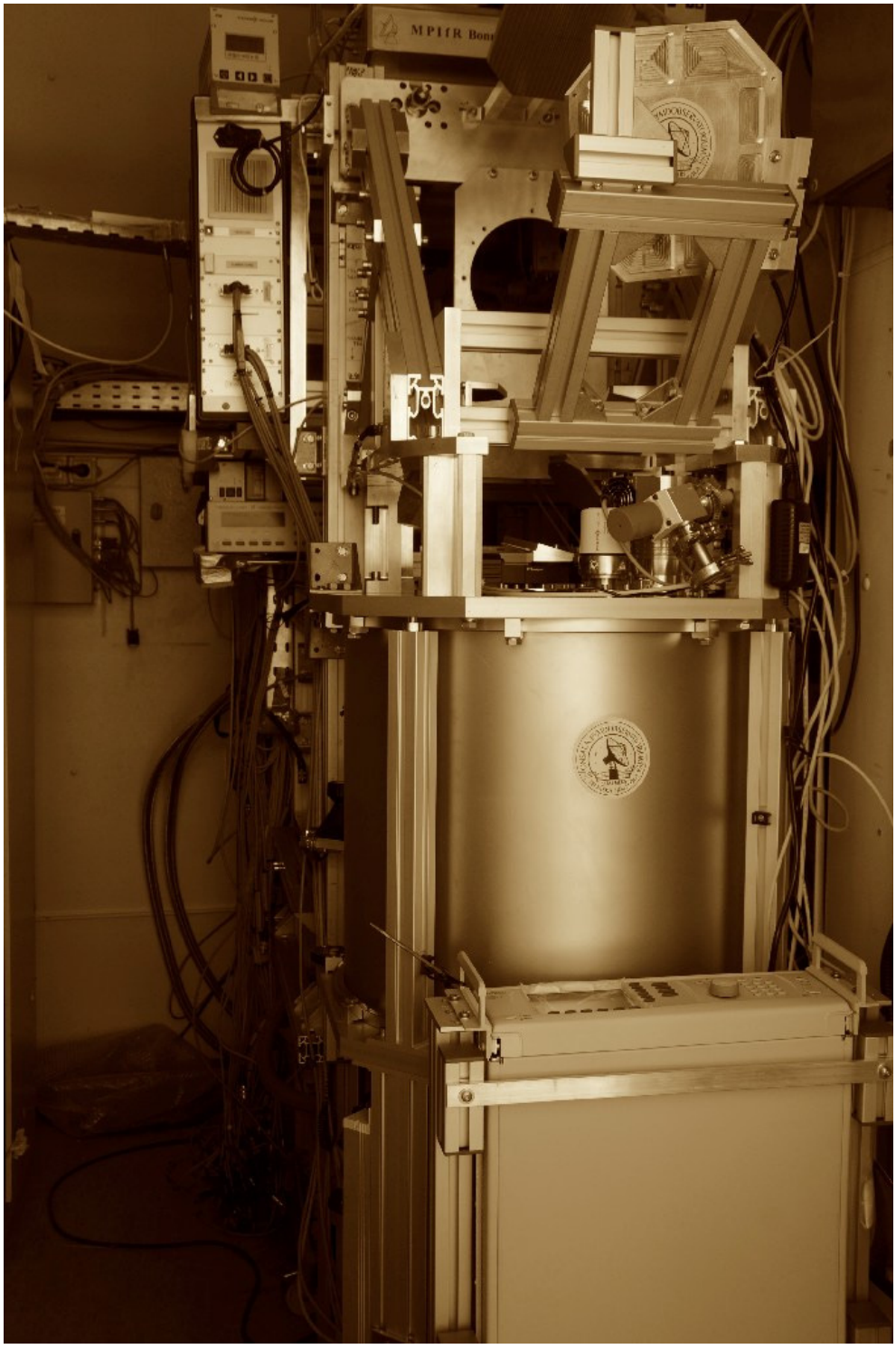

Figure 3: SEPIA is a single-pixel heterodyne receiver with a cryostat that can accommodate 3 receiver cartridges: SEPIA660 (597-725 GHz for optimum operations), plus SEPIA345 (272 to 376 GHz) and SEPIA180 (159 to 211 GHz).

The other bands (nFLASH) were delivered in 2020 by the MPIfR Sub-mm technology division in Bonn. It is a receiver with two independently tunable frequency channels: nFLASH230 and nFLASH460. Both channels are dual polarization (2 SIS mixers per channel) and dual sideband (2SB) meaning 4 SIS junctions in total. The instrument is designed to work as a dual color receiver to allow simultaneously observing in both 230 and 460 channels.

- **nFLASH230 (196-281 GHz)** has an extended IF coverage, comprising from 4 to 12 GHz, and therefore it covers up a total of 32 GHz IF instantaneous bandwidth including both sidebands and polarizations. The separation between the center of the two sidebands is 16 GHz. Each sideband (and polarization) is recorded by two spectrometer processors units (FFTS), each of them recording 4 GHz in the following configuration: FFTS1: 4.17 8.17 GHz IF bandwidth, FFTS2: 8.07 12.07 GHz IF bandwidth. Therefore, both units overlap in the middle for about 100 MHz and the full coverage is slightly smaller than 8 GHz (7.9 GHz). The typical receiver temperature is 80-90 K, increasing up to 100-120 K at the extremes of the frequency window (<210 GHz or >260 GHz LO frequencies). The sideband rejection is typically around 15 dB.
- **nFLASH460 (378-508 GHz)** has 4-8 GHz output IF bandwidth, so half the bandwidth that is covered by the nFLASH230 channel. The separation between the center of the two sidebands is 12 GHz and each sideband (and polarization) is covered by one FFTS unit of 4 GHz bandwidth. The receiver temperatures are typically below 150 K, except at the high frequency end of the spectral window (LO frequency > 480 GHz) where this increases to higher values. Sideband rejection is typically better than 15 dB all over the band.

The large sideband rejection ratio in all these bands is of the highest importance in this study. Nevertheless, as atmospheric lines appear everywhere in the spectrum, we have carefully checked for artifacts that may appear from the image band but, luckily, this issue has a very limited impact on the final stitched spectra.

The above mentioned heterodyne receivers are connected to the fourth generation dual-input Fast Fourier Transform Spectrometer (dFFTS4G) back-end, see [Klein et al. (2012)], as back-end. The spectral resolution is the main improvement, by more than three orders of magnitude, with respect to our previous work conducted ∼25 years ago from Mauna Kea in Hawaii [Pardo et al. (2001a)], see Fig. 4. However, the latter experiment had the advantage of simultaneously covering hundreds of GHz in frequency in just a few minutes, thus reducing the chances for noticeable water vapor fluctuations.

3 Calibration

The final products of the observations presented in this work are atmospheric spectra in the form of Equivalent Blackbody Temperature as a function of frequency, $T_{EBB}(\nu)$. If $F_{atm}(\nu)$ is the calibrated atmospheric flux at frequency ν, $T_{EBB}(\nu)$ is derived from: $F_{atm}(\nu)$=B[$T_{EBB}(\nu)$] with B being the blackbody function. In order to get $F_{atm}(\nu)$ or $T_{EBB}(\nu)$ free from the optical-electrical functions of the observing system, two blackbodies at different temperatures are observed with the receiver ([Ulich & Haas (1976)]; [Ulich (1980)]). These blackbodies are implemented using a microwave absorber material, one at the receiver cabin temperature (T_{hot}), and the other one at a temperature near that of liquid N_2 at 5105 m altitude (≈73 K). The second absorber is installed in a small dewar and connected to a closed cycle cryocooler. Its radiation is observed through a dewar window which exhibits frequency-dependent transmission coefficients. We measured these coefficients by comparing calibrations with this cold load against those using a liquid N_2 absorber, with a common coupling $\eta(\nu)$. The deviation from a perfect coupling is described as a spillover, 1-$\eta(\nu)$, from surfaces at cabin temperature leading to an effective cold absorber temperature of

$$T_{cold,effective}(\nu) = T_{cold,physical} \cdot (\eta_{cal}(\nu)) + T_{hot,physical} \cdot (1 - \eta_{cal}(\nu)) \quad (1)$$

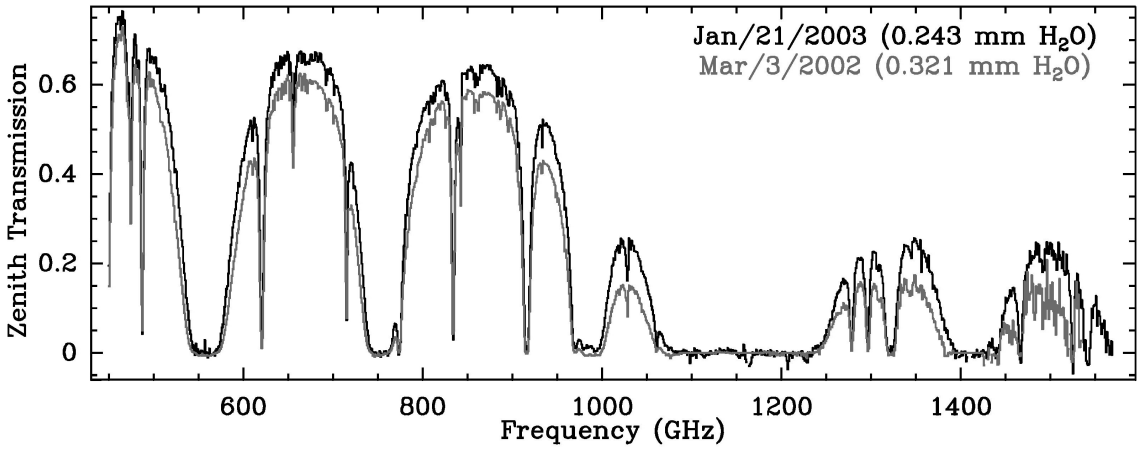

Figure 4: Atmospheric spectra obtained from Mauna Kea with a dedicated FTS installed at the Caltech Submillimeter Observatory. Although the frequency resolution is ∼1 GHz, these data remain today as a reference due to the large frequency coverage (hundreds of GHz) achieved in only about 5 minutes of observing time, thus providing consistent data at all frequencies for a practically constant value of the precipitable water vapor column.

which is somewhat higher than the measured physical temperature. The spillover in the 660 GHz band is estimated using the following linear fit against frequency:

$$(1 - \eta_{\mathrm{cal,660\ GHz\ band}}(\nu)) = 1.903 \cdot 10^{-4} \cdot \nu[\mathrm{GHz}] - 5.083 \cdot 10^{-2} \quad (2)$$

This fit was obtained using the early DSB version of the Band 9 receiver (later replaced by the sideband-separating (2SB) version described in section 2), which was installed in 2016. At the time, there were some differences between the two polarizations, but as they were rather small, it was decided to use an average spillover number. This leads to an uncertainty of $\eta_{\mathrm{cal,660\ GHz\ band}}$ of the order 0.01. In order to obtain the $T_{\mathrm{EBB}}(\nu)$ spectra, we modified the APEX Calibrator software [Polehampton et al. (2019)] to compute this quantity and write it out in CLASS format [Pety (2018)].

Back in 2020, at the time of the first observing runs, this was essentially the calibration procedure. We should recall that for this study, contrary to astronomical observations that are performed in differential mode, we need an absolute calibration as accurate and reliable as possible. However, we noticed serious problems with the data already at first sight such as weird discontinuities and slopes, and a signal offset at some frequencies for which, due to the high atmospheric opacity, we should expect $T_{\mathrm{EBB}}(\nu)$ values very close to the temperature of the ground atmospheric layer. Despite these problems, many sections of the data provided a quite clean view of the atmospheric lines, with almost no ripples or baseline artifacts. It was also noticed that ghost lines that could be attributed to the image side band were not visible. A first publication [Pardo et al. (2022)] was done based on those data with manual corrections of the mentioned calibration problems.

4 Results

The starting point of this study can be established at these first atmospheric scans obtained in the second half of 2020, and the ATM version implemented in 2018 as part of the software maintenance for ESO. After two observing sessions on Oct. 31^{st} and Dec. 5^{th} 2020, that served to define the observing strategy and writing the automatic procedures for it, the first useful observing session took place on Dec. 6^{th} 2020. All frequencies reachable by SEPIA660 (∼575-742 GHz) were scanned for 5 different air masses (1.00, 1.25, 1.50, 1.75, and 2.00) under very good atmospheric conditions (less than ∼0.45 mm of precipitable water vapor column, reaching sometimes very close to 0.33 mm). The tuning to a

new frequency was done after all air masses had been scanned at the previous one (instead of keeping constant the air mass and going through all the tunings before moving the telescope to a different air mass).

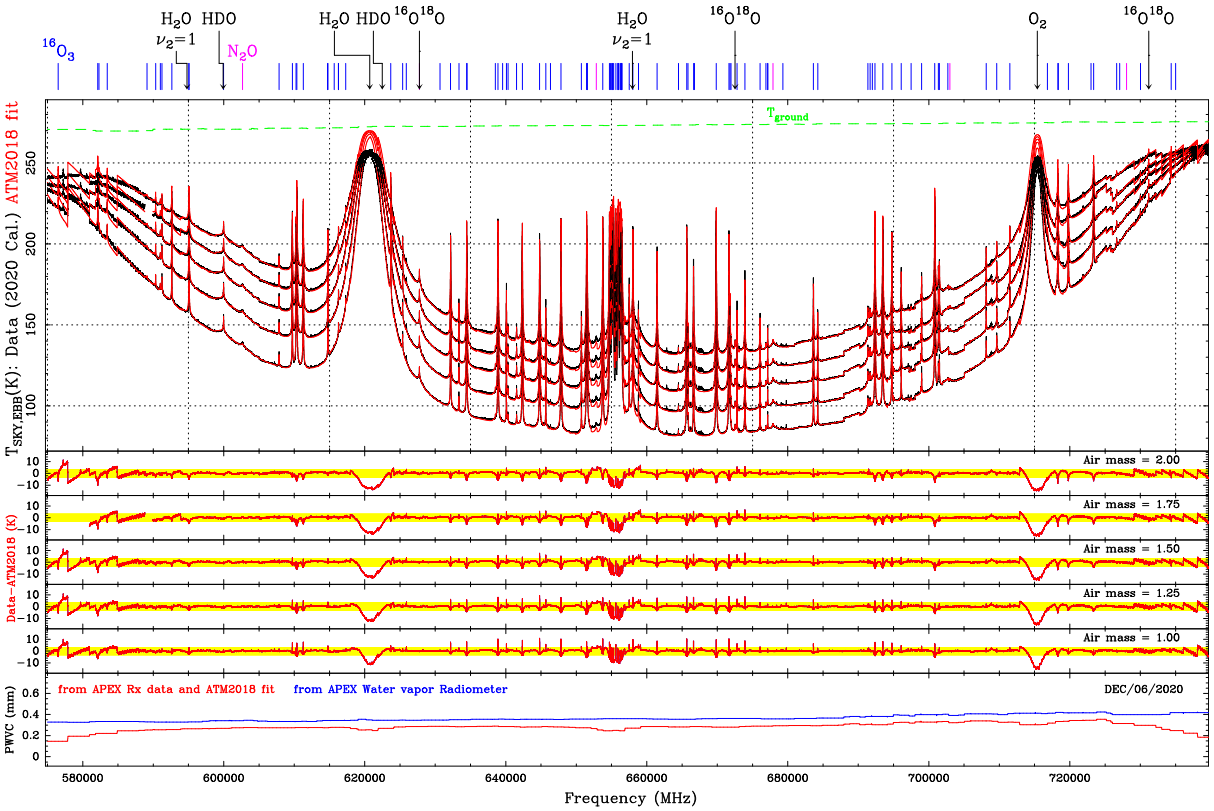

Figure 5: Starting point of this study. SEPIA660 atmospheric scan acquired on Dec 6^{th} 2020, with their original calibration, and the attempt to fit them with the 2018 version of ATM delivered to ESO. The yellow strip in the residual panels marks the ±3 K level.

There are different ways to try to fit the data. For example, one can merge all the $T_{EBB}(\nu)$ single spectra (∼7.8 GHz bandwidth) to generate a single spectrum for each air mass that can be smoothed to a reasonable frequency resolution for manageable numerical treatment, and use the ATM model to try fitting the resulting spectrum with the PWVC as free parameter. This exercise is not, from the beginning, the best approximation since PWVC changed by about 40% from the start (lower frequencies) to the end of the observations (high frequency end). The alternative is to fit each individual scan, therefore getting a PWVC value and a fit model for each one, and then merge all scans (calibrated spectra), fit models and PWVC values into final curves as a function of frequency (by averaging PWVC retrieved at each frequency from the different scans including that frequency, see Figure 6. Note that due to the tuning procedure and the instantaneous width of the receiver pass-band, some frequencies are present in more individual scans than others before the merging is done, as seen in the same figure.

The first fits we did in this study used the original (2020) calibration on the Dec 6^{th} 2020 sky dip data and the ATM model in its ESO 2018 version with the standard minor gases profiles. The results are shown in Fig. 5, illustrating the serious problems that needed to be solved before we could make any progress in the study. First of all, abnormally low T_{EBB} on both ends of the spectral window (limited by two very strong water lines) and also around 620 GHz (H_2O) and 715 GHz (O_2). Those values are nonphysical. Even for very low PWVC values of ∼0.35 mm, $T_{EBB}(\nu)$ should be much closer to the ground temperature provided by the weather station. Due to that, the model tries to reach a fit by lowering

the PWVC value to an unrealistic value of ∼0.2 mm or less at those frequencies, nevertheless resulting in large data-model residuals. Even by lowering the PWVC, the resulting opacity at, for example, 620 GHz is so high that it is impossible to match the data to a model. The unrealistically low PWVC value provides larger tropospheric transmission to stratospheric O_3 lines. Their emission appears stronger than with the correct PWVC value (the one provided by the 183 GHz radiometer should, in principle, be trusted as we will explain later). This causes large residuals near O_3 lines, to be added tho those expected from the fact that we are using in these ATM2018 calculations standard U.S. 1976 Atmosphere profiles for O_3 and other minor gases.

The ATM2018 model itself had several minor issues, such as HCl, HCN or $O_2(^1\Delta)$ lines not included (they appear in the data but are difficult to see in Figure 13 at this scale), and O_3 ν_2=1 lines were deactivated to save calculation time. In fact, several lines from this vibrational mode are visible in the data and a few of them reach more than 1 K above the broad H_2O+O_2+CIA shape of the atmospheric spectrum at these very dry conditions. As a result we have far from flat (and/or close to zero) residual data-model curve, and a PWVC curve that is in large discrepancy 40% or more underestimation with respect to the reliable value provided by the 183 GHz Water Vapor Radiometer.

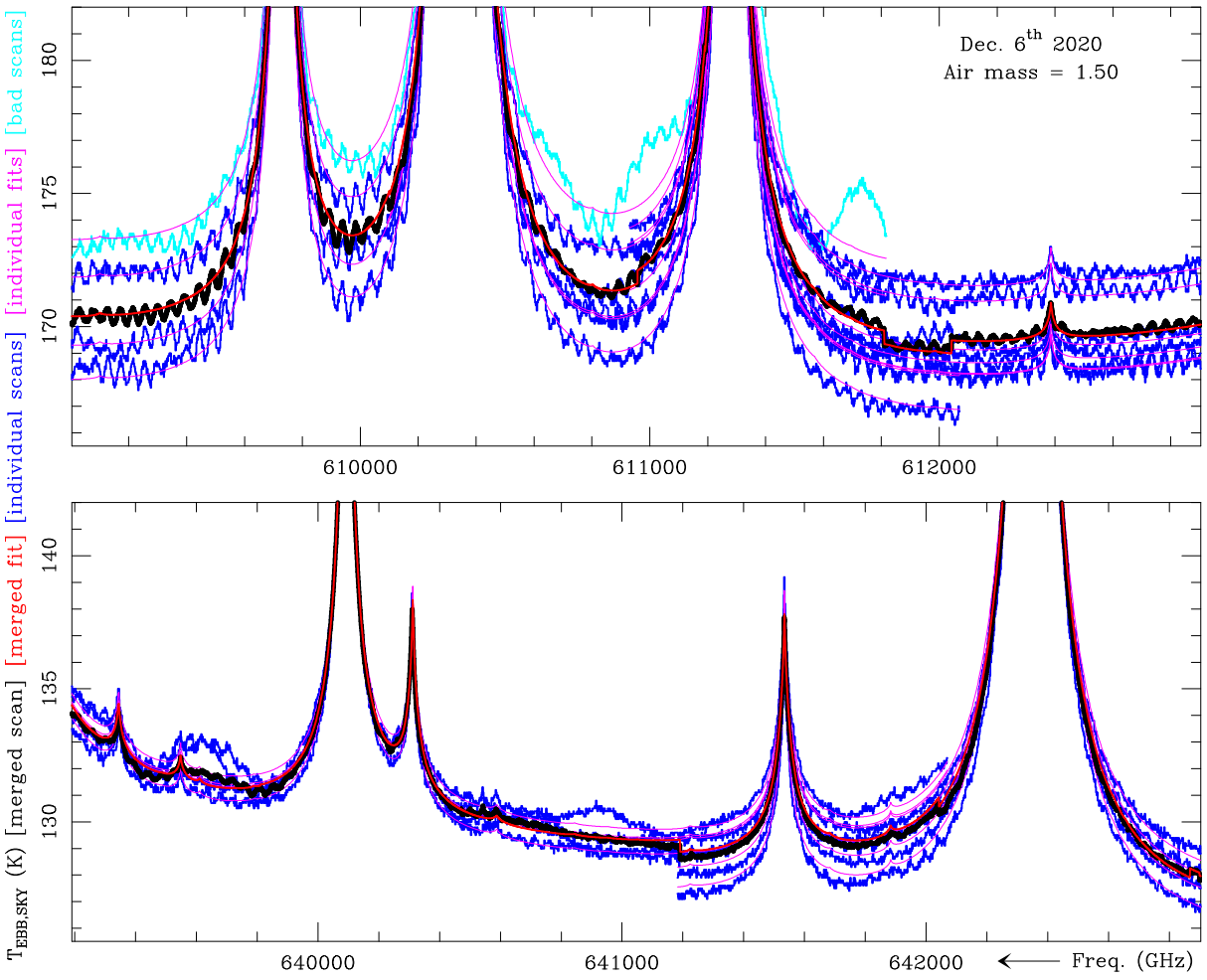

Figure 6: Process of merging the data to create final products in this study. From several individual scans, the bad ones due to large ripples or offsets are discarded, the others are fitted individually, then data and model fits are merged together. See also Figures 7 and 8.

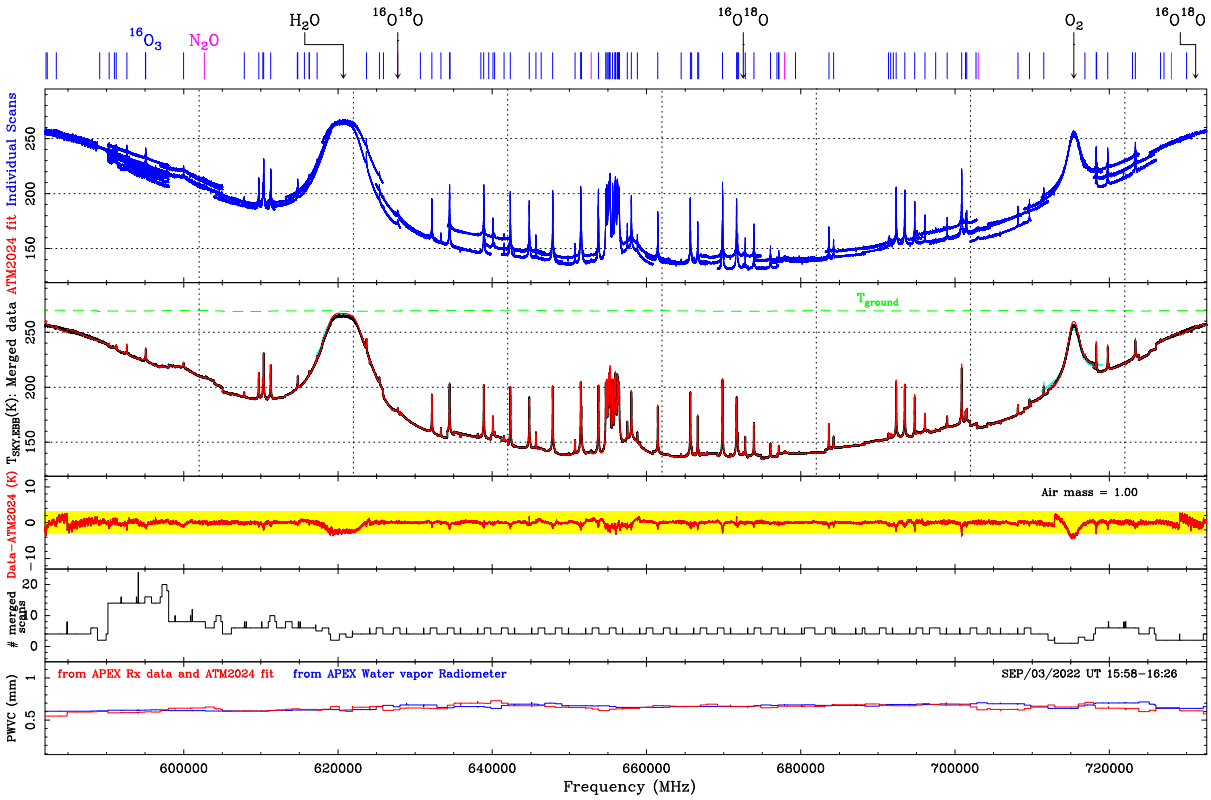

Figure 7: SEPIA660 Zenith scans on September 3, 2022, showing all the individual scans, the number of them, the merged data and model fit, retrieved PWVC from those data and from the 183 GHz WVR. See text for additional details.

The end of this study for this particular frequency range leads us to Figure 13 for which we have found and solved the calibration problems, updated the vertical profiles of minor atmospheric gases profiles, added some missing molecules to the model, activated O_3 ν_2=1, corrected just a few bugs in frequency lines, analyzed the validity of CIA terms, and added a few missing lines originating at very high rotational levels of O_3. Overall, the increase of computation time has only been around 5-10% since we adopted numerical solutions for a direct access to only the lines needed at each frequency, and the new layering for the vertical profiles only adds 3-4 layers out of ∼40.

4.1 Final data set

For this study it was important to cover a wide range of PWVC conditions, but also different seasons and day times. The idea was to gather a data base covering as many situations as possible in order to perform model fits and statistical analysis that would help us in refining the ATM model for its ESO implementation. In order to conduct the necessary observing campaigns, we applied for APEX telescope time via a calibration proposal in 2019, and again in 2022. In total, we got around 40 hours of observations that were divided into several observing sessions that are summarized in Table 1.

The observational part of this study was affected by the global COVID-19 pandemic that prevented some necessary trips to the observatory for conducting these highly non-standard observations on-site. Nevertheless, the team managed to have a series of on-line meetings to refine the observing strategy after each run and to discuss different technical aspects of these observations and the progressing results. Normal operations were resumed in 2022, and J.R. Pardo was also able to travel to the telescope in August-September 2022 for scheduled observations.

YYYY- -MM-DD	UT (hh:mm)	ATM Profile	Receiver	Freq. (GHz)	Air Mass	P_{gr}(hPa) logfile	T_{gr}(K) logfile	PWVC (mm) logfile	 ATM fit	Figures
2020-10-21	06:42-08:00		nFLASH230	204.9-271.1	1.00	554.67	273.01	3.471	3.220	
2020-10-21	06:42-08:00		nFLASH230	204.9-271.1	1.25	554.68	273.01	3.438	3.342	12, 32,
2020-10-21	06:42-08:00	S/N	nFLASH230	204.9-271.1	1.50	554.66	272.95	3.399	3.376	38 -
2020-10-21	06:42-08:00		nFLASH230	204.9-271.1	1.75	554.66	272.95	3.418	3.387	- 42
2020-10-21	06:42-08:00		nFLASH230	204.9-271.1	2.00	554.67	272.92	3.431	3.460	
2020-12-05	01:05-02:59		SEPIA345	274.8-343-1	1.00	555.08	269.37	1.005	0.899	
2020-12-05	01:05-02:59		SEPIA345	274.8-343-1	1.25	555.12	269.51	1.006	0.876	12, 28,
2020-12-05	01:05-02:59	S/N	SEPIA345	274.8-343-1	1.50	555.13	269.54	0.966	0.864	43 -
2020-12-05	01:05-02:59		SEPIA345	274.8-343-1	1.75	555.14	269.59	0.944	0.829	- 47
2020-12-05	01:05-02:59		SEPIA345	274.8-343-1	2.00	555.15	269.79	0.937	0.753	
2020-12-06	10:45-13:55		SEPIA660	582.1-742.1	1.00	554.98	273.16	0.366	0.354	12,
2020-12-06	10:45-13:55		SEPIA660	582.1-742.1	1.25	554.95	273.07	0.371	0.346	5,
2020-12-06	10:45-13:55	S/N-D	SEPIA660	582.1-742.1	1.50	554.96	273.13	0.364	0.340	13,
2020-12-06	10:45-13:55		SEPIA660	582.1-742.1	1.75	554.97	273.13	0.359	0.338	48 -
2020-12-06	10:45-13:55		SEPIA660	582.1-742.1	2.00	554.98	273.19	0.364	0.338	52
2021-06-24	20:50-21:08	W/D	SEPIA345	291.0-371.0	1.41	553.68	260.78	0.973	0.977	12,28,29,53-55
2021-10-31	23:41-00:00		SEPIA180	157.3-205.2	1.00	556.19	271.01	1.753	1.705	12,34,
2021-10-31	00:01-00:18	S/N	SEPIA180	157.3-208.7	1.50	556.20	270.67	1.628	1.652	56-
2021-10-31	00:19-00:44		SEPIA180	157.3-208.7	2.00	556.28	270.41	1.547	1.535	-58
2021-10-31	00:48-01:00		nFLASH230	195.9-271.1	1.00	556.26	270.82	1.356	0.903	
2021-10-31	01:01-01:12	S/N	nFLASH230	195.9-271.1	1.50	556.28	270.94	1.302	1.051	12
2021-10-31	01:13-01:24		nFLASH230	195.9-271.1	2.00	556.32	270.67	1.265	1.089	
2021-10-31	01:28-01:46		SEPIA345	270.9-371.5	1.00	556.35	269.98	1.302	1.348	12,
2021-10-31	01:47-02:04	S/N	SEPIA345	274.0-371.5	1.50	556.48	269.57	1.321	1.267	30,
2021-10-31	02:05-02:22		SEPIA345	274.0-371.5	2.00	556.48	272.28	1.257	1.242	59-63
2021-10-31	03:44-04:08		nFLASH460	453.0-518.0	1.00	556.25	272.11	1.263	1.351	12, 24,
2021-10-31	04:35-04:58	S/N	nFLASH460	453.0-518.0	1.50	555.97	270.41	1.157	1.244	26,
2021-10-31	02:38-03:17		nFLASH460	453.0-518.0	2.00	556.42	272.41	1.251	1.300	64-68
2022-05-11	12:32-14:32	W/D	SEPIA460	386.0-518.5	1.00	555.94	272.87	0.705	0.726	12,27
2022-05-11	12:32-14:32		SEPIA460	386.0-528.5	2.00	555.94	272.92	0.691	0.730	69-73
2022-05-11	11:18-12:30	W/D	SEPIA660	582.0-739.0	1.00	555.58	269.50	0.727	0.756	12, 17,
2022-05-11	11:18-12:30		SEPIA660	582.0-739.0	2.00	555.58	269.43	0.715	0.736	74-78
2022-08-25	21:41-21:59		SEPIA345	270.9-371.1	1.00	555.08	270.92	0.558	0.535	12,
2022-08-25	20:57-21:19	W/D	SEPIA345	270.9-371.1	1.50	554.92	271.82	0.519	0.493	30,
2022-08-25	21:21-21:39		SEPIA345	270.9-371.1	2.00	555.01	271.33	0.530	0.514	79-83
2022-08-25	18:03-19:05	W/D	nFLASH460	382.8-518.2	1.00	555.14	272.88	0.442	0.443	12, 84-88
2022-08-25	19:07-20:06	W/D	nFLASH460	382.8-517.1	1.00	554.92	272.55	0.462	0.468	12,27,
2022-08-25	20:07-20:56		nFLASH460	382.8-517.1	2.00	554.90	272.23	0.487	0.479	89-93
2022-08-25	16:37-17:05		SEPIA660	582.0-739.0	1.00	555.46	272.71	0.399	0.390	12,
2022-08-25	17:06-17:32	W/D	SEPIA660	582.0-739.0	1.50	555.34	272.72	0.398	0.379	18,
2022-08-25	17:33-17:59		SEPIA660	582.0-739.0	2.00	555.20	273.03	0.389	0.371	94-98
2022-08-25	21:41-22:42	W/D	SEVERAL	174.8-371.1	1.00	555.11	270.27	0.562	0.516	12
2022-08-27	02:07-02:43		SEPIA660	582.0-739.0	1.00	555.19	265.99	0.550	0.519	12,
2022-08-27	02:44-03:18	W/N	SEPIA660	582.0-739.0	1.50	555.05	266.04	0.546	0.514	15,
2022-08-27	03:19-03:52		SEPIA660	582.0-739.0	2.00	555.05	263.984	0.541	0.509	99-103
2022-08-28	14:19-14:37		SEPIA180	158.8-211.2	1.00	556.23	272.80	3.002	3.119	12,
2022-08-28	14:39-14:55	W/D	SEPIA180	158.8-211.2	1.50	556.31	272.96	2.891	3.091	35,
2022-08-28	14:56-15:13		SEPIA180	158.8-211.2	2.00	556.26	273.24	3.200	3.580	104-106
2022-08-28	15:14-15:26		nFLASH230	195.9-271.1	1.00	556.13	273.39	3.256	3.189	12,
2022-08-28	15:28-15:39	W/D	nFLASH230	195.9-271.1	1.50	556.06	273.53	3.039	3.102	107-
2022-08-28	15:41-15:52		nFLASH230	195.9-236.1	2.00	556.03	273.80	2.850	2.925	-111
2022-08-28	15:53-16:25		SEPIA345	270.9-371.1	1.00	556.01	273.82	2.879	2.985	12,
2022-08-28	16:26-16:42	W/D	SEPIA345	270.9-371.1	1.50	556.00	273.67	2.667	2.807	31,
2022-08-28	16:44-17:00		SEPIA345	270.9-371.1	2.00	555.93	273.37	2.585	2.683	112-114
2022-08-28	17:02-17:32	W/D	S180/N230	158.8-271.1	1.00	555.83	273.20	2.354	2.318	12
2022-09-01	16:38-16:46	W/D	SEPIA660	587.9-649.1	1.00	551.85	268.80	1.050	1.173	12, 19
2022-09-01	17:06-17:18	W/D	SEPIA660	587.9-649.1	1.00	551.89	269.30	0.897	0.945	115-119
2022-09-03	15:58-16:26	W/D	SEPIA660	587.9-732.0	1.00	553.01	269.47	0.653	0.648	12,7,120-124
2022-09-05	16:53-17:22	W/D	SEPIA660	587.9-732.0	1.00	552.75	267.65	0.375	0.412	8,125-129

Table 1: Summary of 59 atmospheric spectra, obtained with APEX from October 2020 to September 2022, that form the data base used for this study. Four basic types of atmosphere are used in the analysis identified by: W: Winter, S: Summer, D: Day, N: Night.

The overall analysis that we can carry out will finally use data obtained in 11 different runs between October 21^{st} 2020 and September 3^{rd} 2022 for which we are now convinced to have the best possible calibration and clean enough spectra. The main difference between using the telescope for atmospheric measurements and for astronomical observations is that in the first case we have to achieve an accurate absolute calibration using two reference loads, and in the second case we work in differential mode between the astronomical target and the sky around it. In addition, the strong signal from the atmosphere can cause baseline problems and we cannot subtract any baseline.

Within each observing date, spectra at different air masses were recorded in order to check for consistency in the PWVC retrievals. However, two different strategies were followed for those sky dips as several tunings are necessary to cover all frequencies reachable by one particular receiver.

In some cases, the tuning was done and the telescope moved to the different air masses to take data in all of them before moving to the next frequency tuning. This implies that a quite long time was necessary to complete the frequency coverage in one band for all the air masses, giving enough time to the PWVC to significantly change. In other runs the elevation was kept constant, passing through all frequency tunings before moving to a different elevation or air mass. In those cases, also, the number of air masses was reduced to three (1.0, 1.5 and 2.0) thus allowing a complete coverage of a particular band for a given elevation in a much shorter time, and reducing the chances of strong PWVC changes. However, the PWVC evolution can show up from one air mass to another, as Table 1 shows.

The final data set allows for a quite detailed study on the collision induced absorption (CIA) terms, diurnal changes in minor gases profiles, missing lines, frequency errors, etc. However, the sampled dates do not provide a good basis, with the exception of SEPIA660 (measurements in May, August, September and December), to draw a strong conclusion on seasonal trends.

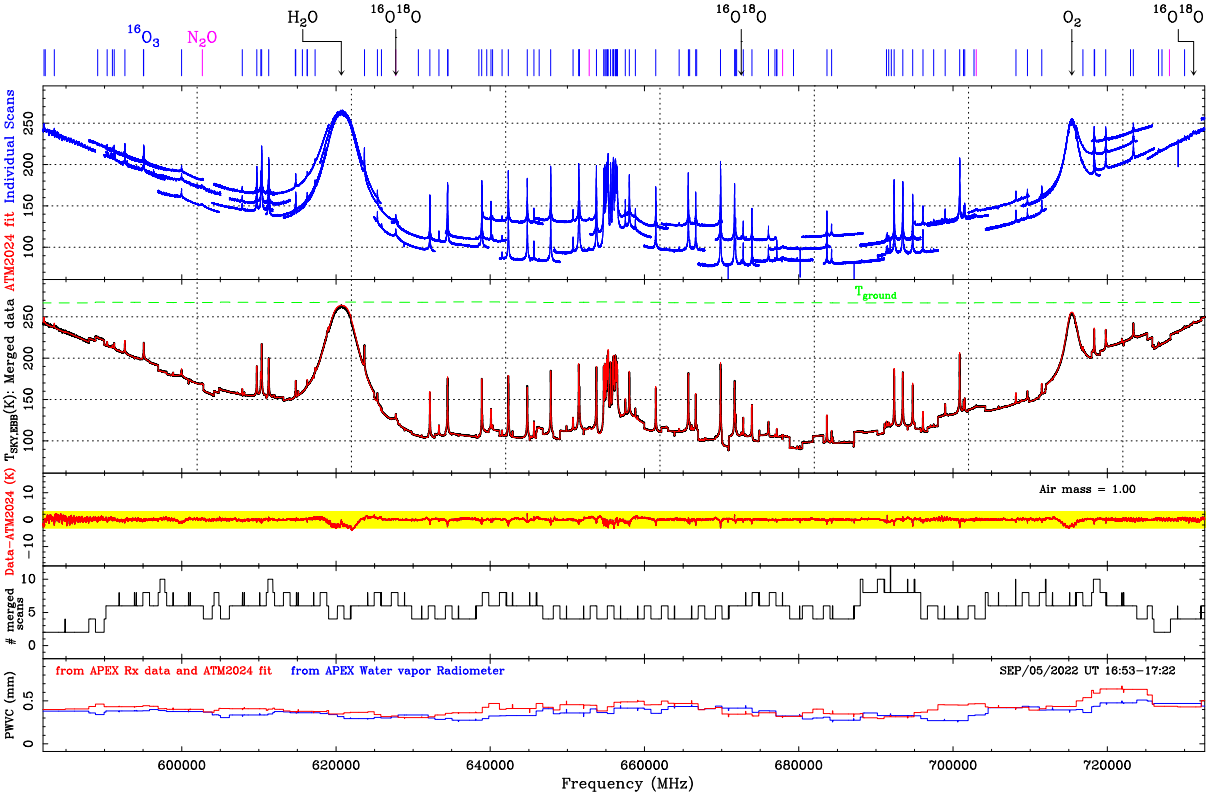

Figure 8: SEPIA660 Zenith scans on September 5, 2022, showing all the individual scans, the number of them, the merged data and model fit, retrieved PWVC from those data and from the 183 GHz WVR. See text for additional details.

ATM2024 provides new adequate vertical profiles (especially for ozone) that make a better compromise when fitting the actual observations. It is important to point out that the difficulty of the study is to get reliable absolutely calibrated data. For this reason, most of our efforts were focused towards understanding, and correcting if necessary, all calibration issues. The problems that we had to face are explained with several examples throughout this report.

Another issue is how to show and compare retrieved parameters such a PWVC. We adopted the decision to show the derived PWVC values as a function of frequency, and not time, since the log file provides the link between observed frequencies in each tuning and the time interval of that observation.

Since we average PWVCs from several air masses, it means that there are data from different times in many PWVC(ν) curves displayed in this report. However, in a few cases, and due to the needs of the discussion, we display individual values of PWVC(ν) retrieved for each air mass.

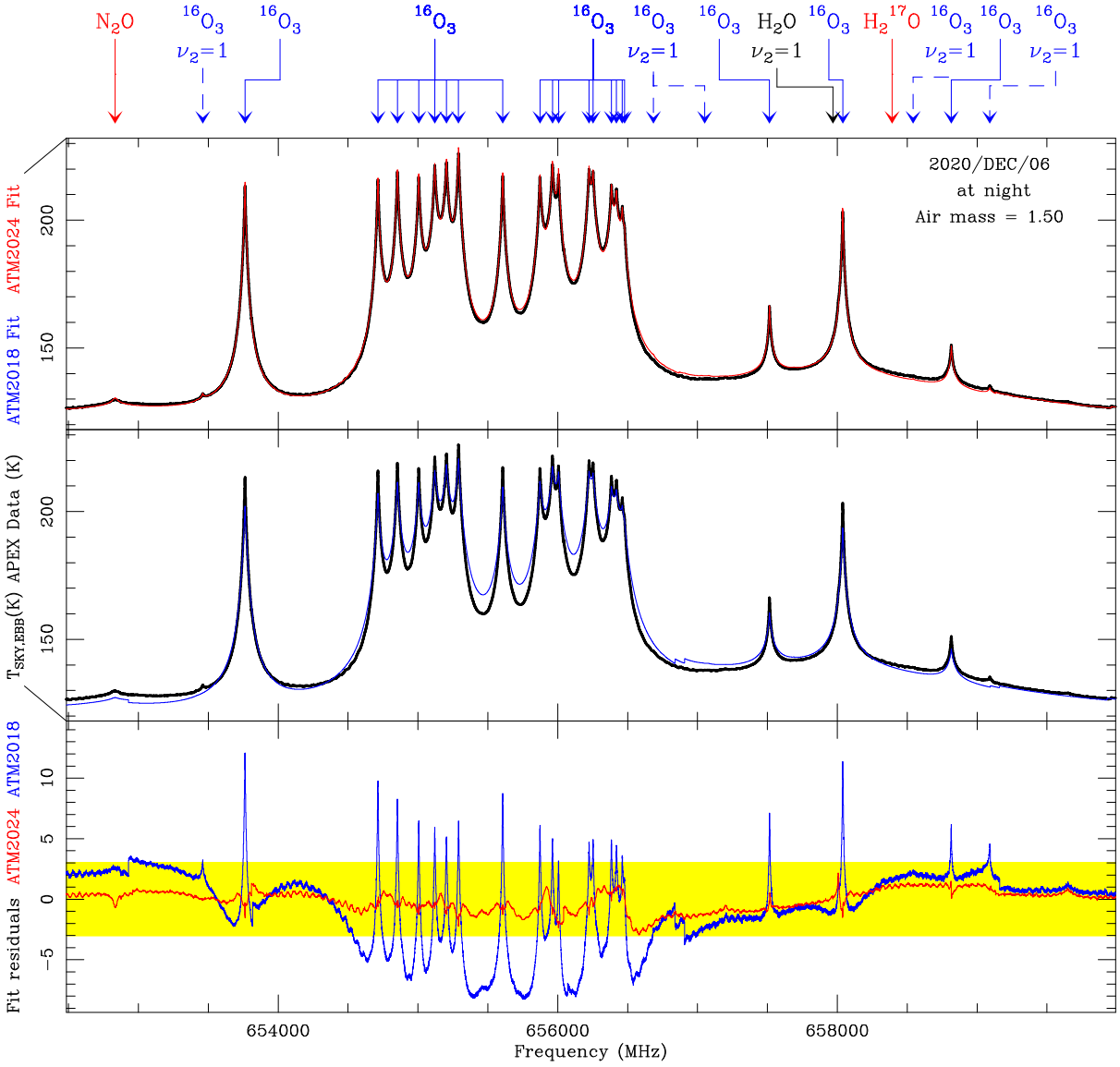

Figure 9: Comparison of Dec. 6^{th} 2020 SEPIA660 data fit using the old 2018 ATM version and the new one (ATM2024) resulting from this study (part 1). See text.

In order to reduce the residuals in the fitting process as much as possible, we have to take into account that the vertical distribution of minor gases is expected to vary with season and time of the day. The observing geometry is not well adapted to retrieve very accurate vertical profiles. In addition, our sample is not large enough for a detailed diurnal and seasonal study.

Therefore, we decided to use four types of basic vertical profiles for minor gases (Winter/Day, Winter/Night, Summer/Day and Summer/Night), as noted on Table 1 that were hand-adjusted, based on our extensive previous experience.

By using those vertical profiles, the fit residuals are much reduced with respect to residuals resulting for ATM2018 fits using fixed U.S. Stnd. 1976 Tropical profiles. To illustrate the improvement, please see Figures 9, 10 and 11.

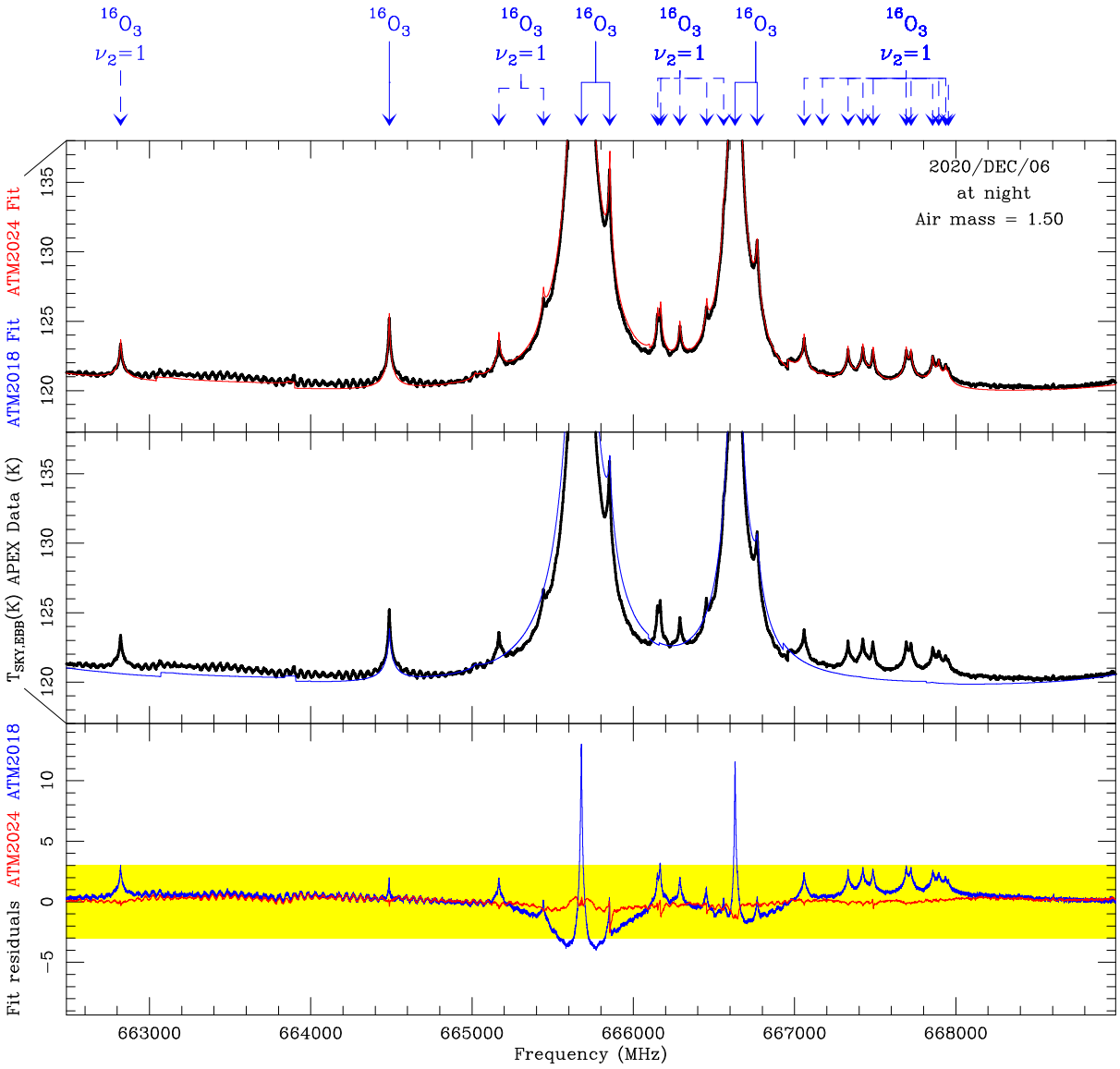

Figure 10: Comparison of Dec. 6^{th} 2020 SEPIA660 data fit using the old 2018 ATM version and the new one (ATM2024) resulting from this study (part 2). See text.

The first one (Fig. 9) shows how the residuals can be reduced to an almost flat histogram well within

the ±3 K deviation, even at frequencies where the atmospheric spectrum becomes quite complicated due to a cluster of at least 15 O_3 lines 665.5 and 667.0 GHz. Some tiny ν_2=1 O_3 lines are well reproduced by ATM2024 whereas they were missing in ATM2018 output.

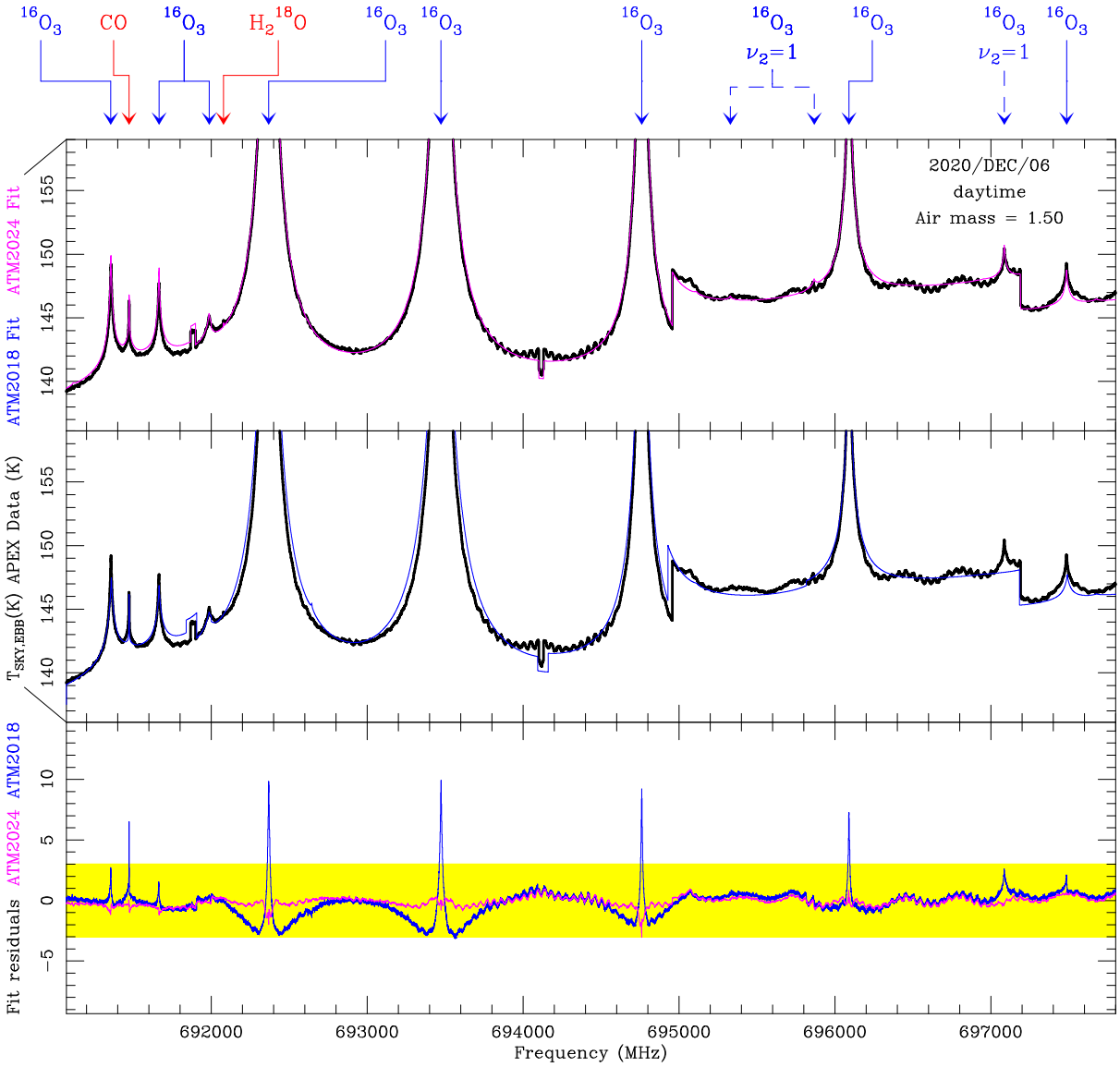

Figure 11: Comparison of Dec. 6^{th} 2020 SEPIA660 data fit using the old 2018 ATM version and the new one (ATM2024) resulting from this study (part 3). See text.

An analogous cluster of lines, but for ν_2=1 O_3, appears between ∼665.8 and 668.2 GHz, that is totally missed in ATM2018 but nicely reproduced by ATM2024, as seen in Fig. 10. In fact the red residuals shown in this figure are almost entirely within an astonishing ±1 K range.

The data displayed in Figures 9, 10 and 11 were obtained mostly at night. However, the end of the Dec. 6^{th} 2020 run (frequencies above ∼690 GHz) occurred after sunrise. Therefore, we adjusted here a new (Summer/Day) vertical profile for ozone, trying again to reduce the residuals of the ATM fits to the data as much as possible. The result is again excellent (see Fig. 11). Also, within the same frequency range there is a CO line, also perfectly fitted with the CO vertical profile from [Pardo et al. (2022)].

A ∼2 K O_3 ν_2=1 feature at 697.1 GHz according to the data is missed by ATM2018 (O_3 ν_2=1 was implemented in ATM2018 but disabled) and appears in ATM2024, with almost no residual.

We checked if any O_3 ν_1=1 or ν_3=1 lines are visible in the data, with negative results. It seems that the excitation temperature of these two vibrational modes (1588.41 and 1500.48 K respectively), ∼500 K higher that that of the ν_2=1 mode (1009.5 K) is enough to make the rotational lines in those vibrational modes not visible for our sensitivity. Therefore, in order to save computing time, we advise to keep the O_3 ν_1=1 and ν_3=1 vibrational modes disabled in ATM2024 for ALMA and similar observatories.

4.2 Collision Induced Absorption (CIA)

One of the main goals of this atmospheric study with APEX is to check for the consistency of the atmospheric radiative transfer model described in [Pardo et al. (2001b)] at all frequencies covered by these observations. On one side, the model relies upon a description of the different opacity terms (lines + CIA). On the other side, the model uses a priori vertical profiles of pressure, temperature and molecular abundances based on simple assumptions from the available data provided by auxiliary instruments such as weather stations, water vapor radiometers (WVR), etc.

The APEX WVR provides measurements of the atmospheric brightness temperature of the 183 GHz water line and over 6 defined band passes to spectrally characterize the emission. The band passes are placed symmetrically from the center of the water line (183.310 MHz) with a given bandwidth. From the closest to the line center outwards, the offsets are (in GHz): ±0.6, ±1.5, ±2.5, ±3.5, ±5.0, and ±7.5. Their bandwidths, respectively, are (also in GHz): 0.2, 0.2, 0.2, 0.2, 0.4 and 0.5. Once these simple spectral data are taken, an atmospheric radiative transfer model (ATM) is used to fit the observations and estimate the PWVC. The key point here is that the atmospheric opacity, and therefore its brightness temperature are both largely dominated by the 183 GHz water vapor line so that the derived PWVC would barely reflect other aspects of the model such as minor gases, CIA or far wings of other H_2O lines. The percentage of the total opacity in the central three channels due to the water line exceeds 95% for 1 mm PWVC and the dry opacity represents less than 1.5% (see Figure 1). However, the APEX spectra presented in this work have many frequency ranges where H_2O line opacity is not as dominant, or even not the main contributor to the total opacity and, therefore, sky brightness temperature. Therefore, the study is based on keeping the PWVC derived from the WVR as a reference to be compared to PWVC retrieved from the different APEX spectra. In other words, we are not questioning here the WVR retrievals. Any errors on the model description of opacity components other than the 183.31 GHz H_2O line should show up as discrepancies in this comparison.

Minor gases and CIA opacity are much more important in our APEX atmospheric data because these spectra cover large frequency ranges where water lines do not dominate the opacity. Therefore, a simple exercise comparing PWVC derived from WVR data versus that derived from fitting the APEX spectra themselves, would provide a very strong validation tool for CIA in the model.

In order to do the proposed validation, we smoothed the 56 spectra to a resolution of 9.7 MHz, large enough for the broad atmospheric H_2O and O_2 lines and still providing several tens of channels on narrower O_3, N_2O, CO and other features. We used those spectra to perform PWVC fits under some simple assumptions:

- Pressure and temperature at the ground are fixed to the average values provided by the weather station during the scan.
- Tropospheric temperature lapse rate is fixed to -5.6 K/km.
- Tropospheric water vapor scale height is fixed to 2.5 km.
- Stratospheric and mesospheric P/T profiles are fixed to the [U.S. Standard Atmosphere (1976)] values for a Tropical atmosphere, with a transition zone numerically adjusted to match the temperature values in the tropopause reached with the above assumptions.
- The ozone profile is fixed by hand to minimize residuals near its lines, but with no true fit.

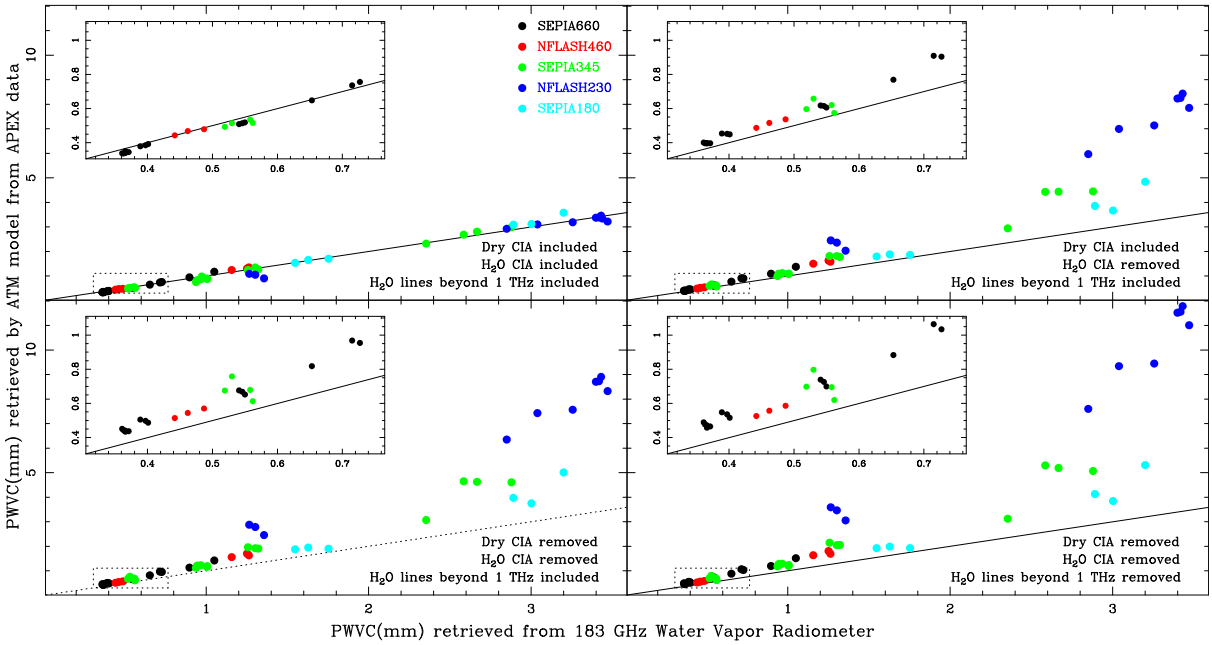

Figure 12: PWVC provided by the water vapor radiometer (average over the scan) versus the one derived from ATM fitting of the whole APEX spectrum under various scenarios. The inset in each panel corresponds to a zoom in the area marked by the dotted box.

- Vertical distributions of other minor gases are left as in the [U.S. Standard Atmosphere (1976)] Tropical atmosphere.

Ahead in this report, finer fits for O_3 and other gases will be performed. For now, a first fit is carried out with the full opacity breakdown in the ATM model: H_2O and dry atmospheric lines below 1 THz, including all relevant isotopologues and vibrationally excited states, dry and wet CIA, and far wings of water vapor lines with central frequencies beyond 1 THz. Then other fits are carried out removing one or several of these opacity contributions.

4.2.1 Discussion on CIA

In recent years, a number of publications have addressed the question of the non-resonant foreign wet and dry CIA in the atmosphere from theoretical calculations or laboratory experiments under well controlled conditions ([Boissoles et al. (2003)], [Podobedov et al. (2008)], [Tretyakov at al. (2015)], [Serov at al. (2020)]). Our observations, of course, are under less controlled conditions and we detect the radiation after its propagation through the whole atmosphere to our detectors. Therefore, we cannot address the fine details given in the above-cited publications. However, the description of these opacity terms in ATM for the conditions of millimeter and submillimeter ground-based observatories can be validated with our data, even with the experimental data scattering that we can expect in this 3 year study. Even so, this validation is a big step forward in the state-of-the-art of atmospheric models used by the observatories.

Following the procedure explained in the previous subsection we have plotted, for each one of the 56 APEX spectra, PWVC fit results against the temporal average of the WVR-based PWVC. Although experimental scatter should be expected, if the model has a correct CIA description, an alignment around the diagonal line should be found. On the contrary, a misalignment should appear if the full model is inconsistent, or if different terms of the correct model are removed. Figure 12 shows the results of this exercise. The top-left panel, corresponding to the full ATM model shows a relatively good agreement

for the whole PWVC range of ∼ 0.35 mm to 3.5 mm, or one order of magnitude. An inset provides a fit into the 0.3-0.8 mm PWVC range. There are three dark blue dots around 1.0-1.3 mm corresponding to a three air mass sky dip taken with nFLASH230 on Oct. 31^{st} 2021 that are a bit off the line. Since the nFLASH230 band does not include any strong water line, it is the most sensitive to possible calibration issues. Nevertheless we have decided to keep those spectra in the analysis as they provide significant information on all other panels. The disagreement between the data in this top-left panel and the perfect diagonal line is only 6.25%, well within the expected experimental scatter.

The top-right panel of Figure 12 shows that, as expected, the "foreign" wet CIA due to both O_2-H_2O and N_2-H_2O collision mechanisms, is a relevant element in the model as its removal from the model produces a large disagreement in that panel (55.79% overall difference from the diagonal line). The largest disagreement appears in the nFLASH230 spectra in a frequency range where "foreign" wet CIA is the dominant opacity term. On top of that, there is a general trend of more disagreement for wetter situations, and this can be also seen in SEPIA180 or SEPIA325 because these spectra cover not only the strong 183 GHz or 325 GHz water lines, but a significant range of "window" frequencies where, in fact, "foreign" wet CIA opacity has a large share to the total opacity.

In general, the dry CIA (N_2-N_2, N_2-O_2, O_2-O_2 collisions) is much more constant and weaker (except for very dry situations) than the wet CIA. Therefore its effect is much more limited, as shown by the plot in the bottom-left panel where we have removed the dry CIA term from the model in addition to the "foreign" wet CIA. The overall difference from the diagonal line increases now to 63.10%.

Finally, removing additionally the far wings of H_2O lines centered above 1 THz also adds to the disagreement (bottom-right panel in Figure 12). It increases to 89.60%.

These results are quite conclusive: The ATM model needs all the original opacity terms to provide consistent results at least for the atmospheric conditions corresponding to high and dry millimeter and submillimeter observatories, as it was the case for Mauna Kea and now Chajnantor. Based on these results we would not suggest any changes in the model that may affect broadband opacity terms.

4.3 Fine structure of the atmospheric mm/submm spectrum

We can now focus on the line-by-line details of the model. For that we will follow the strategy of fitting individual scans following the 4.2 list of assumptions. We can now adjust the vertical profile of each individual molecule in order to minimize the residual for its lines, and check for consistency between the retrieved PWVC from each individual scan, merged into a curve as function of frequency, against the same parameter as measured by the Water Vapor Radiometer (although this has already been analyzed in the previous section). This fine analysis provides also the opportunity for:

- Check for artifacts coming from the image side band.
- Check for standing waves and other instrumental issues affecting the overall spectral shape.
- Check for missing molecules.
- Check for missing lines of an included molecule.
- Check for errors in the frequency and/or line shape of particular lines.

Here we need to use a relatively fine spectral resolution, although the original one (∼61kHz) will make the calculations extremely long without adding any information due to the short frequency ripples in the data. Since typical half power line widths for atmospheric lines are at least several hundred MHz, smoothing the data to ∼1 MHz is a good compromise. In practice, we decided to work with two different final resolutions: 512 and 2048 kHz, the last one for quicker preliminary calculations and the second one for final calculations once the basic parameters are correctly set-up. Also, due to clear differences in performance between the different receivers, we present separately the data obtained with each one of them and their analysis.

4.3.1 SEPIA660 data and analysis

Since the beginning of this study it appeared that this receiver, designed to cover the 450μm window (∼575-740 GHz) was the more stable and the one providing cleaner spectra. Once the calibration issues were solved, we have good spectra from six different dates: Dec/06/2020 (summer), May/11/2022 (fall), and four dates in the winter of 2022 (Aug. 25 and 27, Sep. 1 and 3). Only one of those observing runs took place completely in the middle of the night (Aug/27/2022). The observations of Dec/06/2020 were in transition from nighttime to daytime. All other runs ere achieved during daytime. The sample is far from ideal for an exhaustive research on seasonal variations, but the day/night differences become immediately clear, especially for mesospheric ozone. The range of PWVC covered by these observations is ∼0.3-1.2 mm, which is just ideal for this atmospheric window since dryer conditions are rare, and the window becomes useless for astronomy if PWVC exceeds ∼1 mm. We start our analysis with the data acquired on Dec. 6^{th} 2020, presented in Figure 13 and, for a better vision of data and model fits, es a series of Zooms on Figures 48 through 52.

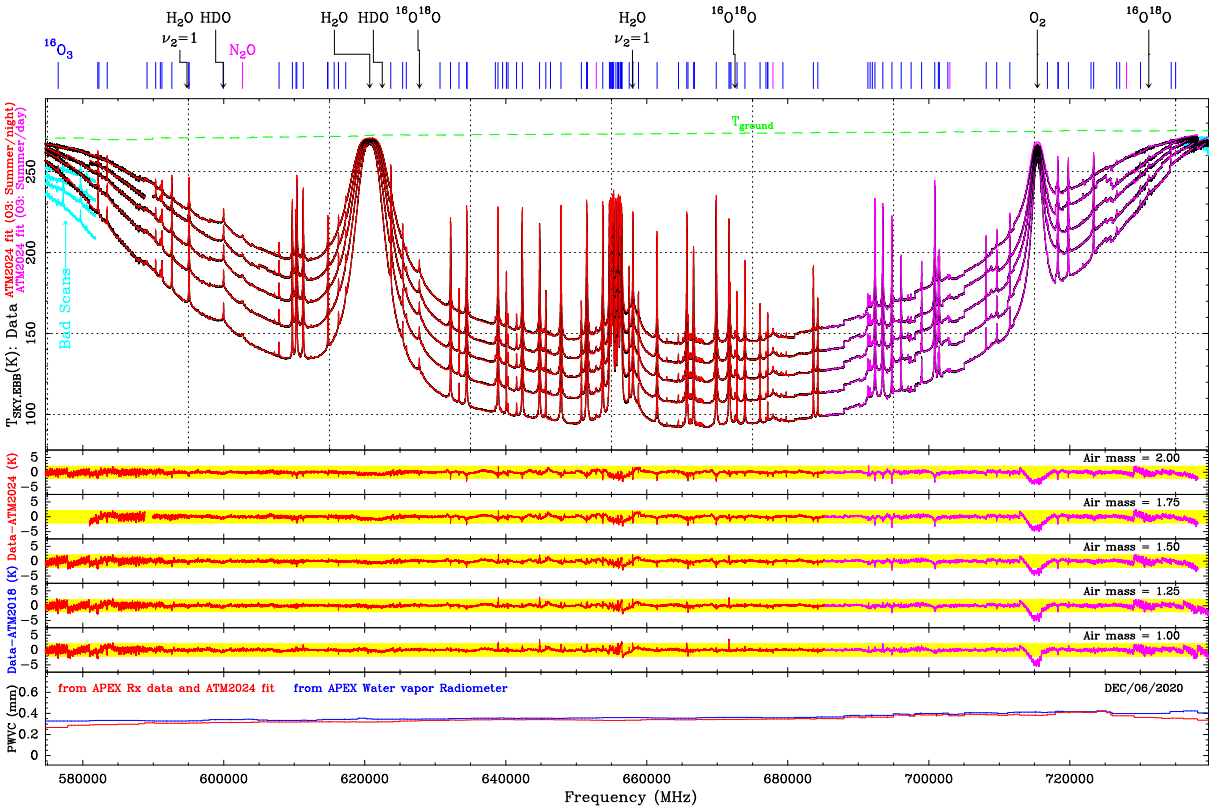

Figure 13: Ending point of this study. SEPIA660 atmospheric scan acquired on Dec 6^{th} 2020, with their correct calibration, and their fit them with the new 2024 version of ATM that will be delivered to ESO.

The data (black histograms) in Figures 13 and 48-52 have been fitted with the 2018 and 2024 versions of the ATM code using the PWVC as the only free parameter for each individual scan (∼ 3.9 GHz) and then all scans and fit curves have been merged into a single file for the whole atmospheric window. An automatic procedure has been implemented to discard bad scans (shown in the figures). Although the best fit PWVC values are stored for each air mass as a function of UT and frequency, they are merged into a single average curve for all air masses to simplify the figure. Vertical profiles of O_3, N_2O, CO and HCl have been adjusted prior to the general PWVC fits by using just frequencies around a few sample lines, since the retrieval of those profiles is not possible for all scans.

This is the best SEPIA660 that we have, and it corresponds to the driest situation. The main conclusions from it are the following:

- Artifacts from the image side band: We did not notice any line showing up.
- Standing waves: They exist, especially noticeable near the edges of the band, but they are much shorter than the typical line widths, even for minor gases s, and do not compromise the fits.
- Missing molecules. This data set has served us to see that O_3 ν_2=1 lines should be activated in the ATM code (they are coded in the 2018 version but disabled to reduce calculation time). Three species that were not included in the 2018 code have detected lines in this range: HCl, HCN and O_2 ($^1\Delta$). All three have been included in the ATM 2024 implementation from the MADEX Database [Cernicharo(2012)].
- Missing lines of an included molecule. Three weak O_3 lines, visible in the data, were missing in ATM 2018, due to the energy level cutoff, and they have been included in ATM 2024 from the MADEX Database [Cernicharo(2012)].
- Errors in the frequency and/or line shape of particular lines. Small errors have been detected in the central frequencies of a few O_3 ν_2=1. They have been corrected for the ATM 2024 implementation.
- In addition to that, the O_3 has been adjusted to minimize the residuals for about 2/3 of the observing time. However, those residuals appear larger towards the end of the observations (high frequency end) because it was the moment of sunrise and the mesospheric O_3 profile was obviously changing rapidly.

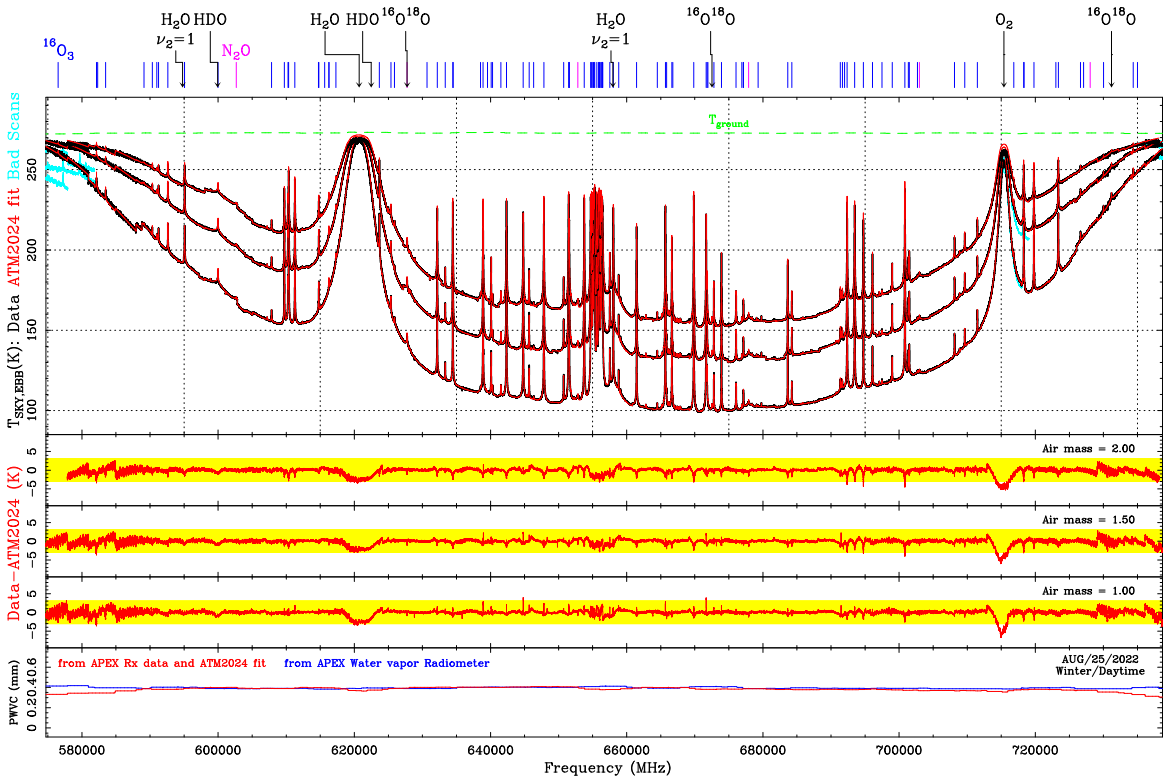

Figure 14: Three air mass sky dip carried out with SEPIA660 on Aug. 25, 2022, and ATM model fits using the Winter/Day O_3 vertical profile from Table 2 and the PWVC as free parameter.

Complementary data sets in this frequency range have been obtained at different dates. Since the SEPIA660 receiver is the most stable of all receivers used in this work, these additional results provide further support to the above conclusions. The observation strategy is, however, different. The number of air masses was reduced form 5 to 3, and the elevation of the telescope was not changed until all frequencies have been scanned. This change in the observational procedure does not have a noticeable impact on the experiment's output as one can see in Figures 94-98 of the next 5 pages (Aug. 25^{th} 2022 data).

We did find some inconsistencies around the 715 GHz O_2 line but a closer look to the data allow to identify again several bad scans with inconsistently low $T_{SKY,EBB}$ near the line center. Those scans were discarded for the fits.

Also, some bad scans on the lower frequency end of the receiver (∼575-582 GHz) display too low $T_{SKY,EBB}$ and ghost lines. Although we kept other scans that did not show these ghost lines and for which the signal was higher, the PWVC derived is not very consistent. In addition, the data have important ripples at different scales. Although a fit can be obtained, these frequencies are outside the optimal range of the receiver (see Section 2).

The ATM2024 fit residuals are again remarkably low, well within the ±3 K yellow strip displayed in Figures 94-98 We should especially note the very good fit obtained for the cluster of O_3 lines in the range ∼354.5-357.0 GHz. The 626 GHz HCl line recently added to ATM2024 also fits very well, and the agreement between the two PWVCs (WVR and SEPIA660 based) is remarkably good. After all the calibration issues and our work in refining the ATM model, the outcome is even beyond our expectations.

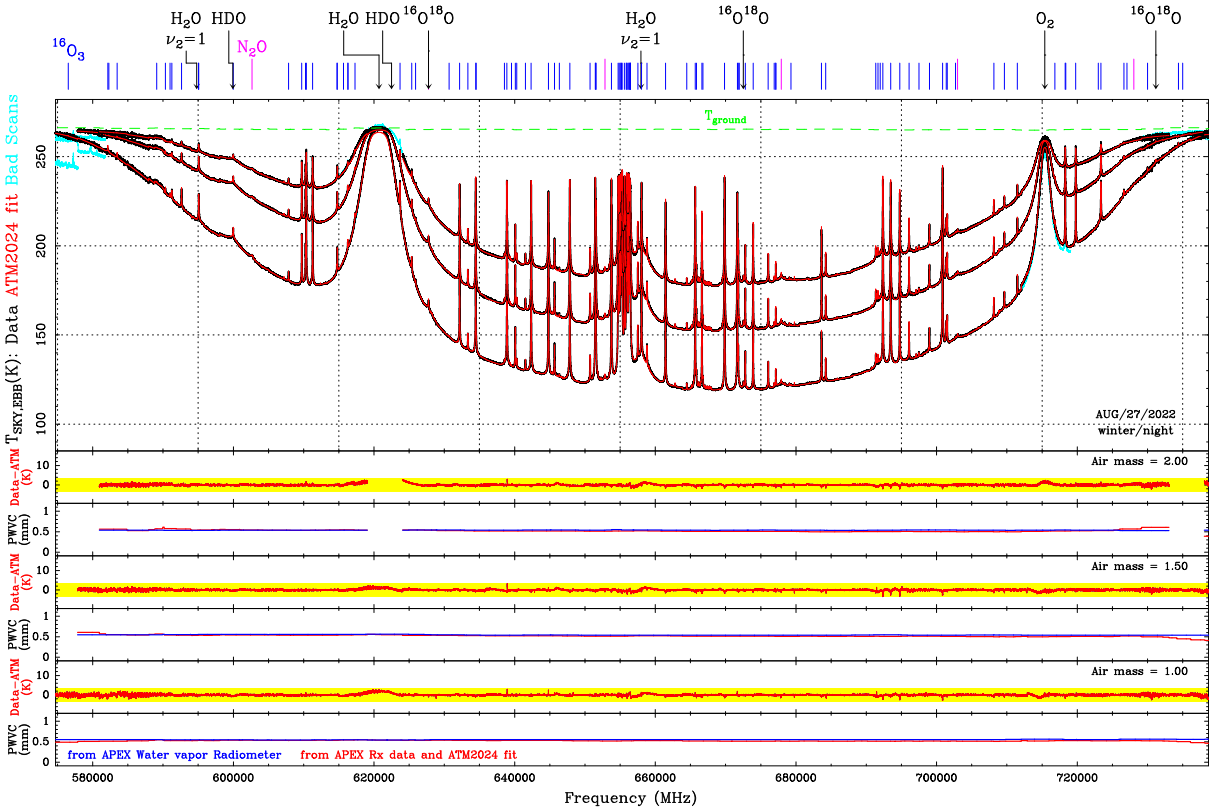

Figure 15: Three air mass sky dip carried out with SEPIA660 on Aug. 27, 2022, and ATM model fits using the Winter/Night O_3 vertical profile from Table 2 and the PWVC as free parameter (upper panel).

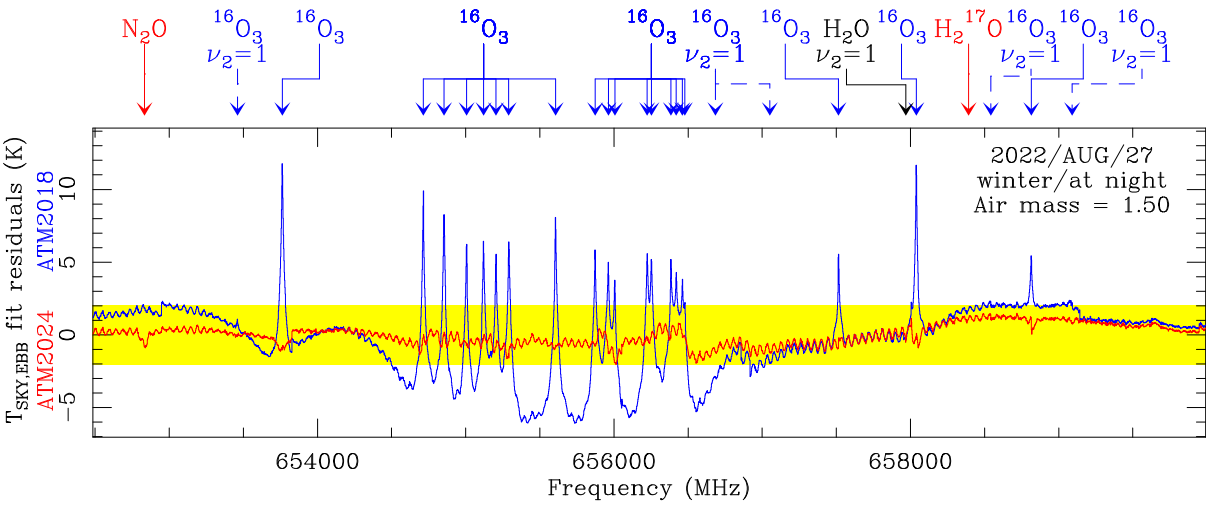

Figure 16: Fit residuals on SEPIA660 Aug/27/2022 data resulting from ATM2024 around 656 GHz.

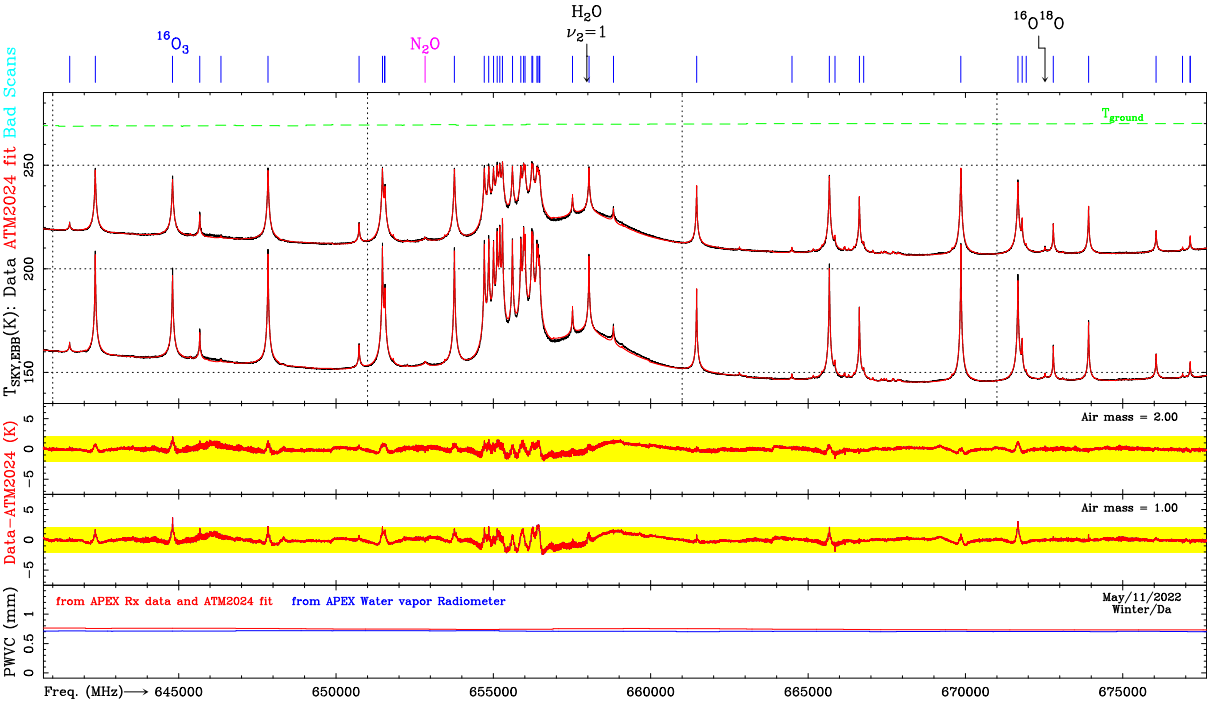

Figure 17: May 11^{th} 2022 SEPIA660 data collected at air masses 1.0 and 2.0 (central frequency section), with ATM fit results. Residuals on O_3 probably indicate the need of an specific early winter O_3 profile.

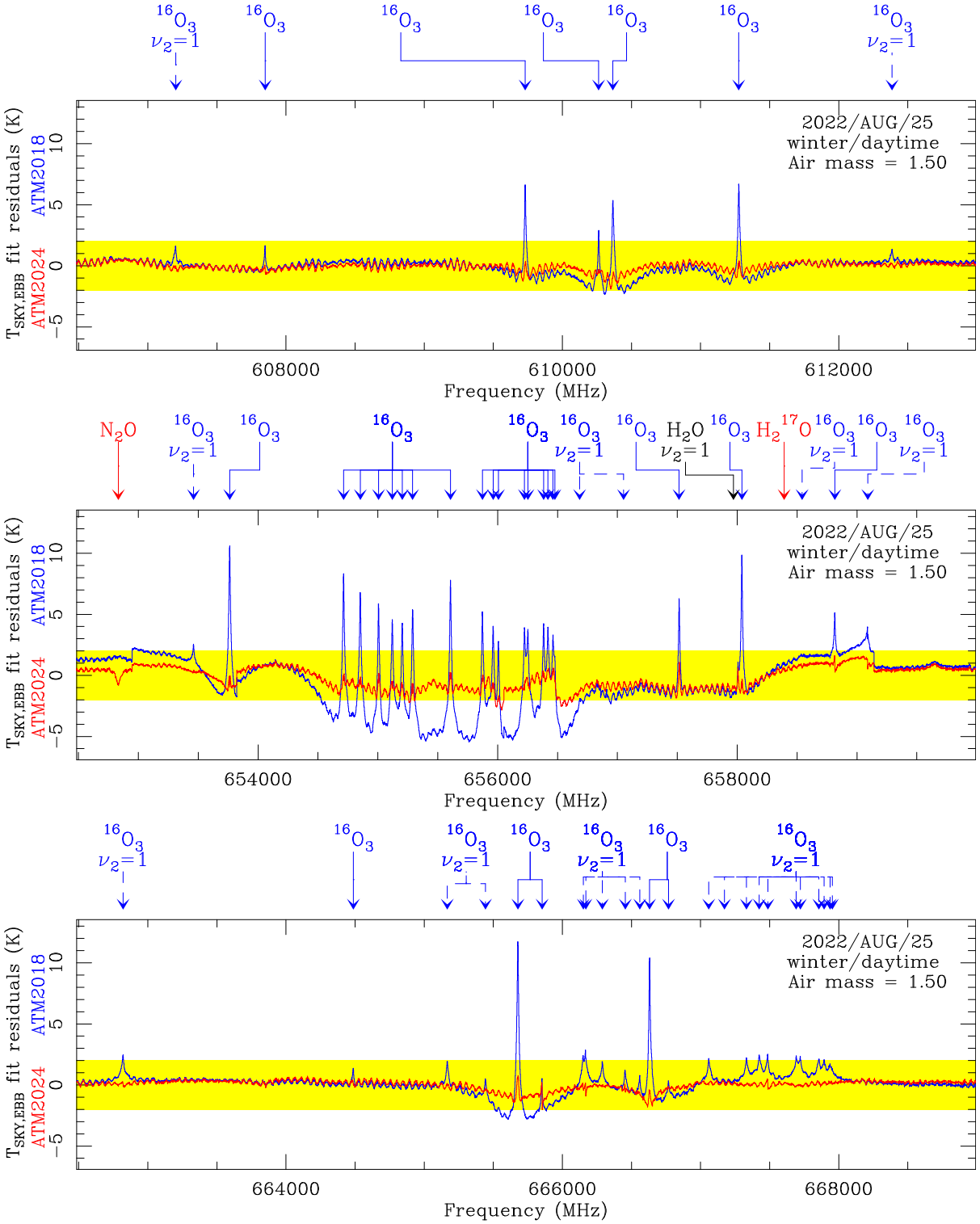

Figure 18: Fit residuals on SEPIA660 Aug/25/2022 data resulting from ATM2018 and ATM2024 at selected frequency ranges.

4.3.2 Seasonal and diurnal variations of O_3 vertical profiles and lines from other minor gases

Since SEPIA660 is the most stable and reliable receiver in this study, we have accumulated more data with it than with all the other receivers. In addition, due to the high frequency, the observing runs with this receiver have been carried out always under dry or very dry conditions (PWVC < 1 mm). The range of frequencies accessible with this receiver hosts many ozone lines and, in particular, a cluster of lines between ∼654 and 660 GHz. Therefore, those data are the best we have to check for diurnal or seasonal variations (known to exist) in O_3 vertical profiles, in order to implement new reference profiles in ATM2024 taking into account season and day/night conditions. This is aimed at improving the current implementation using just one reference O_3 profile coming from the U.S. Stnd. 1976 Atmosphere (Tropical), which is proved to be far from ideal, but cannot be taken as the final solution since we still have only a few valid data sets so that no statistical study can be performed.

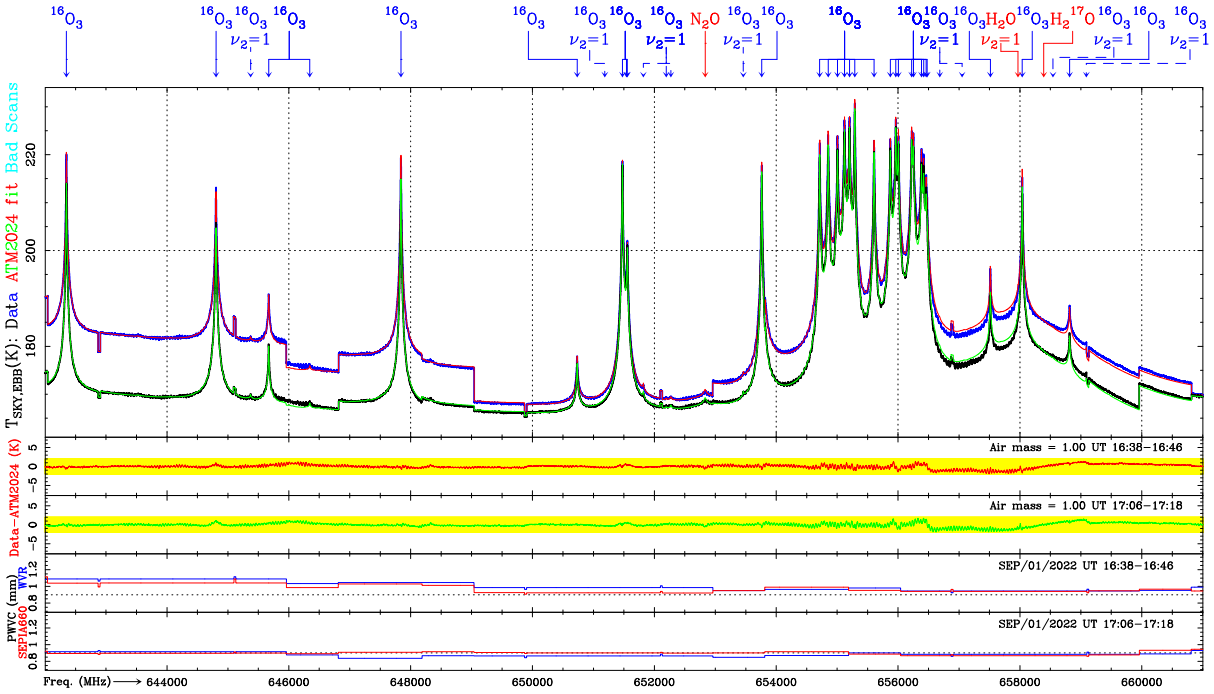

Figure 19: Two consecutive observations carried out on Sept. 1^{st} 2022 with SEPIA660 at air mass 1.0. The PWVC was evolving as tracked in a similar way by the 183 GHz WVR and by the SEPIA660 spectra. Residuals on O_3 lines are almost nonexistent with the Winter/Day vertical profile from Table 2.

Figures 14 and 18 show final calibration and analysis of the the sky dip taken on Aug/25/2022 during daytime (Winter/Day). It is interesting to see that the agreement of PWVC retrieved from SEPIA660 and the 183 WVR is very good except for the edges of the receiver, where the atmosphere gets almost opaque and the performance of the receiver is not optimized.

It is impossible to get perfectly flat residuals but the adopted Winter/Day vertical profiles for ozone reduce significantly those residuals that are kept well within the ±3 K range (marked as a yellow strip in Figures 14 and 18 for almost the entire frequency range. However, the peculiar residual around the 715 GHz O_2 line needs further investigation.

The only SEPIA660 sky dip performed in August 2022 during the night was on the 27^{th}. In this case, probably due to the better stability in the middle of the night (compared to daytime), the ATM2024 fits have particularly low residuals (within ±1.5 K, see Figure 15) with a very good match between data and model even at the center of the 620 GHz H_2O line and the 715 GHz O_2 line. In that figure, the

PWVC are shown separately for each airmass. The agreement between the WVR and the SEPIA660 derived values for all three airmasses is very good because the night was very stable and the sky dip is very consistent.

The two air mass sky dip achieved on May/11/2022 during daytime has been fitted for PWVC using as default the same O_3 vertical profile used for the diurnal August scans (Winter/Day from Table 2). The residuals are reasonably low although we should explore if an early-winter specific profile would be necessary. Figure 17 zooms on the central part of the SEPIA660 band, where the PWVC column agreement, between the two methods to obtain that parameter, is very good.

Some additional data (single air mass = 1.0) were taken on Sept 3 and 5, 2022 that are displayed on Figures 7 and 8. In the analysis of those spectra we used the same O_3 Winter/Day profiles from Table 2 with similar results.

In the following sections we will analyze data obtained with other receivers. For them, the reference vertical O_3 profiles are those obtained from the SEPIA660 receiver because, as we said, is the one that has provided the best performance in this experiment.

h	O_3 (cm^{-3})				N_2O	CO	HCl	HCN
(km)	Winter/Night	Winter/Day	Summer/Night	Summer/Day	(cm^{-3})	(cm^{-3})	(cm^{-3})	(cm^{-3})
5.137	3.6484e+17	3.6484e+17	2.8065e+17	2.8065e+17	4.7309e+18	1.9256e+18	3.4009e+15	2.1289e+15
5.290	3.6237e+17	3.6236e+17	2.7874e+17	2.7874e+17	4.6576e+18	1.8941e+18	3.2057e+15	2.0959e+15
5.462	3.5958e+17	3.5958e+17	2.7660e+17	2.7660e+17	4.5764e+18	1.8589e+18	2.9982e+15	2.0594e+15
5.655	3.5644e+17	3.5644e+17	2.7419e+17	2.7419e+17	4.4867e+18	1.8173e+18	2.7792e+15	2.0190e+15
5.872	3.5290e+17	3.5290e+17	2.7146e+17	2.7146e+17	4.3873e+18	1.7705e+18	2.5493e+15	1.9743e+15
6.117	3.4887e+17	3.4887e+17	2.6836e+17	2.6836e+17	4.2771e+18	1.7166e+18	2.3089e+15	1.9247e+15
6.394	3.4429e+17	3.4429e+17	2.6484e+17	2.6484e+17	4.1548e+18	1.6546e+18	2.0611e+15	1.8697e+15
6.709	3.3911e+17	3.3911e+17	2.6085e+17	2.6085e+17	4.0195e+18	1.5841e+18	1.8111e+15	1.8088e+15
7.068	3.3261e+17	3.3261e+17	2.5585e+17	2.5585e+17	3.8704e+18	1.5042e+18	1.5670e+15	1.7416e+15
7.480	3.2421e+17	3.2421e+17	2.4939e+17	2.4939e+17	3.7066e+18	1.4138e+18	1.3375e+15	1.6676e+15
7.957	3.1854e+17	3.1854e+17	2.4503e+17	2.4503e+17	3.5205e+18	1.3072e+18	1.1093e+15	1.5842e+15
8.513	3.1817e+17	3.1817e+17	2.4474e+17	2.4474e+17	3.3073e+18	1.1778e+18	8.8940e+14	1.4889e+15
9.169	3.1667e+17	3.1667e+17	2.4359e+17	2.4359e+17	3.0686e+18	1.0353e+18	6.8462e+14	1.3835e+15
9.954	3.1769e+17	3.1769e+17	2.4438e+17	2.4438e+17	2.7966e+18	8.8004e+17	5.0543e+14	1.2663e+15
10.911	3.3295e+17	3.3295e+17	2.5611e+17	2.5611e+17	2.4717e+18	7.1226e+17	3.6578e+14	1.1322e+15
12.112	3.5359e+17	3.5359e+17	2.7199e+17	2.7199e+17	2.1027e+18	5.2047e+17	3.0825e+14	9.7959e+14
13.687	3.6471e+17	3.6471e+17	2.8055e+17	2.8055e+17	1.6868e+18	3.0320e+17	4.8640e+14	7.9369e+14
16.000	3.8334e+17	3.8334e+17	2.9488e+17	2.9488e+17	1.1749e+18	1.2532e+17	9.6799e+14	5.5865e+14
19.288	1.5924e+18	1.5924e+18	1.2249e+18	1.2249e+18	5.6047e+17	3.3297e+16	1.0322e+15	2.8409e+14
23.163	3.5794e+18	3.5794e+18	3.2174e+18	3.2174e+18	2.2243e+17	1.5030e+16	6.5856e+14	1.2707e+14
27.163	3.9858e+18	3.9858e+18	3.5828e+18	3.5828e+18	9.5824e+16	1.0057e+16	4.3395e+14	1.5773e+14
31.288	2.6977e+18	2.6977e+18	2.4249e+18	2.4249e+18	1.0069e+17	6.7100e+15	3.5690e+14	7.3350e+13
36.413	1.9551e+18	1.9551e+18	2.2248e+18	2.2248e+18	1.6999e+16	3.8164e+15	8.4084e+14	2.9932e+13
42.413	5.9272e+17	5.5568e+17	6.2977e+17	6.2977e+17	2.6161e+15	2.1748e+15	3.8318e+14	1.1375e+13
48.413	2.2797e+17	2.1456e+17	2.2350e+17	2.1456e+17	3.0997e+14	1.3174e+15	1.7594e+14	4.6004e+12
54.413	6.5598e+16	6.1739e+16	6.4312e+16	6.1739e+16	6.4182e+13	7.9475e+14	8.5212e+13	2.1081e+12
60.538	1.7201e+16	1.6189e+16	1.6863e+16	1.6189e+16	1.9287e+13	4.3930e+14	4.0595e+13	9.6728e+11
67.663	2.9491e+15	2.7757e+15	2.8913e+15	2.7757e+15	5.2012e+12	2.9822e+14	1.6750e+13	3.8624e+11
75.663	4.3216e+14	4.0674e+14	4.2368e+14	4.0674e+14	1.1025e+12	5.3115e+14	5.3725e+12	1.1949e+11
83.663	2.7932e+14	2.6289e+14	2.7384e+14	2.6289e+14	2.1156e+11	7.4482e+14	1.4707e+12	3.1536e+10
90.913	8.0550e+13	7.5812e+13	7.8971e+13	7.5812e+13	4.1311e+10	4.2860e+14	3.8101e+11	8.4647e+09

Table 2: Minor atmospheric gases profiles used in this study to minimize fit residuals on the lines from these molecules.

The impact of new molecules added to the model (HCN and HCl), as well as the updates on the vertical profiles of other already included (CO and N_2O) is very limited since all lines from these minor gases are very weak. In any case, this study has allowed to detect many of these lines and, therefore, improve ATM as Figures 20, 21, 22 and 23 show.

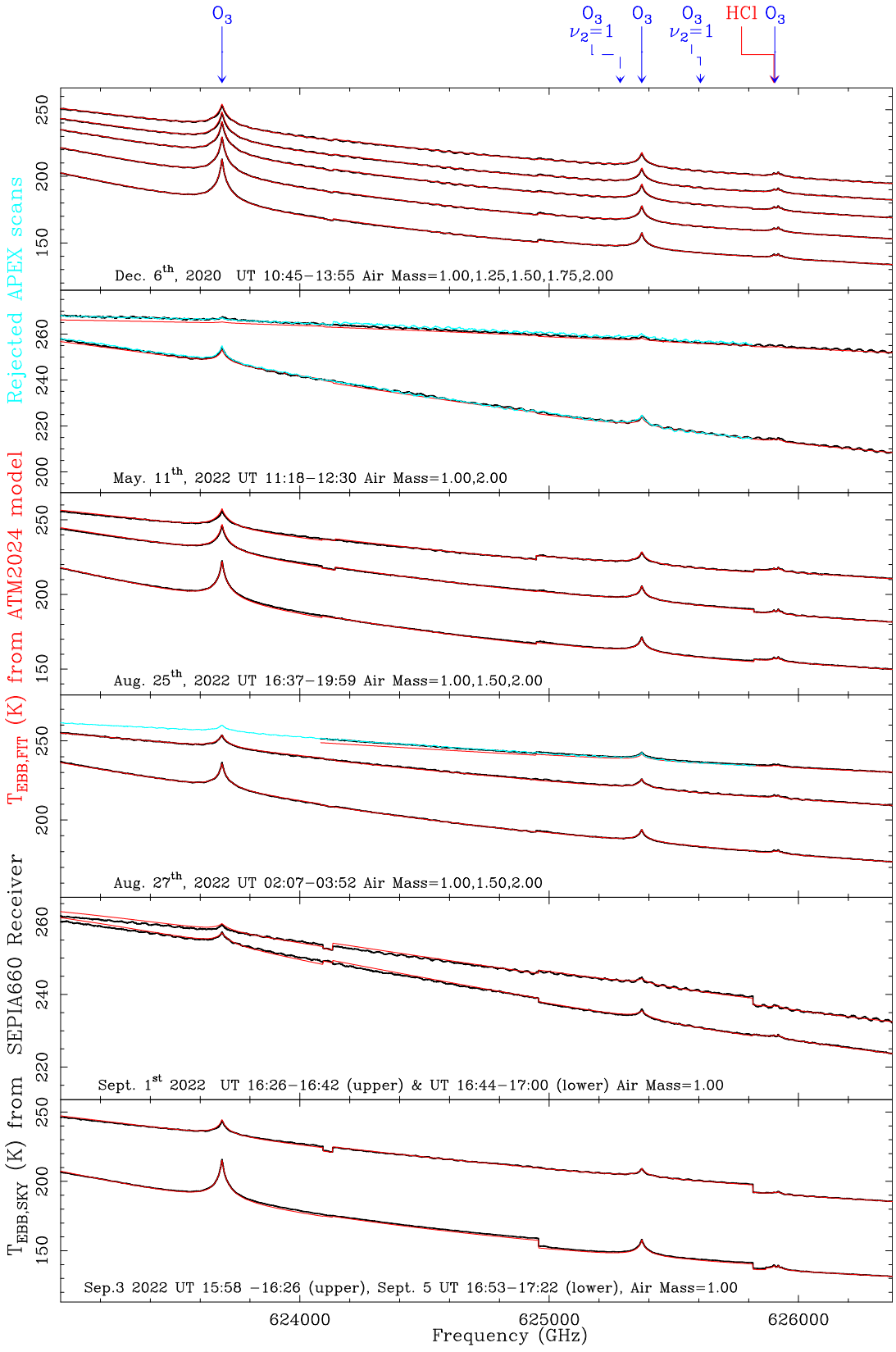

Figure 20: Data and model fits showing the molecule HCl, added to the ATM model in this study (see Table 2).

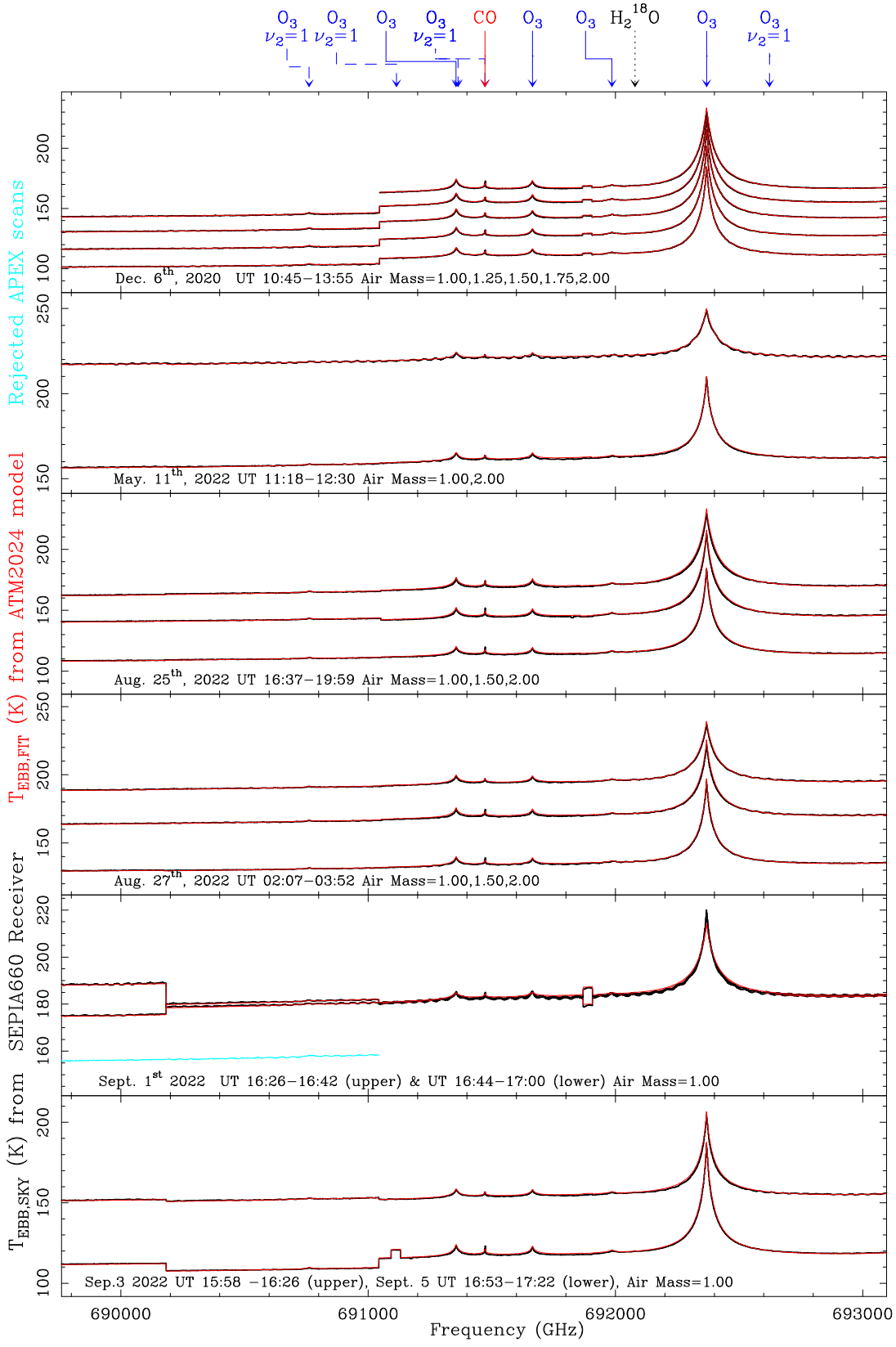

Figure 21: Data and model fits showing a line of CO, a molecule for which the vertical profile has been updated in the ATM model in this study (see Table 2).

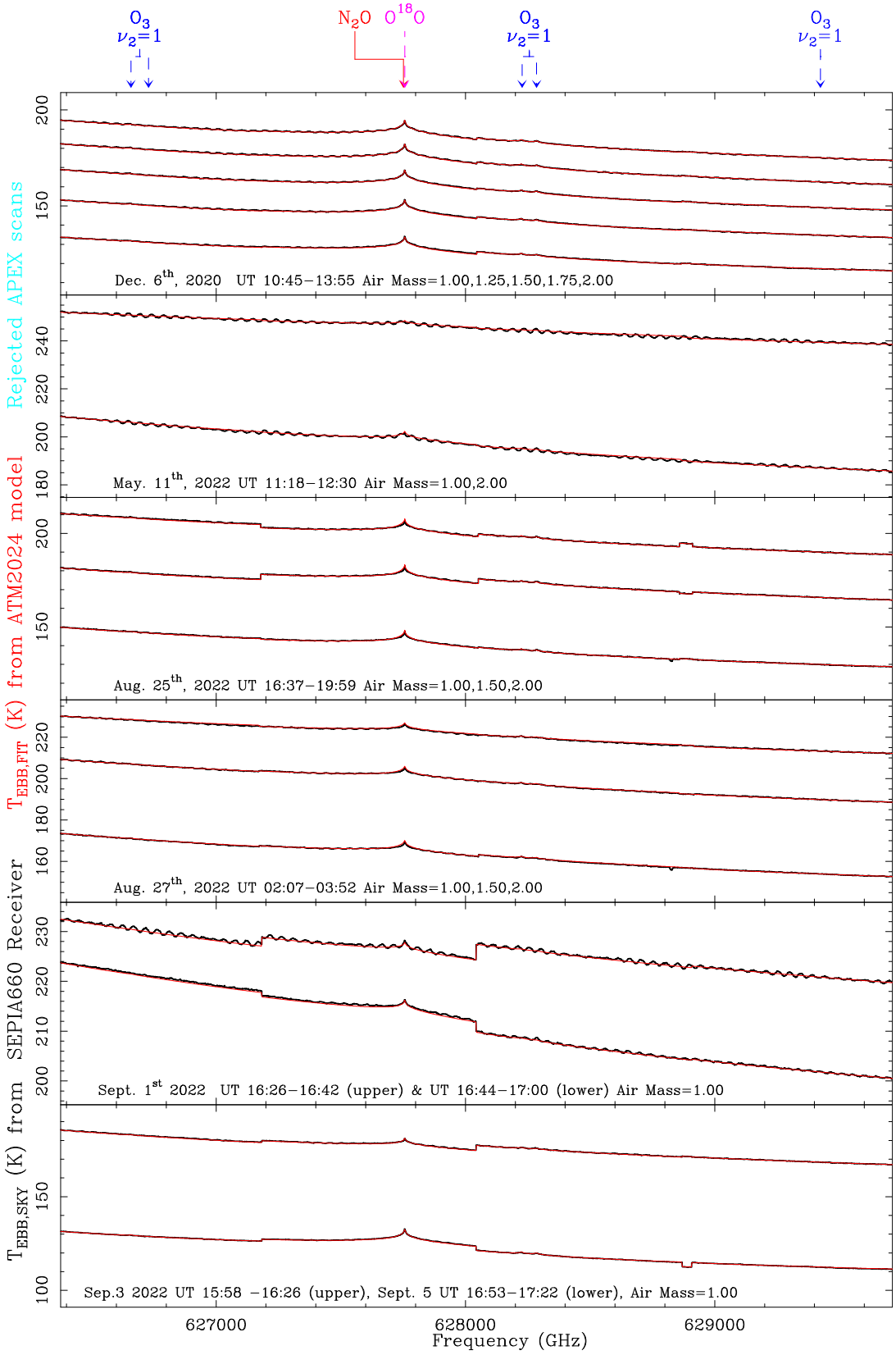

Figure 22: Data and model fits showing a line of N_2O, a molecule for which the vertical profile has been updated in the ATM model in this study (see Table 2).

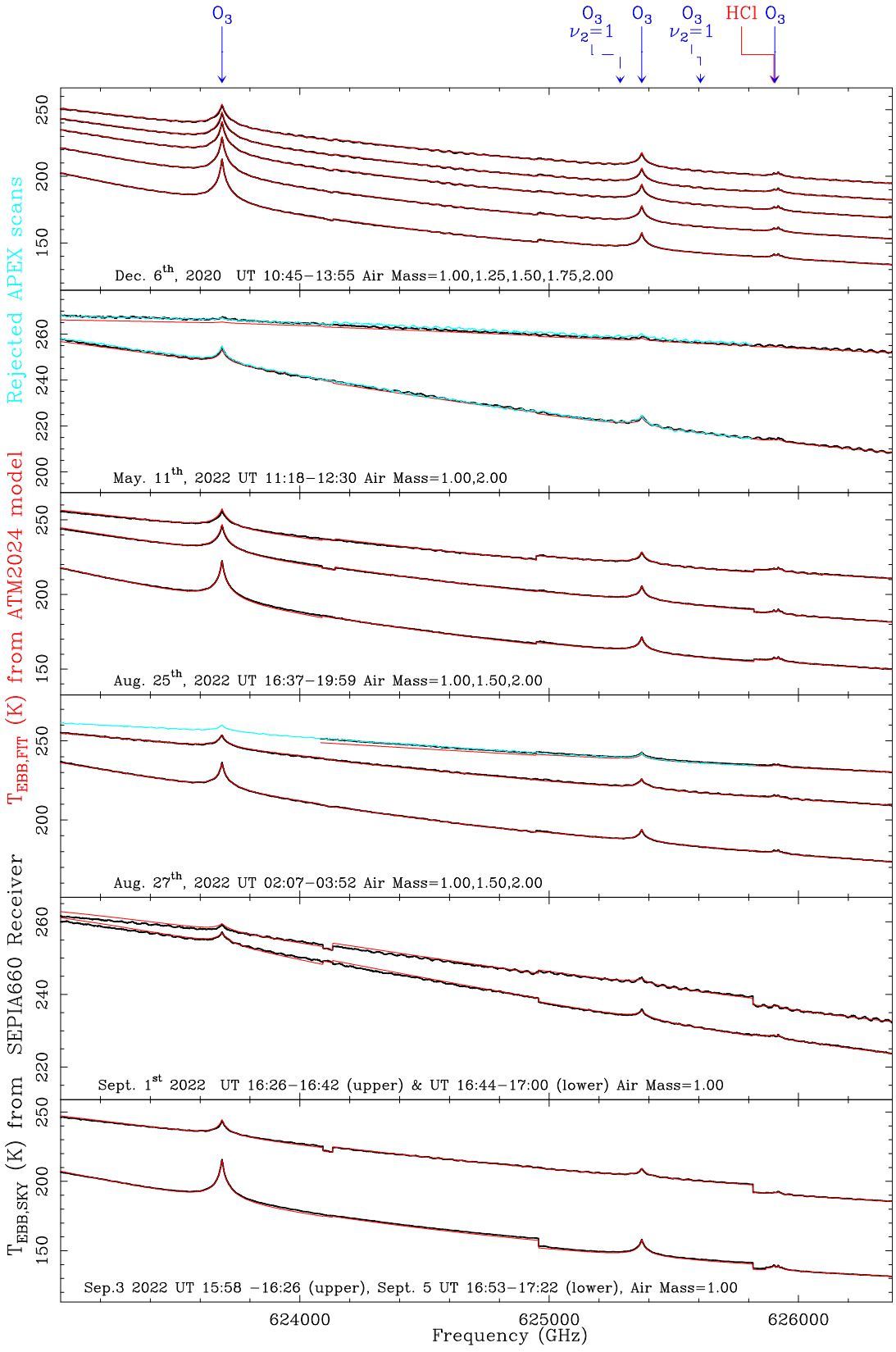

Figure 23: Data and model fits showing a line for the molecule HCN, added to the ATM model in this study (see Table 2).

4.3.3 nFLASH460 data and analysis

This receiver is designed to cover a complicated range of frequencies from the atmospheric point of view, limited by the strong water lines at 380 and 557 GHz, but with several other strong lines in between. A design characteristic of this receiver that is relevant for the study is that it contains two LO chains, one below 450 GHz and one above. This means that the spectral scans need to switch from LSB to USB across this dividing frequency. Both LO chains also have different behaviors in terms of stability, sideband rejection, etc. These technical peculiarities show up in the results as we will see in this section. We have basically two exploitable runs with this receiver, one on Oct. 31^{st} 2021 with PWVC ∼1.3 mm, and another one on Aug. 25^{th} 2022 with much dryer conditions (PWVC ∼ 0.4-0.5 mm). Both observing runs are very helpful because the PWVC was more than 1 millimeter and, in these conditions we have a good reference at the center of several H_2O and O_2 lines that should reach saturation and, therefore, with $T_{SKY,EBB}$ values very close to the ground temperature provided by the weather station.

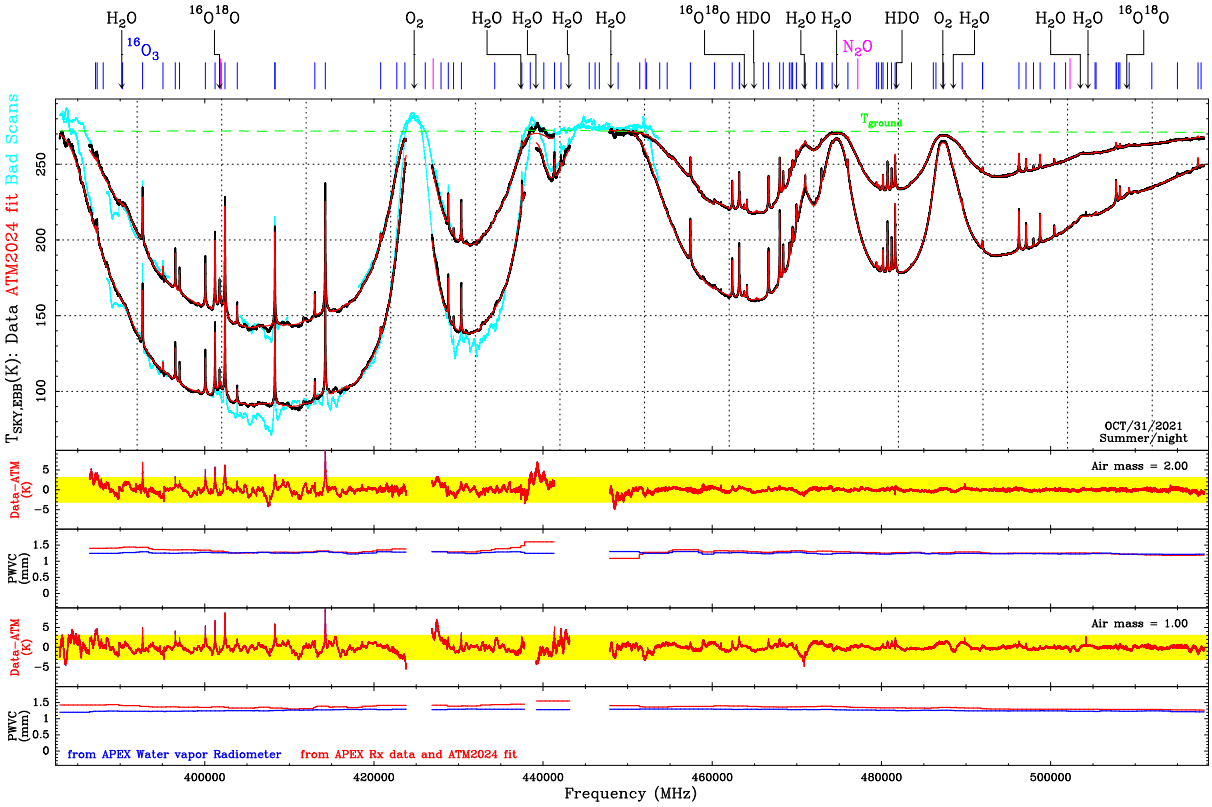

Figure 24: nFLASH460 3 air mass sky dip obtained on Oct. 31^{st} 2021.

In the 2021 data we can distinguish two frequency intervals with quite different quality output, that correspond to the two LO chains of this receiver. First, ∼382-450 GHz in which many scans have to be discarded (see Figure 24, some of them due to nonphysically high $T_{SKY,EBB}$ at frequencies where the signal is expected to saturate). Even for the scans that are kept for analysis, large residuals appear on some O_3 lines. The coincidence between PWVC derived for the heterodyne data and from the 183 GHz water vapor radiometer is more satisfactory as the opacity is lower, but it fails as the center of strong atmospheric lines is reached, most probably due to the fact that the offset in discarded scans still exists here at a lower extent. On the other hand, in the ∼455 to ∼520 GHz range, the data are much better, no nonphysical values of $T_{SKY,EBB}$ appear, the fit residuals are very small with the exception of ∼488 GHz for air mass = 1.5 (center of an O_2 line) and ∼471 GHz (center of a H_2O line) for air mass = 1.0. Even so, these residuals remain within the ±3 K yellow strip highlighted in the figure and the agreement in

the retrieved PWVC values is very good. In order to better understand what is going on with the lower LO chain it would be helpful to have a look to the other useful data set obtained with this receiver. The shape of the atmospheric spectrum is quite complex between ∼ 466 and 478 GHz due to the presence of two not so strong water lines with several ozone and N_2O lines superimposed, some of them quite weak but detectable. The fact that the ATM2024 fit residuals in this range are below 1 K, for typical $T_{SKY,EBB}$ values between ∼ 170 and 263 K is a very beautiful result. In order for the O_3 lines to fit, their attenuation in the troposphere by the water lines is correctly reproduced by the model.

The data obtained on Aug. 25^{th} 2022 in the same frequency range correspond to a quite different, much drier, situation (PWVC ∼ 0.5 mm). The ATM2024 fit residuals remain largely within the ±3 K but their appearance is not as smooth as in the October 31^{st} data. The discontinuities between tuning sections also appear larger, something that is related to the non-linearity of $T_{SKY,EBB}$ with PWVC. Any fluctuations of PWVC when its average value is low produce larger $\Delta T_{SKY,EBB}$ than the same absolute fluctuations over larger PWVC average values. Especially problematic is the frequency range ∼435-455, as it was on the October 31^{st} data, with a concentration of bad scans that need further investigation.

As it is the case in previously discussed data sets, the larger residuals obtained with ATM2018 are basically related to the standard O_3 profile used in that version being not appropriate for the true profile over Chajnantor. On the other hand the model fit around the center of the 487 GHz O_2 works once obvious bad scans with ∼30 K offsets in the line center are discarded. The technical origin of those bad scans is being investigated. The following pages show again a zoom over 12.6 GHz sections of the results presented globally in Figure 27. It can be seen that the local residuals are even better than in the previous case but the data contain probably more artifacts and steps due to a combination of relatively large PWVC fluctuations during a dry situation.

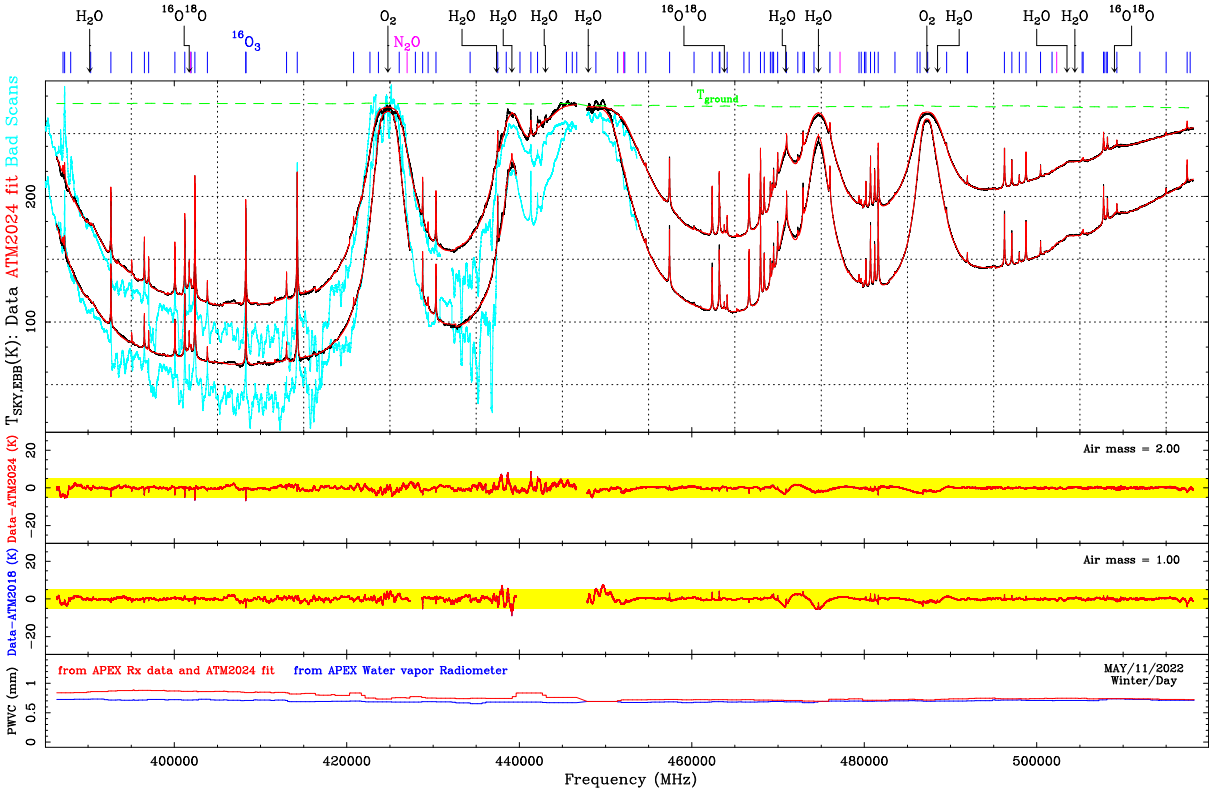

Figure 25: nFLASH460 atmospheric data recorded on May 11^{th} 2022 under PWVC around 0.5 mm. After discarding several bad scans shown in light blue, the ATM2024 fit provides a good match with 183 GHz WVR results. The residuals are less smooth, however, than for higher PWVC values.

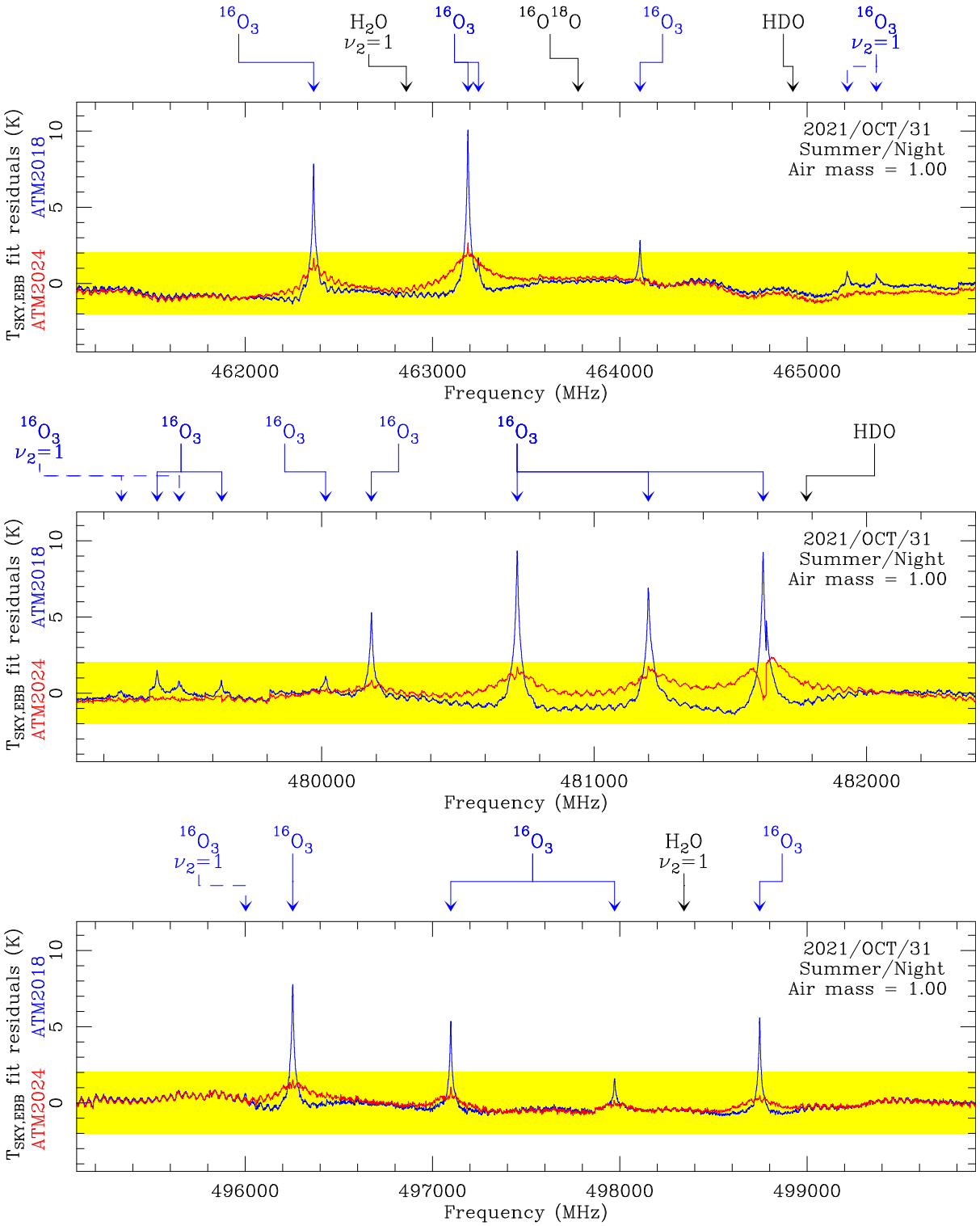

Figure 26: Zoom on the ATM2018/ATM2024 fit residuals at selected frequency intervals from the Oct. 31^{st} 2021 nFLASH460 2 air mass sky dip data.

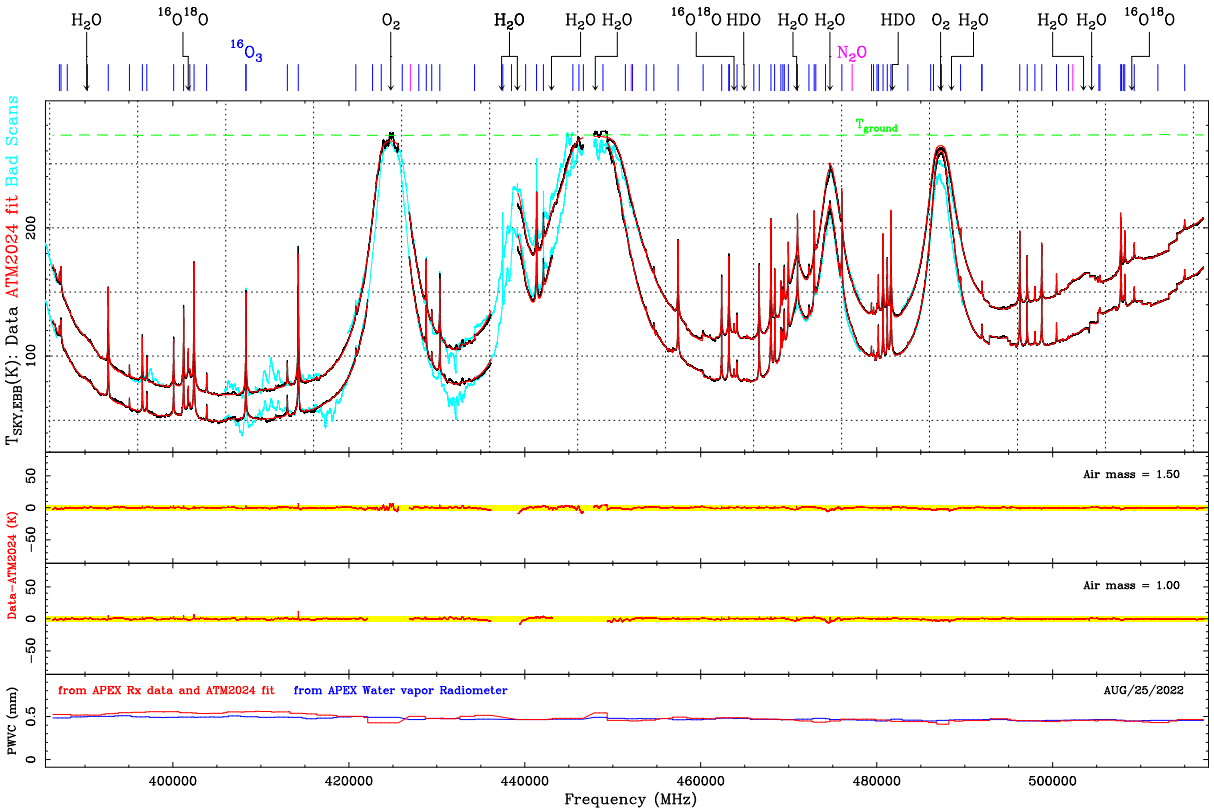

Figure 27: nFLASH460 atmospheric data recorded on Aug. 25^{th} 2022 under PWVC around 0.5 mm. After discarding several bad scans shown in light blue, the ATM2024 fit provides a good match with 183 GHz WVR results. The residuals are shown using the same vertical scale separation as in the upper panel.

4.3.4 SEPIA345 data and analysis

The fact that the frequency range of the SEPIA345 receiver hosts the 325 GHz water line, that in terms of strength and shape is quite similar to the 183 GHz one, makes this receiver quite well adapted for this study. Typical $T_{SKY,EBB}$ values would range from a few tens of K outside the water line, and the center of it would reach saturation for PWVC above ∼1.2 mm. The far wings of stronger water lines peaking at higher frequencies play a role here, as well as the CIA and many lines from minor gases.

On June 24^{th} 2021 we were trying to measure the atmospheric transmission against the full Moon. This experiment did not work because the intense flux from the Moon caused a lot of artifacts in the data. However, from the reference sky scans next to the Moon, we could assemble a whole spectrum with tunings taken at elevations between 43 and 47 degrees (air mass = 1.41 on average). The spectrum was quite clean and could be used for model fitting (see lower panel of figure 28).

Again, we found some bad scans at the water line center (∼20 K offset), probably of the same origin as others described in the previous section. A bad scan centered at ∼358 GHz is interesting because is one of the few examples of scans where apparently the frequency scale is totally wrong. The false ozone features exhibited in this scan mirror true ozone lines ∼7.8 GHz below in frequency. Similar problems happen with some (discarded) scans above ∼367 GHz (not shown on the lower panel of Figure 28). The ATM2024 residuals are generally within the ±3 K yellow strip, although not totally flat due to baseline artifacts that need to be carefully checked to see if they are actually weak missed lines. The agreement between WVR and SEPIA180 based PWVC is very good with the exception of the lowest frequency section (up to ∼308 GHz).

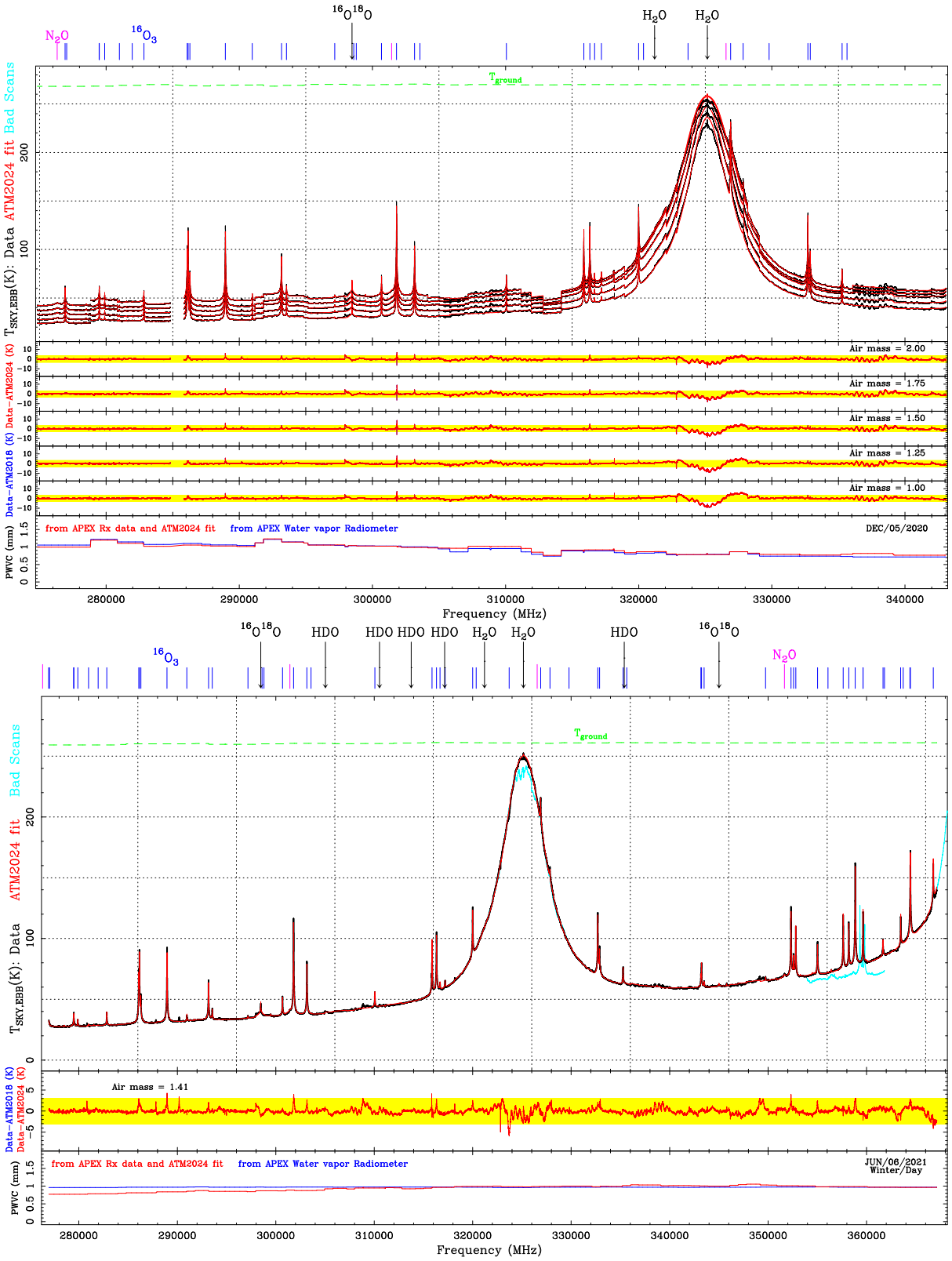

Figure 28: Upper panel: SEPIA345 atmospheric sky dip performed on Dec 5^{th} 2020 and ATM model fit with PWVC retrieval. Lower panel:SEPIA345 atmospheric data collected on June 24^{th} 2021 at elevations of 43 to 47 degrees.

This needs further investigation as the lowest frequency end corresponds to where the CIA is relatively more important. However, since a similar effect is seen in Figures 30 and 30 (lower panel) but not on Figures 28 (upper panel), 31, 32 and 33 corresponding to the same receiver.

In addition to that, O_3 line residuals appear larger in this frequency section on the positive side (data larger than model towards the line centers) which is exactly what we would expect if somehow the PWVC is underestimated. A small calibration error affecting this section could be the explanation.

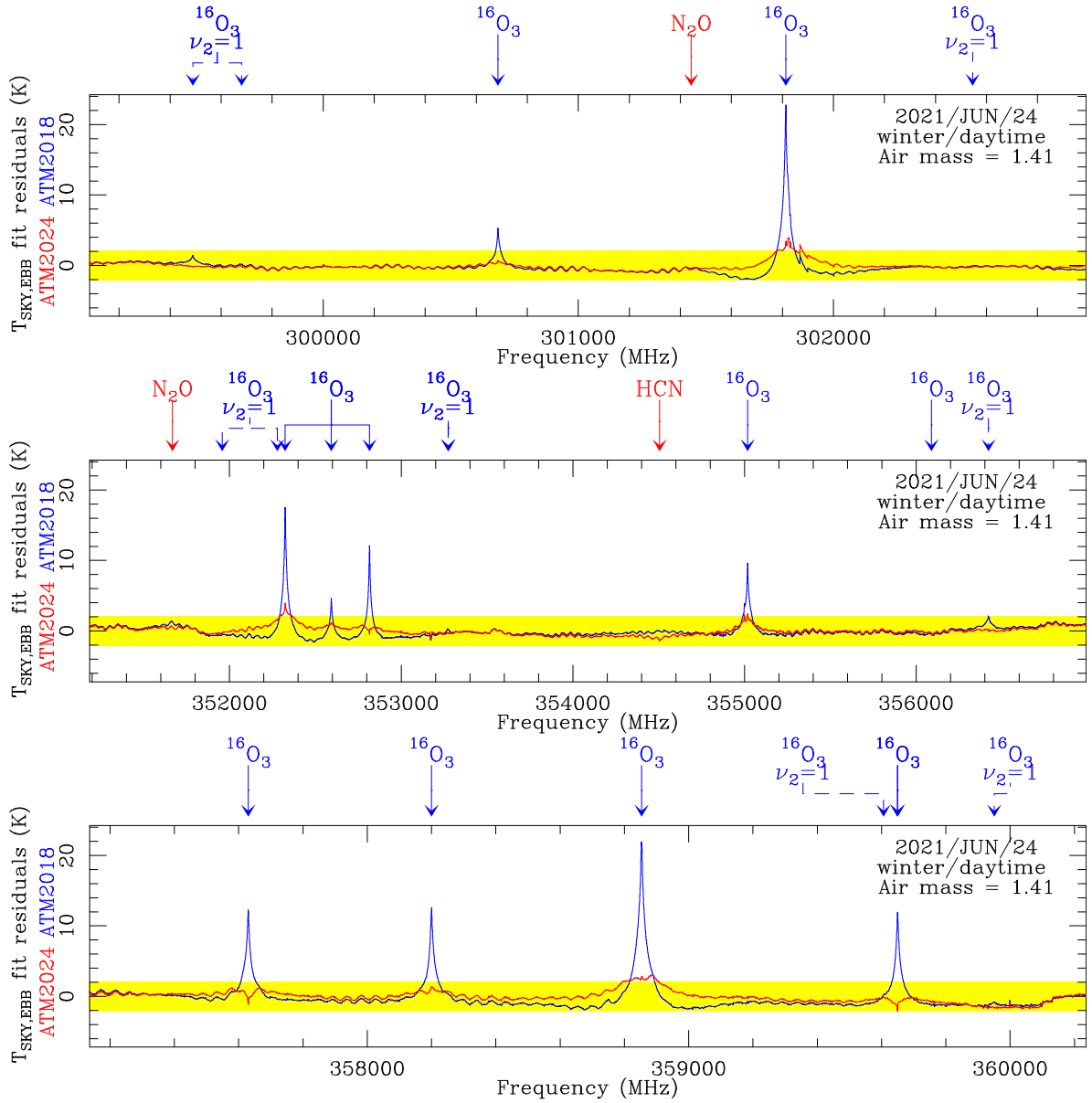

Figure 29: Zoom on selected frequency ranges of the SEPIA345 atmospheric data collected on June 24^{th} 2021 at elevations between 43 and 47 degrees.

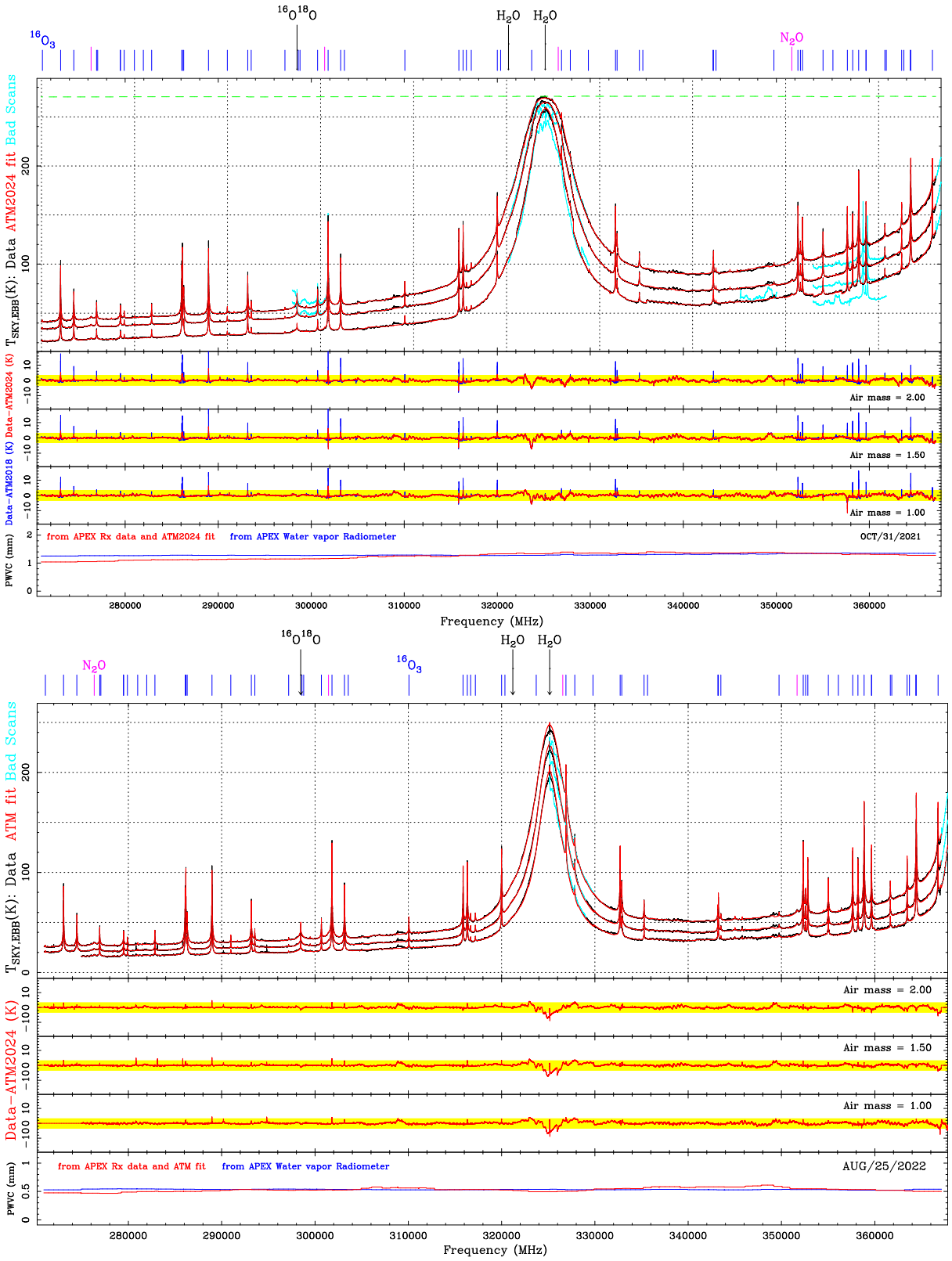

Figure 30: SEPIA345 atmospheric sky dip performed on Oct 31^{st} 2021 (upper panel) and Aug. 25^{th} 2022 (lower panel) with ATM model fits from PWVC retrievals.

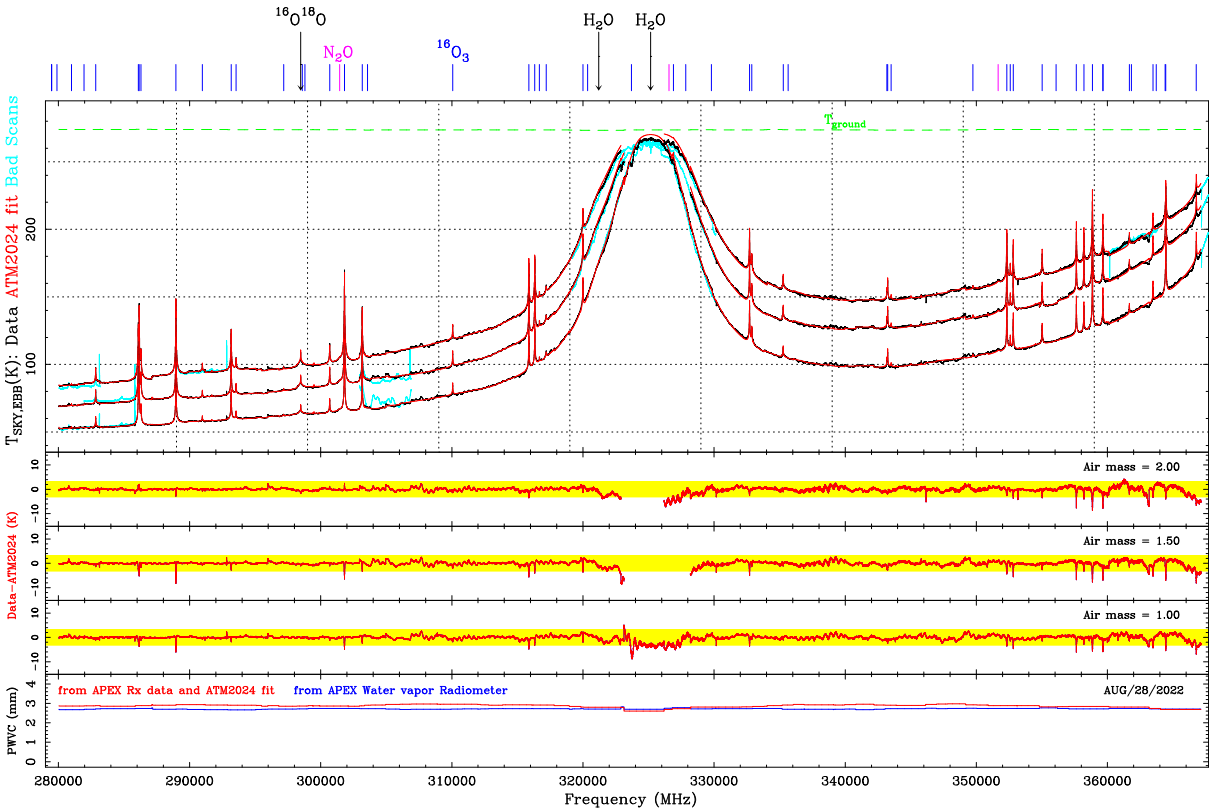

Figure 31: SEPIA345 atmospheric sky dip performed on Aug. 28^{th} 2022 and ATM model fit with PWVC retrieval.

4.3.5 nFLASH230 data and analysis

The frequency range (∼196-281 GHz) of this receiver is the only one, among the five used in this study, that does not include a relatively strong water line. Therefore, PWVC retrievals are here more difficult, especially for low PWVC (below ∼1.5 mm). Nevertheless, we have a 5 air mass sky dip recorded on Oct. 21^{st} 2020 under more than 3 mm PWVC conditions that is well adapted for our goals (see Fig. 32).

The calibration issues explained in Section 3 had a particular bad impact on nFLASH230 data due to the low atmospheric signal (relative to higher frequency receivers) that is expected here. In order to understand these issues, please see Figure 32 (for clarity, the original 2020 calibration is shown for all 5 airmasses in the upper panel of Figure 32).

The original calibration of the data (shown as blue histograms in the Figure 32) made for us impossible to get any consistent fit. First, the retrieved PWVC was way too low with respect to the one derived by the WVR and stored on the log file. Second, even if the observations were "simultaneous" for all air masses (each new tuning was done after all air masses had been observed in the previous one), the retrieved PWVC values were air mass dependent. It was clear that the $T_{EBB,SKY}$ values in this first calibration were wrong (too low). The final calibration, shown as black histograms in Figure 32, gave consistent results (as for the other receivers). We now get PWVC that are not air mass dependent and agree well with those derived for the WVR, and the residuals are low (after removal of many spikes present in this particular data set).

Other data sets obtained with this receiver in drier situations, could not be analyzed at all for the original calibration since the data were directly corrupted in many channels. After recovering reasonably good data with the final calibration, several observing sessions with this receiver were also included in the

CIA study (see Figure 12). In fact, those sessions and some that could be also recovered for SEPIA180 are crucial for that study since they cover PWVC ranges where other receivers are not so useful.

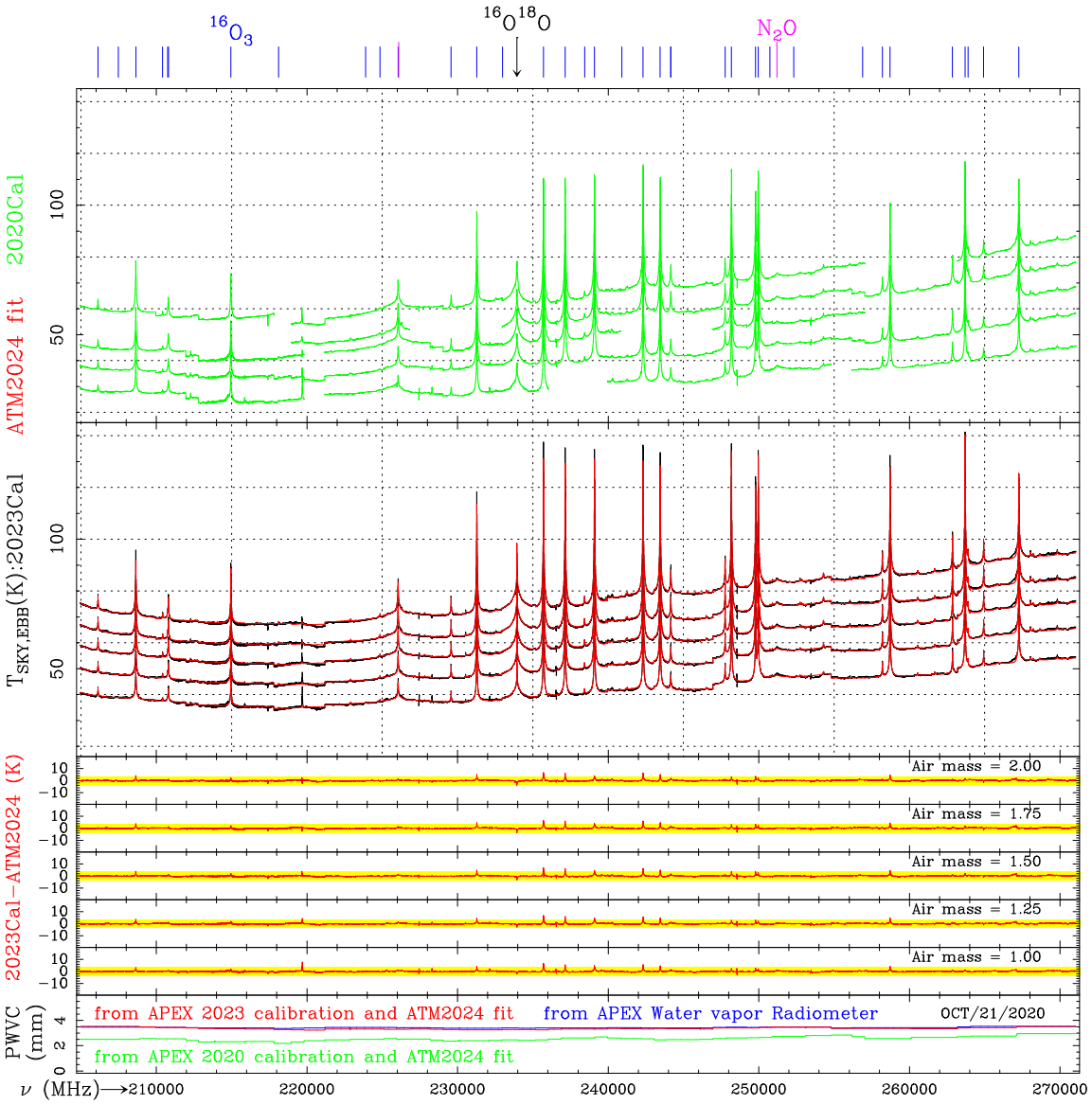

Figure 32: Complete nFLASH230 atmospheric data collected on October 21st 2020, with ATM2024 fits. Green histograms in the top panel correspond to the first calibration back in 2020. See zooms for this figure in the appendix, Figures 38-42.

4.3.6 SEPIA180 data and analysis

With SEPIA180 it happens something similar to nFLASH230 with the exception that in the frequency range of this receiver we have the 183 GHz H_2O line. It means that it is possible to recognize any calibration issues much more easily than with the nFLASH230 receiver since we know that this line reaches saturation for PWVC∼1.5 mm and beyond.

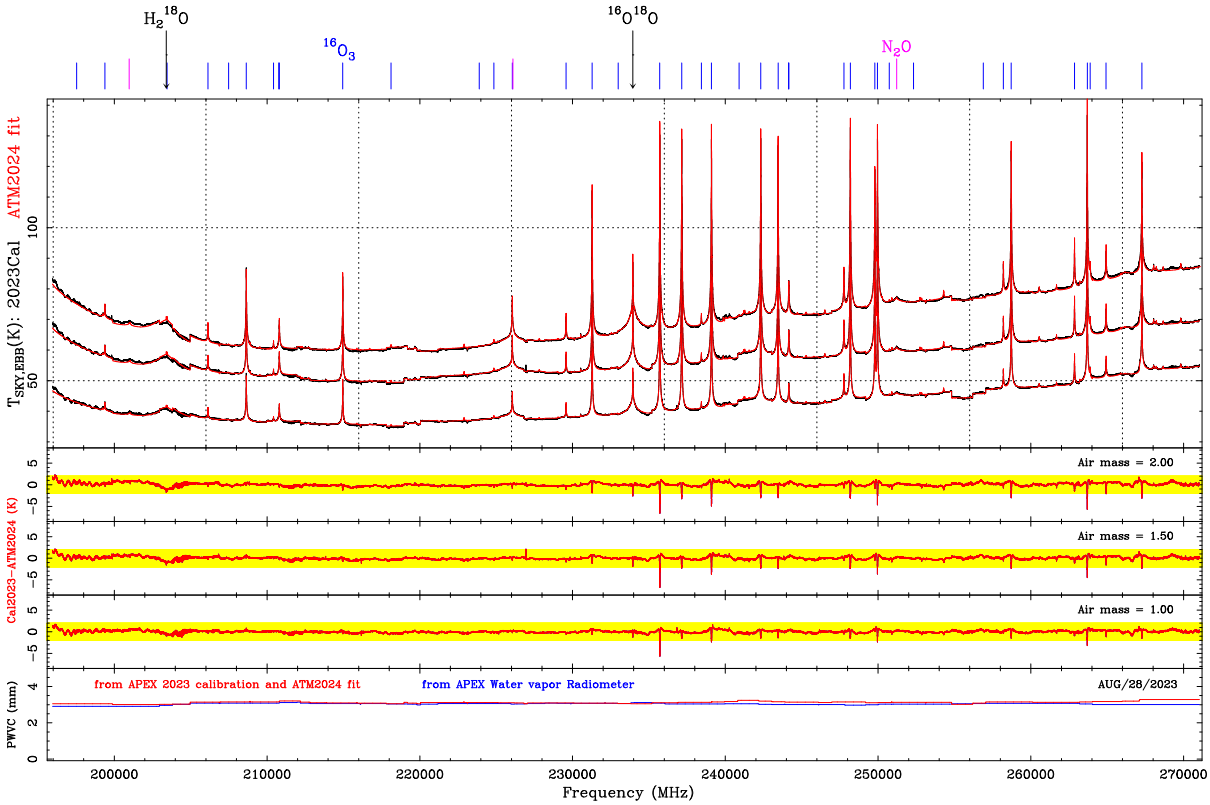

Figure 33: Complete nFLASH230 atmospheric data collected on August 28^{th} 2022, with ATM2024 fits. See zooms for this figure in the appendix, Figures 107-111.

In the situations of PWVC$\gtrsim$1.5 mm we should get at the center of the line $T_{EBB,SKY}$ very close to the ground temperature. However, Figure 34 shows again that data as originally calibrated in 2021 give $T_{EBB,SKY}$ values impossible to fit near the center of the line. Although far from that line center ($\pm$ $\sim$15 GHz or more apart) the fits of individual scans are possible with low residuals, the PWVC values necessary for those fits are unrealistically low.

The final 2023 calibration again solved these issues in a consistent way. The air mass 2.0 spectrum reaches the correct $T_{EBB,SKY}$ level near the line center and the PWVC columns derived from these 3 spectra match well with the ones derived from the WVR operating at similar frequencies. The residuals with the ATM2023 are well within the $\pm$3 K level marked in the figure with a yellow strip, although some artifacts and standing waves appear at different places, the central part of the water line being one of them.

There are not too many O_3 lines in this frequency range, but the detailed Figures 56-58 show how we have improved the residuals in ATM2023 with respect to ATM2018.

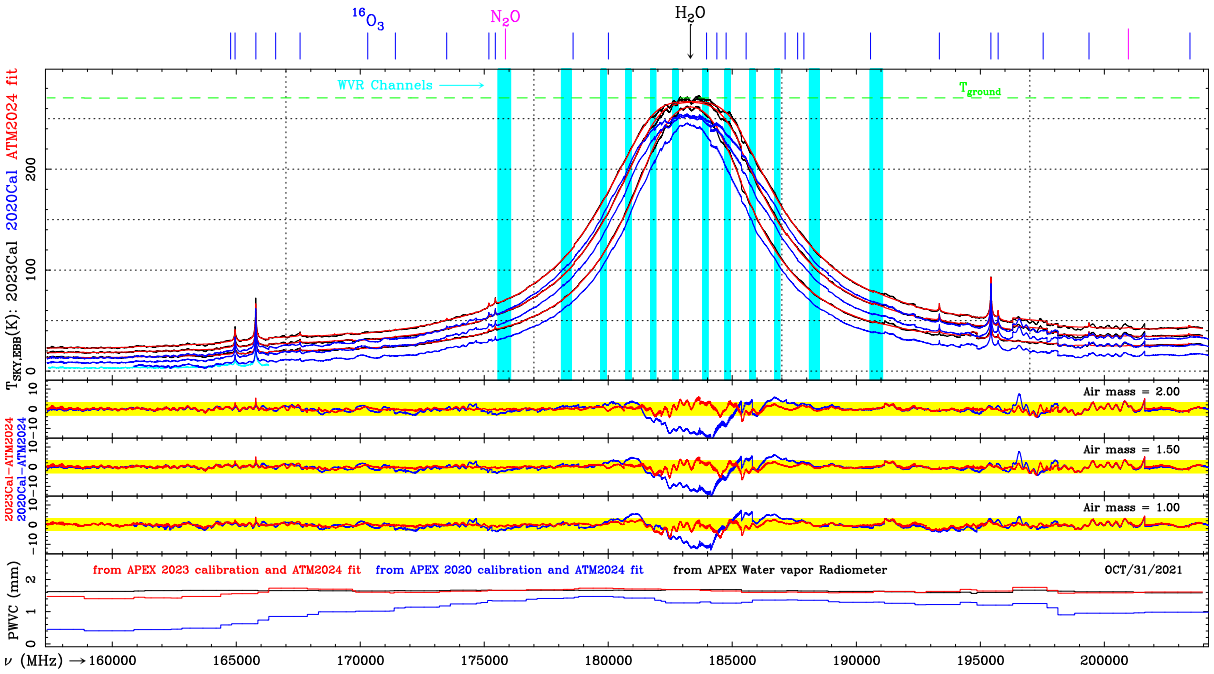

Figure 34: SEPIA180 atmospheric data collected on October 31st 2021 according to the original (problematic) calibration and the final one (consistent). The position of the of the actual APEX water vapor radiometer from which the PWVC is retrieved and stored in the log files is indicated as light blue bands.

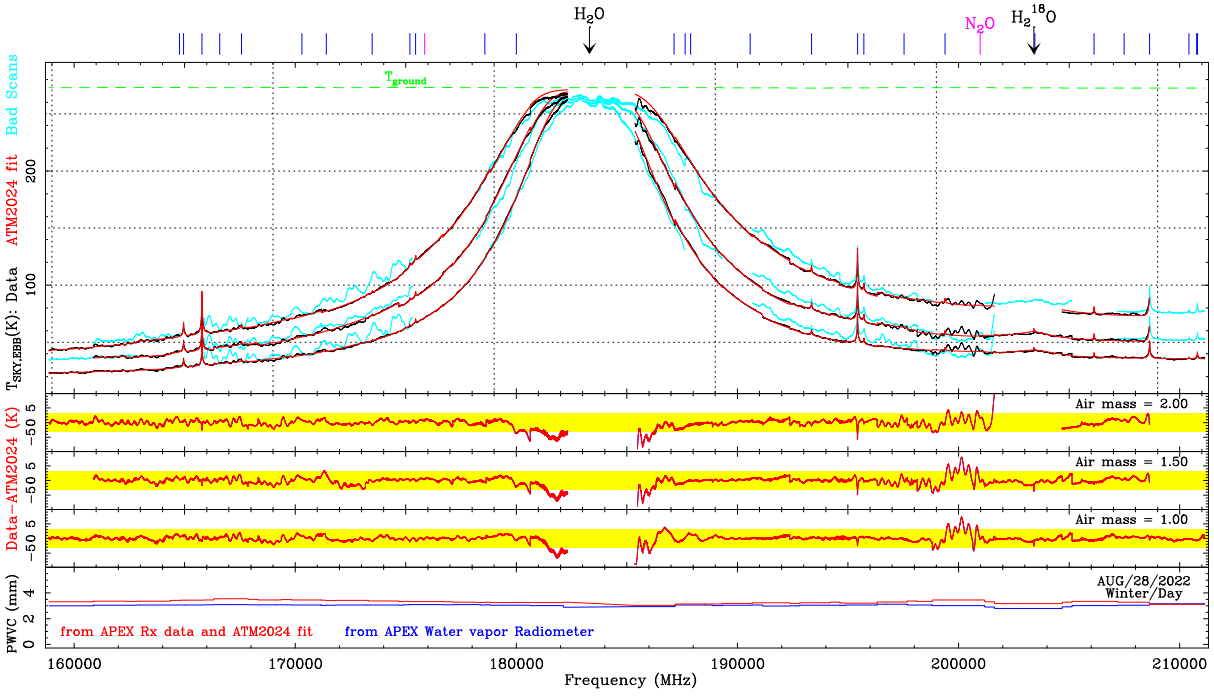

Figure 35: SEPIA180 atmospheric data collected on August 28th 2022 and ATM fit. Note that the PWVC agreement is not so good at frequency ranges with a concentration of bad scans. Also note the detection, and correct fitting, of and $H_2^{18}O$ line.

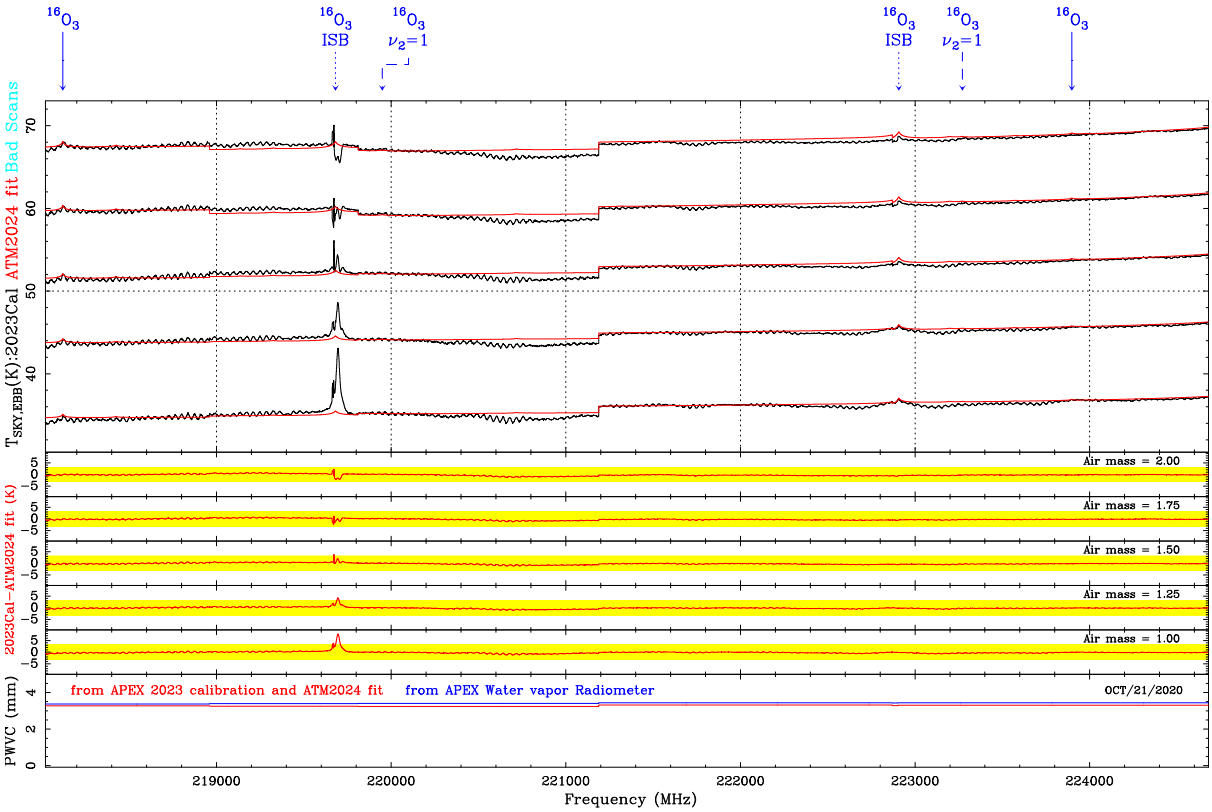

Figure 36: Portion of nFLASH230 sky dip achieved on October 21, 2022. In the data, there is an artifact at exactly the frequency of an O_3 line from the image side band (242.3187 GHz) as well as a small ghost line corresponding to leakage at ∼-15 dB level from another ISB O_3 line at 239.0933 GHz.

4.4 Artifacts, bad scans and image band leakage

We have seen through this report that the data, although very nice in general, present sometimes bad scans usually due to receiver performance degradation towards the edges of the frequency range for which they have been optimized, or near strong atmospheric lines (the pattern here is not so easy to understand since a few scans appear to be wrong an many others are O.K.). So far the only receiver where we have found clear artifacts or ghost lines due to image band leakage (at a level of ∼-15 dB) is nFLASH230 (see figure 36). The only receiver with an unusual amount of bad scans is the lower LO chain of nFLASH460, as already mentioned. The three SEPIA receivers have very few scans to be discarded and we did not found systematic artifacts or ghost lines from image band leakage.

4.5 Impact of the assumed tropospheric temperature profile in the analysis

One of the main assumptions in our overall analysis concerns the vertical atmospheric profile. Indeed, all our fits have considered the tropospheric temperature to decrease with height according to a lapse rate of -5.6 K/km. In order to check the impact that other scale heights or temperature inversion layers at the site would have we have performed the simulations presented in Figure 37. Different scenarios show atmospheric brightness temperature differences never exceeding ±2 K, with the smaller residuals at “window” frequencies. Interestingly enough, the larger offsets are seen at the central frequencies of strong H_2O and O_2 lines for atmospheric temperature profiles with inversion layers. This shows that the analysis is basically consistent with the assumptions we have made, and explains discrepancies that appear precisely in the core of those strong lines (see Figures 28 upper panel and 30 lower panel).

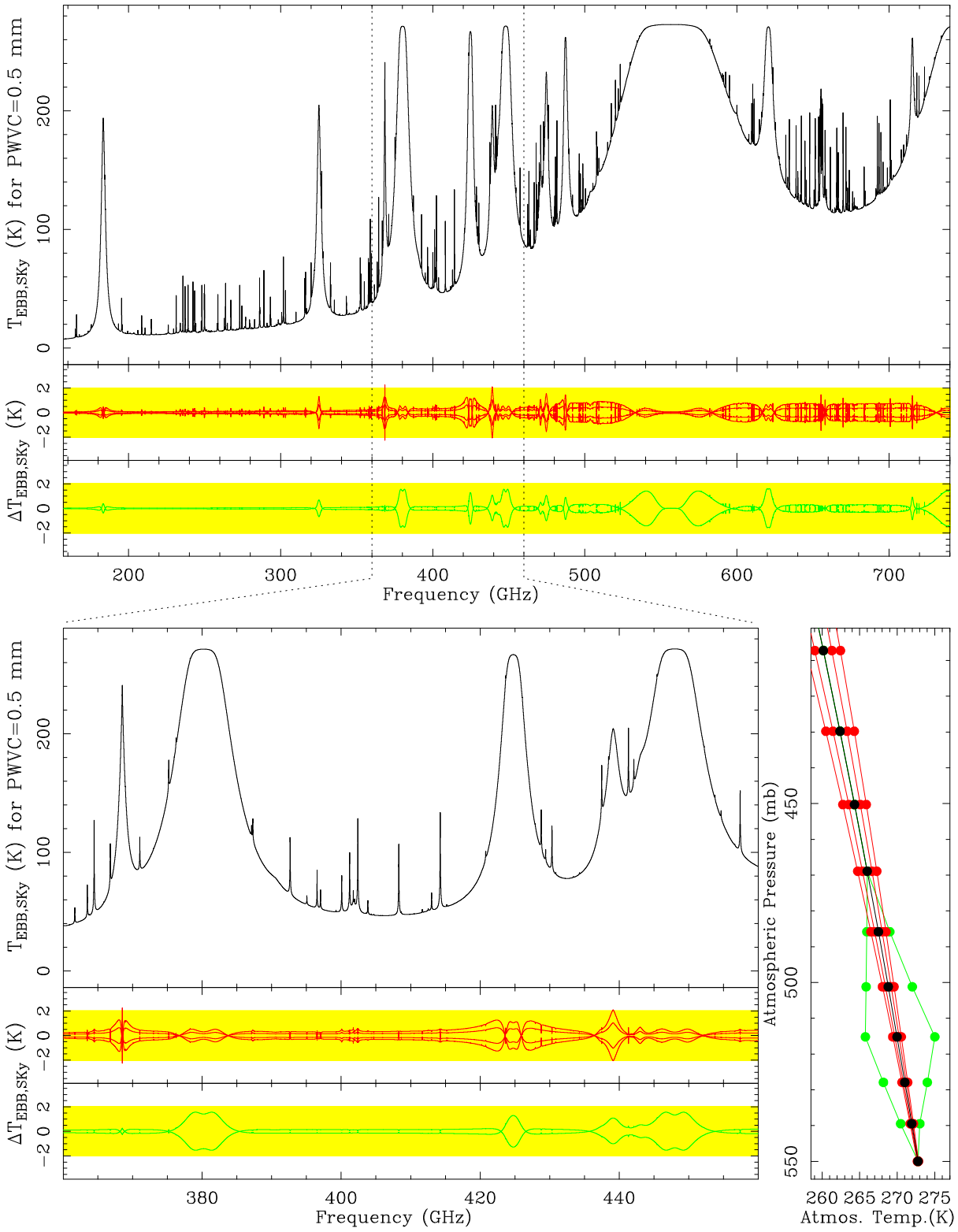

Figure 37: Simulations to asses the impact of atmospheric temperature inversions near the ground (green profiles) or different tropospheric temperature scale heights (red profiles) on the simulated zenith sky brightness temperatures.

5 Conclusions and future work

This report is based on 60 final spectra (i.e. one observing date + one airmass + one receiver) that are valid among all the observations that we performed between October 2020 and September 2022. The frequency coverage is complete, and we are a bit short of data in particular seasonal and diurnal conditions (Summer/Day). The basic idea is to be able to fit the data, with residuals as low as possible, from the basic information provided by the weather station (P, T and relative humidity at the ground), the season and the time of the day, with only one free parameter (PWVC). This is a priori challenging given the complexity of the atmospheric spectrum. Getting low residuals is difficult if we merge all individual scans across the receiver pass-band (¿100 GHz usually), but it is possible if we fit each scan separately and the merge both data and fit into a final spectrum for the whole pass-band (with PWVC being a function of time, or frequency since we have a time for each tuning). The PWVC(ν) obtained this way from our data can be compared with $PWVC(\nu)$ which is the same parameter but provided by the 183 GHz Water Vapor Radiometer, that is supposed to be almost free from any issues with the atmospheric model. All analysis in this report are based on comparing these two independent measurements of the precipitable water vapor column, and the residuals resulting from fitting the data coming from SEPIA and nFLASH. The saturation of very strong atmospheric lines also provide "fixed" data points, or values of the spectra that we know a priori and should be met by the data if the calibration is correct. It has taken a very long time to go through all individual scans and the peculiarities of each observing session to finally generate the final data set and best model to reproduce it. As a result, a new state-of-the-art C++ ATM code is ready for implementation in the ALMA software once this report is approved.

The main goal of ESO/ALMA Development Study CFP/ESO/19/25417/HNE, as indicated in the title, is to get an improved and tested atmospheric model above 300 GHz for its use in ALMA, APEX and other observatories. Within it, in this work we have achieved the following items:

1. Identified and implemented missing lines from already included molecules.
2. Included and implemented missing molecules in the previous ATM2018 model, with lines visible in the data.
3. Checked the accuracy of the intrinsic line shapes.
4. Checked the assumptions made to generate vertical profiles of P/T/H_2O, and their layering in the model, and implemented some updates for a better data fit.
5. Updated the vertical profiles of minor atmospheric gases to minimize residuals on the observed lines. We have introduced, as necessary for O_3, seasonal and diurnal dependent profiles, and new profiles year-round for other molecules as presented in Table 2 (see also Figures 20, 21, 22 and 23). Those profiles have been used in ATM2024 model calculations in this work.
6. Checked for the correctness of all isotopic ratios and vibrational energies so that the smallest features observed are well reproduced.
7. Conducted an in-depth study of the collision induced absorption (CIA) due to its important in a broadband basis.

As a result, a new version of the ATM C++ code for TelCal has to be implemented. Changes have been labeled in the code as **"updated after CFP/ESO/19/25417/HNE study"** comment lines. Also, several test codes aimed at reading and processing the data from this study, have been developed. Juan R. Pardo will travel to ESO in July 2024 to work with Justo González on the integration of the updated software.

For many years, reaching these goals has been impossible due to the lack of submillimeter observing systems able to produce absolutely calibrated atmospheric spectra free from artifacts at the frequency scales of atmospheric lines. However, APEX has produced outstanding data with its SEPIA and nFLASH receivers that meet our needs (and those of the submillimeter community). Although the receivers

are similar, the key difference from APEX to ALMA is the use of two blackbodies for calibration at APEX at cabin temperature (T_{hot}), and that of liquid N_2 at 5105 m altitude (≈73 K), instead of one ("hot") plus the sky for ALMA, which makes almost impossible to separate the sky in an absolute way. Throughout this report we have presented and discussed different observing runs focusing on all items listed above. Although during more than two years we faced serious problems (COVID crisis impacting the observations, and serious calibration issues), the final results have fully achieved the above mentioned items.

In addition to the analysis of the APEX spectra presented in this report, and the resulting implementations in ATM's opacity calculation, the model also provides outputs for the real part of the refractivity, related to pathlength or phase delay calculations. Justo González has carried out simulations (see attached report) that have shown some discontinuities in ATM dry path outputs for some particular situations. After a close investigation we have found that the issue is not coming from the theoretical description of the phase itself but from the vertical layering that ATM generates for different altitudes of the antenna above sea level and the associated vertical T/P profiles. The vertical layering algorithm has therefore being revised to eliminate these discontinuities for the next deliverable version of ATM. In addition to that, since the experimental part of this study only used a single antenna, no validation of the real part of the refractivity model could be conducted. For now, the literature on this type of validations is very scarce [Bendall et al. (2015)] and the subject remains a natural continuation of the investigation presented in this report.

In the future, and taking into account that the observing procedures are now well established and can take advantage of some telescope overhead and technical time, it would be desirable to complete the database with extra measurements with the 5 receivers described in this report. Also, if a new receiver becomes available at higher frequencies (i.e. the ∼350 μm window), using it for similar measurements would be especially valuable for the CIA characterization as well as the role of far wings of H_2O lines with central frequencies beyond 1 THz. Also, it would be interesting to study with SEPIA180 and nFLASH230 the H_2O-H_2O collision induced absorption in the wet (10-15 mm of PWVC) that we may encounter during the altiplanic winter at Chajnantor, since it is not totally negligible as it was the case for all situations presented in this study.

References

[Baryshev et al. (2015)] Baryshev, A. M., Hesper, R., Mena, F. P., Klapwijk, T.M., et al., 2015, A&A, 577, A129

[Belitsky et al. (2018)] Belitsky V., Lapkin I., Fredrixon M., Meledin D., Sundin E., Billade B., Ferm S.-E., et al., 2018, A&A, 612, A23

[Bendall et al. (2015)] Bendall, T. M., Hills, R. E., Naftaly, M., and Molloy, J., 2015, "Refractivity of water vapor at terahertz frequencies – Comparison of measurements with models". The Institute of Electrical and Electronics Engineers, Inc. (IEEE) Conference Proceedings, 1.

[Boissoles et al. (2003)] Boissoles, J., Boulet, C., Tipping, R. H., Brown, A., Ma, Q., 2003, JQSRT, 82, 505

[Cernicharo(2012)] Cernicharo, J., 2012, in ECLA 2011: Proc. of the European Conference on Laboratory Astrophysics, EAS Publications Series, 2012, Ed.: C. Stehl, C. Joblin, & L. d'Hendecourt (Cambridge: Cambridge Univ. Press), 251; `https://nanocosmos.iff.csic.es/?page_id=1619`

[Chamberlin et al. (2003)] Chamberlin, R. A., Martin, R., Martin, C. L., Stark, A. A., 2003, SPIE Proc., 4855, 609

[Gusten et al. (2006)] Güsten, R., Nyman, L. Å., Schilke, P., et al. 2006, A&A, 454, L3

[Hills et al. (1978)] Hills, R. E., Webster, A. S., Alston, D. A., Morse, P. L. R., Zammit, C. C., Martin, D. H., Rice, D. P., Robson, E. I. 1978, Infrared Phys., 18, 819

[Ji et al. (2004)] Ji, Y, Cheng-hua, S, Shu-ping, H., Ohishi, M., Miyazawa, K., 2004, Chinese Astronomy and Astrophysics, 28/3, 367

[Klein et al. (2012)] Klein, B., Hochgürtel, S., Krämer, I., Bell, A., Meyer, K., Güsten, R., 2012, A&A, 542, L3

[Meledin et al. (2022)] Meledin, D., lapkin, I., Fredrikson, M., Sundin, E., et al., 2022, A&A, 668, A2

[Matsushita et al. (1999)] Matsushita, S., Matsuo, H., Pardo, J. R., Radford S., 1999, Publ. Astron. Soc. Japan, 51, 603

[Matsushita et al. (2017)] Matsushita, S., Asada, K. Martin-Cocher, P. L. Chen, M.-T., et al., 2017, Publications of the Astronomical Society of the Pacific, 129, 025001

[Mlawer et al. (2019)] Mlawer, E. J., Turner, D. D., Paine, S. N., Palchetti, L., et al., 2019, JGR Atmospheres 124(14), 8134

[Mlawer et al. (2023)] Mlawer, E. J., Cady-Pereira, K. E., Mascio, J., Gordon, I. E., 2019, JQSRT, 306:108645

[Mattioli et al.(2019)] Mattioli, V., Accadia, Ch., Prigent, C., Crewell, S., Geer, A., Eriksson, P., Fox, S., Pardo, J. R., et al., Bulletin of the American Meteorological Society, 100/12, 291

[Paine et al. (2000)] Paine, S., Blundell, R., Papa, D. C., Barrett, J. W., Radford S. J. E., 2000, PASP, 112, 108

[Pardo et al. (2001a)] Pardo, J. R., Serabyn, E. Cernicharo, J., 2001, JQSRT, 68, 419

[Pardo et al. (2001b)] Pardo, J. R., Cernicharo, J., Serabyn, E. 2001, IEEE Trans. Antennas and Propagation, 49, 12

[Pardo et al. (2005)] Pardo, J. R., Serabyn, E., Wiedner, M. C., Cernicharo, J., 2005, JQSRT, 96, 537

[Pardo et al. (2022)] Pardo, J. R., de Breuck, C., Muders, D., et al., 2022, A&A, 664, A153

[Pety (2018)] Pety, J., 2018, Submillimetre Single-dish Data Reduction and Array Combination Techniques, 11, 11

[Polehampton et al. (2019)] Polehampton, E., Hafok, H., Muders, D., 2019, APEX Calibrator Manual, APEX Report APEX-MPI-MAN-0012, Rev. 1.3

[Podobedov et al. (2008)] Podobedov, V. B., Plusquellic, D. F., Siegrist, K. E., Fraser, G. T., Ma, Q., Tipping, R. H., JQSRT, 109, 458

[Ningombam et al. (2020)] Ningombam, S. S., Sethulakshmy, E. S., Jade, S., Shrungeshwara, T. S., Vivek, C. G., et al., 2020, Journal of Atmospheric and Solar-Terrestrial Physics, 105404

[Serov at al. (2020)] Serov, E. A., Balashov, A. A., Tretyakov, M. Yu, Odintsova, T. A., et al., 2020, JQSRT, 242

[Tretyakov at al. (2015)] Tretyakov, M. Yu., Sysoev, A. A., Odintsova, T. A., Kyuberis, A. A., 2015, Radiophysics and Quantum Electronics, 58, 262

[Tremblin et al. (2012)] Tremblin, P., Schneider, N., Minier, V., Durand, G. Al., Urban, J., 2012, A&A, 548, A65

[Ulich (1980)] Ulich, B. L., 1980, ApJL, 21, 21

[Ulich & Haas (1976)] Ulich, B. L. and Haas, R. W., 1976, ApJS, 30, 247

[U.S. Standard Atmosphere (1976)] U.S. Standard Atmosphere 1976, U.S. Government Printing Office, Washington, D.C., 1976

A Appendix: Detailed figures for each observing run

In this appendix we have placed all available detailed figures corresponding to the current status of the analysis mentioned in the text. The sequence is ordered from the oldest to the latest run and, within each run, from the lower to the higher frequency receiver.

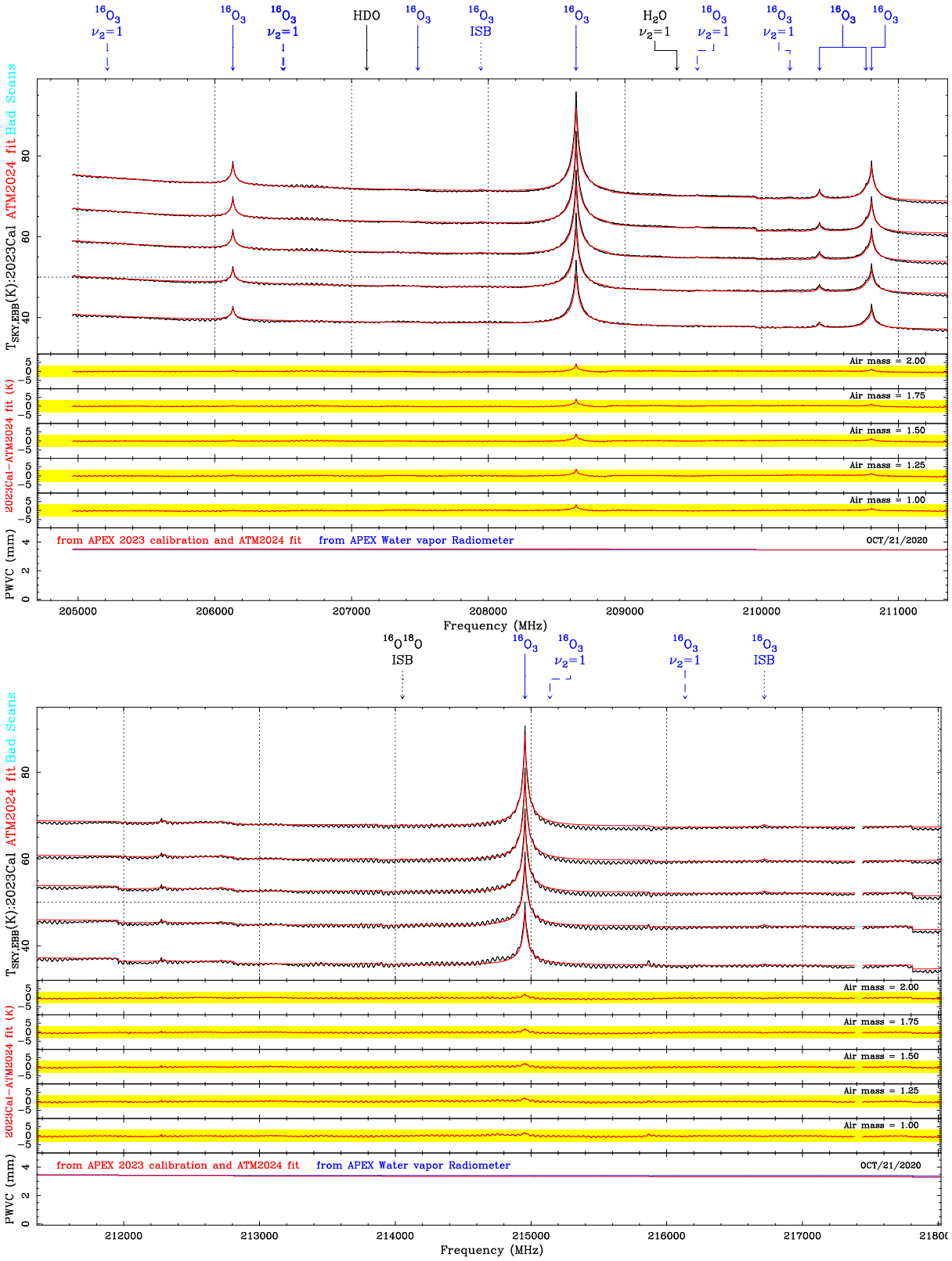

Figure 38: Zoom on Oct. 21st 2020 nFLASH230 5 air mass sky dip data and ATM2024 fit results (part 1).

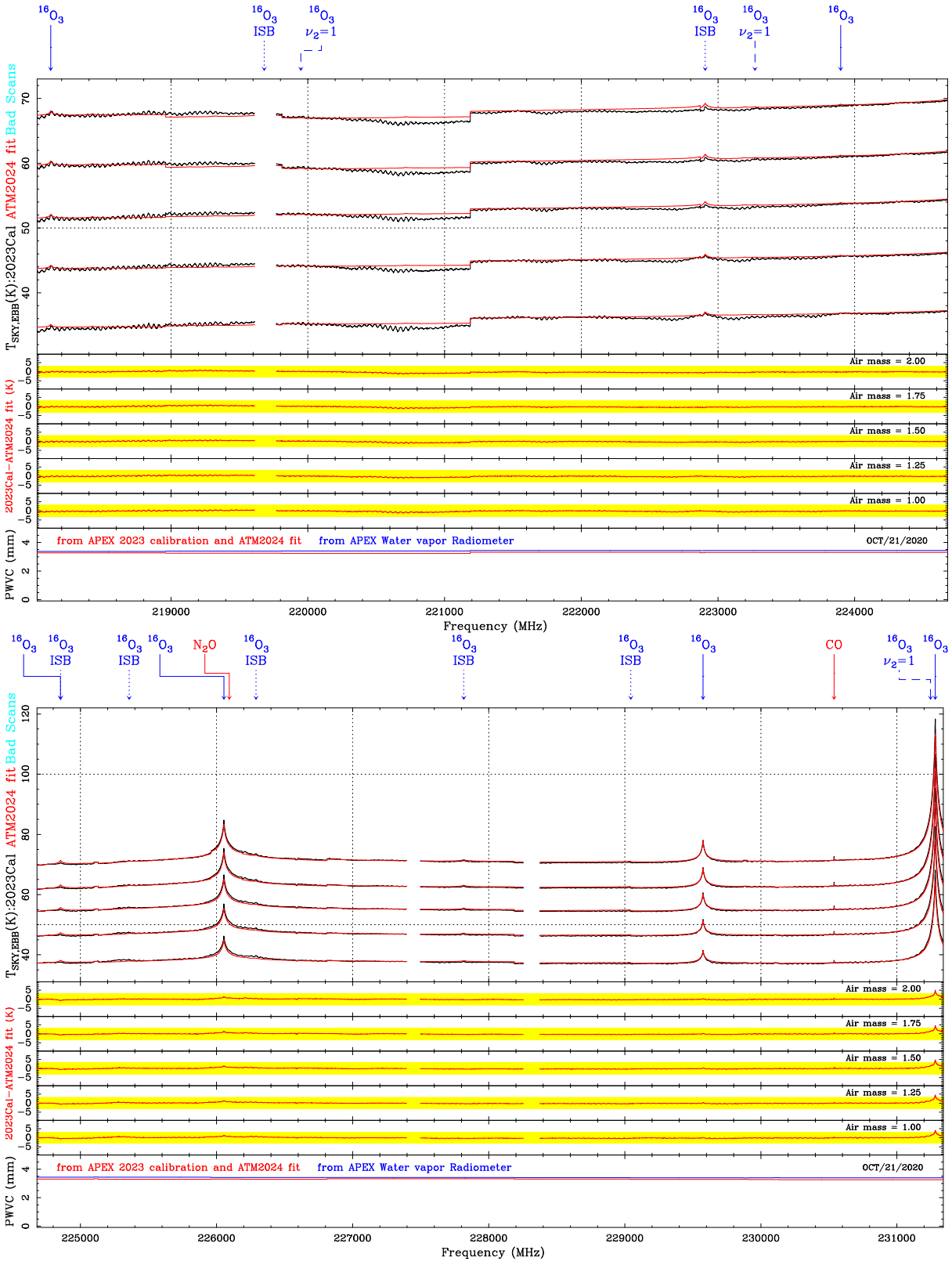

Figure 39: Zoom on Oct. 21st 2020 nFLASH230 5 air mass sky dip data and ATM2024 fit results (part 2).

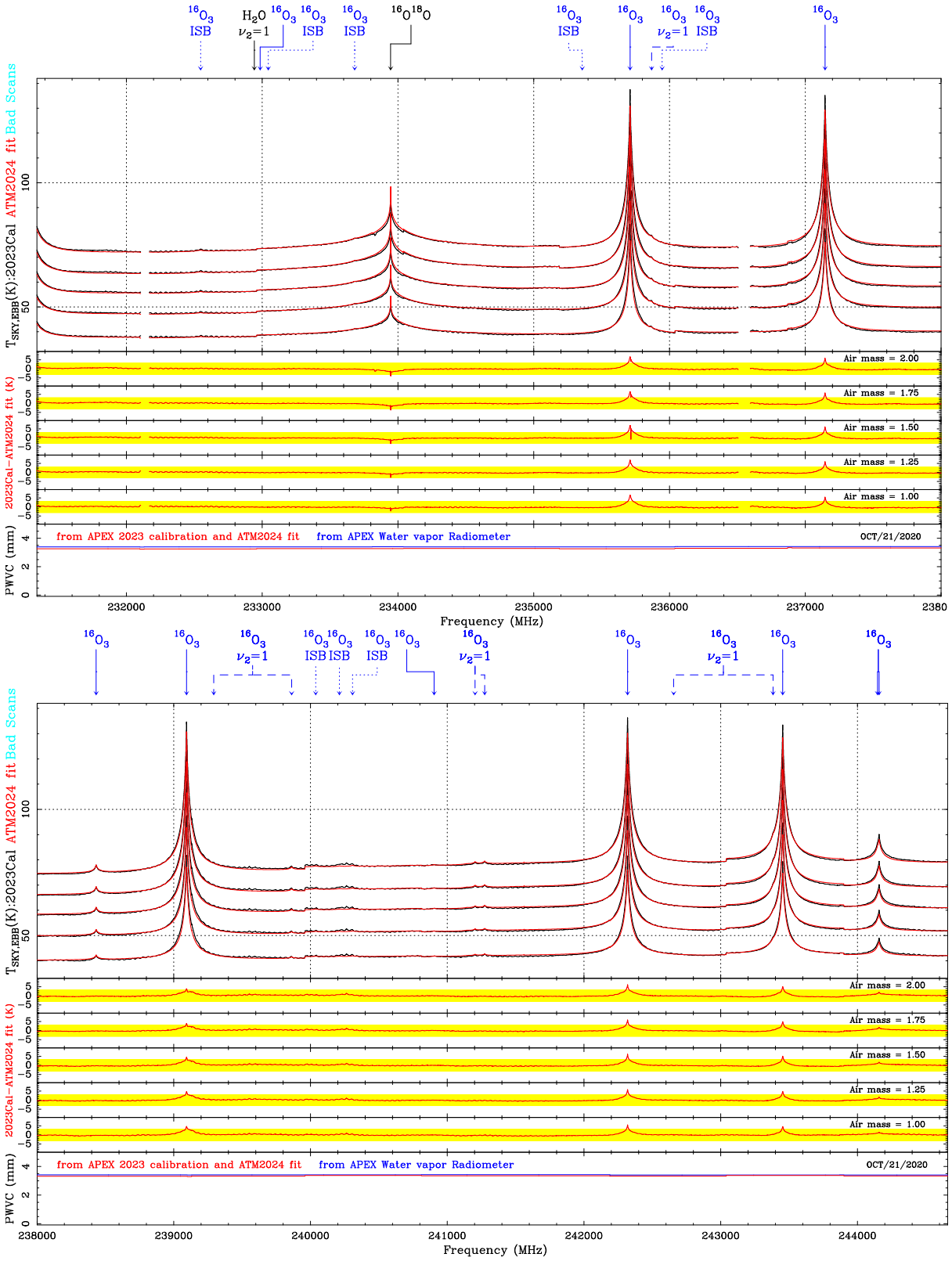

Figure 40: Zoom on Oct. 21st 2020 nFLASH230 5 air mass sky dip data and ATM2024 fit results (part 3).

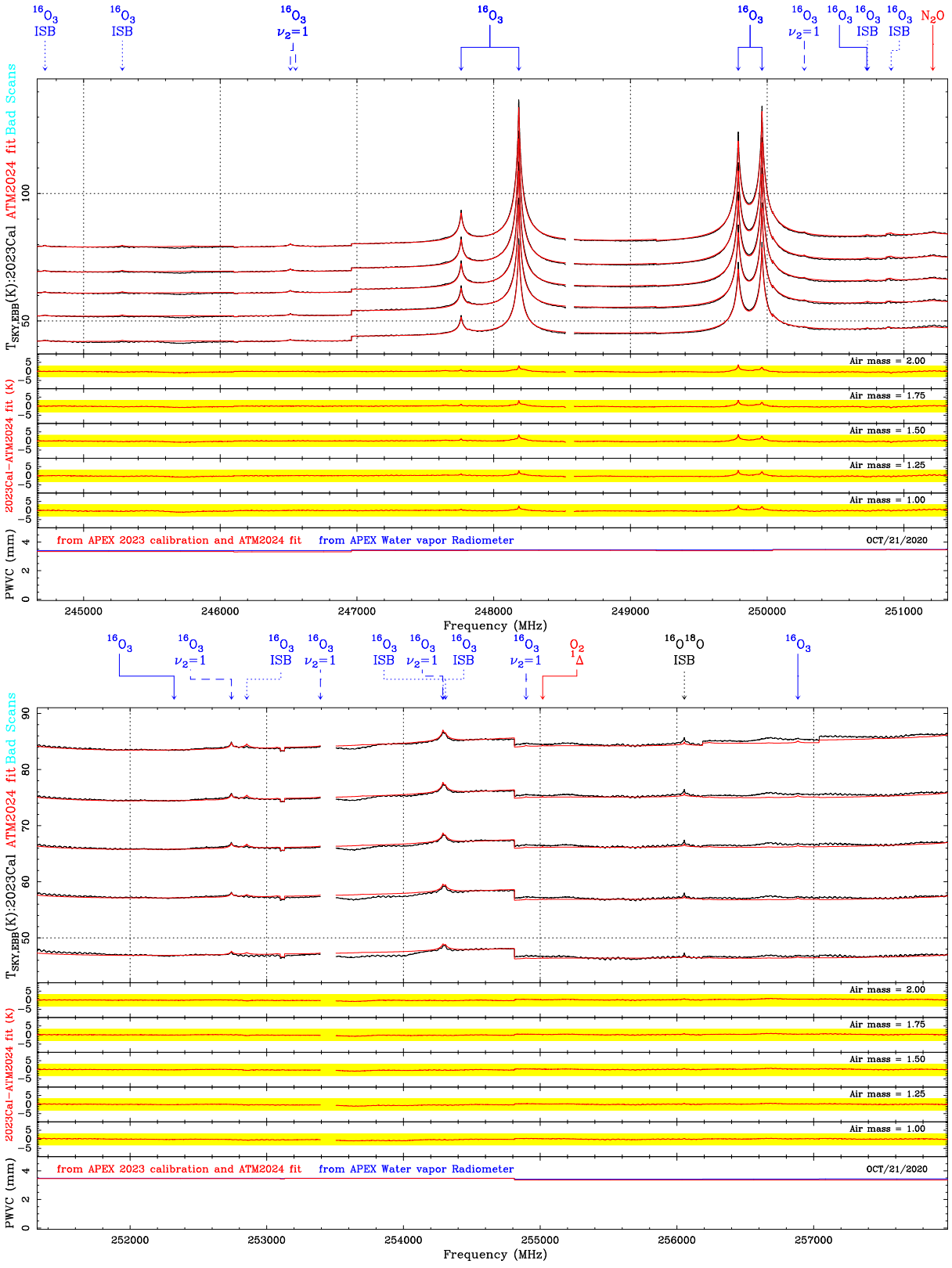

Figure 41: Zoom on Oct. 21st 2020 nFLASH230 5 air mass sky dip data and ATM2024 fit results (part 4).

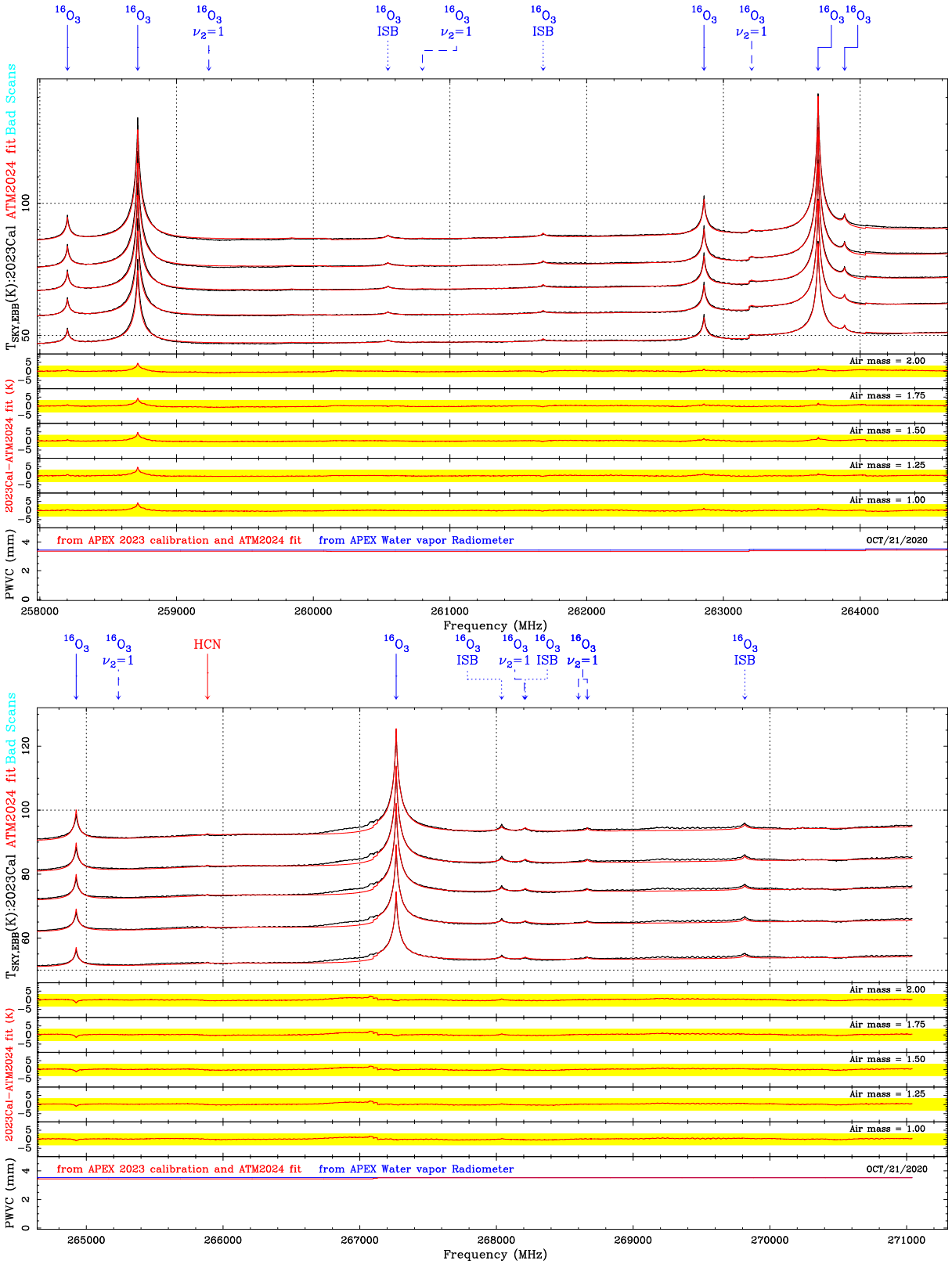

Figure 42: Zoom on Oct. 21st 2020 nFLASH230 5 air mass sky dip data and ATM2024 fit results (part 5).

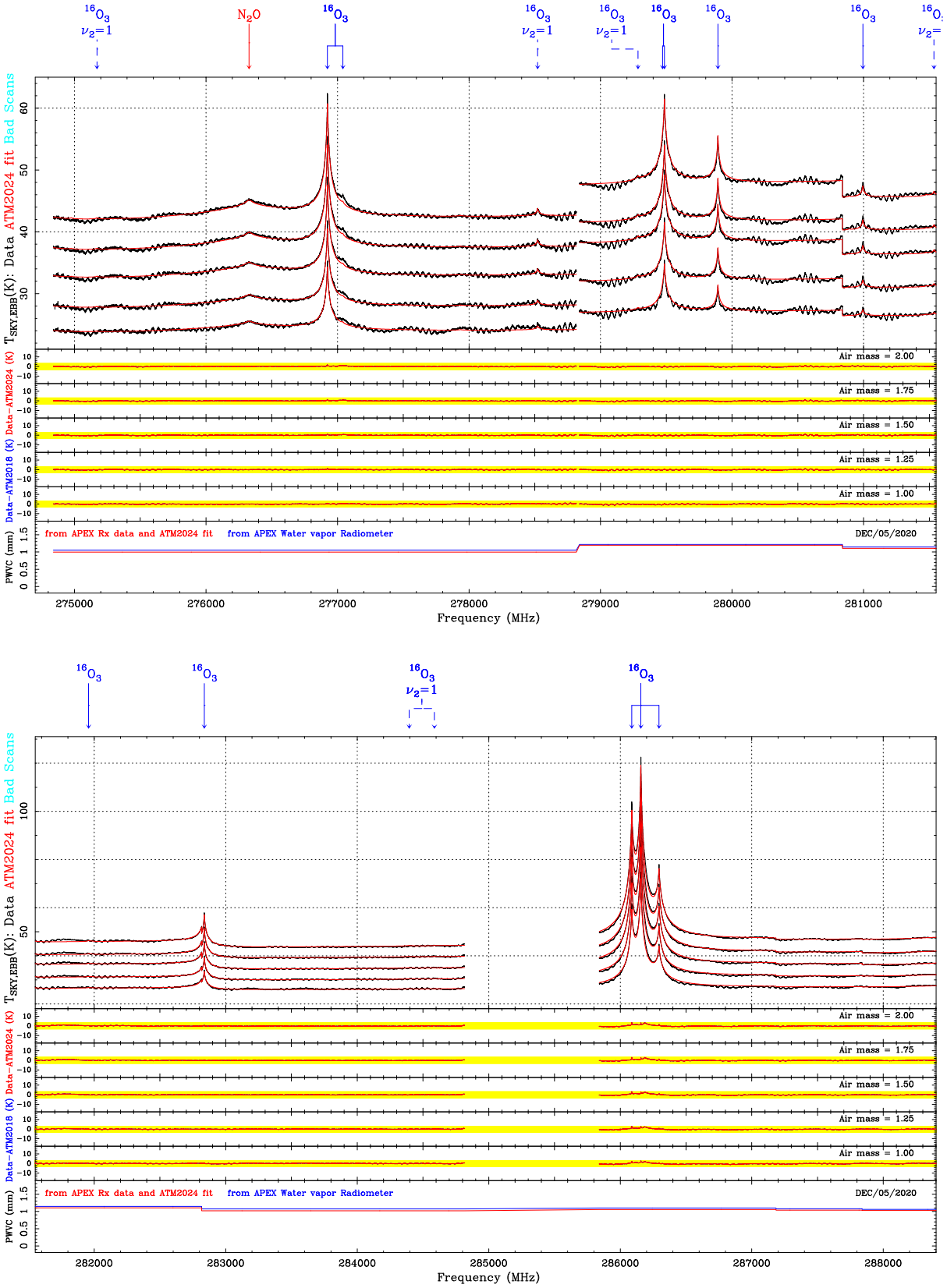

Figure 43: Zoom on Dec. 5^{st} 2020 SEPIA345 5 air mass sky dip data and ATM2024 fit results (part 1).

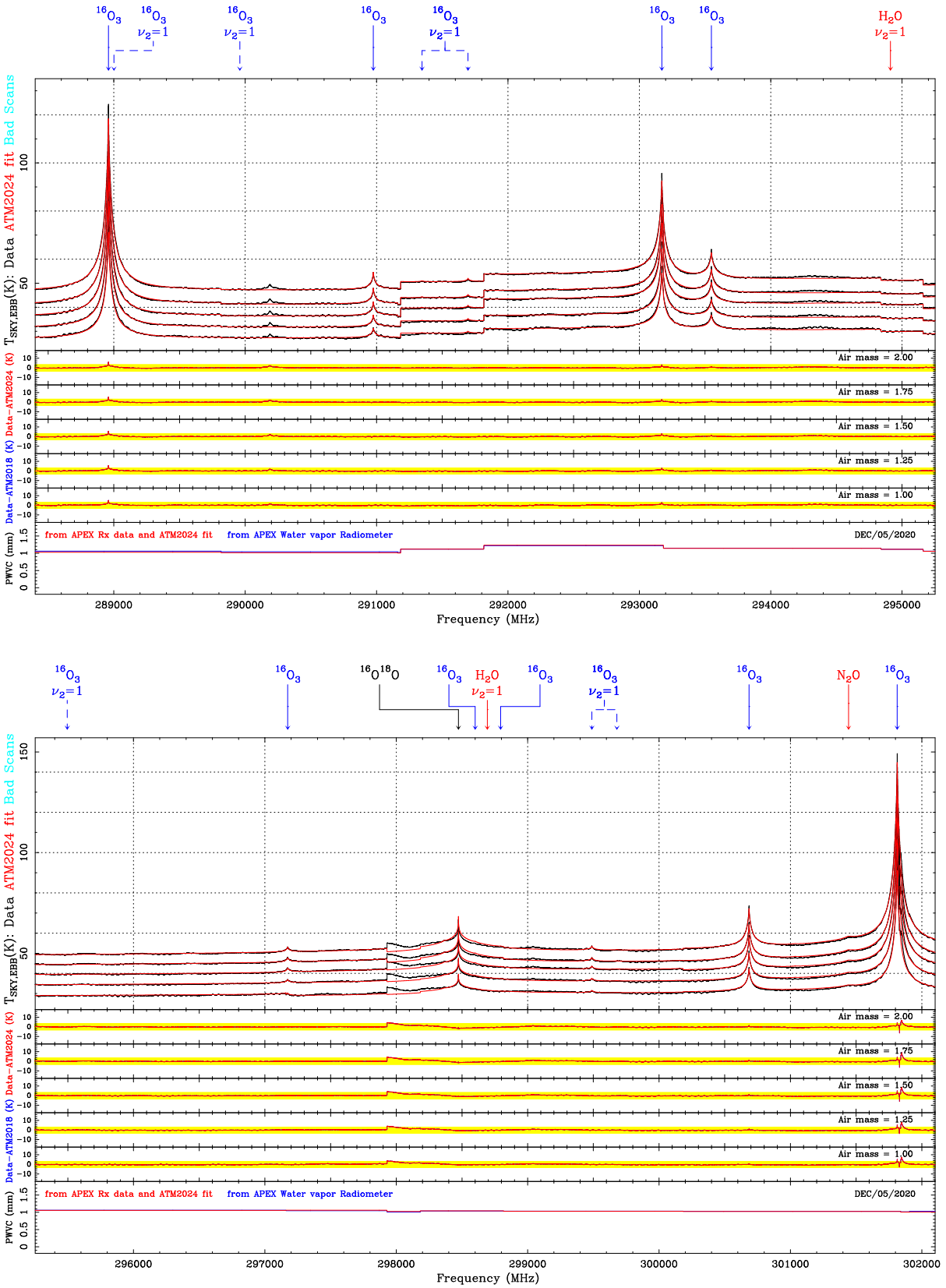

Figure 44: Zoom on Dec. 5^{st} 2020 SEPIA345 5 air mass sky dip data and ATM2024 fit results (part 2).

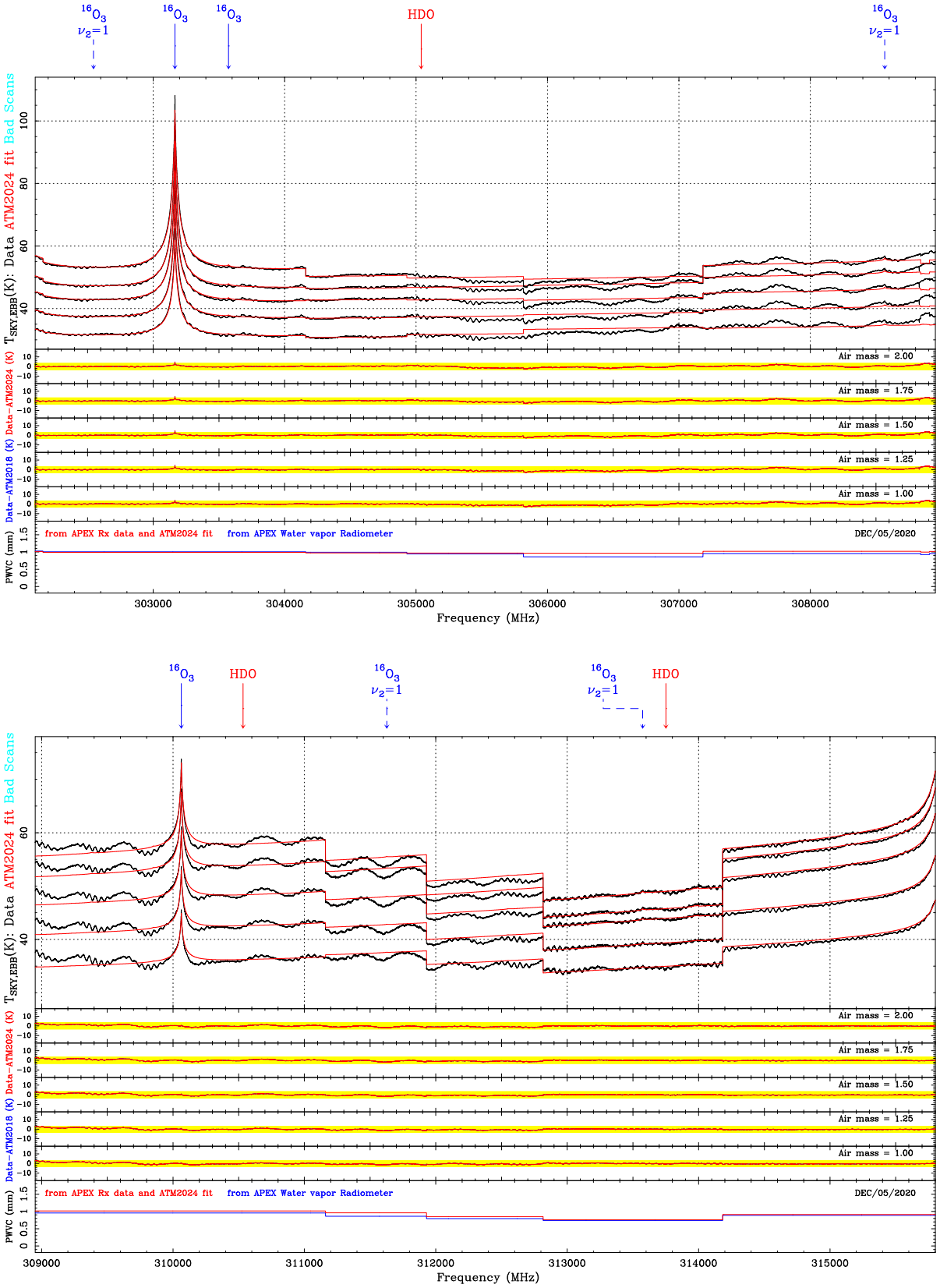

Figure 45: Zoom on Dec. 5^{st} 2020 SEPIA345 5 air mass sky dip data and ATM2024 fit results (part 3).

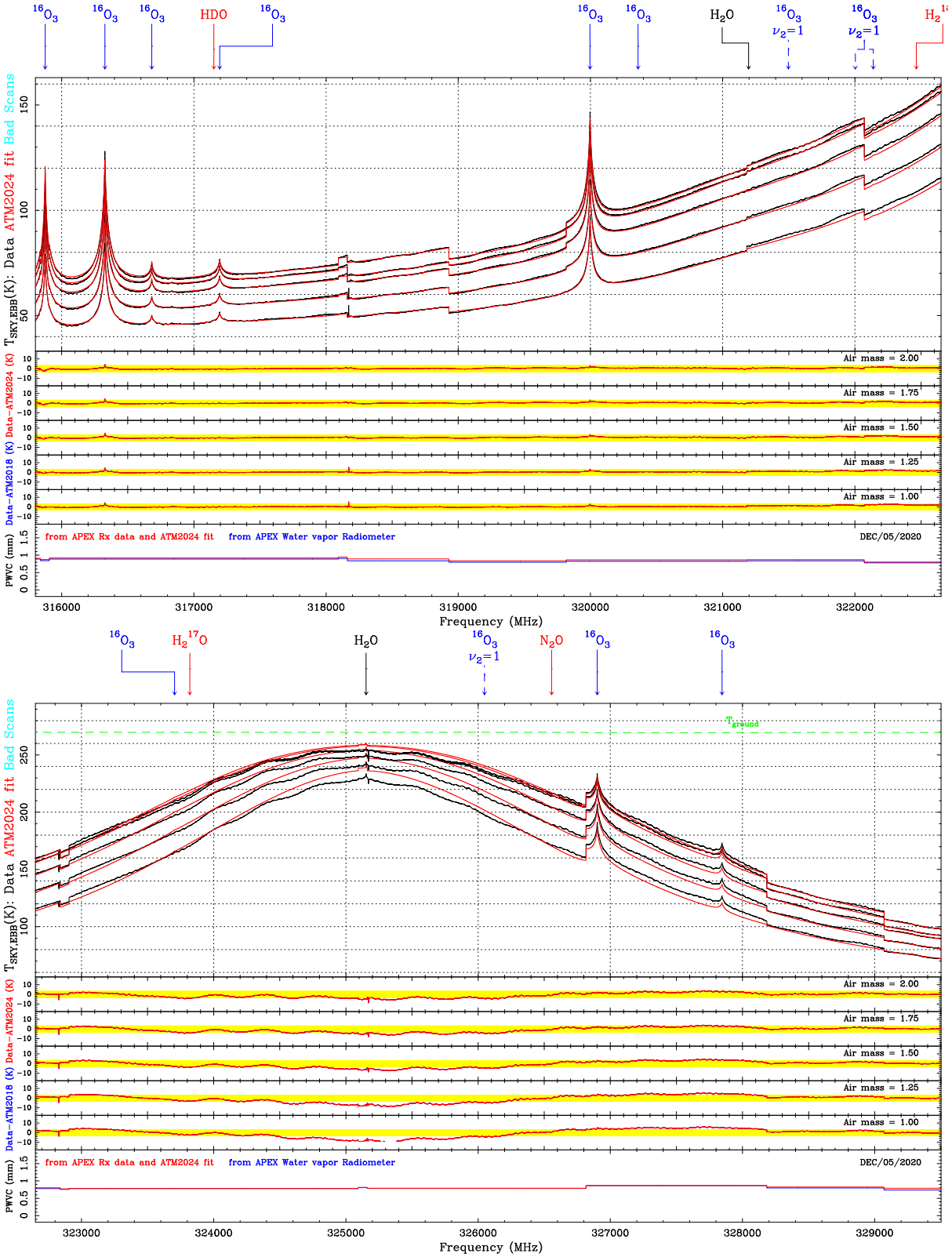

Figure 46: Zoom on Dec. 5^{st} 2020 SEPIA345 5 air mass sky dip data and ATM2024 fit results (part 4).

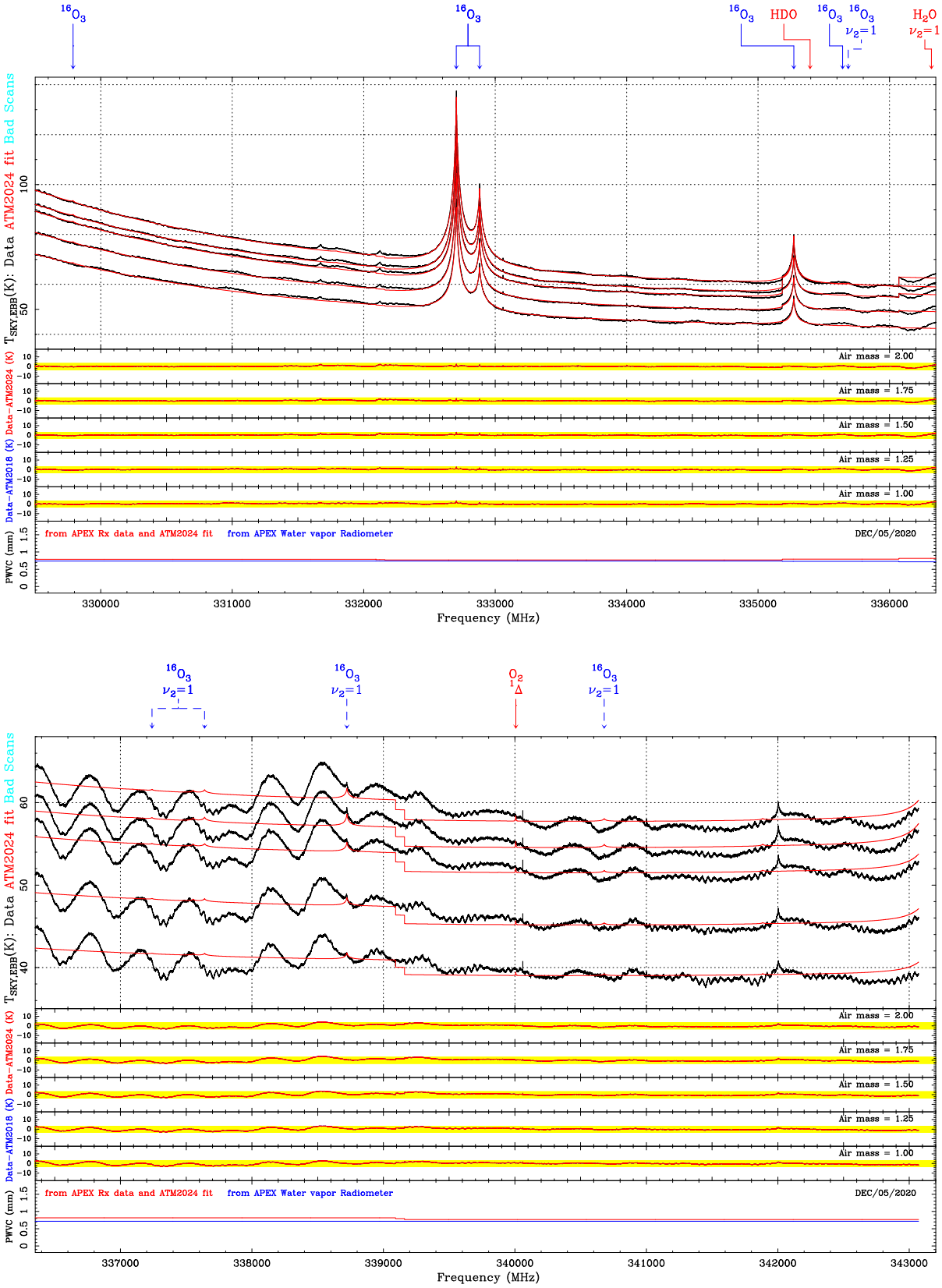

Figure 47: Zoom on Dec. 5^{st} 2020 SEPIA345 5 air mass sky dip data and ATM2024 fit results (part 5).

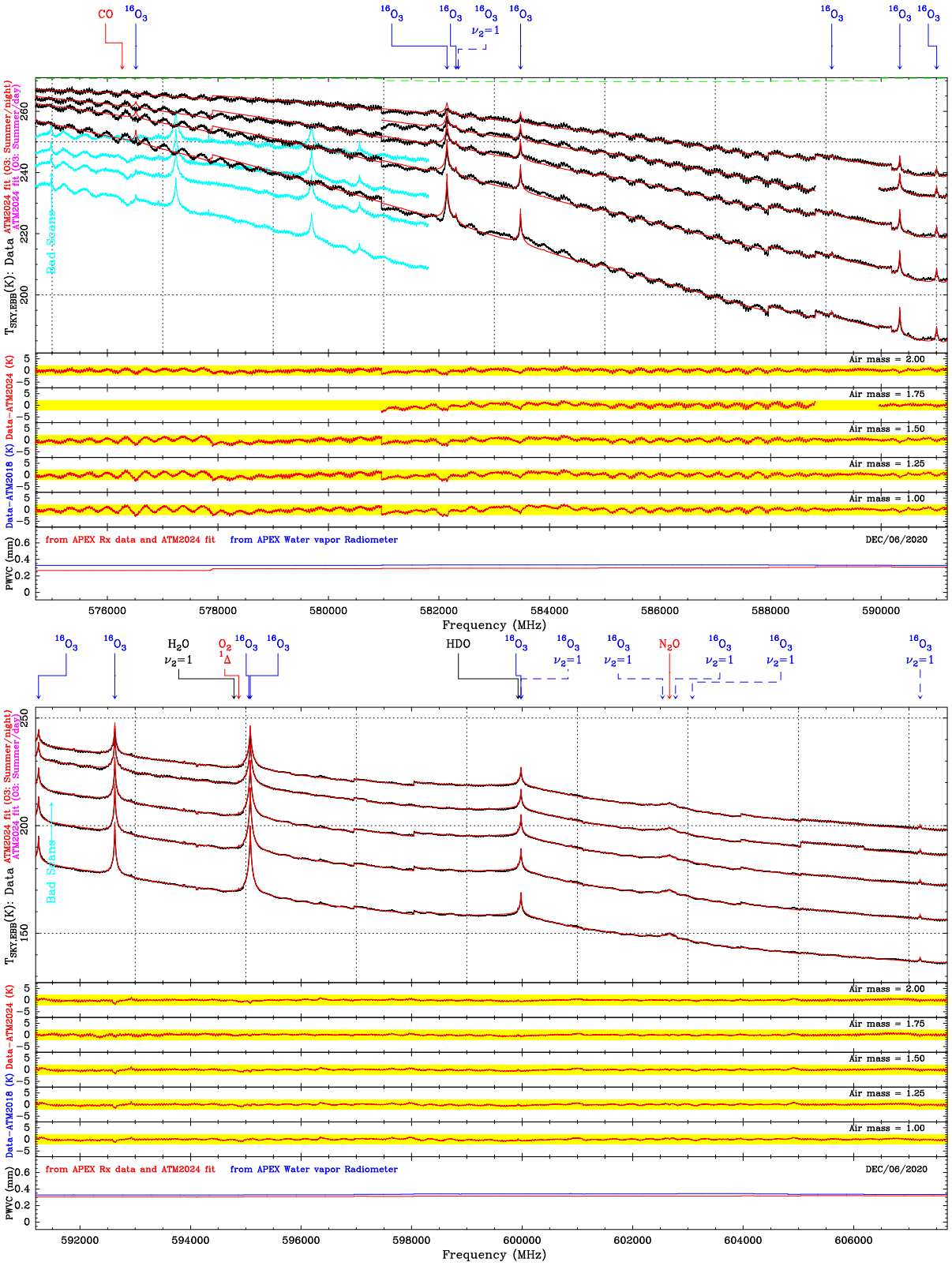

Figure 48: Zoom on Dec. 6^{th} 2020 SEPIA660 5 air mass sky dip data and ATM2024 fit results (part 1).

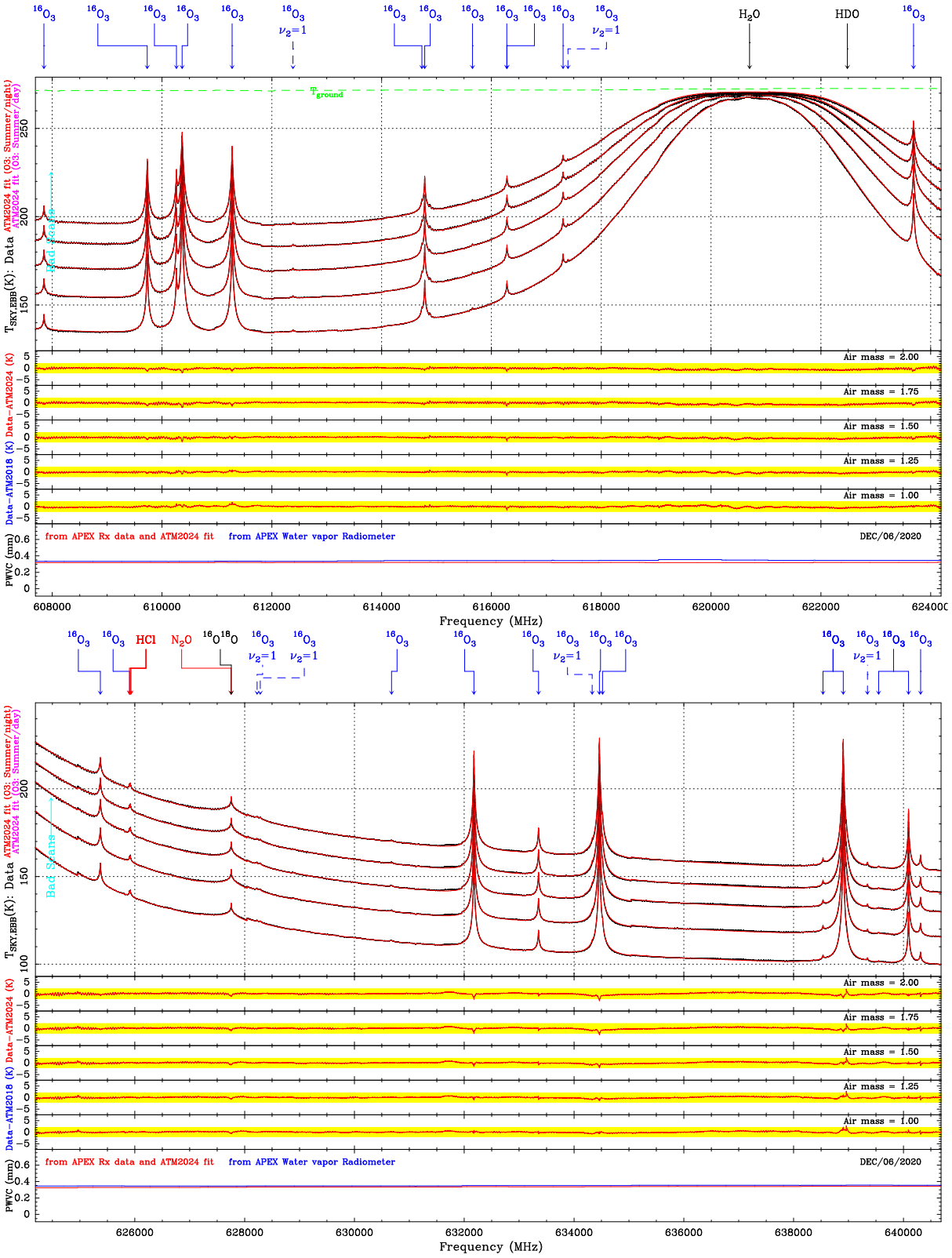

Figure 49: Zoom on Dec. 6^{th} 2020 SEPIA660 5 air mass sky dip data and ATM2024 fit results (part 2).

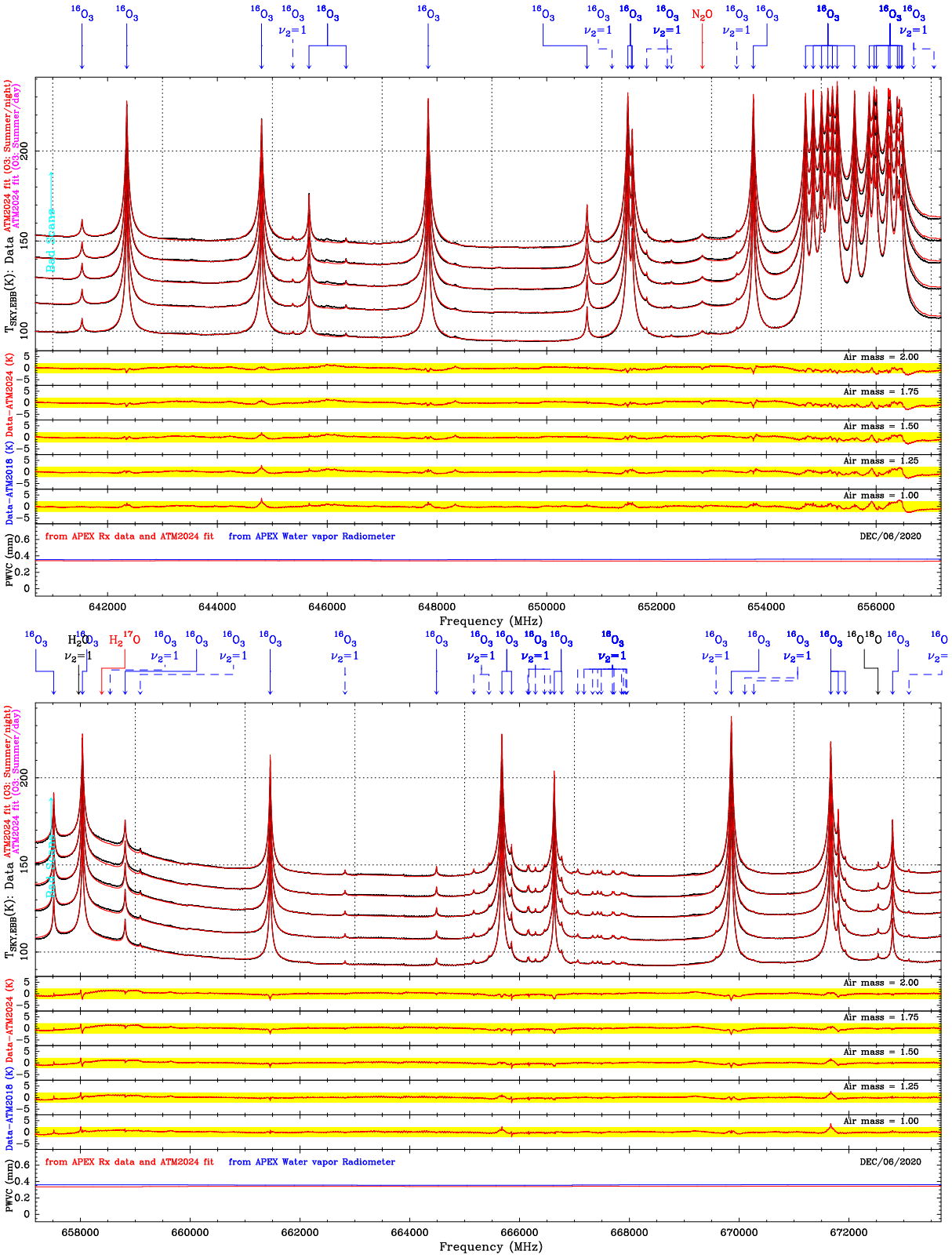

Figure 50: Zoom on Dec. 6^{th} 2020 SEPIA660 5 air mass sky dip data and ATM2024 fit results (part 3).

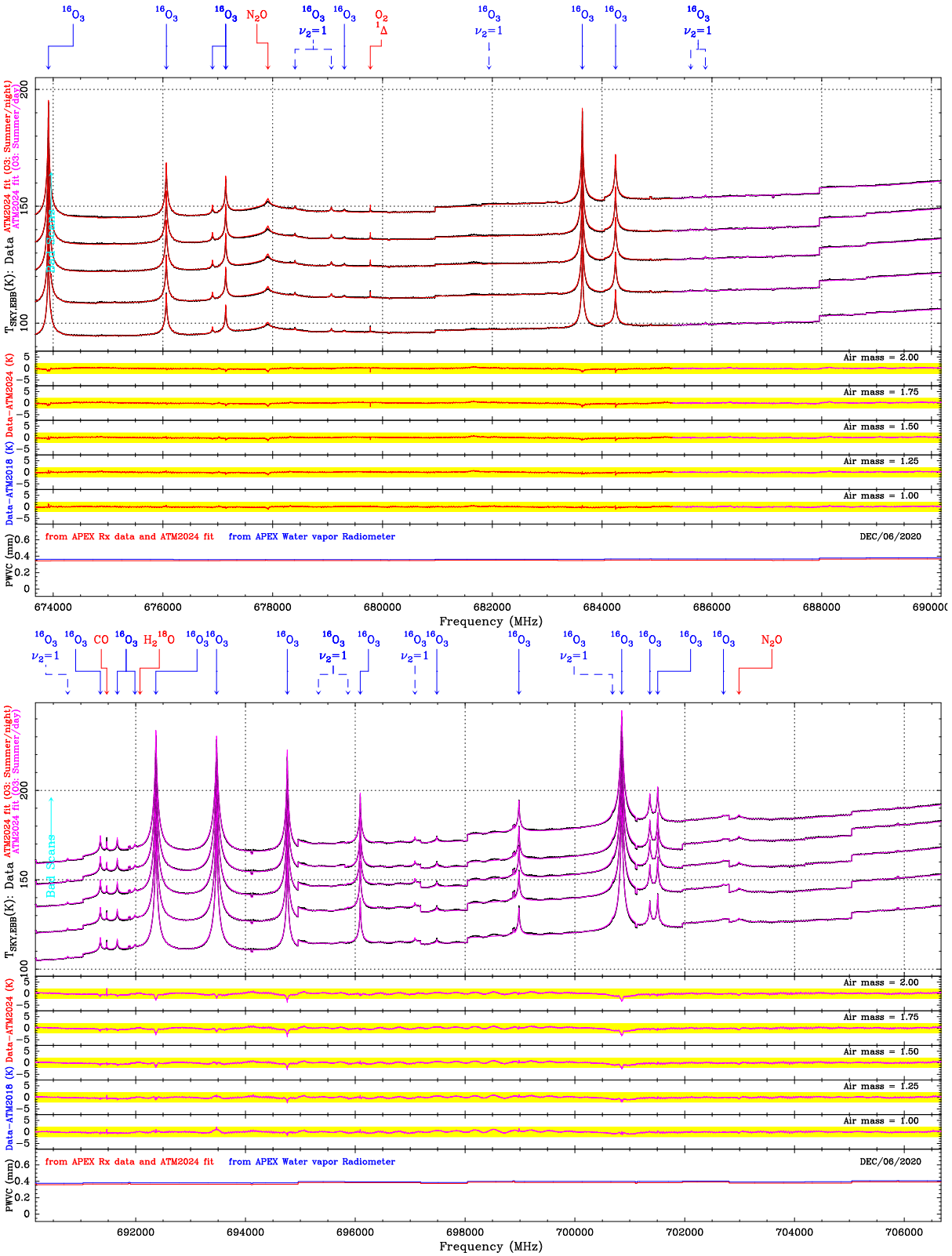

Figure 51: Zoom on Dec. 6^{th} 2020 SEPIA660 5 air mass sky dip data and ATM2024 fit results (part 4).

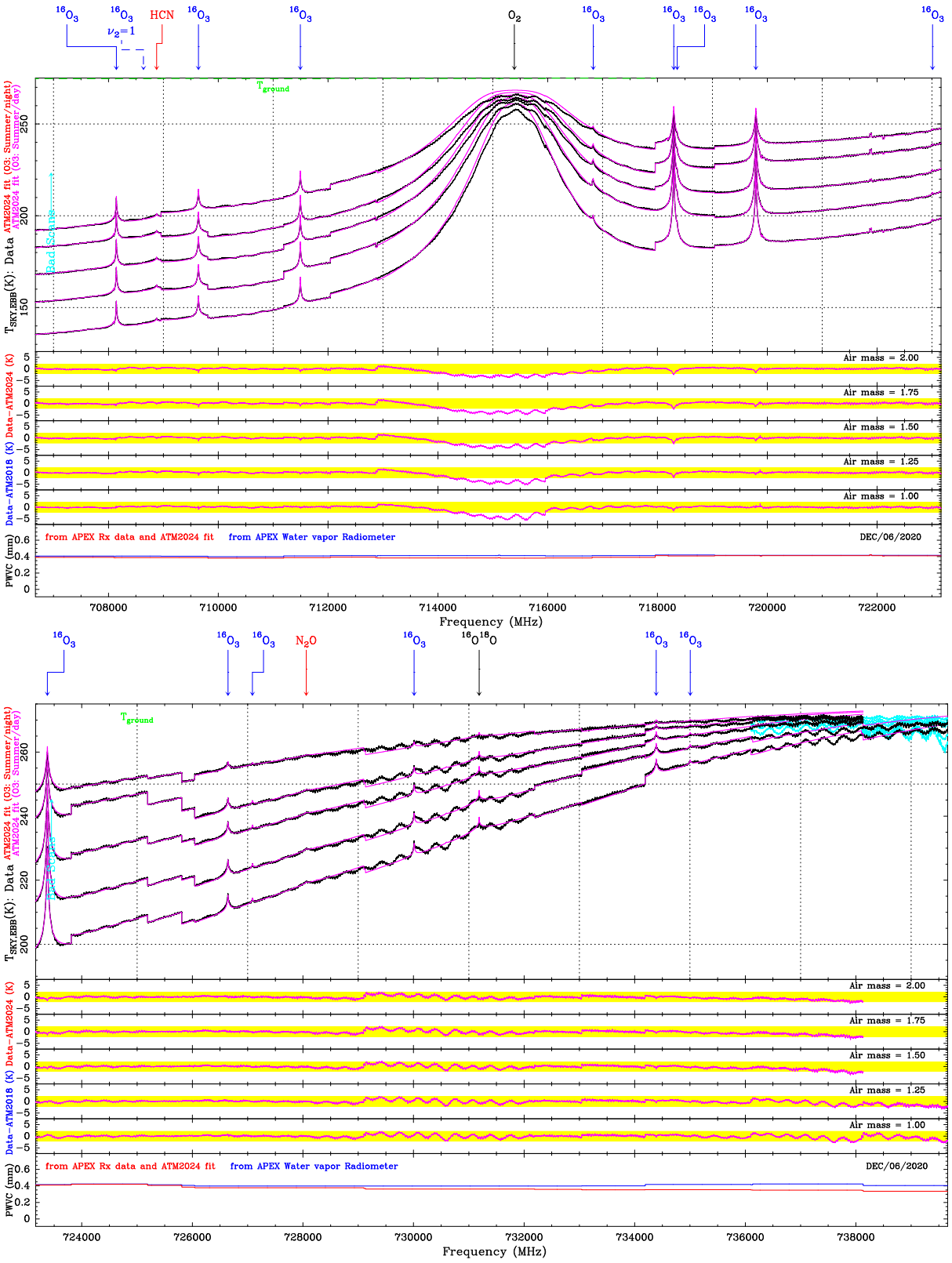

Figure 52: Zoom on Dec. 6^{th} 2020 SEPIA660 5 air mass sky dip data and ATM2024 fit results (part 5).

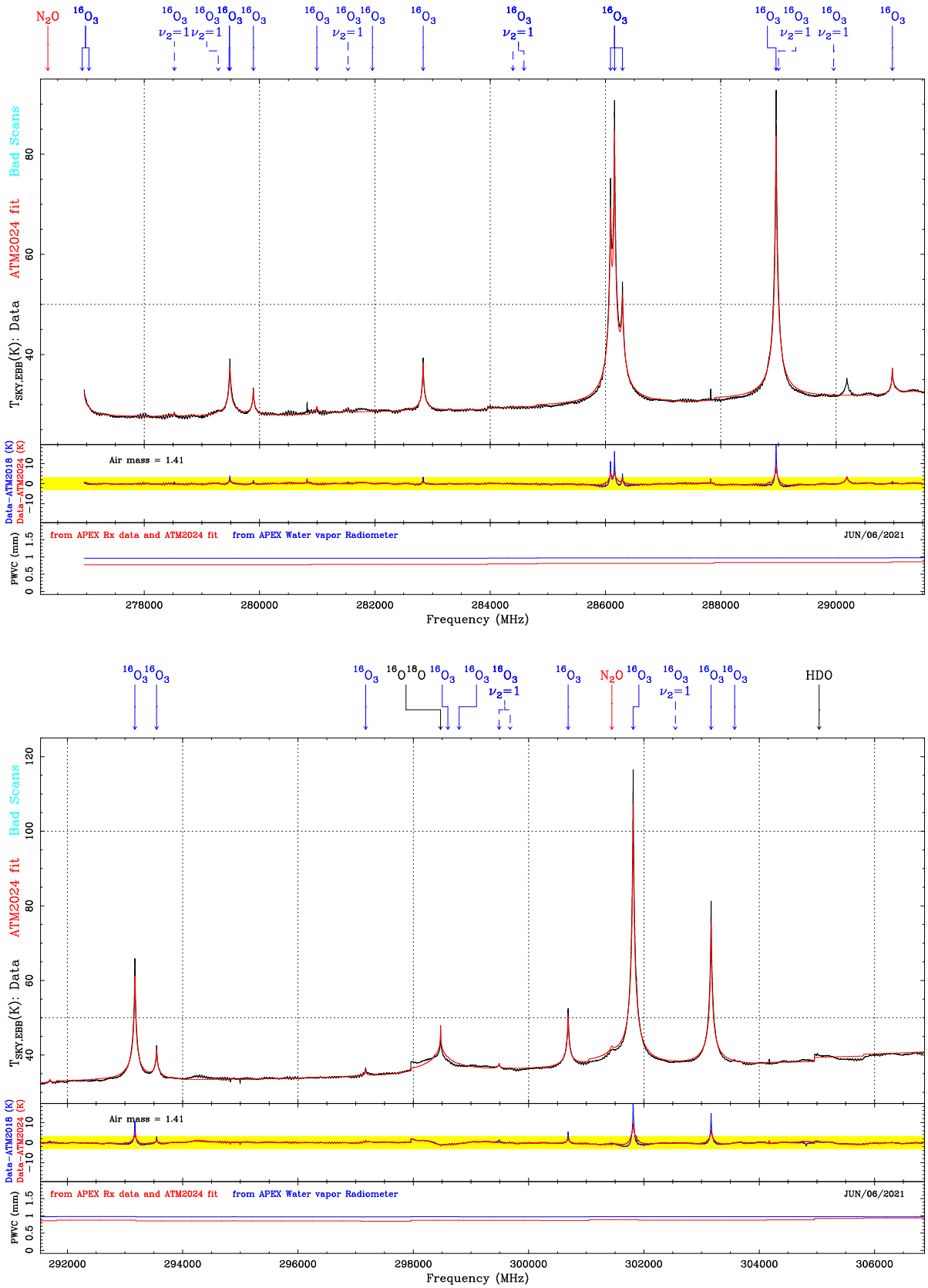

Figure 53: Zoom of SEPIA345 atmospheric data collected on June 24^{th} 2021 at elevations between 43 and 47 degrees and ATM2024 model fit (part 1).

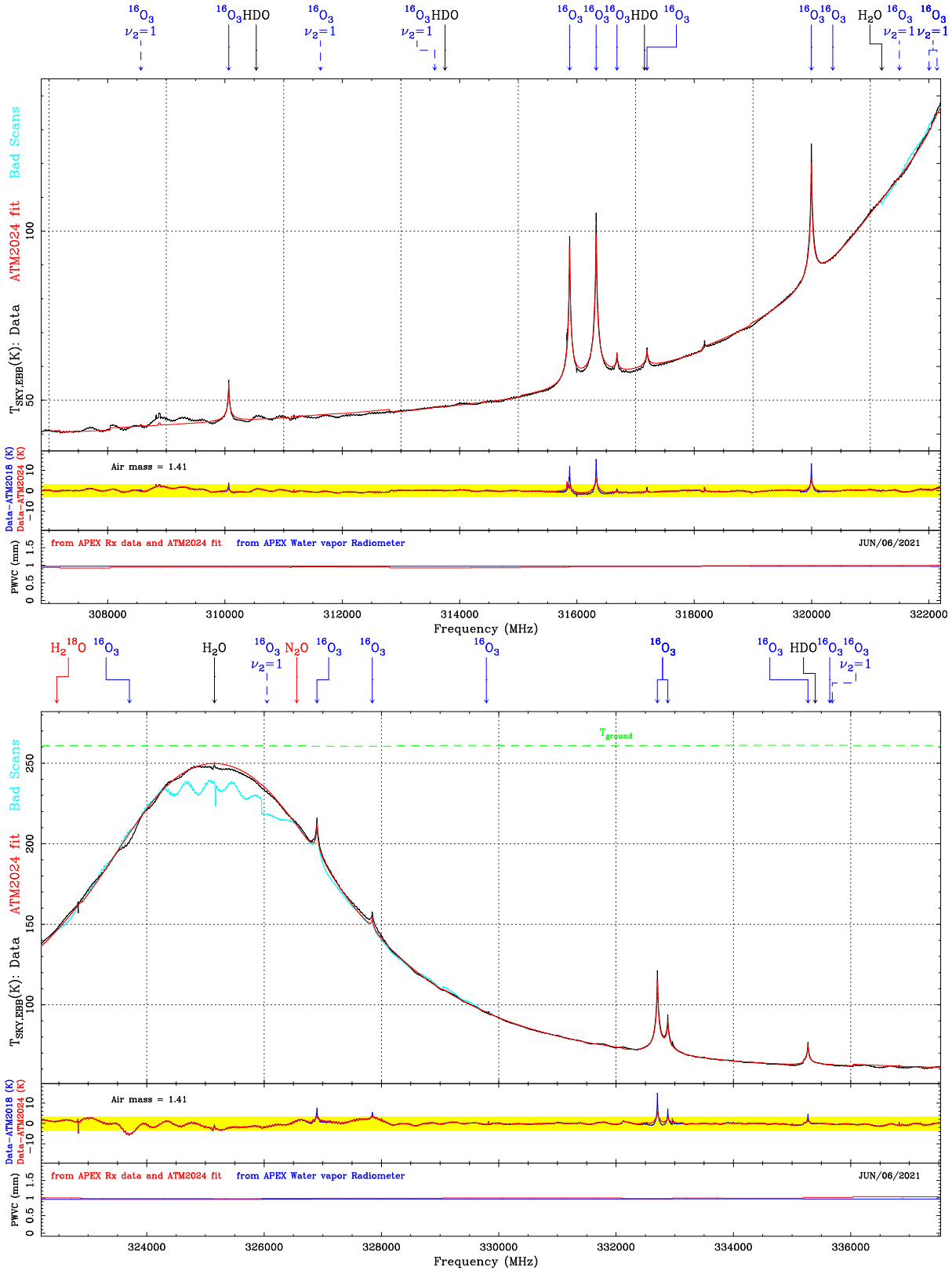

Figure 54: Zoom of SEPIA345 atmospheric data collected on June 24^{th} 2021 at elevations between 43 and 47 degrees and ATM2024 model fit (part 2).

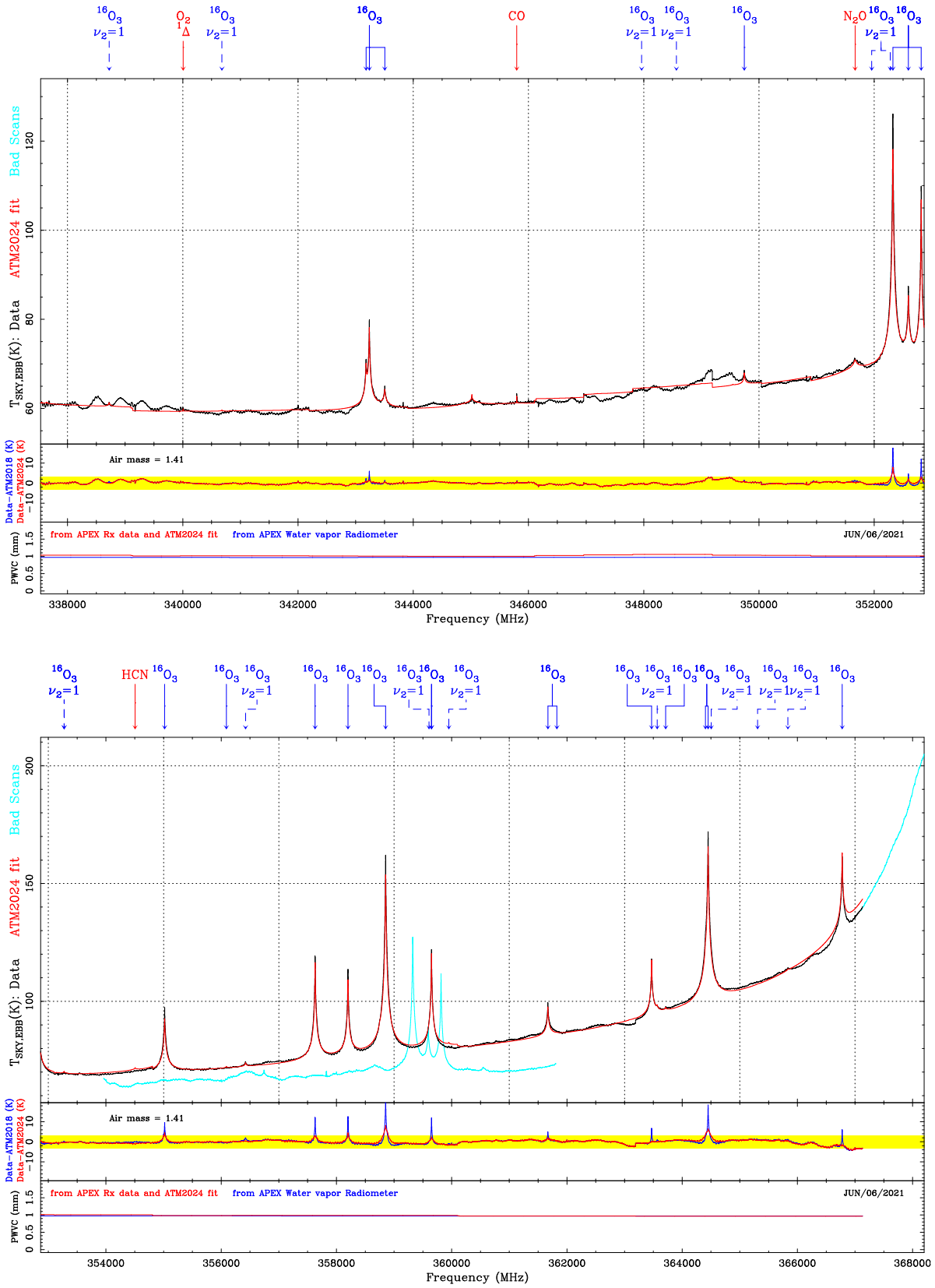

Figure 55: Zoom of SEPIA345 atmospheric data collected on June 24^{th} 2021 at elevations between 43 and 47 degrees and ATM2024 model fit (part 3).

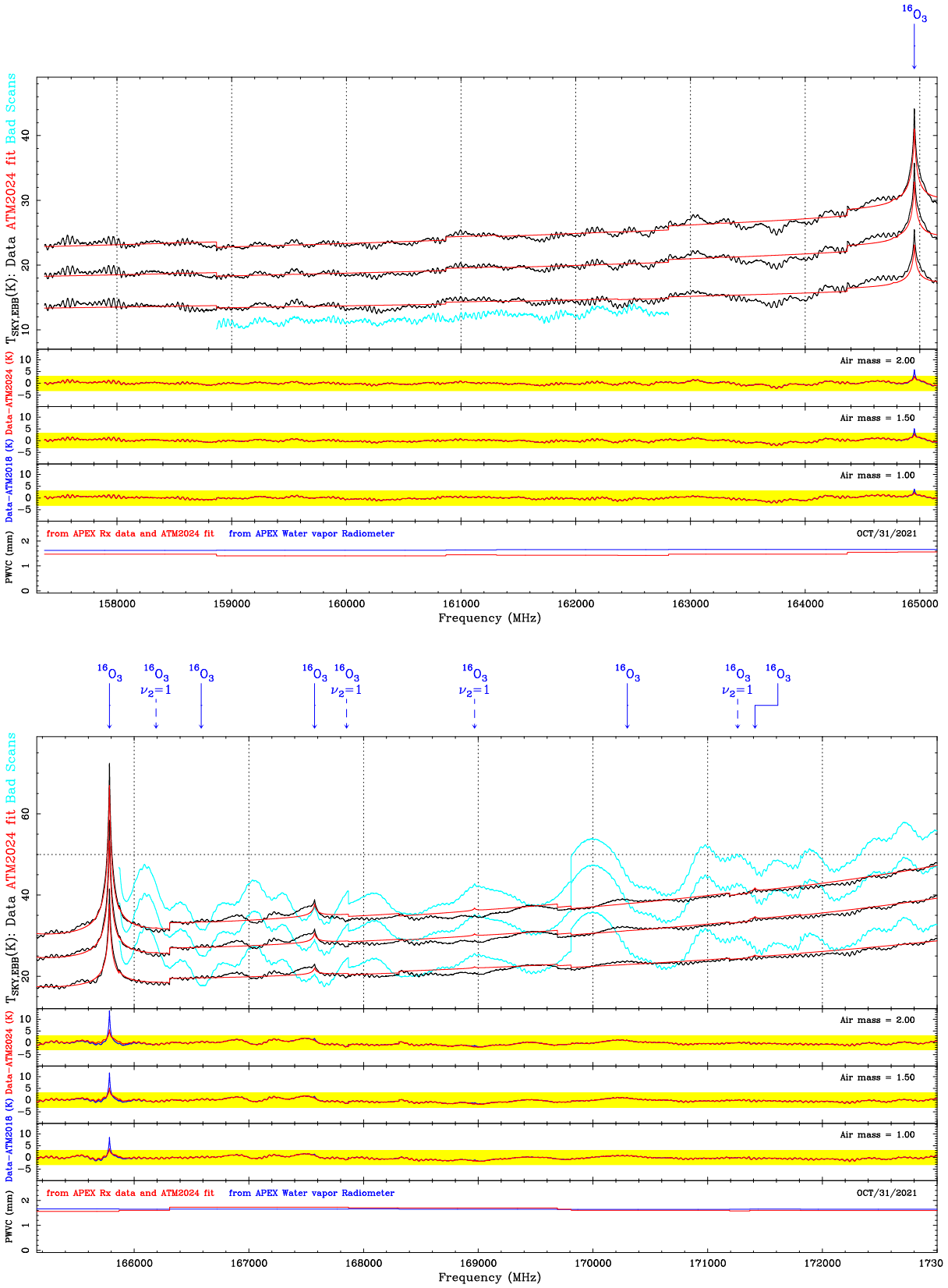

Figure 56: Zoom on SEPIA180 atmospheric data collected on October 31st 2021 and ATM2024 model fit (part 1).

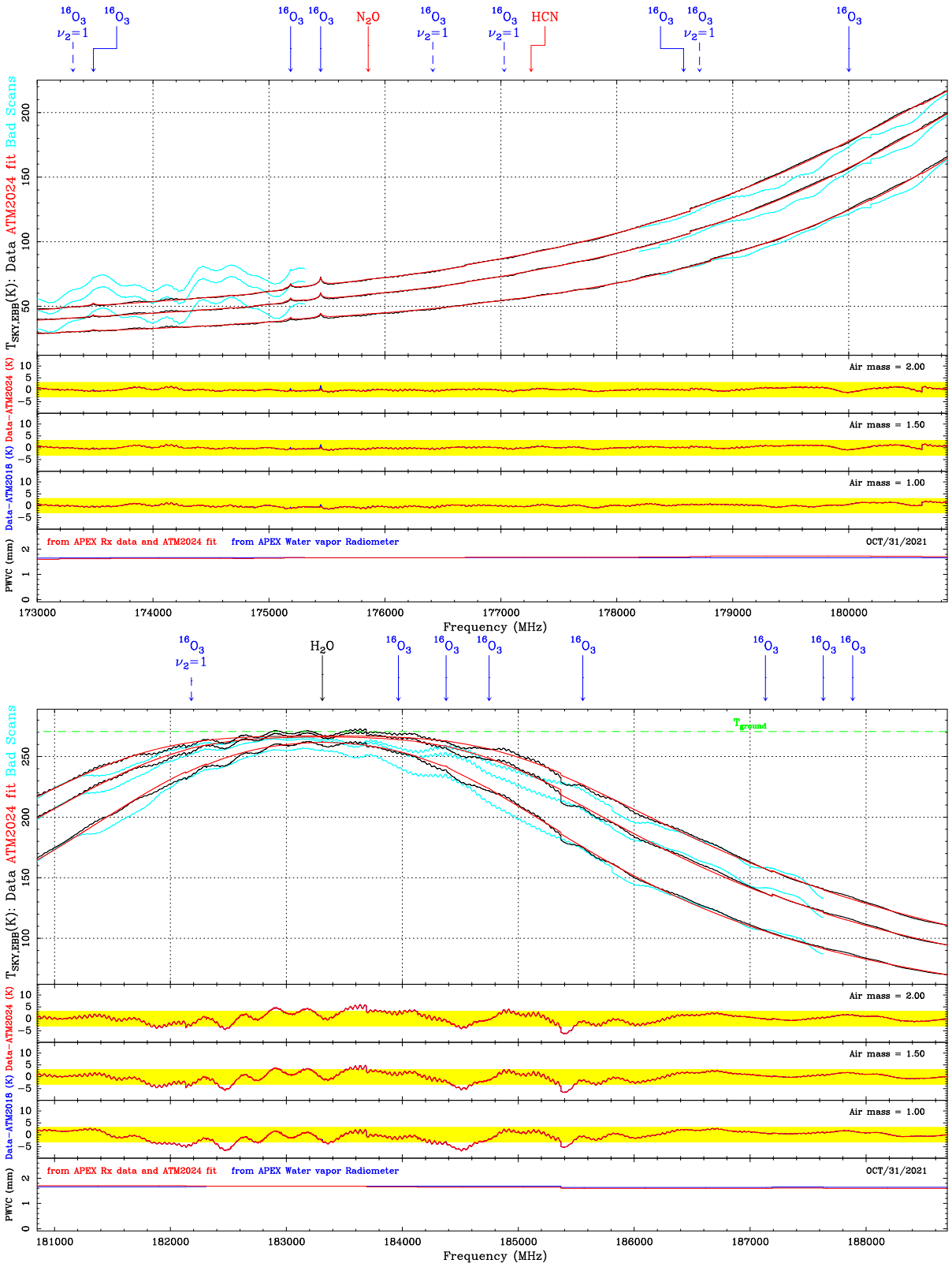

Figure 57: Zoom on SEPIA180 atmospheric data collected on October 31st 2021 and ATM2024 model fit (part 2).

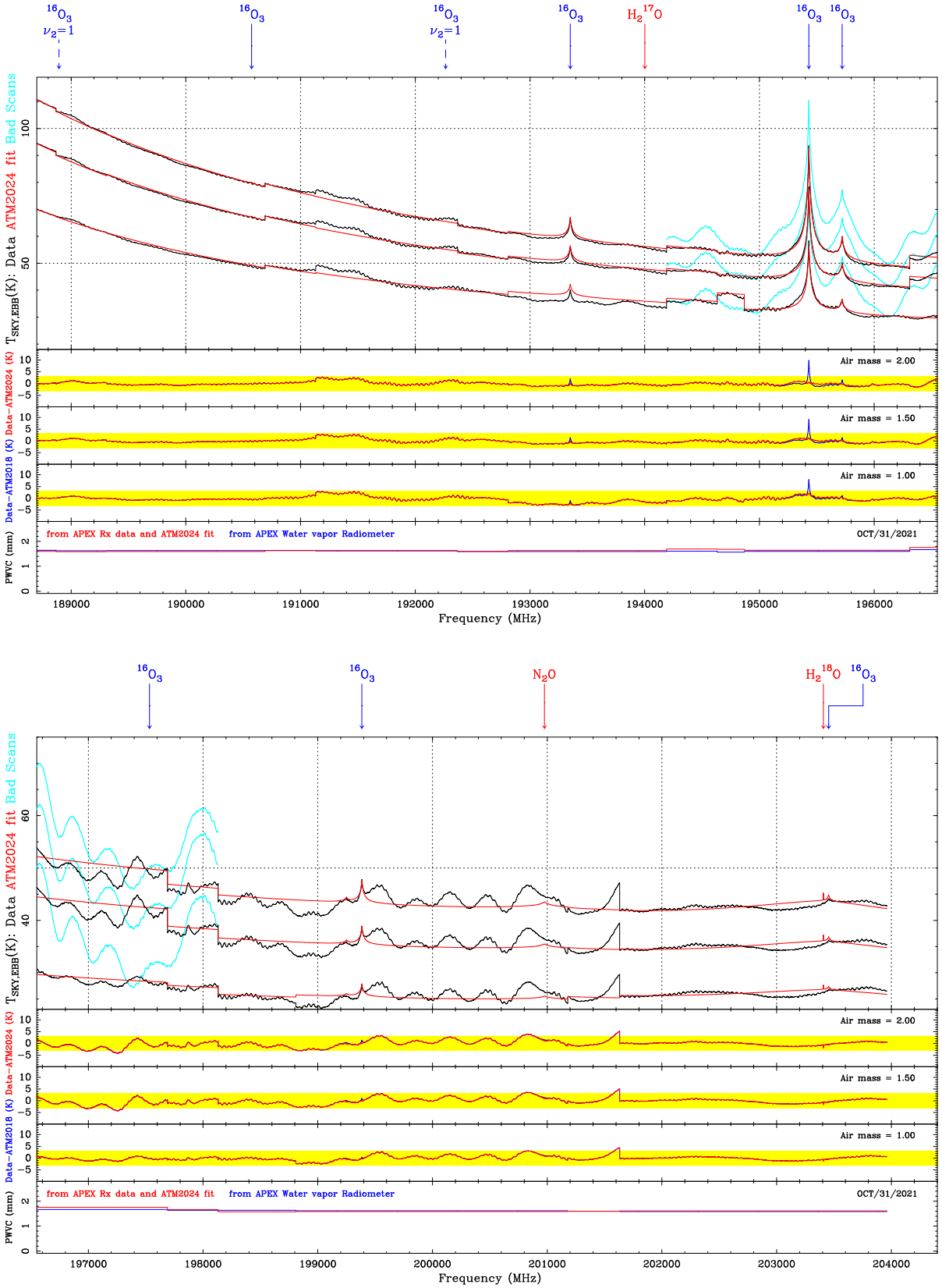

Figure 58: Zoom on SEPIA180 atmospheric data collected on October 31st 2021 and ATM2024 model fit (part 3).

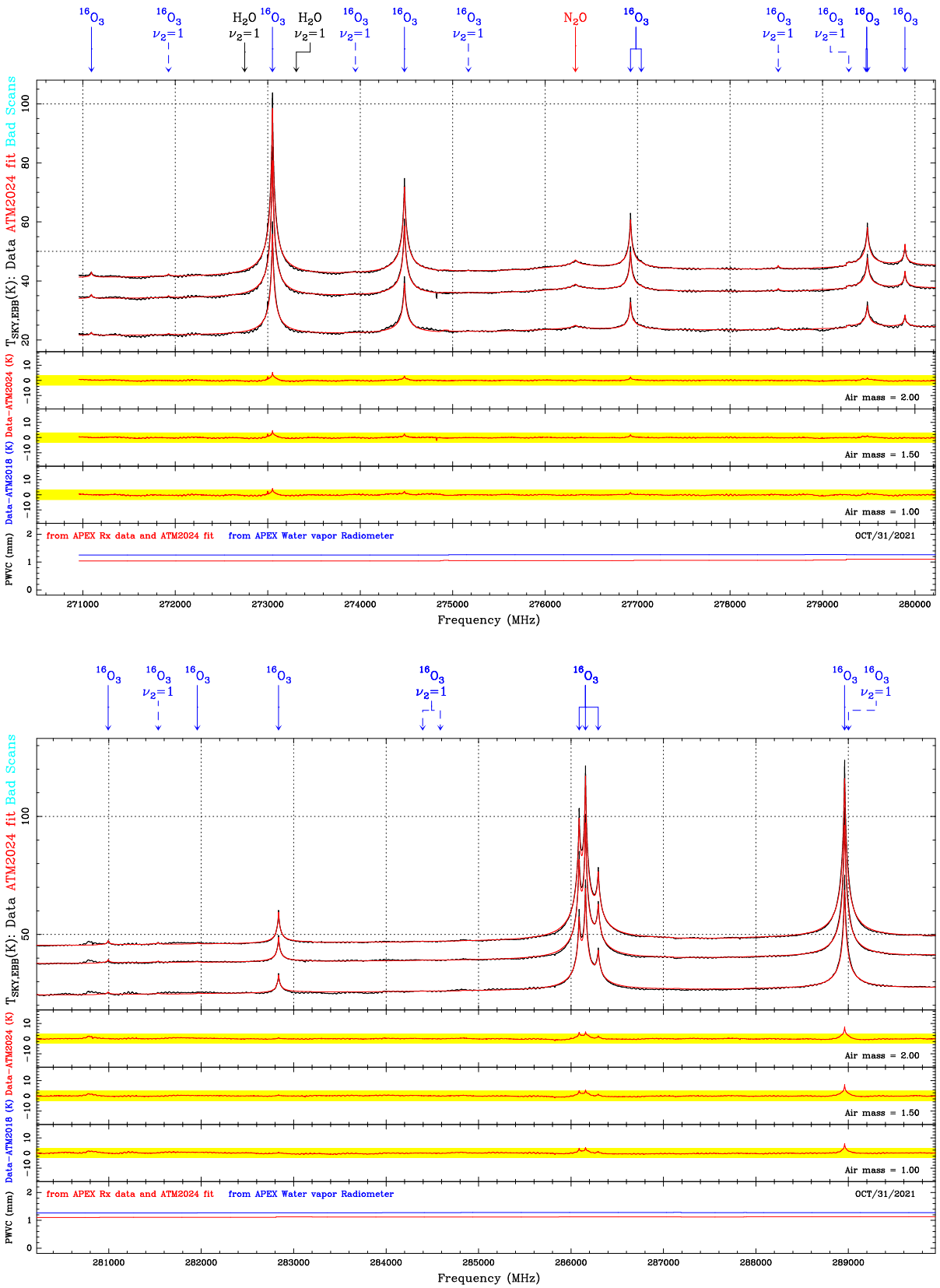

Figure 59: Zoom on Oct. 31^{st} 2021 SEPIA345 3 air mass sky dip data and ATM2024 fit results (part 1).

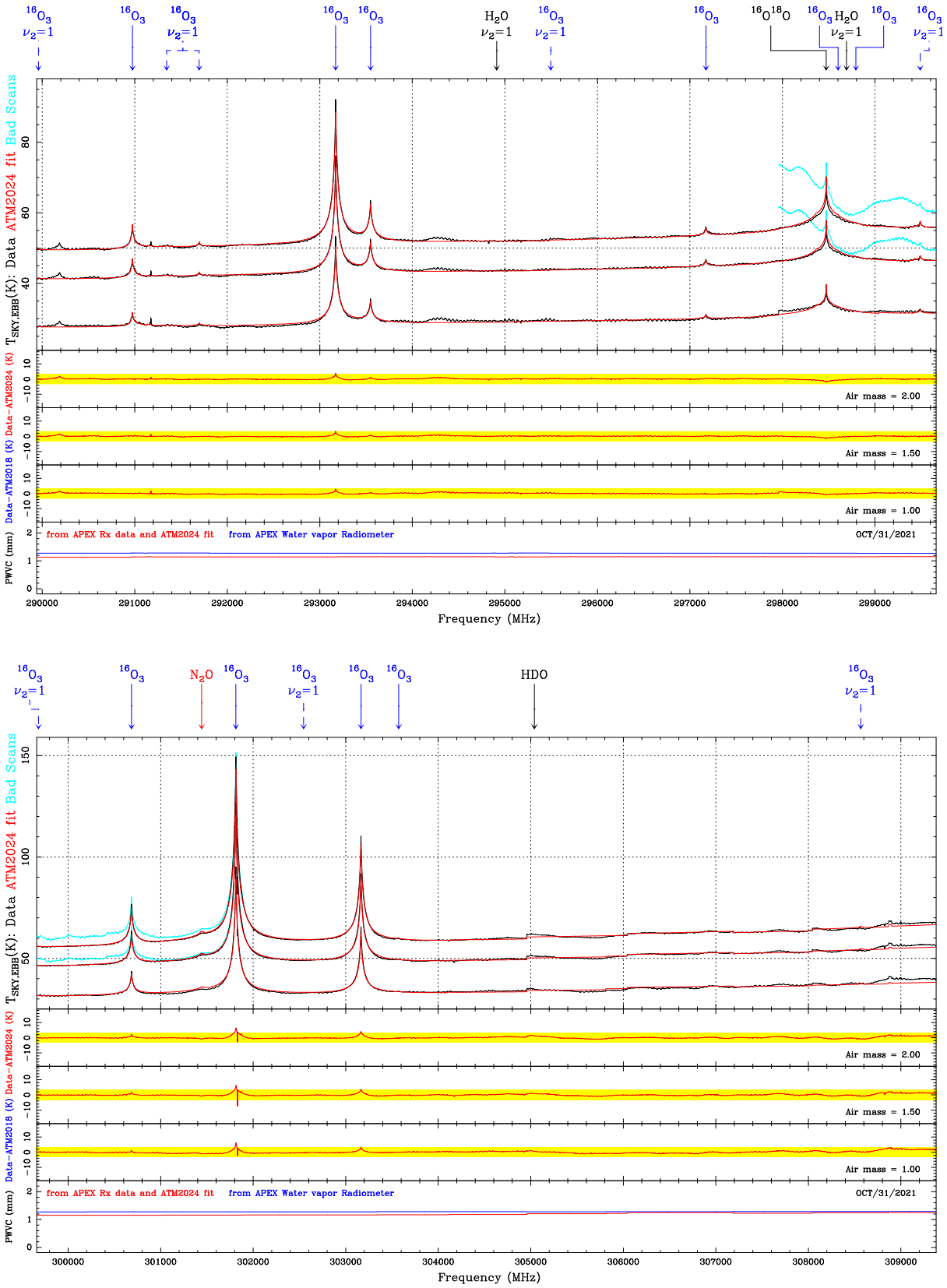

Figure 60: Zoom on Oct. 31^{st} 2021 SEPIA345 3 air mass sky dip data and ATM2024 fit results (part 1).

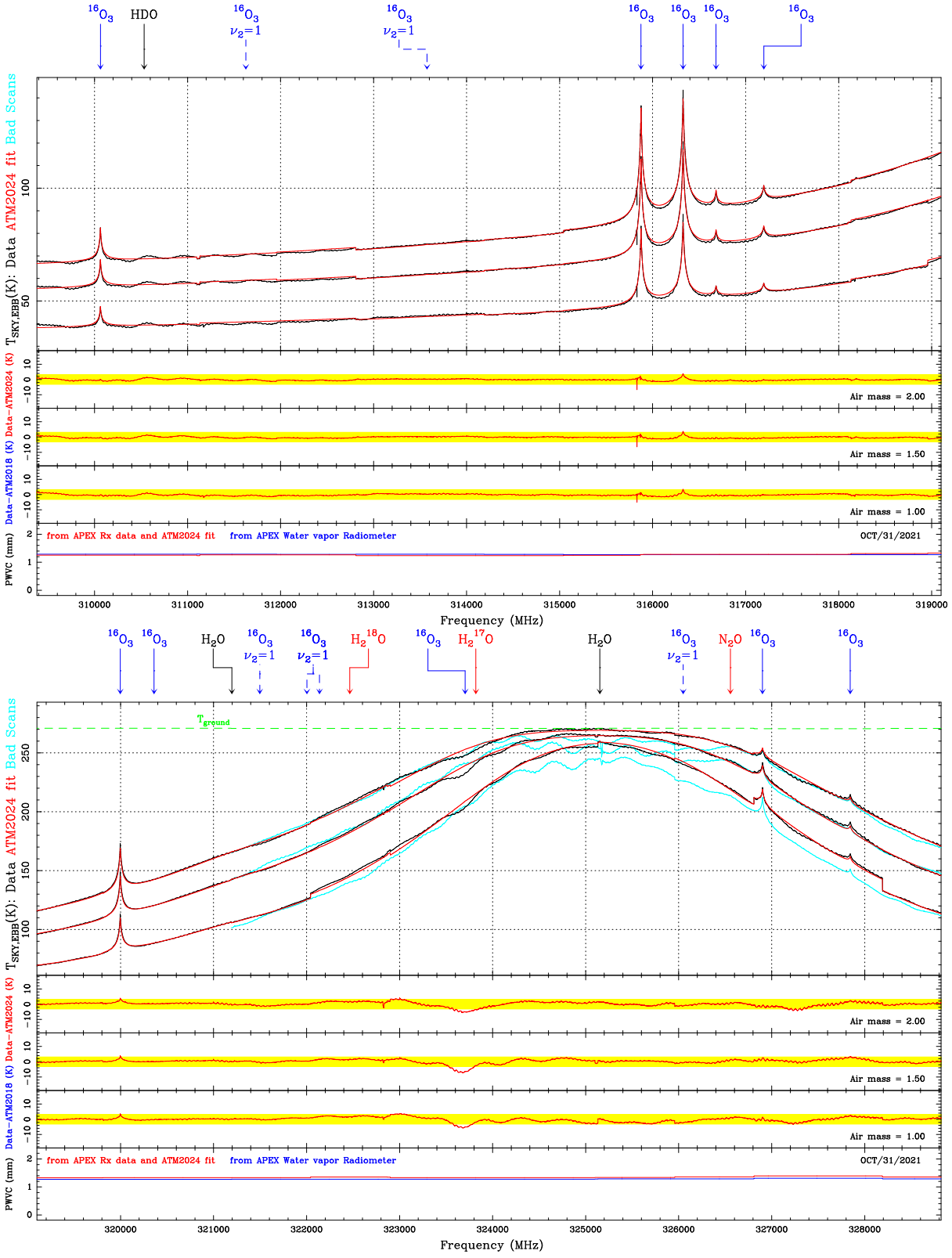

Figure 61: Zoom on Oct. 31st 2021 SEPIA345 3 air mass sky dip data and ATM2024 fit results (part 1).

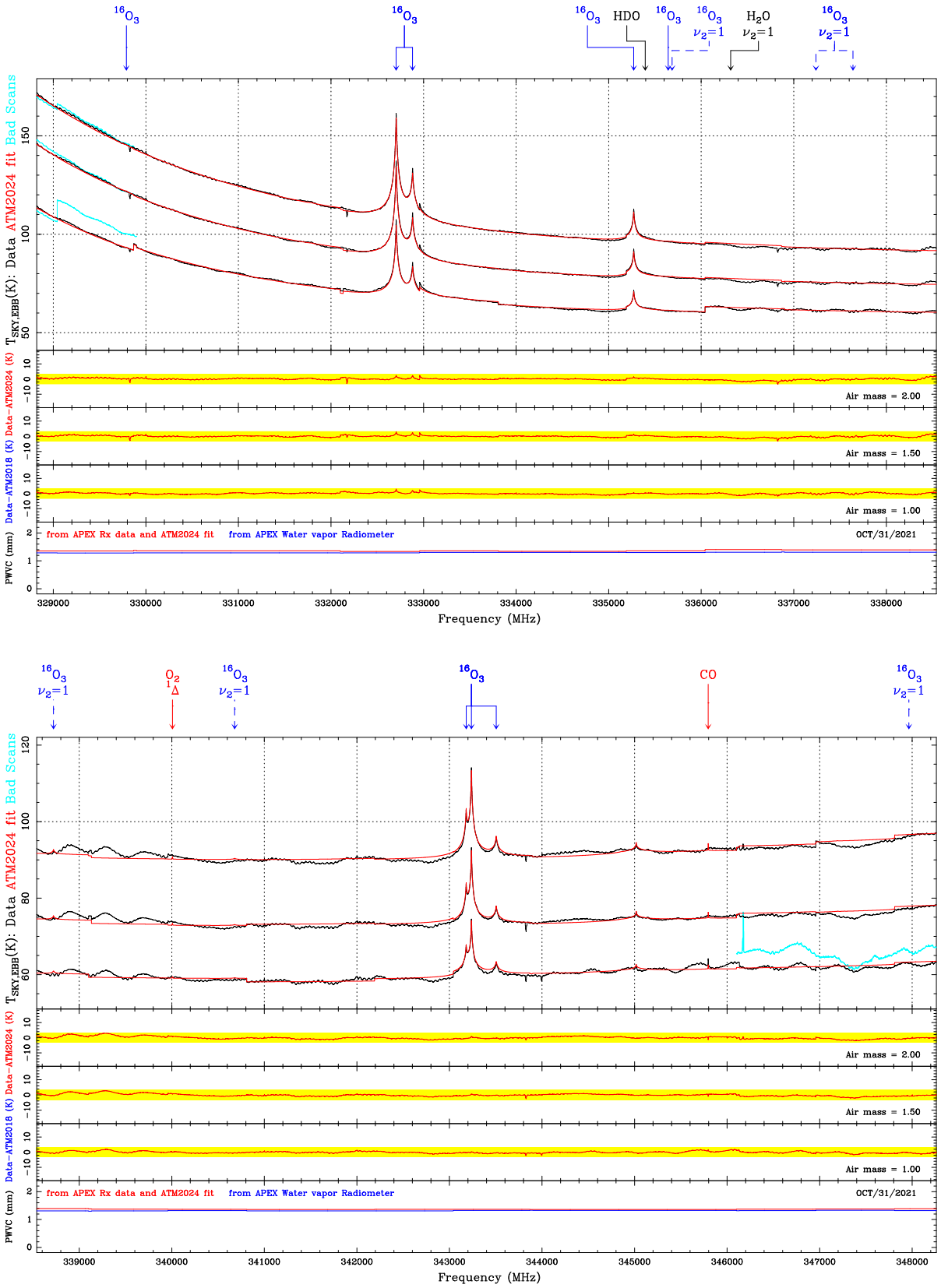

Figure 62: Zoom on Oct. 31^{st} 2021 SEPIA345 3 air mass sky dip data and ATM2024 fit results (part 1).

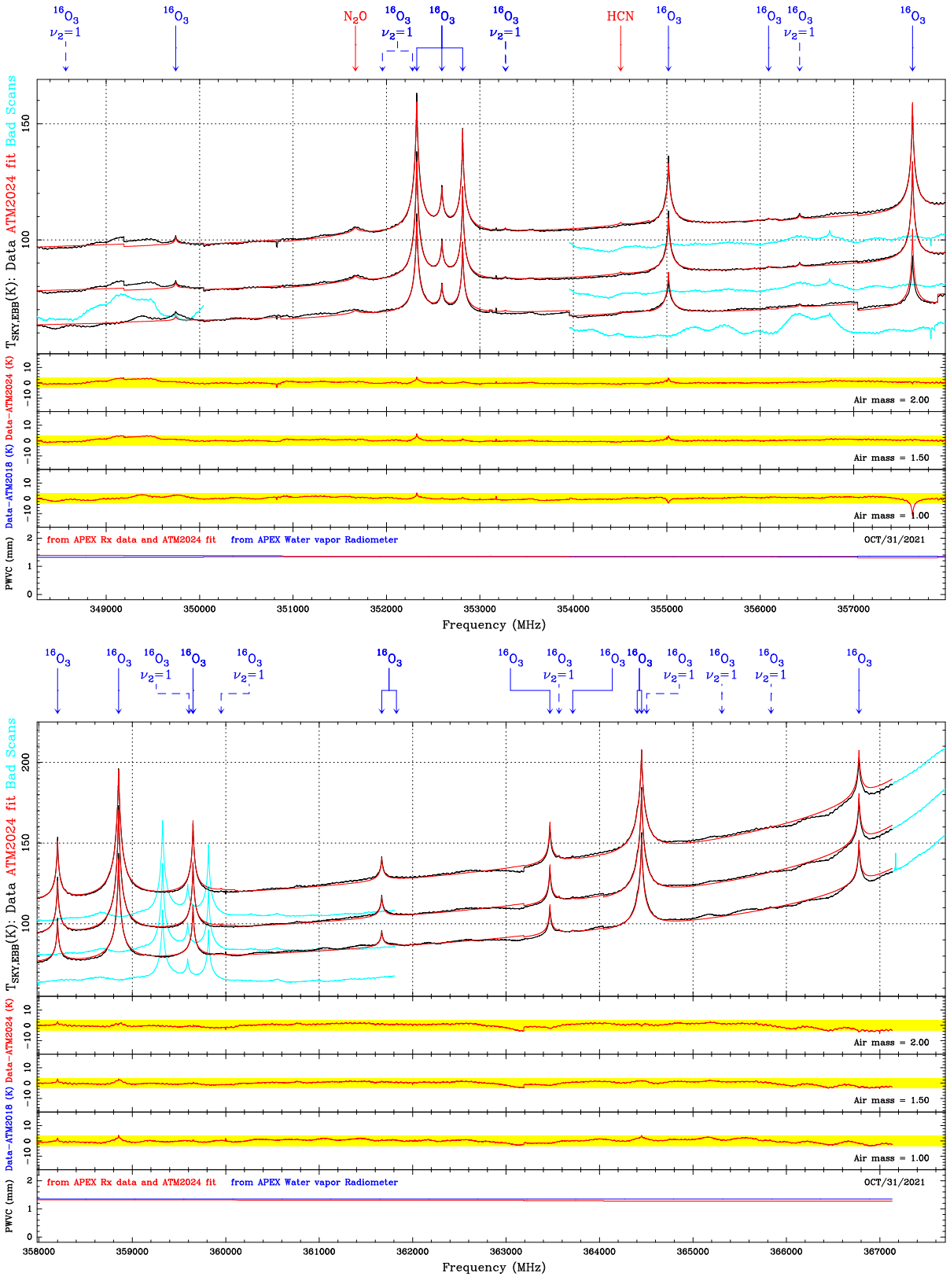

Figure 63: Zoom on Oct. 31st 2021 SEPIA345 3 air mass sky dip data and ATM2024 fit results (part 1).

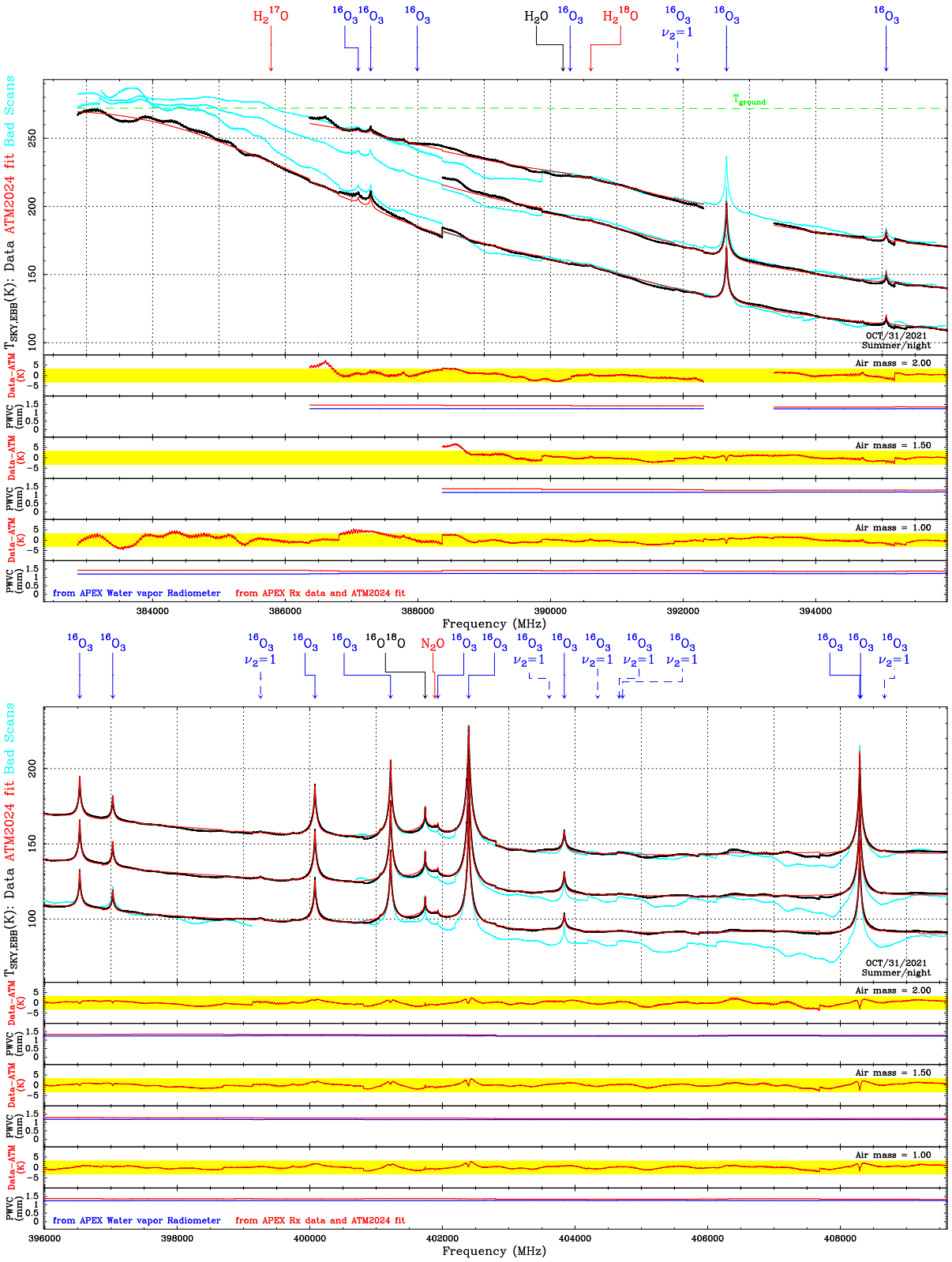

Figure 64: Zoom on Oct. 31st 2021 nFLASH460 3 air mass sky dip data and ATM2024 fit results (part 1). The retrieved PWVC is plotted separately for each air mass.

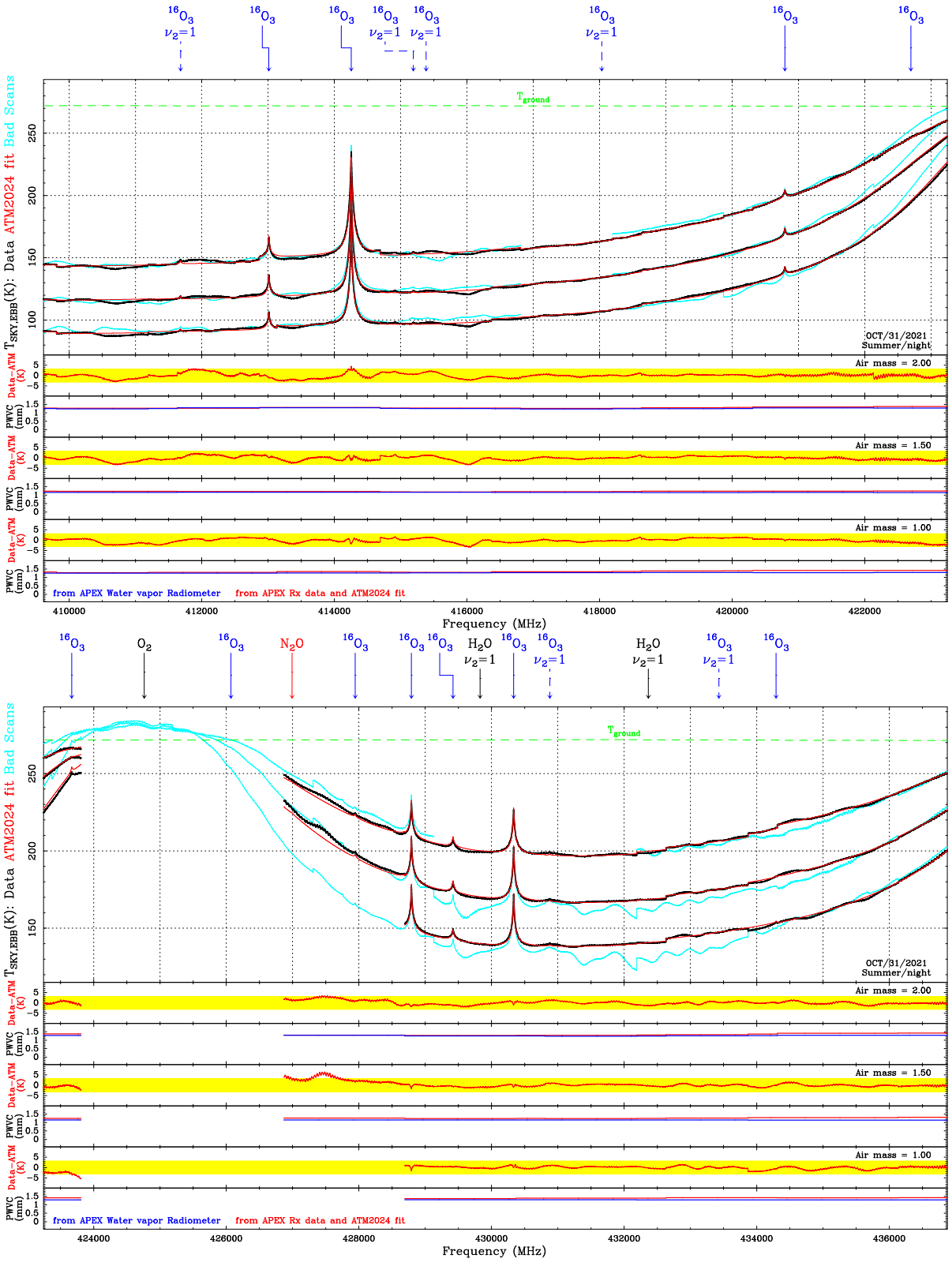

Figure 65: Zoom on Oct. 31st 2021 nFLASH460 3 air mass sky dip data and ATM2024 fit results (part 2). The retrieved PWVC is plotted separately for each air mass.

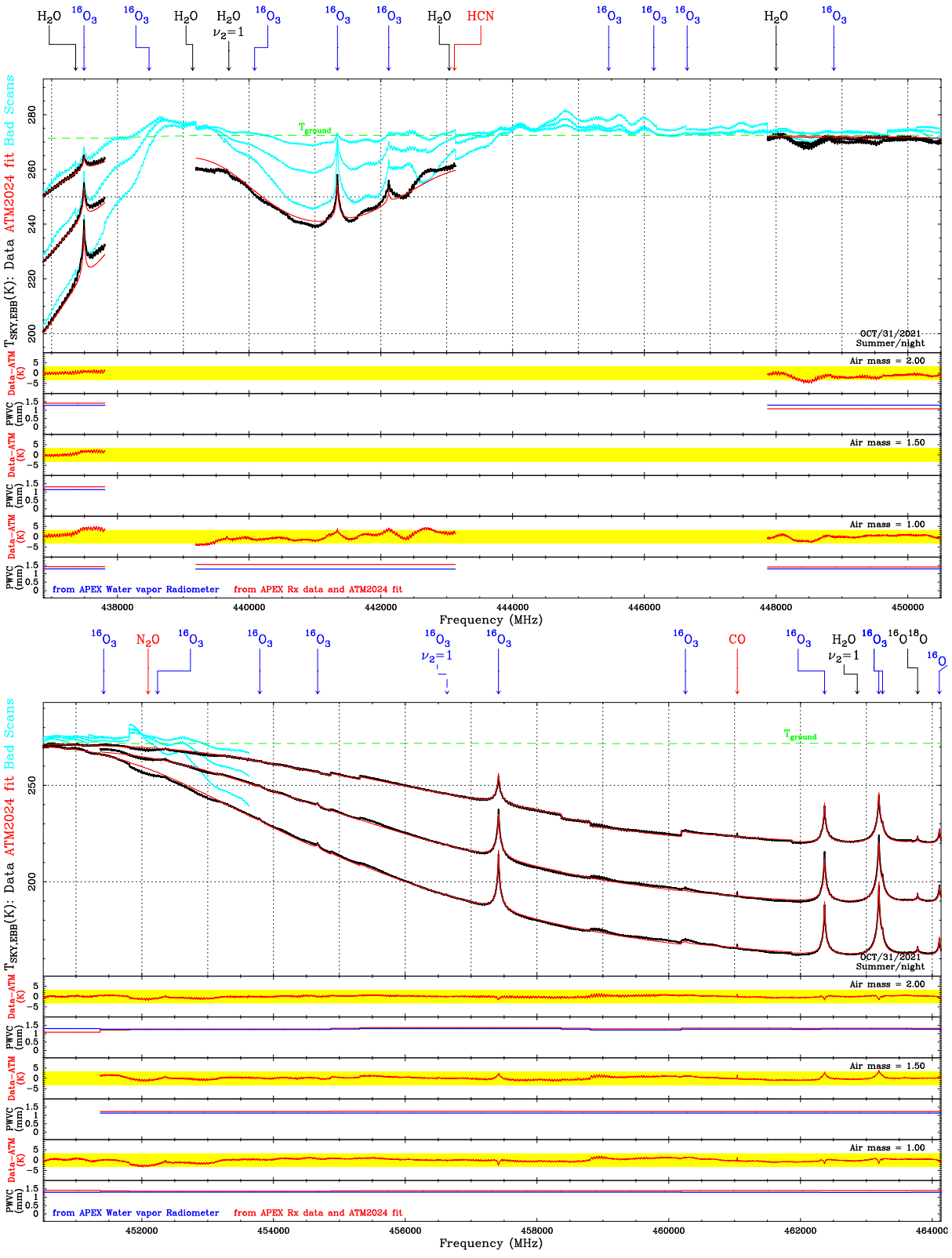

Figure 66: Zoom on Oct. 31st 2021 nFLASH460 3 air mass sky dip data and ATM2024 fit results (part 3). The retrieved PWVC is plotted separately for each air mass.

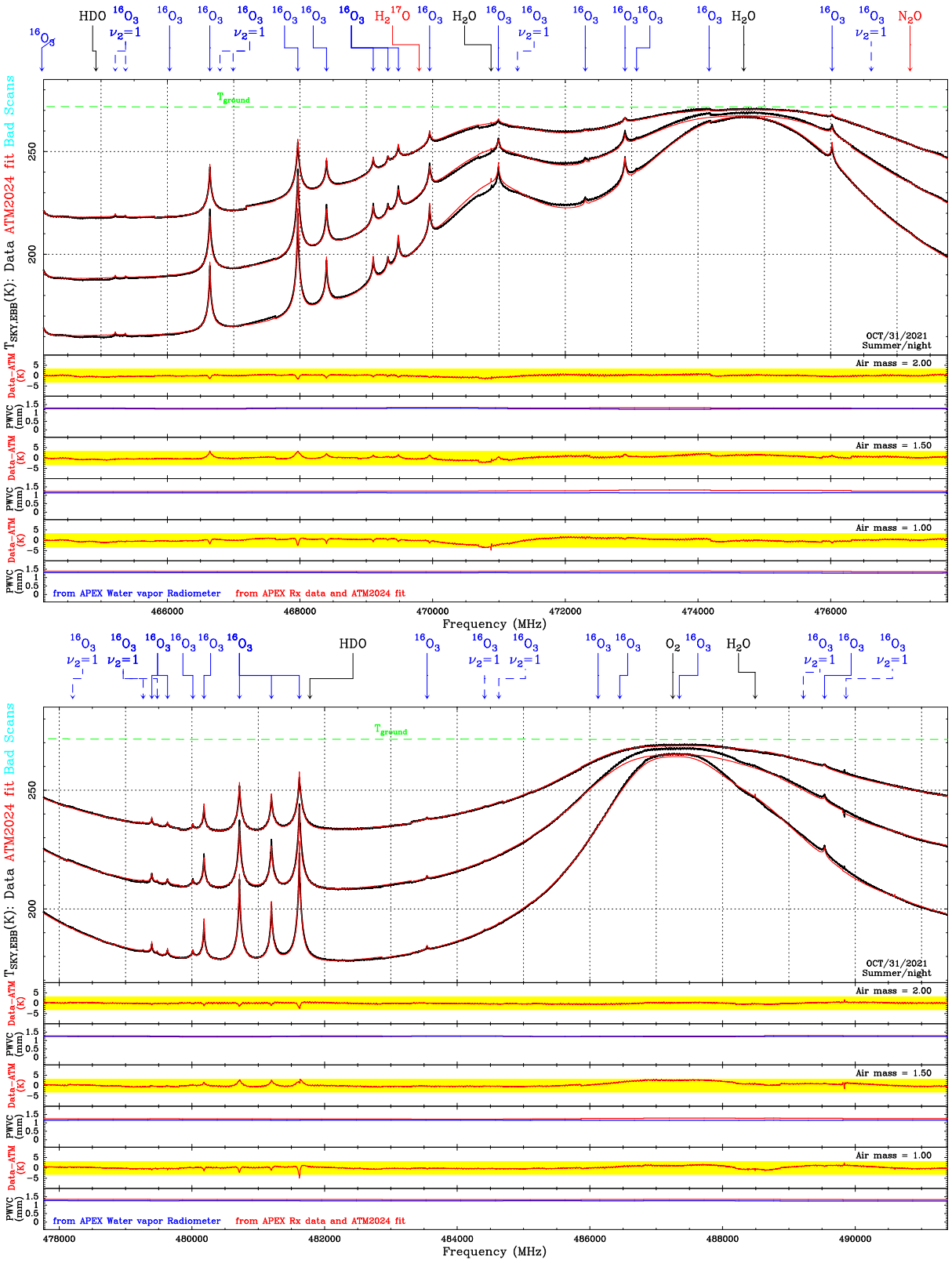

Figure 67: Zoom on Oct. 31st 2021 nFLASH460 3 air mass sky dip data and ATM2024 fit results (part 4). The retrieved PWVC is plotted separately for each air mass.

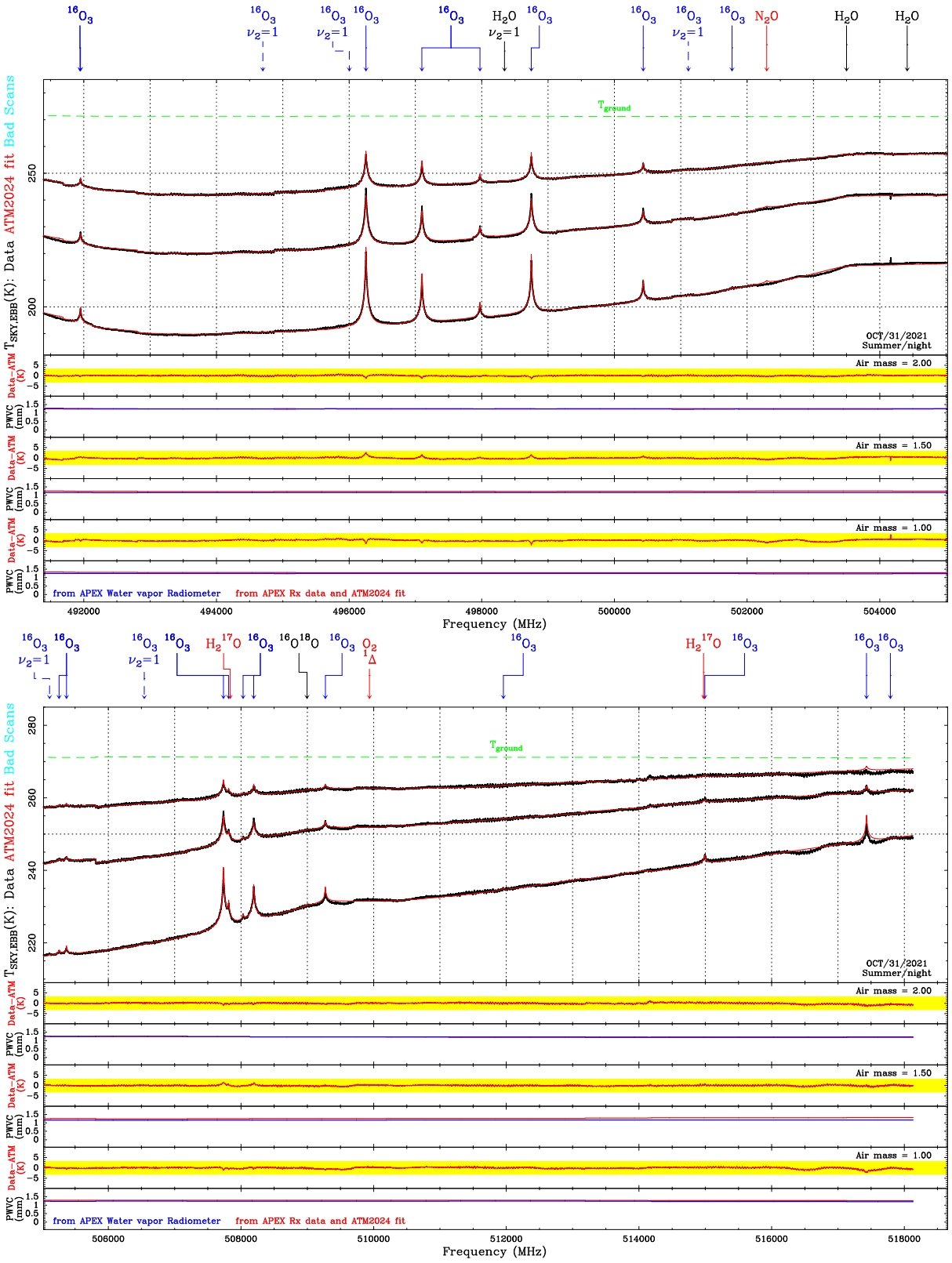

Figure 68: Zoom on Oct. 31st 2021 nFLASH460 3 air mass sky dip data and ATM2024 fit results (part 5). The retrieved PWVC is plotted separately for each air mass.

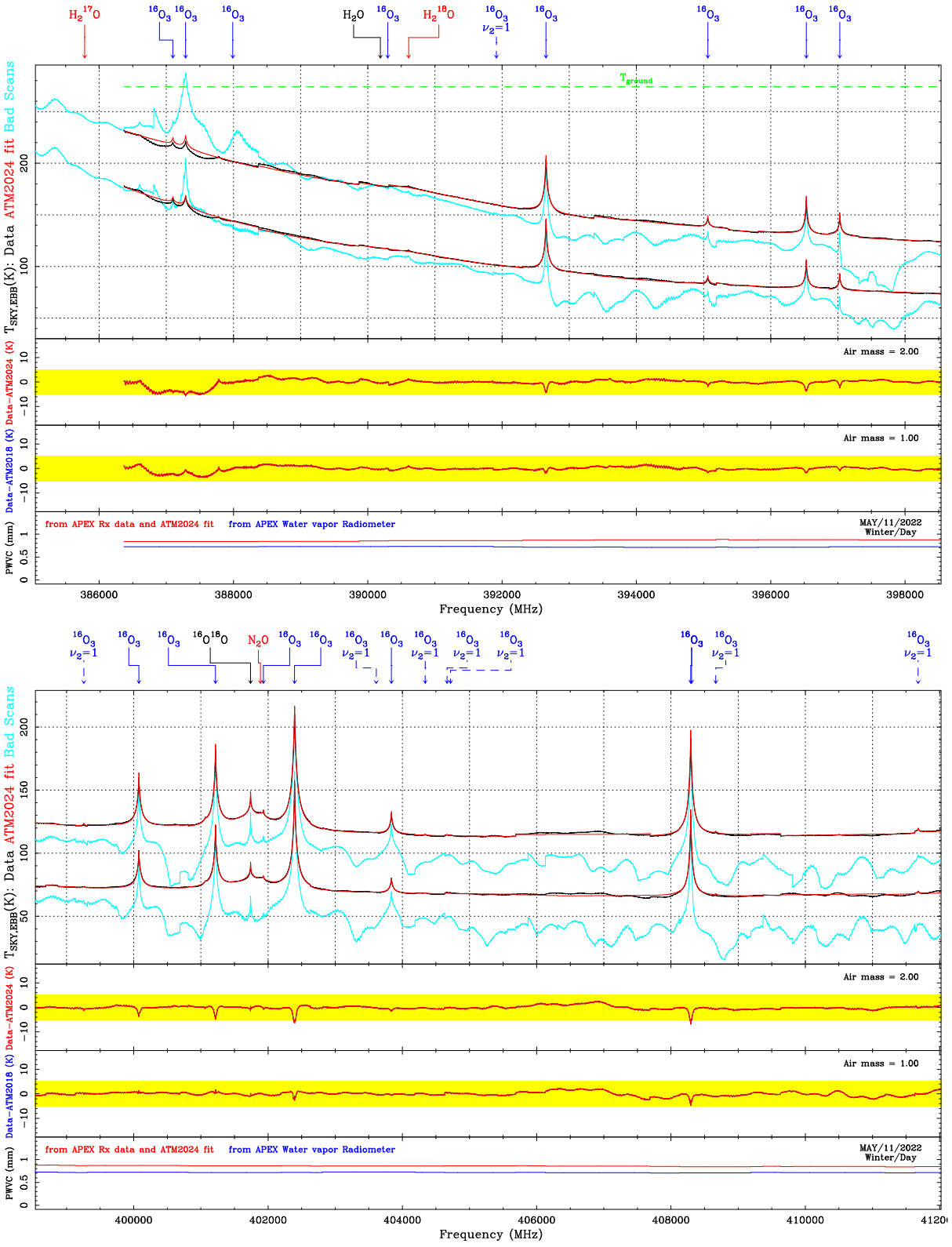

Figure 69: Zoom on May 11^{th} 2022 nFLASH460 2 air mass sky dip data and ATM2024 fit results (part 1).

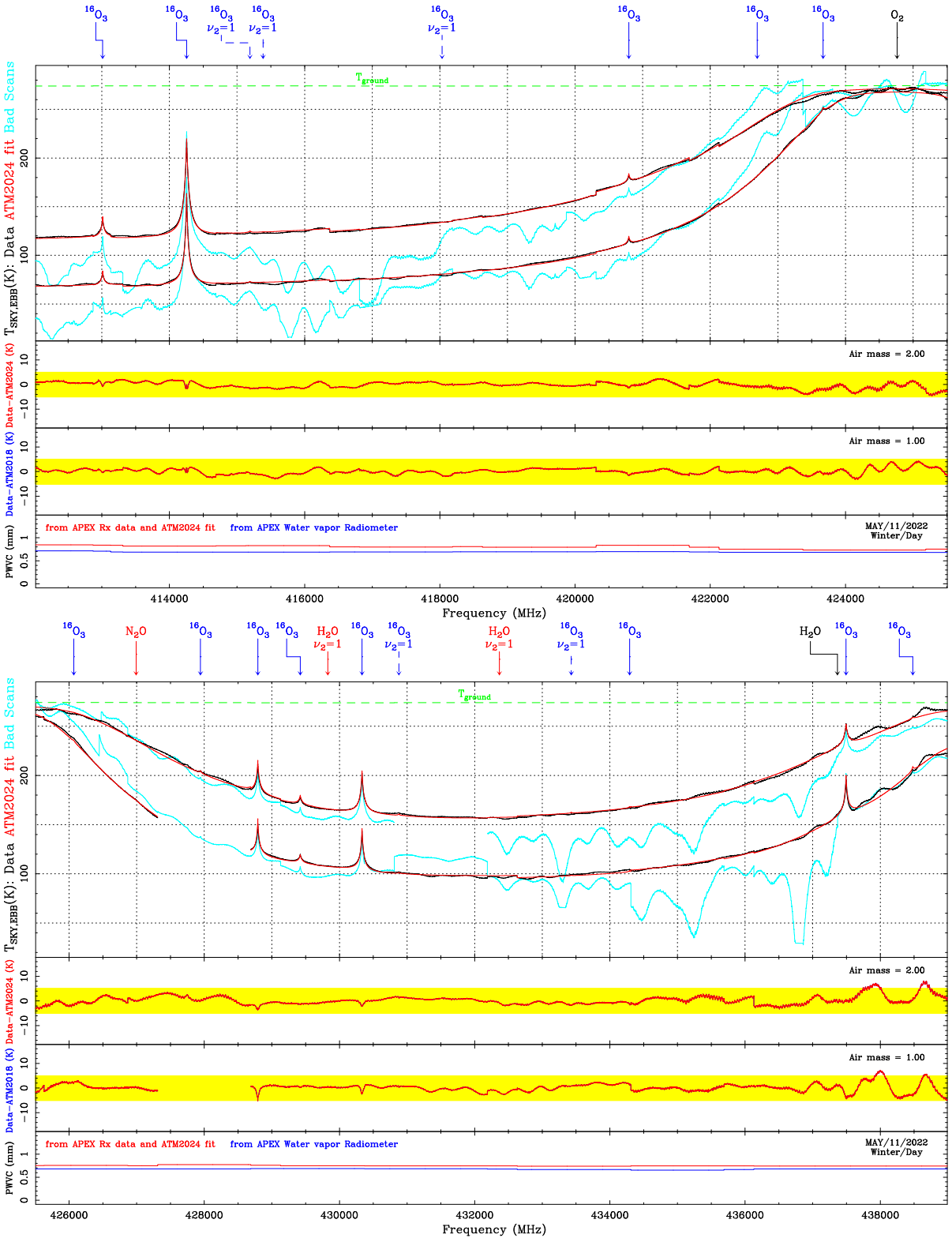

Figure 70: Zoom on May 11^{th} 2022 nFLASH460 2 air mass sky dip data and ATM2024 fit results (part 2).

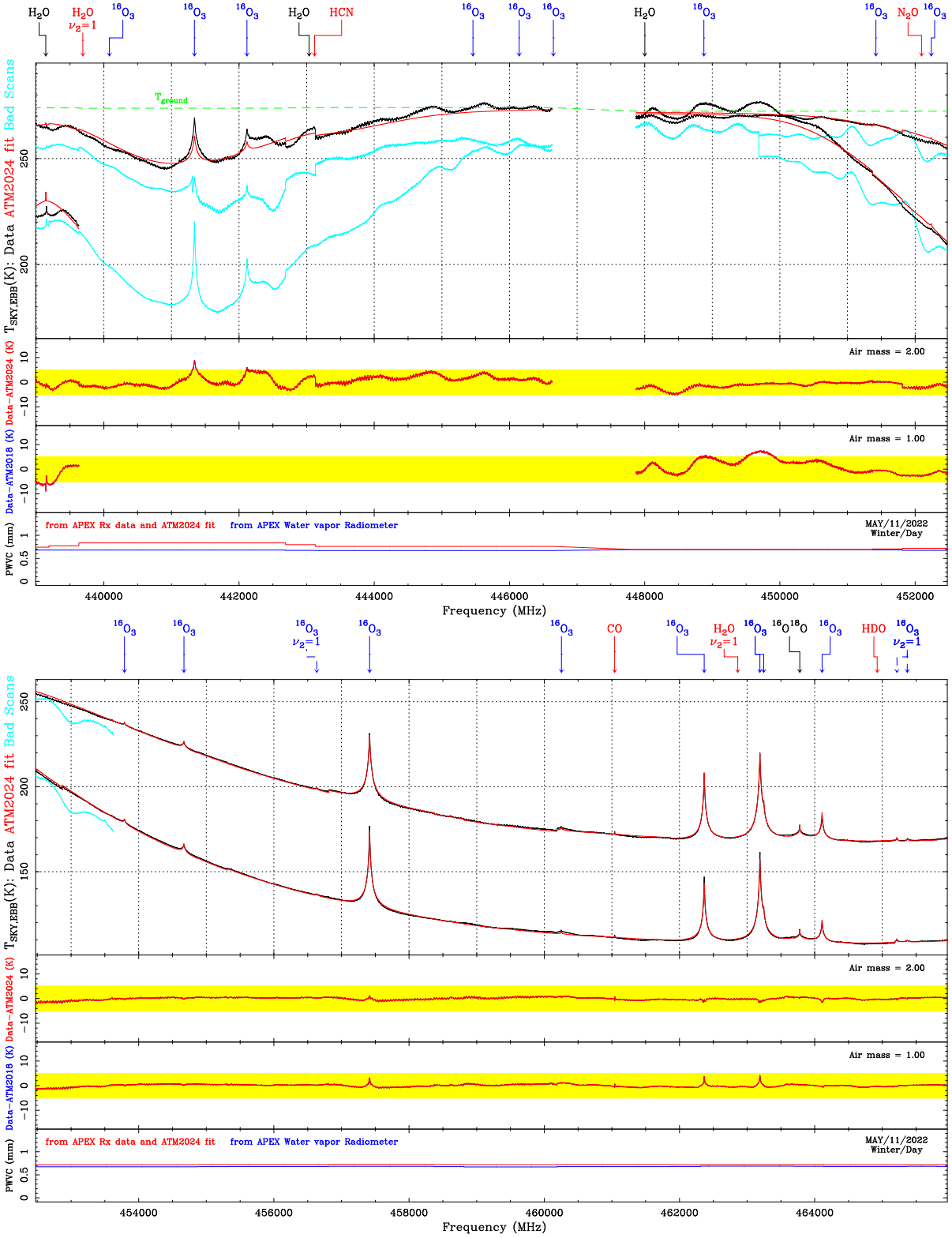

Figure 71: Zoom on May 11^{th} 2022 nFLASH460 2 air mass sky dip data and ATM2024 fit results (part 3).

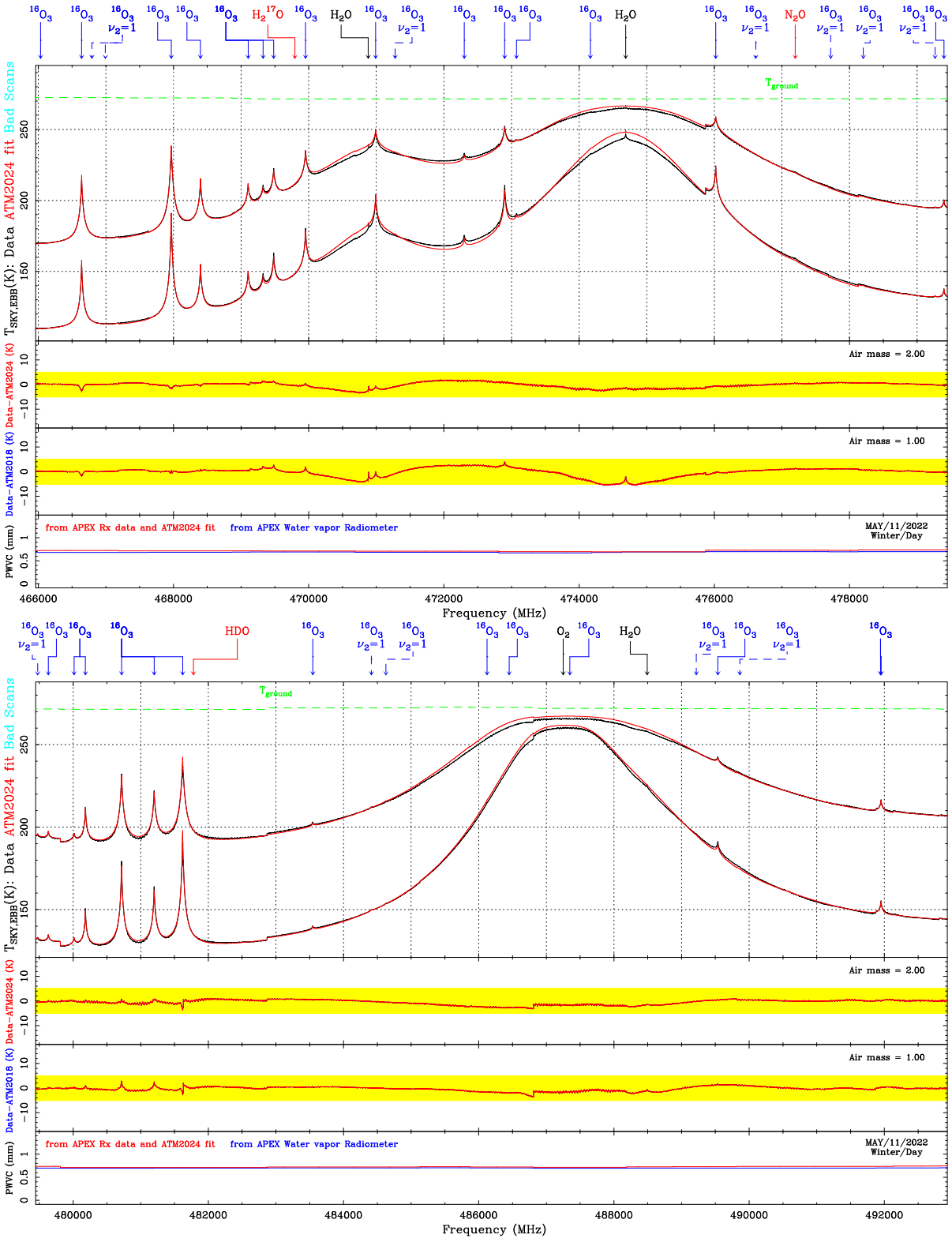

Figure 72: Zoom on May 11^{th} 2022 nFLASH460 2 air mass sky dip data and ATM2024 fit results (part 4).

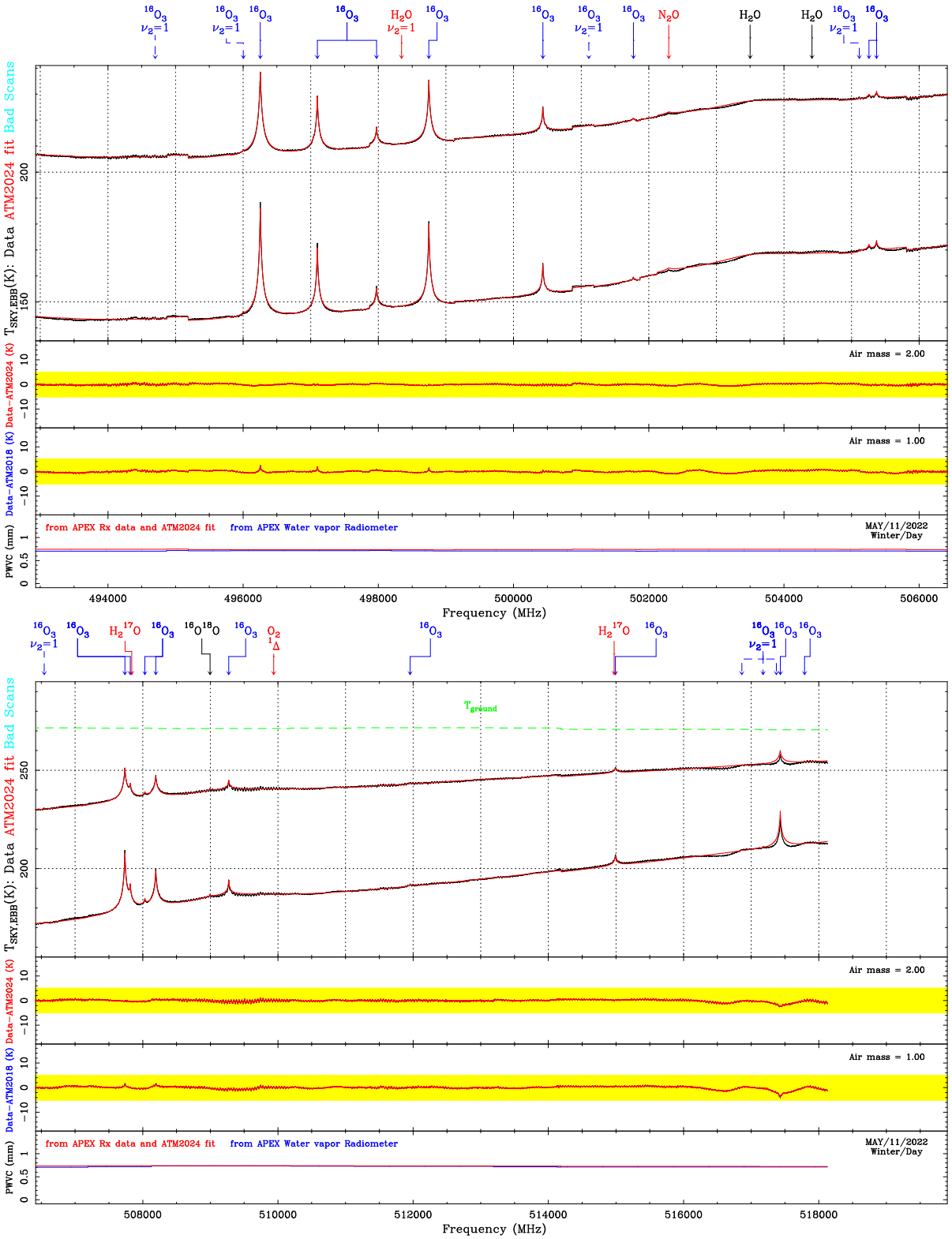

Figure 73: Zoom on May 11th 2022 nFLASH460 2 air mass sky dip data and ATM2024 fit results (part 5).

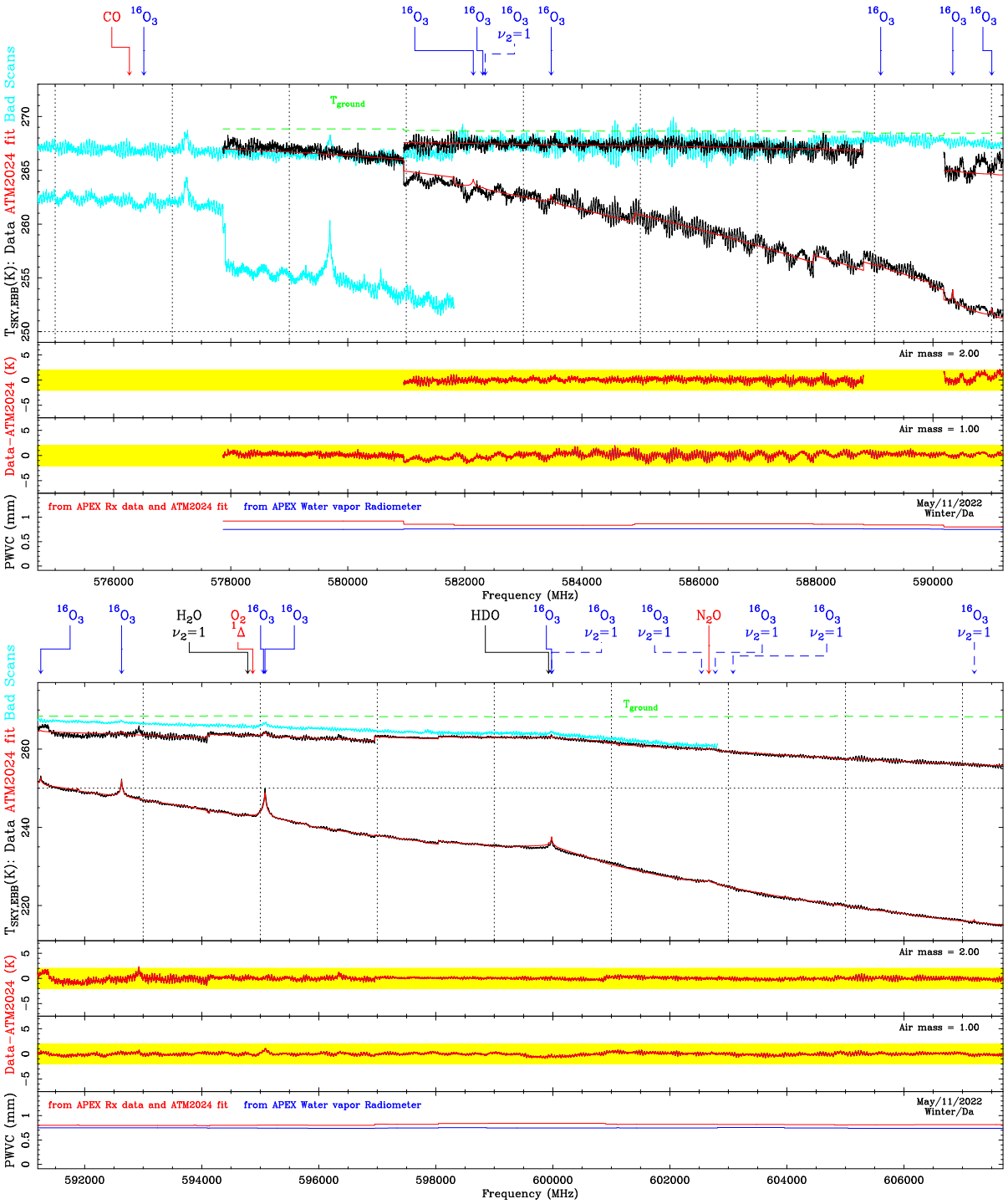

Figure 74: Zoom on May 11^{th} 2022 SEPIA660 2 air mass sky dip data and ATM2024 fit results (part 1).

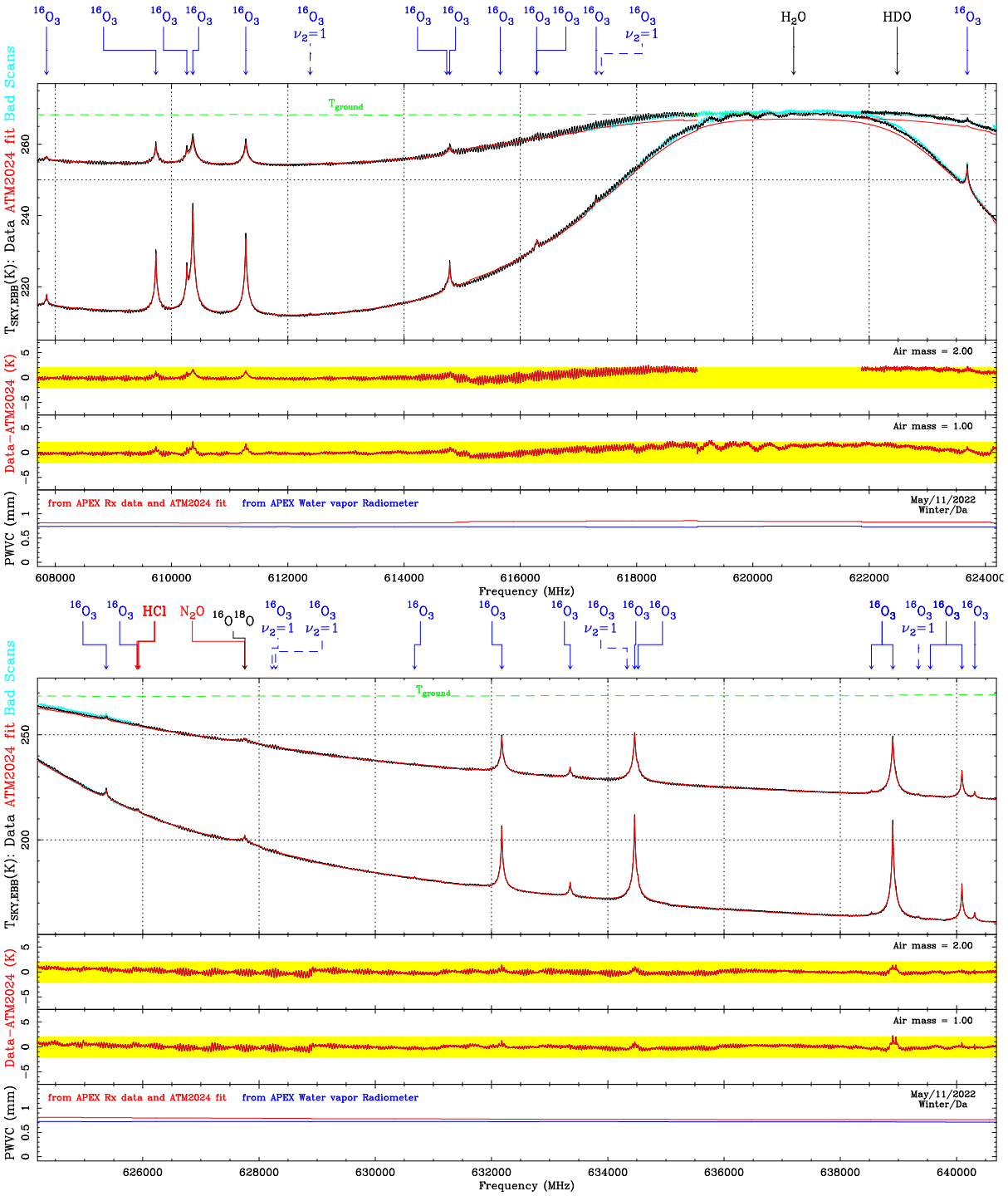

Figure 75: Zoom on May 11^{th} 2022 SEPIA660 2 air mass sky dip data and ATM2024 fit results (part 2).

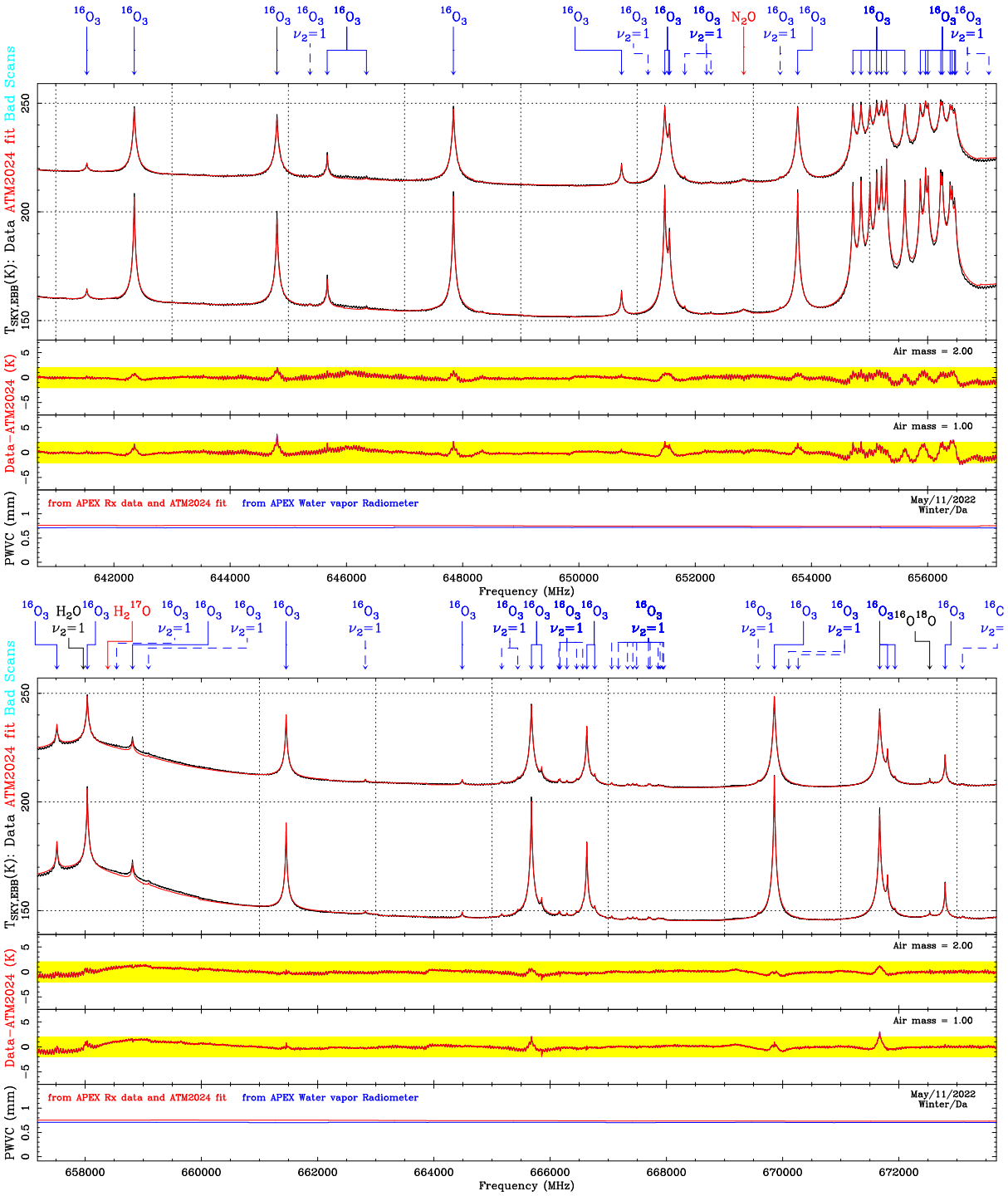

Figure 76: Zoom on May 11^{th} 2022 SEPIA660 2 air mass sky dip data and ATM2024 fit results (part 3).

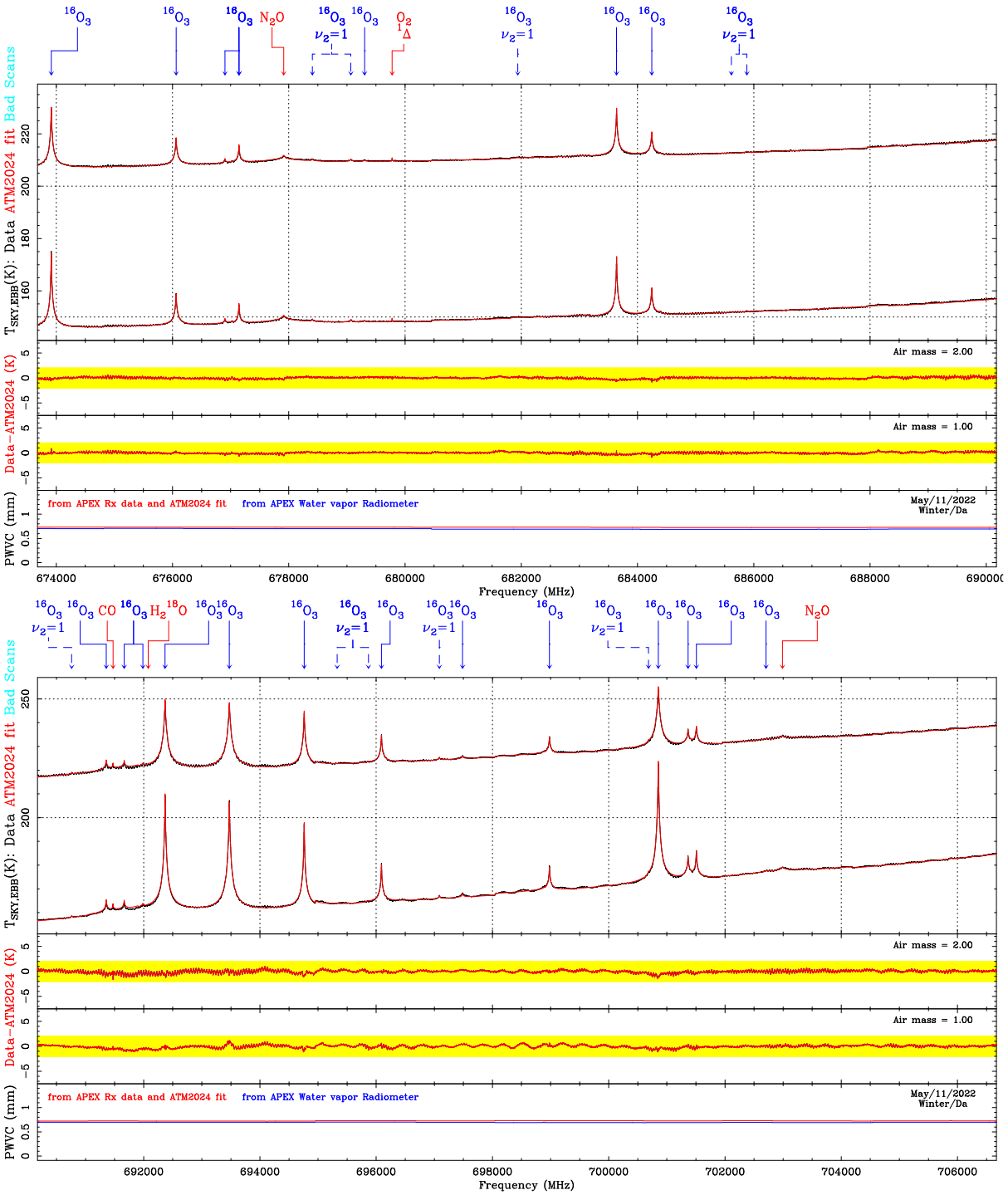

Figure 77: Zoom on May 11^{th} 2022 SEPIA660 2 air mass sky dip data and ATM2024 fit results (part 4).

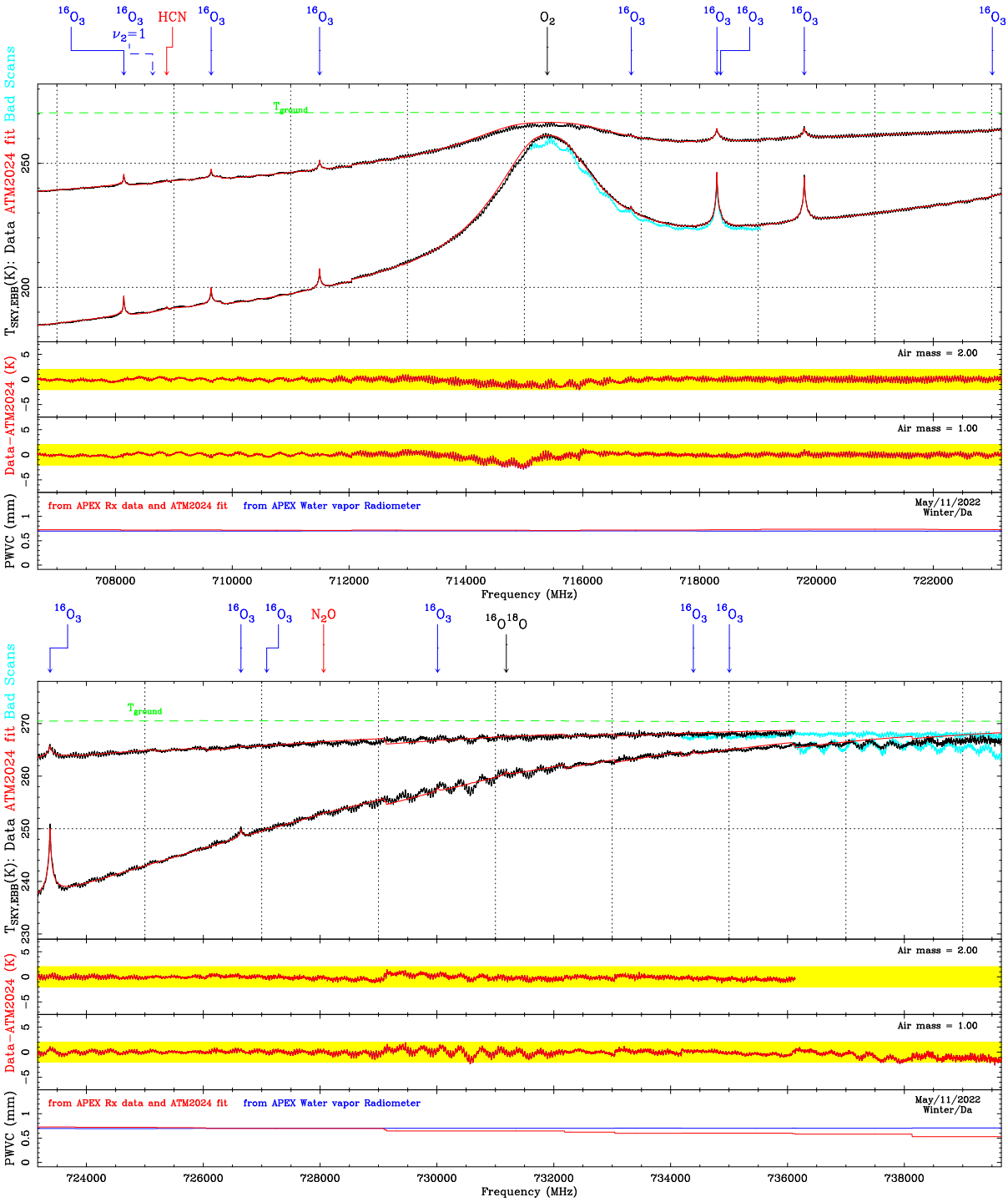

Figure 78: Zoom on May 11^{th} 2022 SEPIA660 2 air mass sky dip data and ATM2024 fit results (part 5).

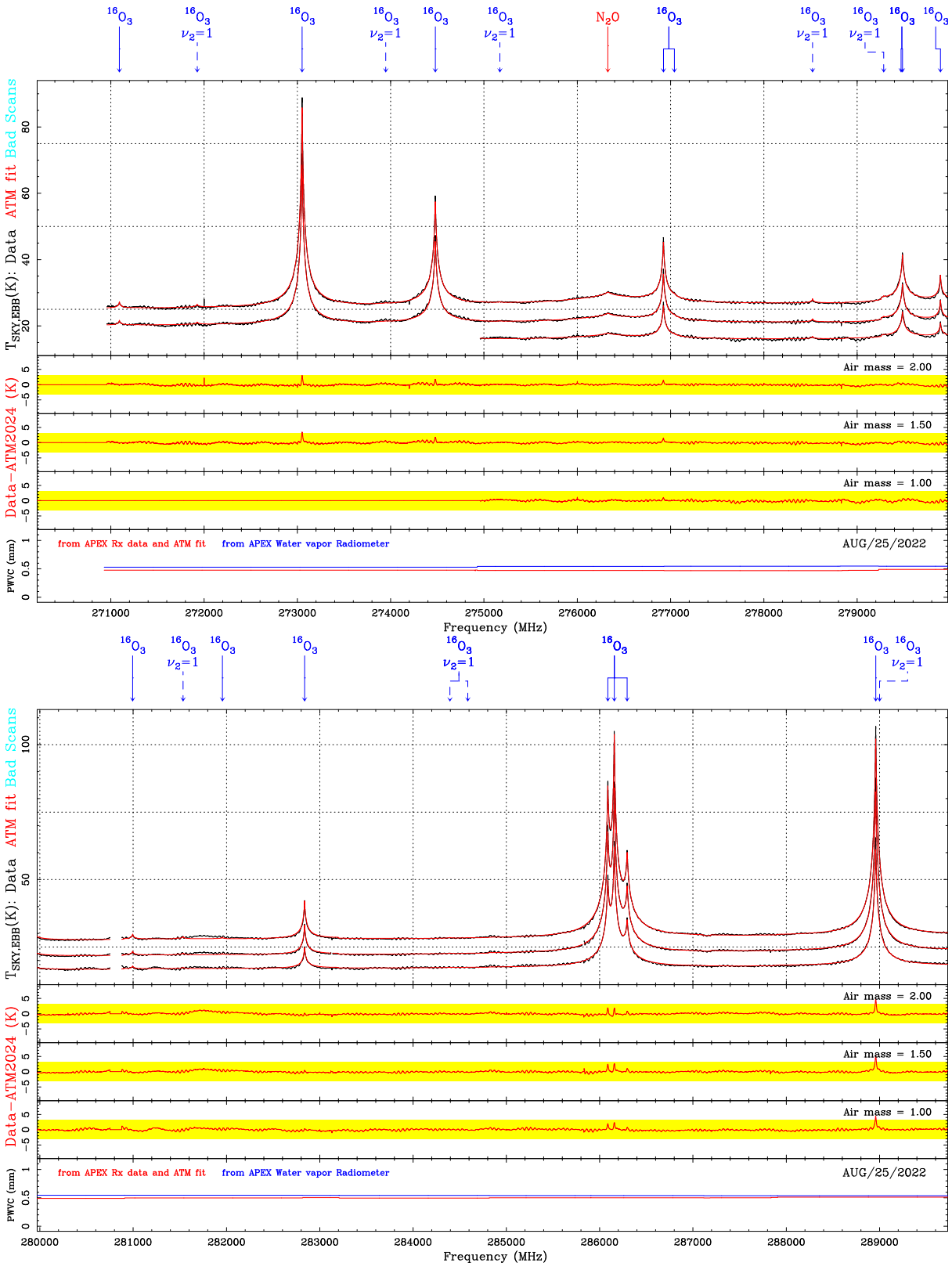

Figure 79: Zoom on Aug. 25^{th} 2022 SEPIA345 3 air mass sky dip data and ATM2024 fit results (part 1).

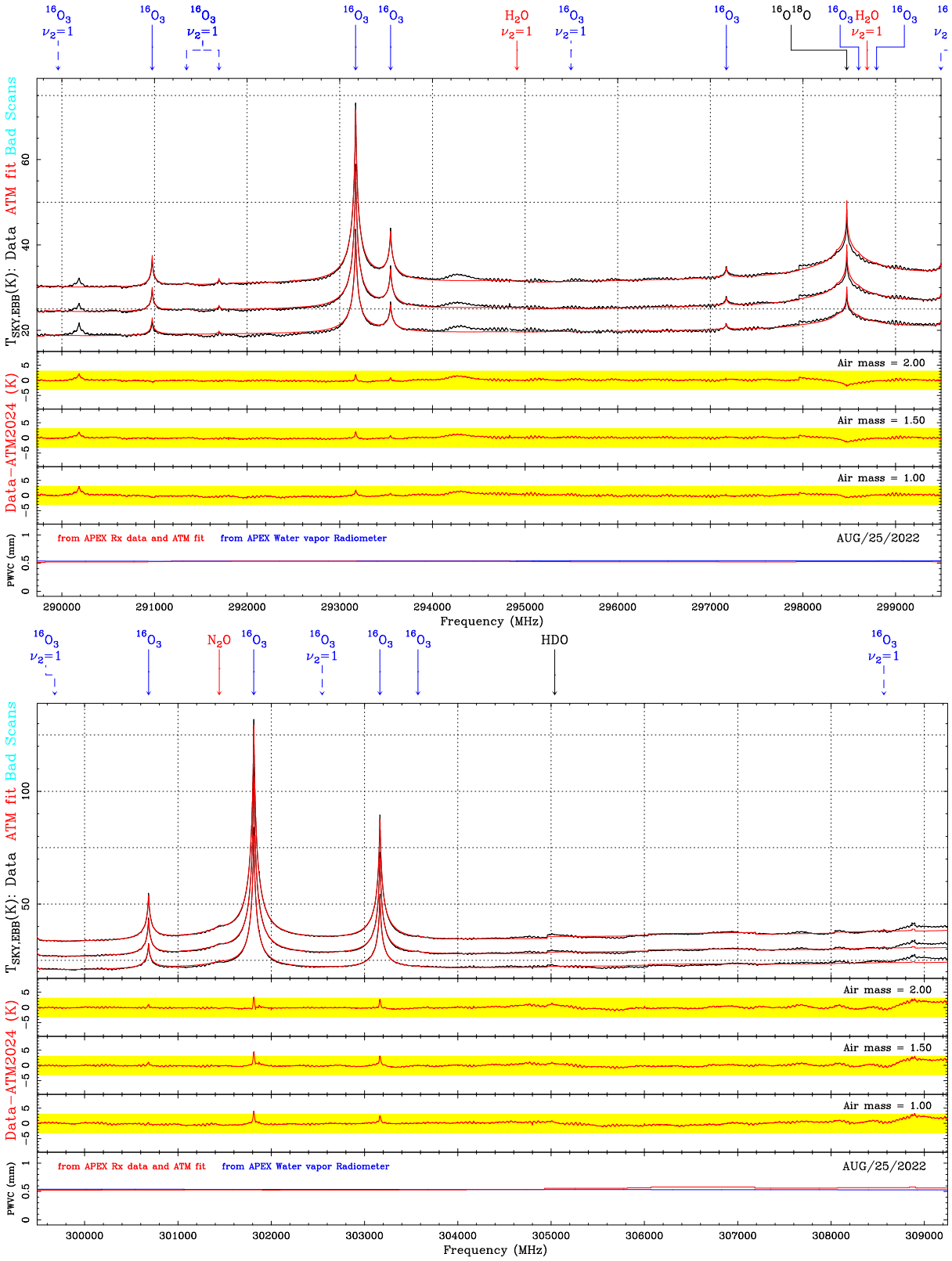

Figure 80: Zoom on Aug. 25^{th} 2022 SEPIA345 3 air mass sky dip data and ATM2024 fit results (part 2).

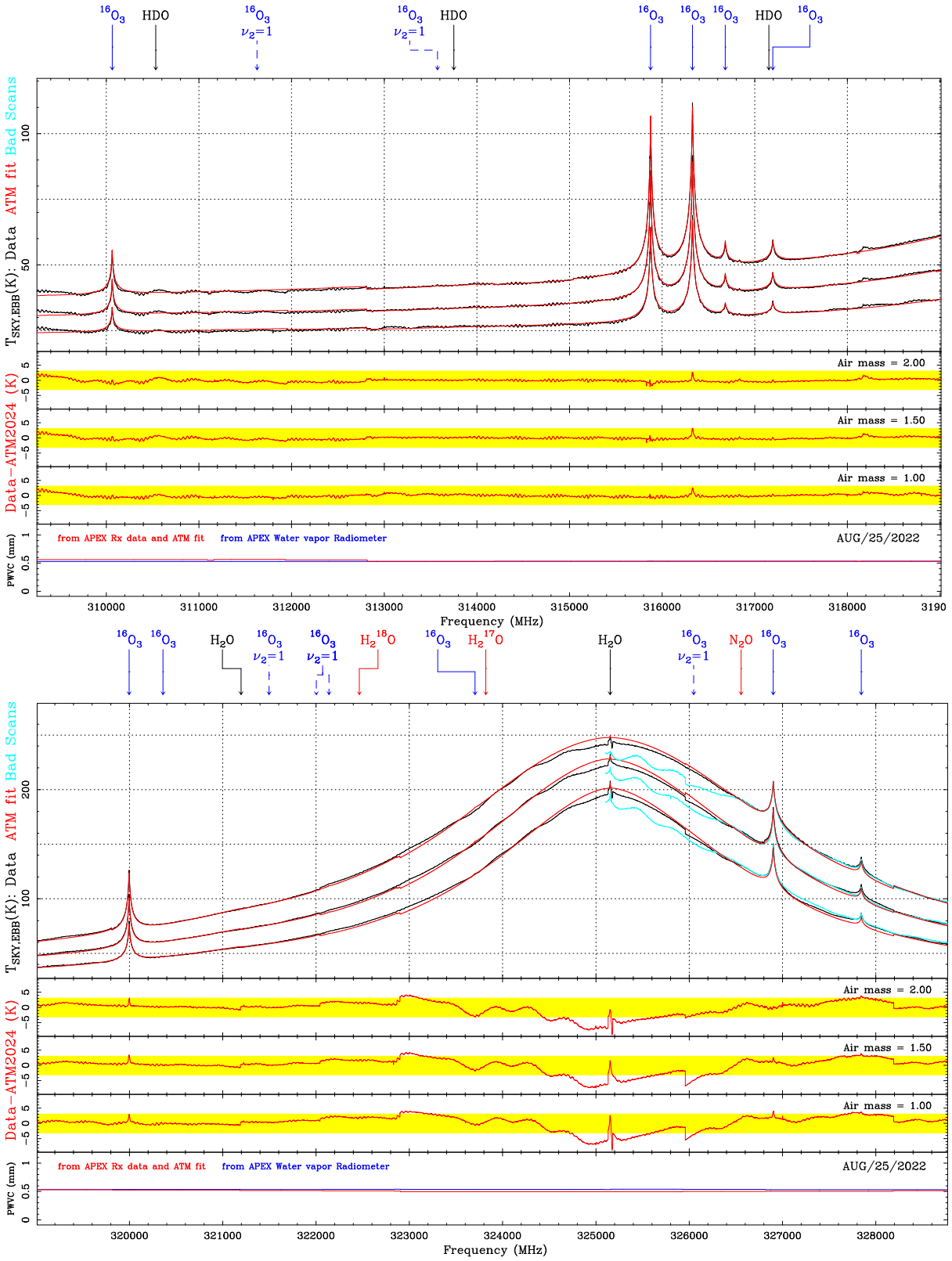

Figure 81: Zoom on Aug. 25^{th} 2022 SEPIA345 3 air mass sky dip data and ATM2024 fit results (part 3).

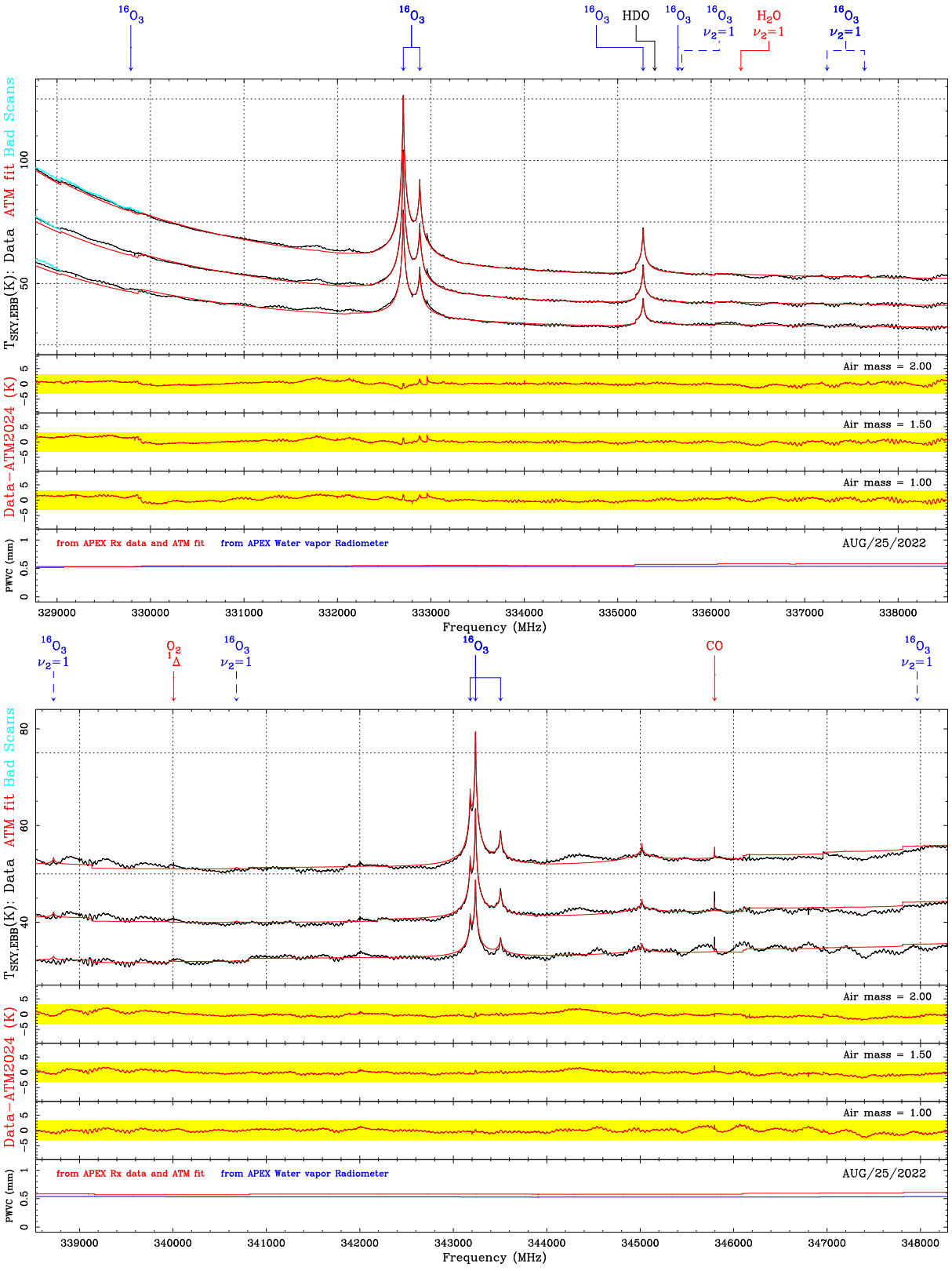

Figure 82: Zoom on Aug. 25^{th} 2022 SEPIA345 3 air mass sky dip data and ATM2024 fit results (part 4).

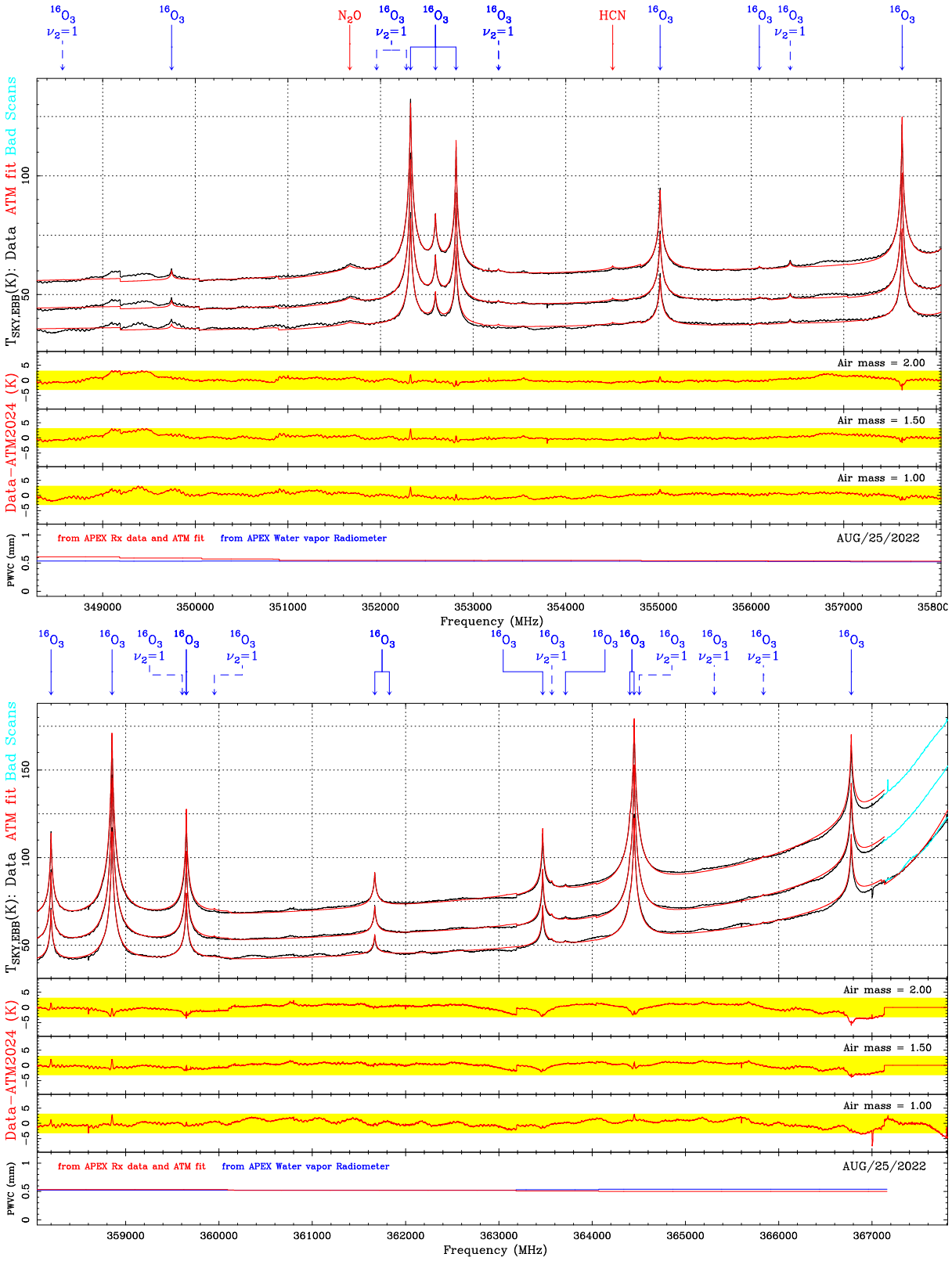

Figure 83: Zoom on Aug. 25^{th} 2022 SEPIA345 3 air mass sky dip data and ATM2024 fit results (part 5).

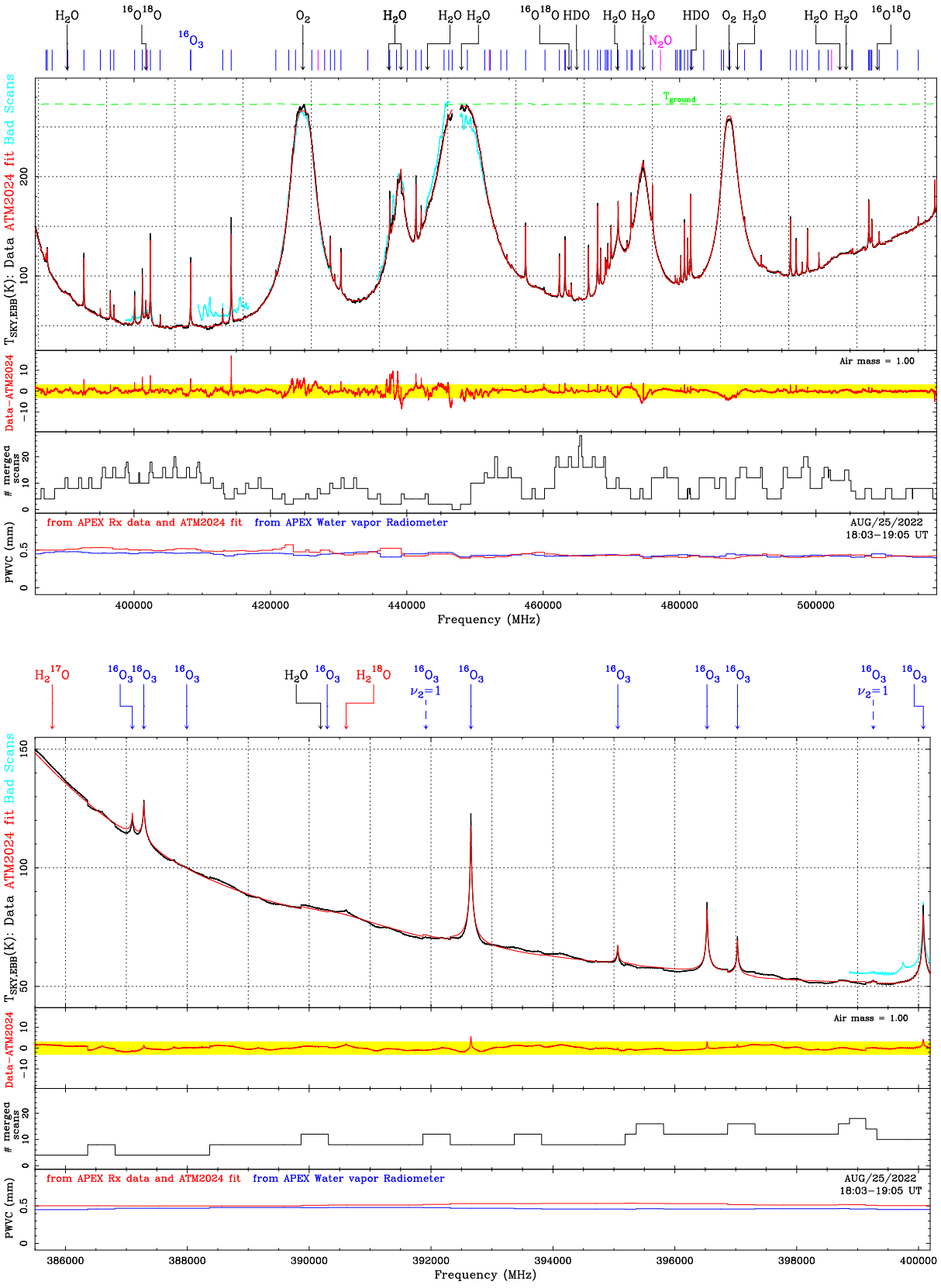

Figure 84: Aug. 25^{th} 2022 18:03-19:05 UT nFLASH460 atmospheric data and ATM2024 fit results (full and zoom, part 1).

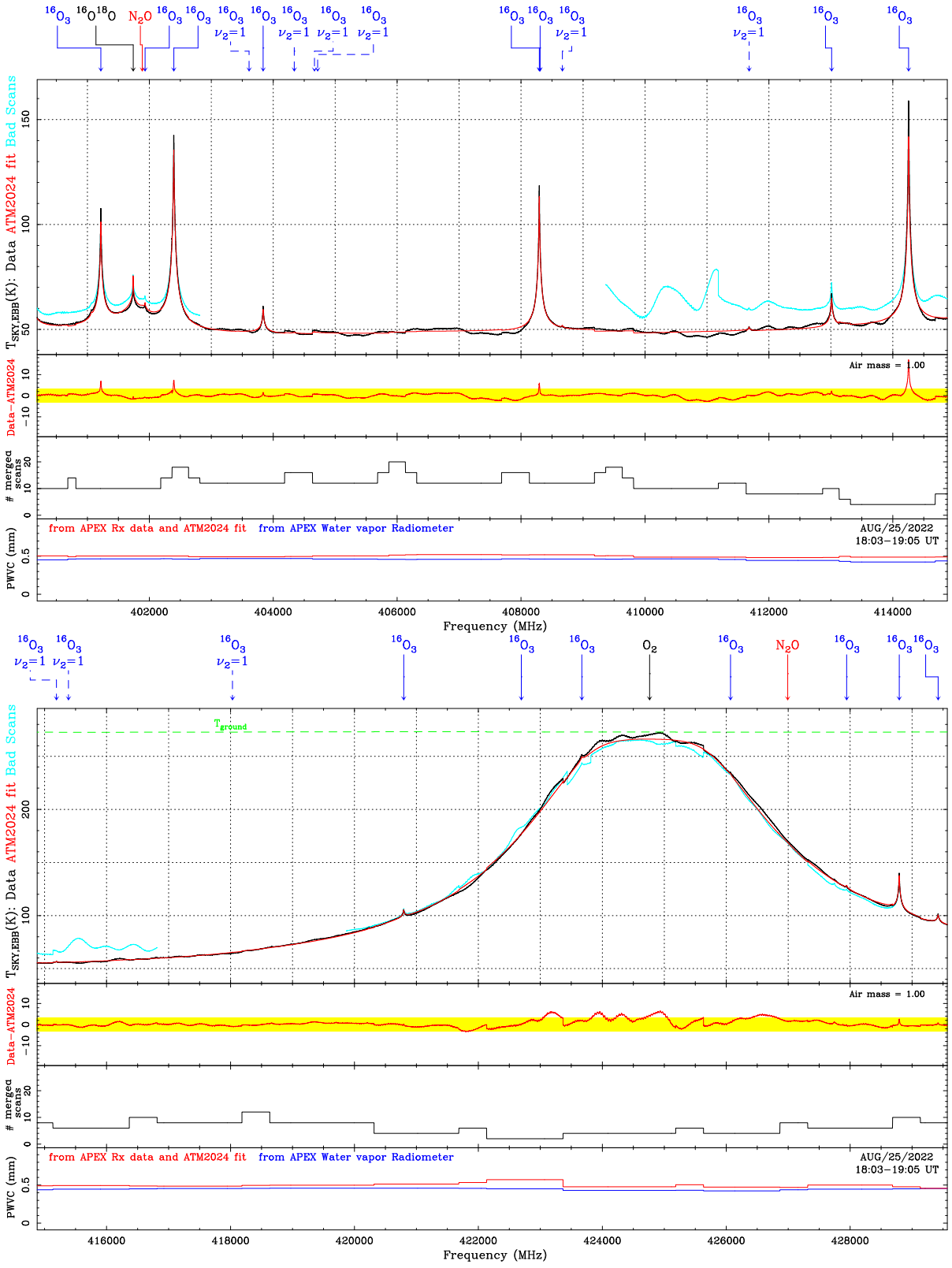

Figure 85: Zoom on Aug. 25^{th} 2022 18:03-19:05 UT nFLASH460 atmospheric data and ATM2024 fit results (parts 2 nad 3).

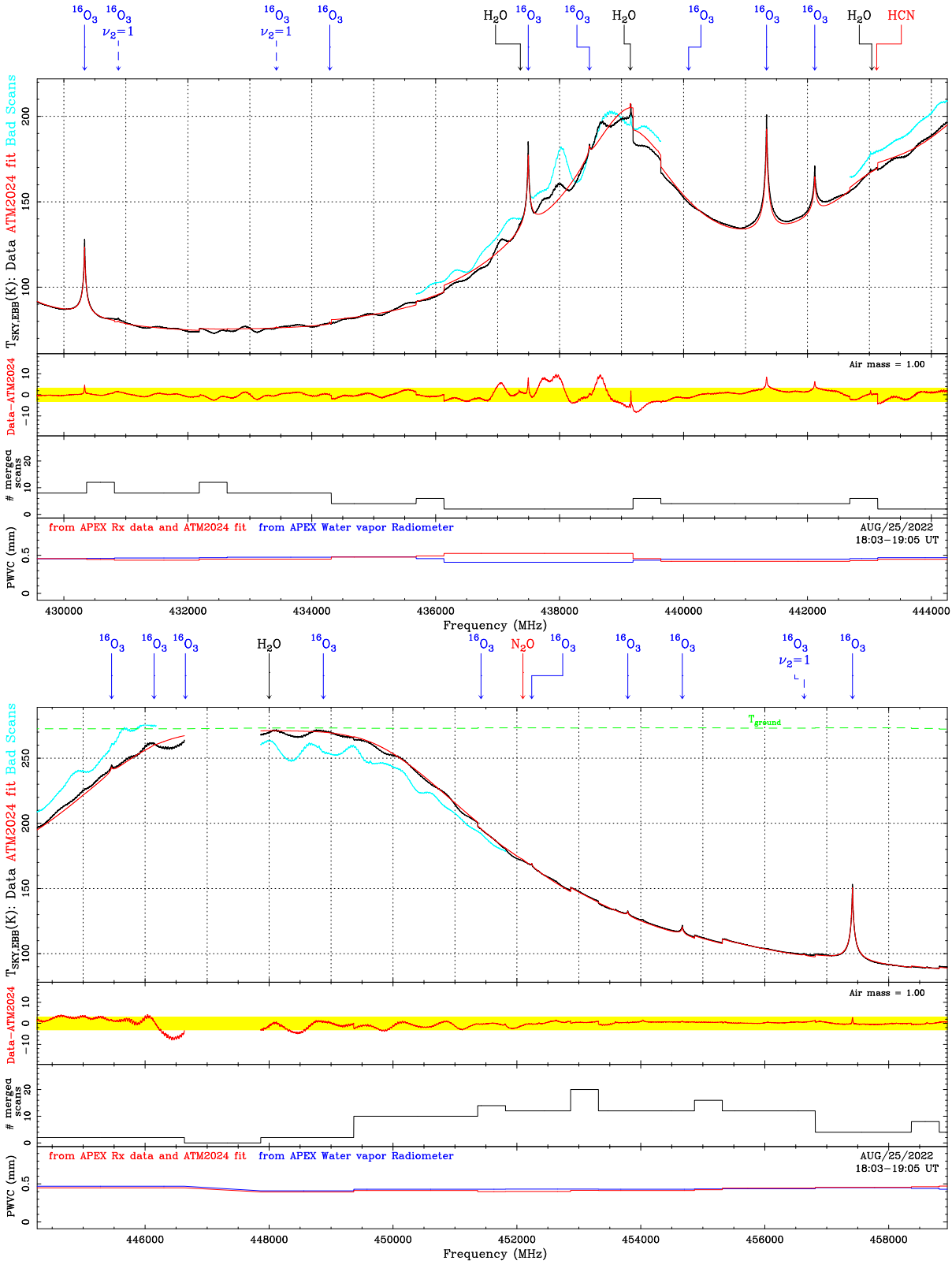

Figure 86: Zoom on Aug. 25^{th} 2022 18:03-19:05 UT nFLASH460 atmospheric data and ATM2024 fit results (parts 4 and 5).

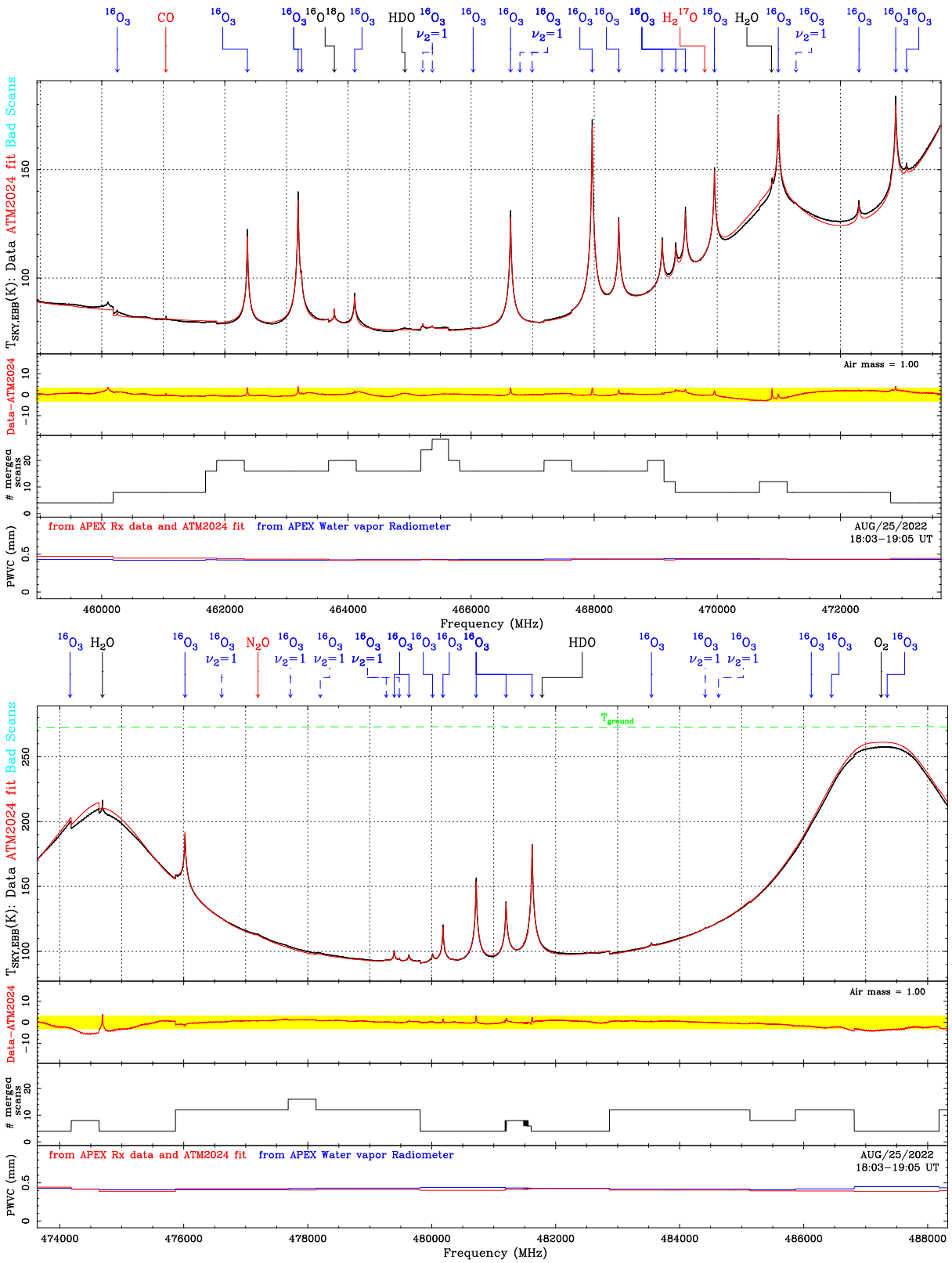

Figure 87: Zoom on Aug. 25^{th} 2022 18:03-19:05 UT nFLASH460 atmospheric data and ATM2024 fit results (parts 6 and 7).

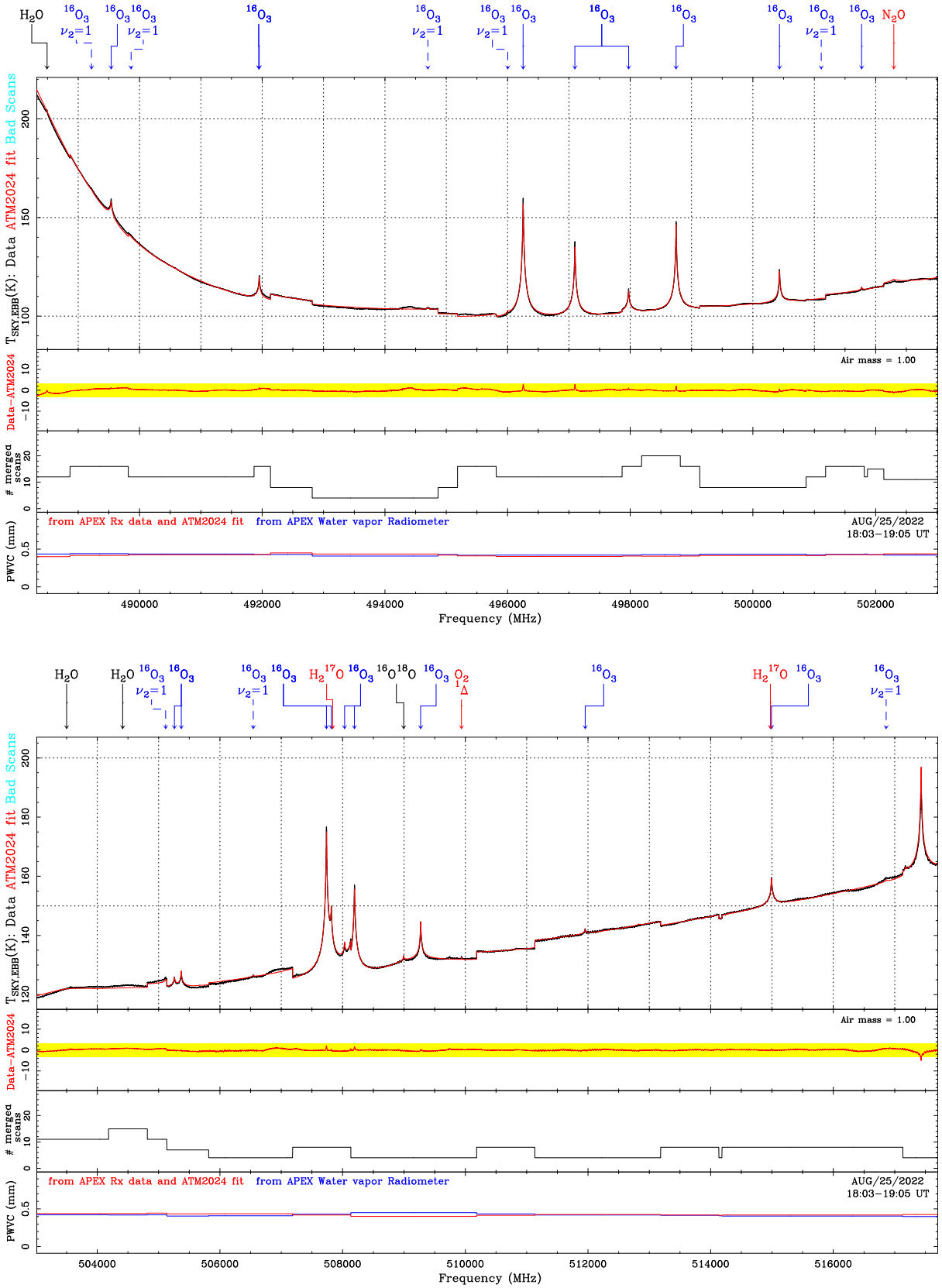

Figure 88: Zoom on Aug. 25^{th} 2022 18:03-19:05 UT nFLASH460 atmospheric data and ATM2024 fit results (parts 8 and 9).

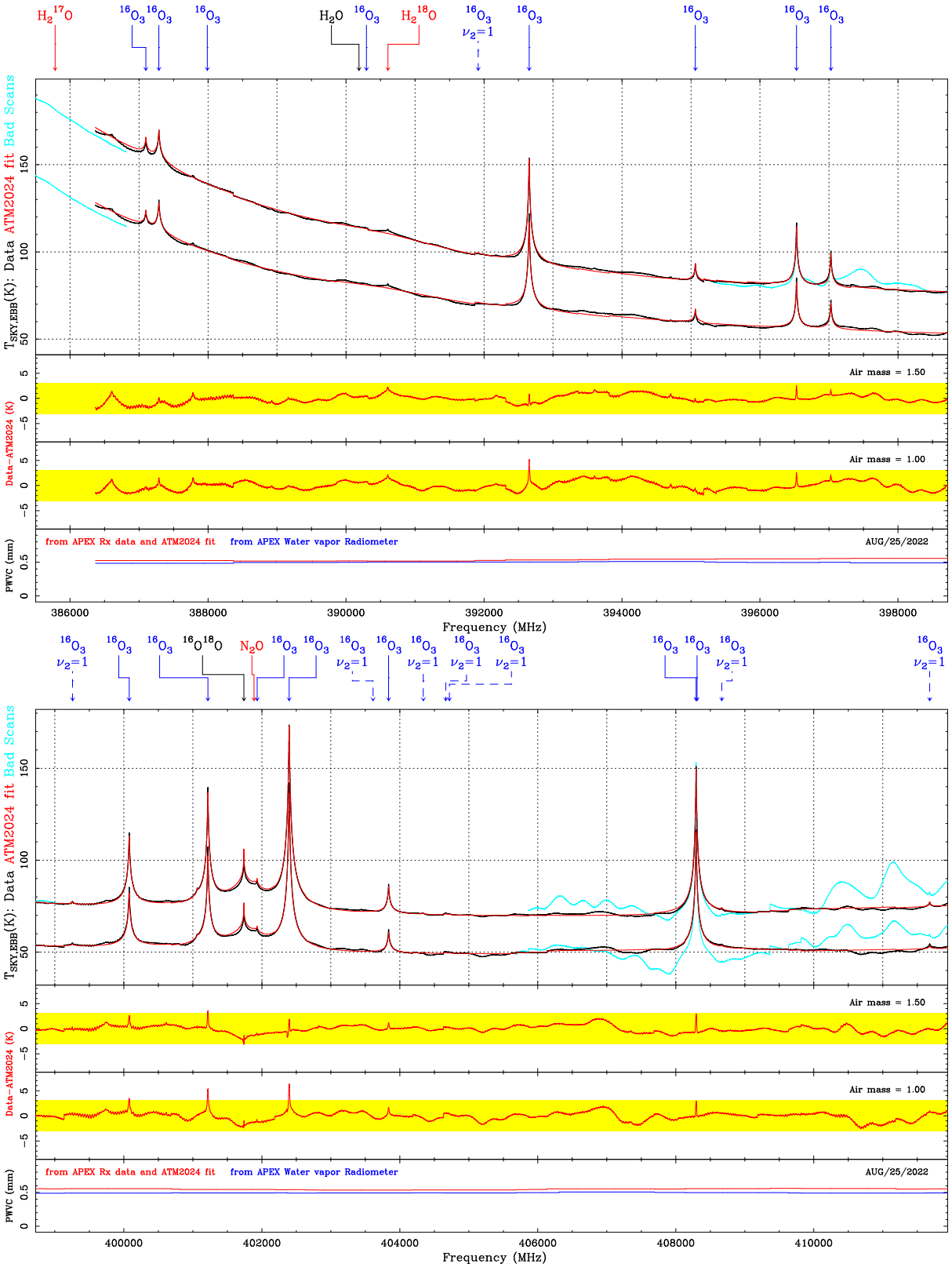

Figure 89: Zoom on Aug. 25^{th} 2022 nFLASH460 atmospheric data and ATM2024 fit results (part 1).

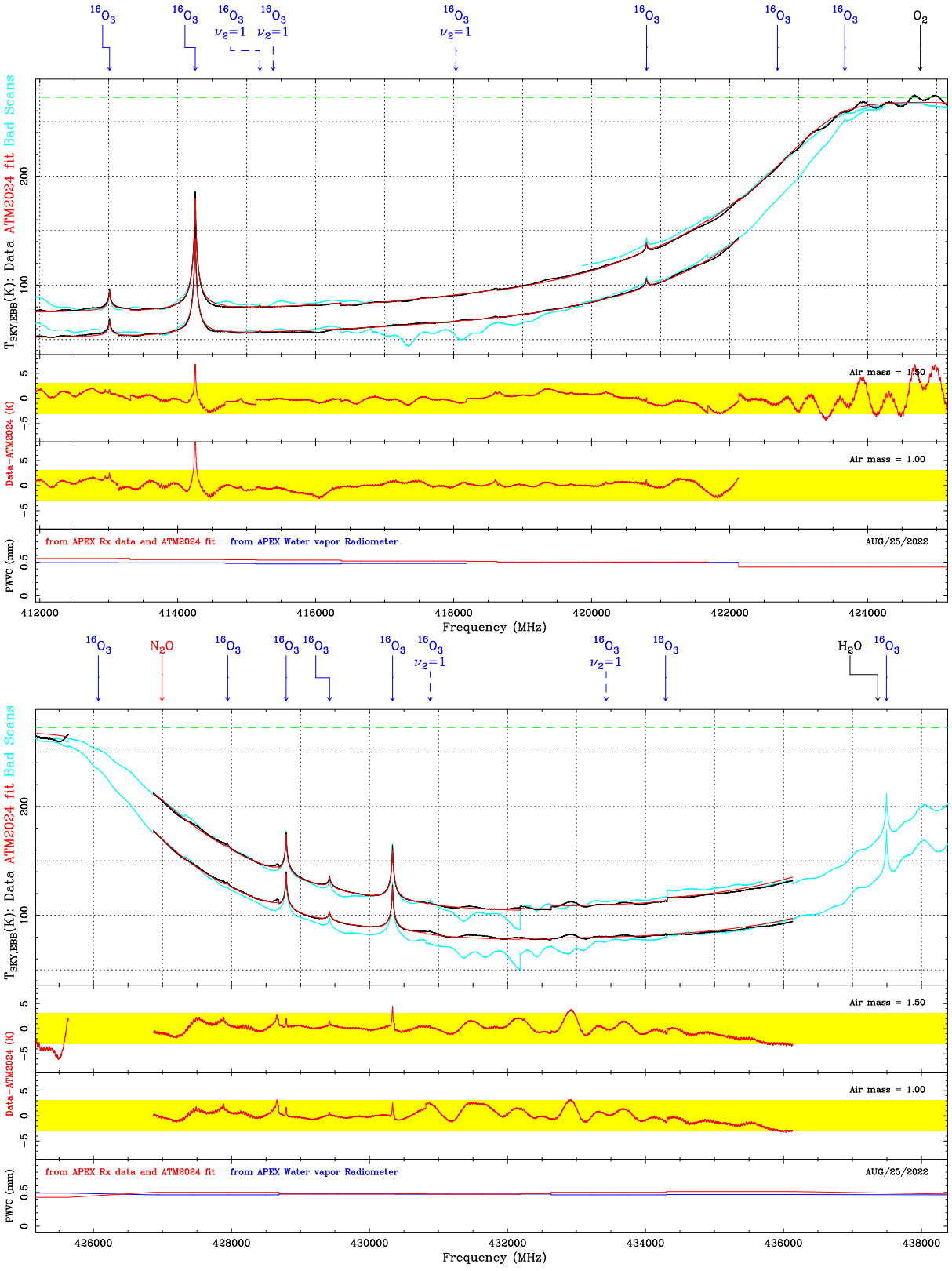

Figure 90: Zoom on Aug. 25^{th} 2022 nFLASH460 atmospheric data and ATM2024 fit results (part 2).

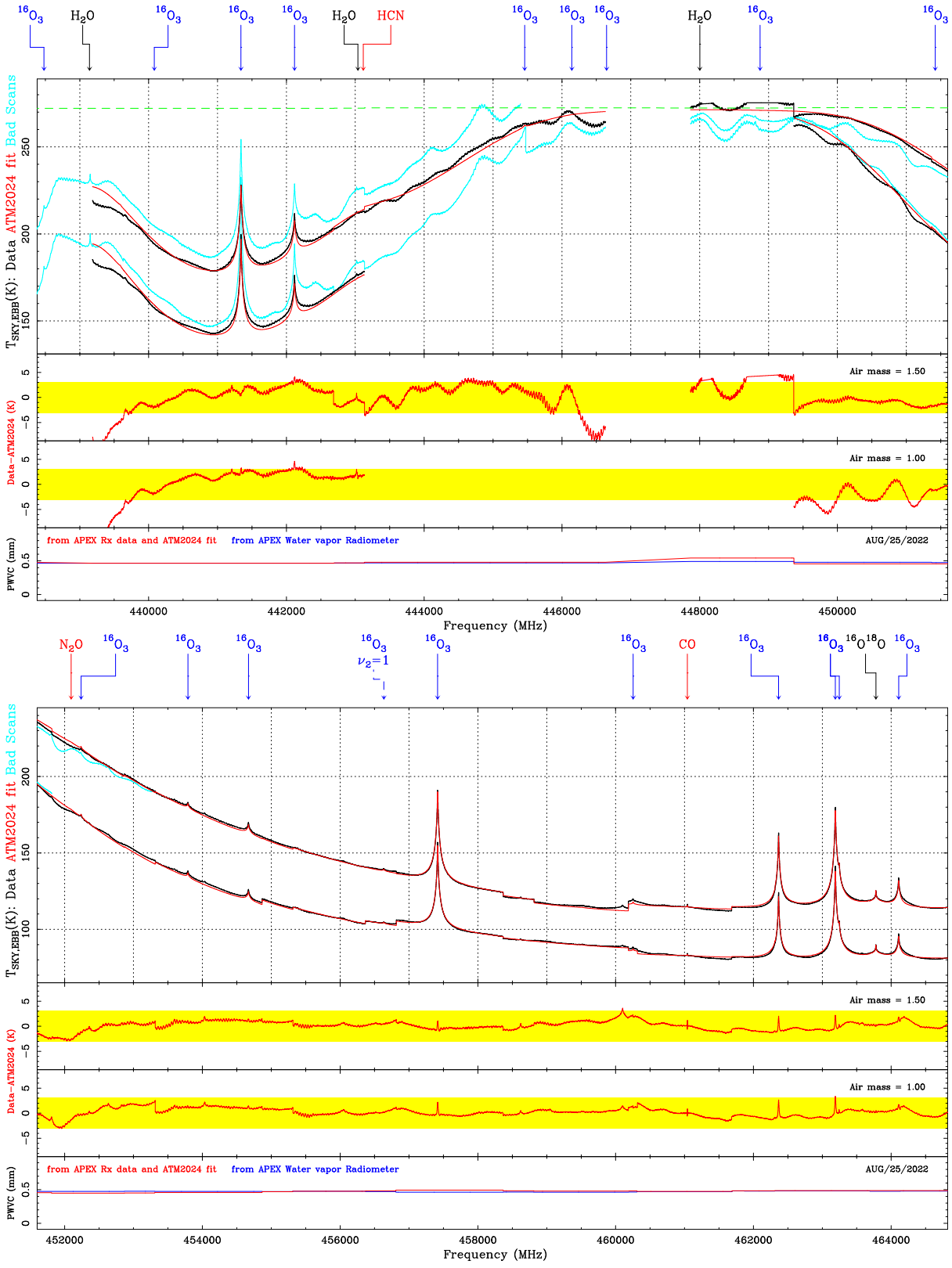

Figure 91: Zoom on Aug. 25^{th} 2022 nFLASH460 atmospheric data and ATM2024 fit results (part 3).

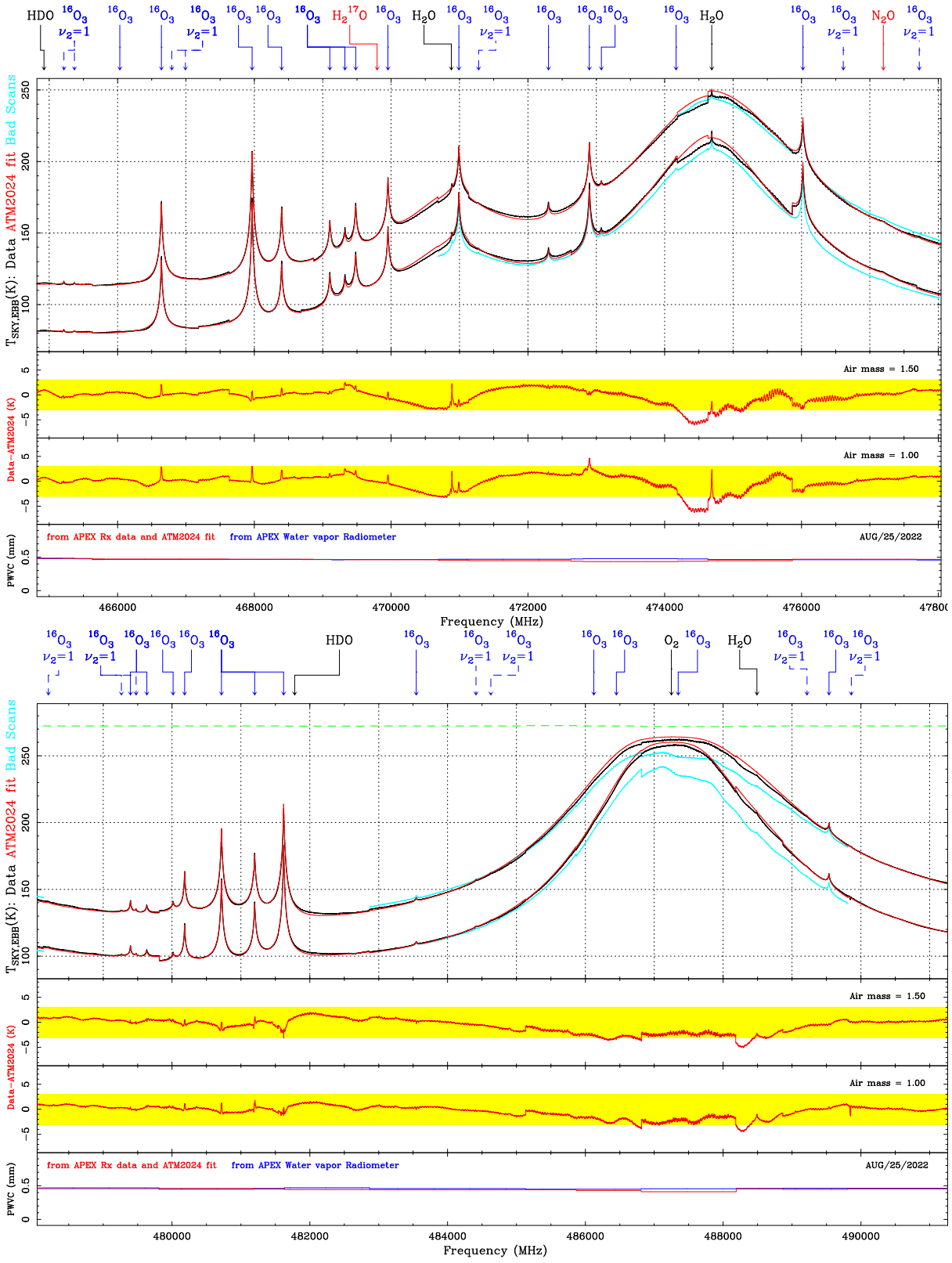

Figure 92: Zoom on Aug. 25^{th} 2022 nFLASH460 atmospheric data and ATM2024 fit results (part 4).

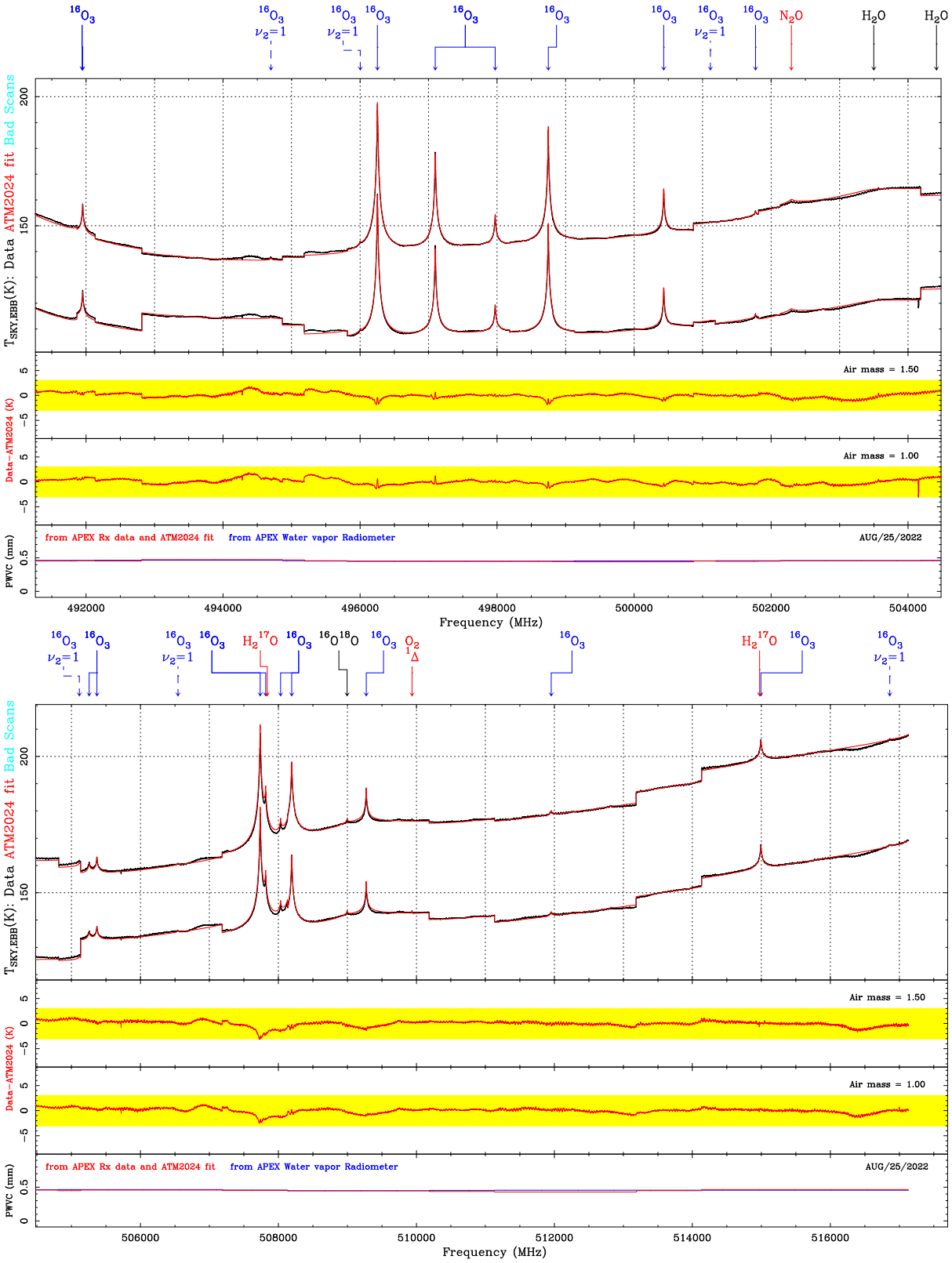

Figure 93: Zoom on Aug. 25^{th} 2022 nFLASH460 atmospheric data and ATM2024 fit results (part 5).

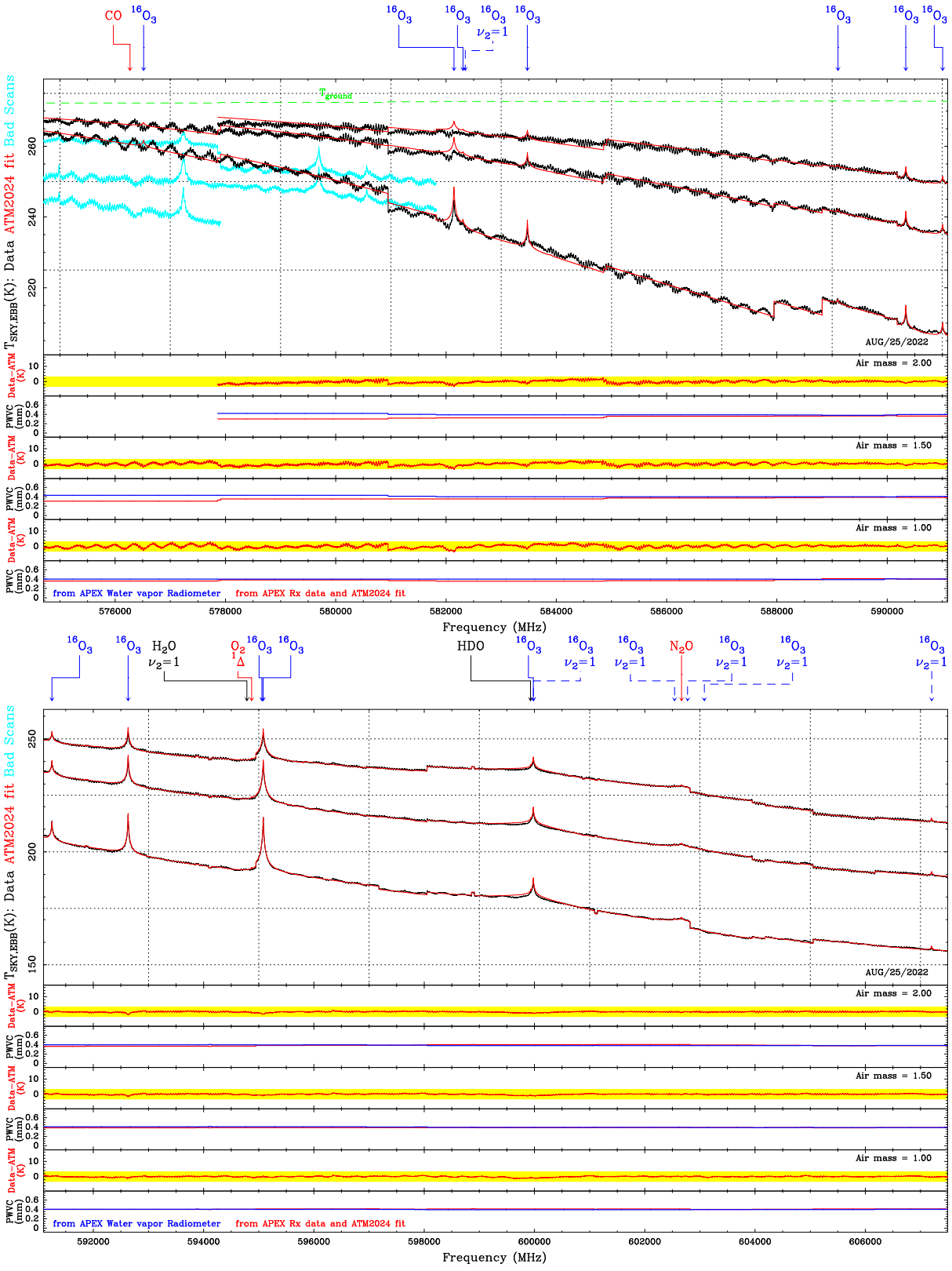

Figure 94: Zoom on Aug. 25^{nd} 2022 SEPIA660 3 air mass sky dip data and ATM2024 fit results (part 1).

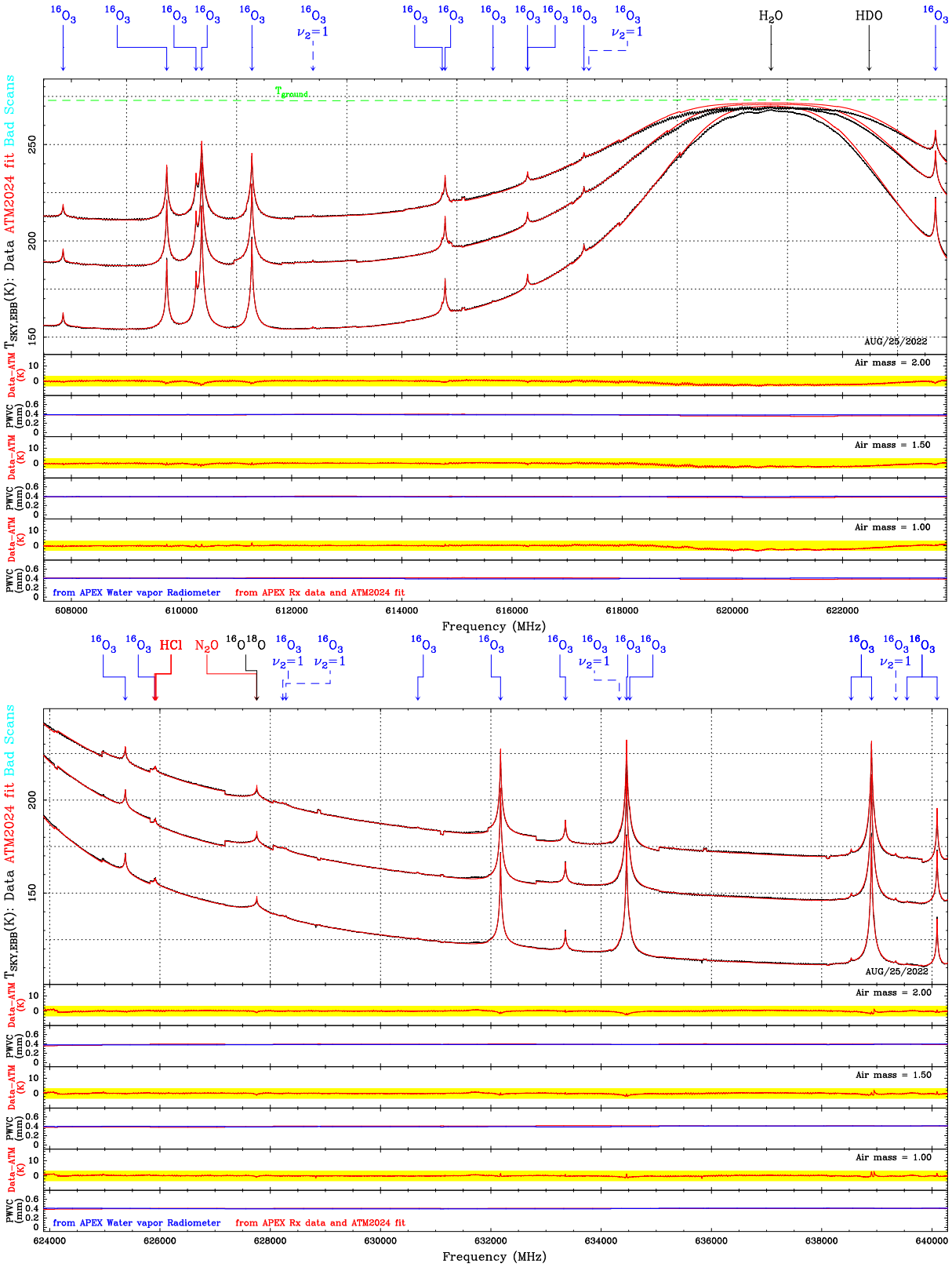

Figure 95: Zoom on Aug. 25^{nd} 2022 SEPIA660 3 air mass sky dip data and ATM2024 fit results (part 2).

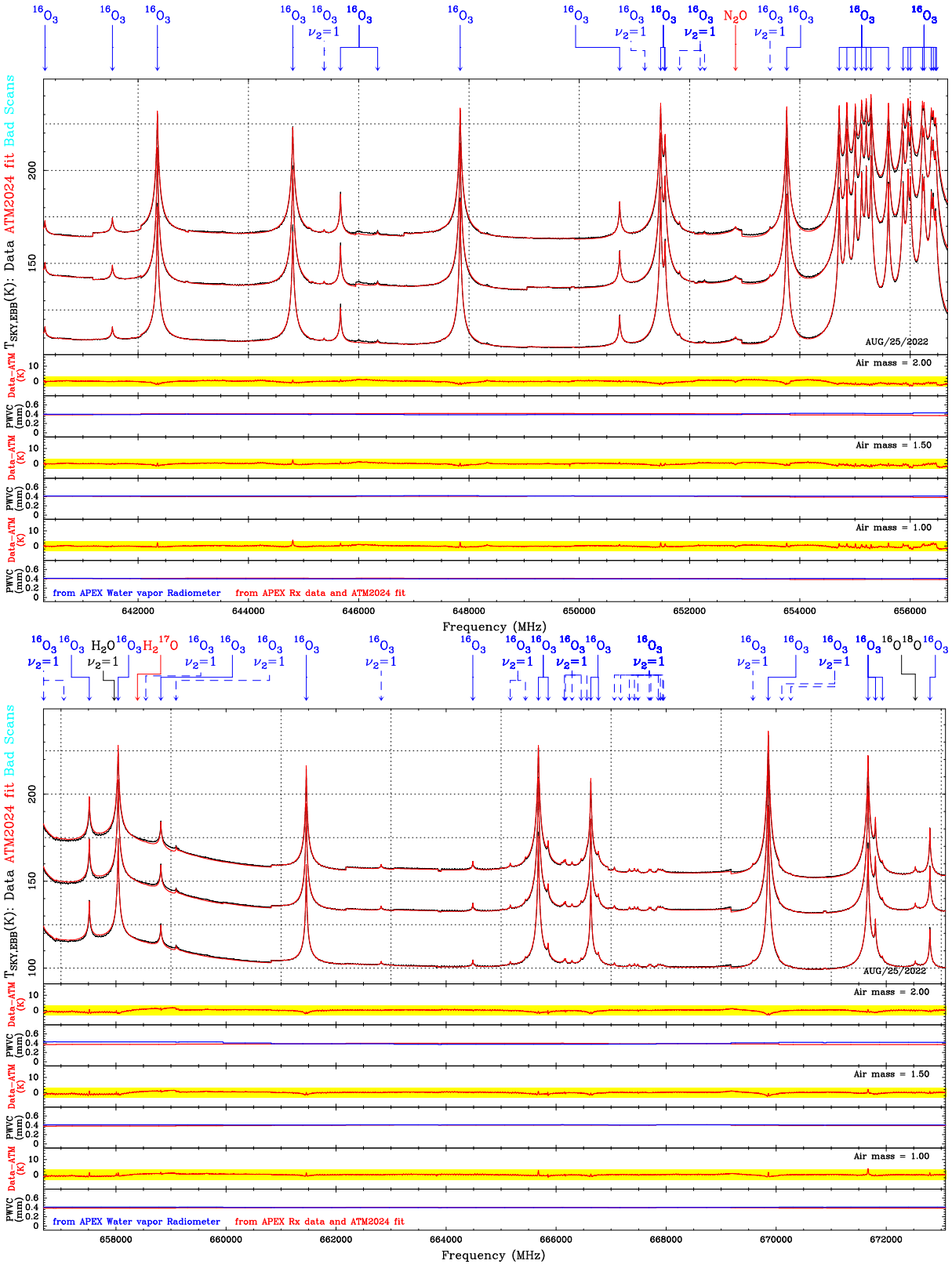

Figure 96: Zoom on Aug. 25^{nd} 2022 SEPIA660 3 air mass sky dip data and ATM2024 fit results (part 3).

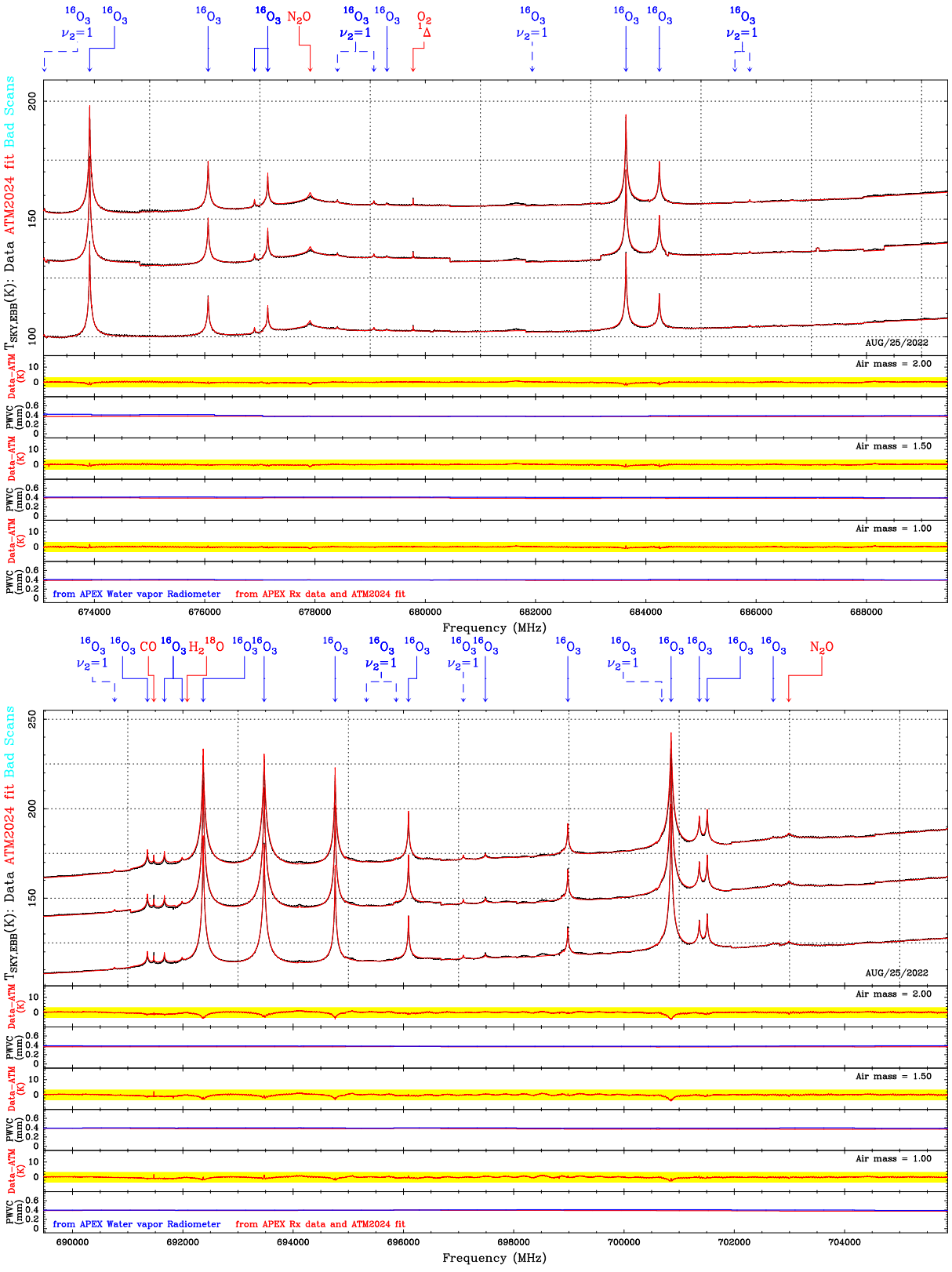

Figure 97: Zoom on Aug. 25^{nd} 2022 SEPIA660 3 air mass sky dip data and ATM2024 fit results (part 4).

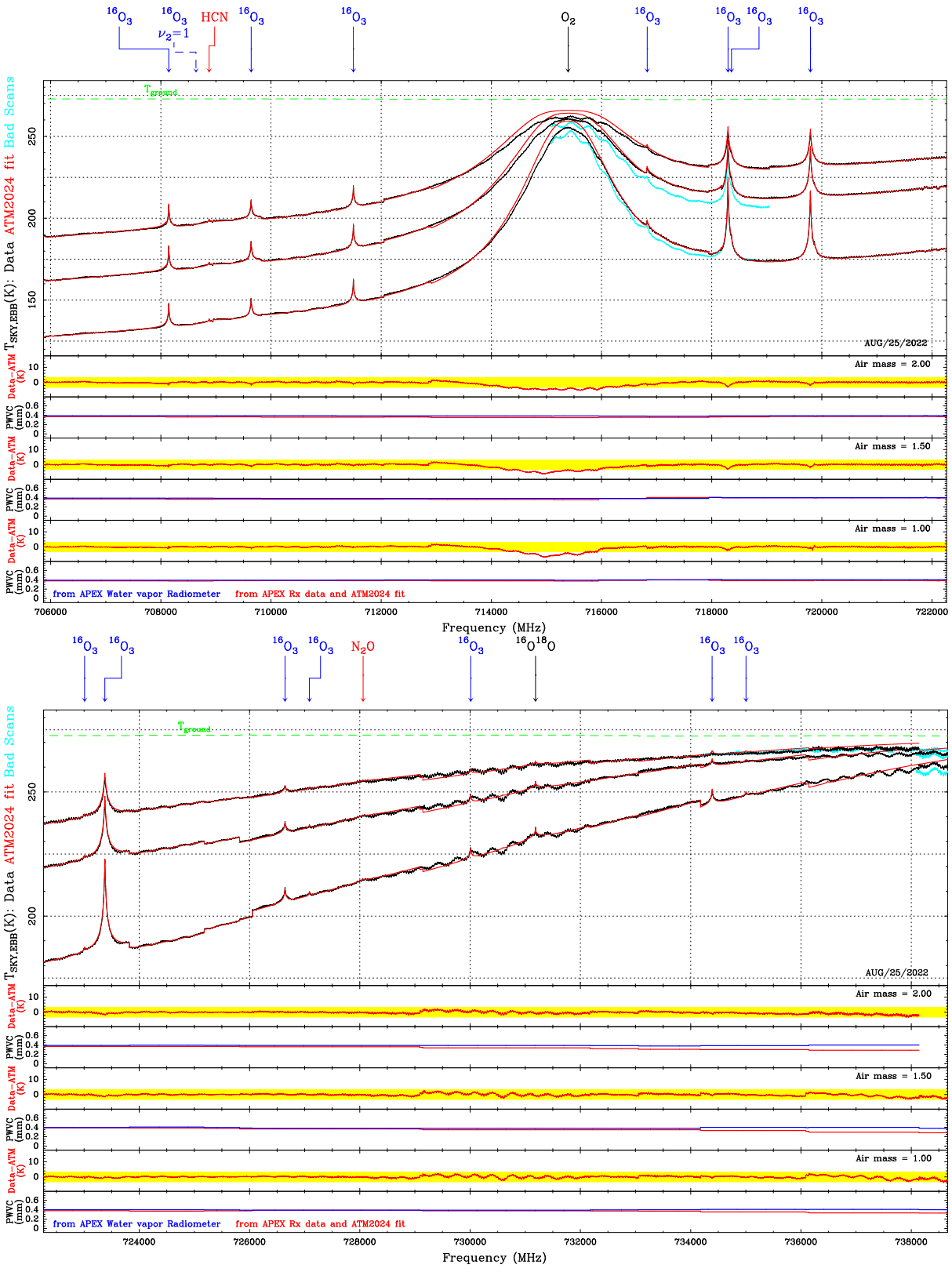

Figure 98: Zoom on Aug. 25^{nd} 2022 SEPIA660 3 air mass sky dip data and ATM2024 fit results (part 5).

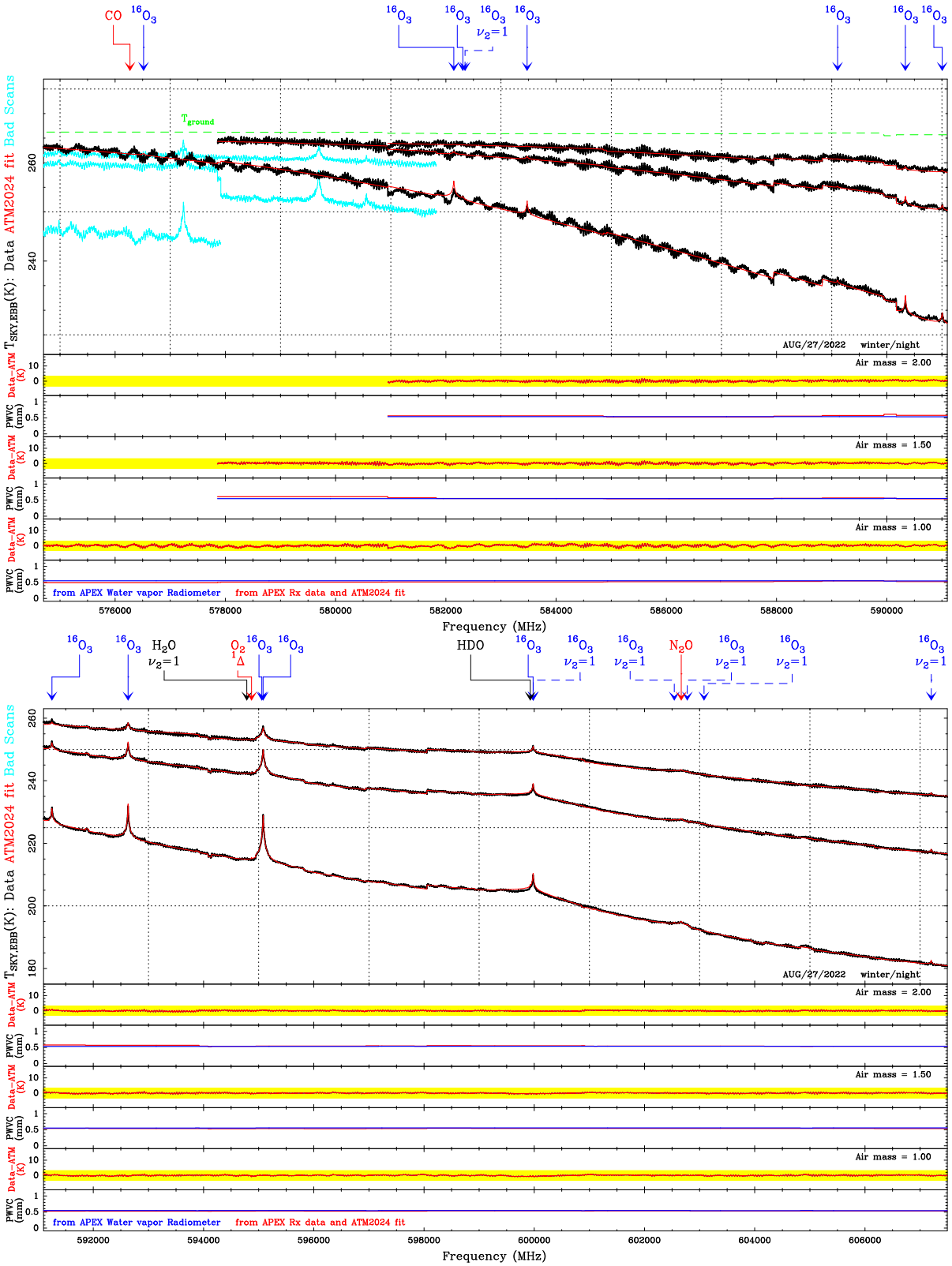

Figure 99: Zoom on Aug. 27^{nd} 2022 SEPIA660 3 air mass sky dip data and ATM2024 fit results (part 1).

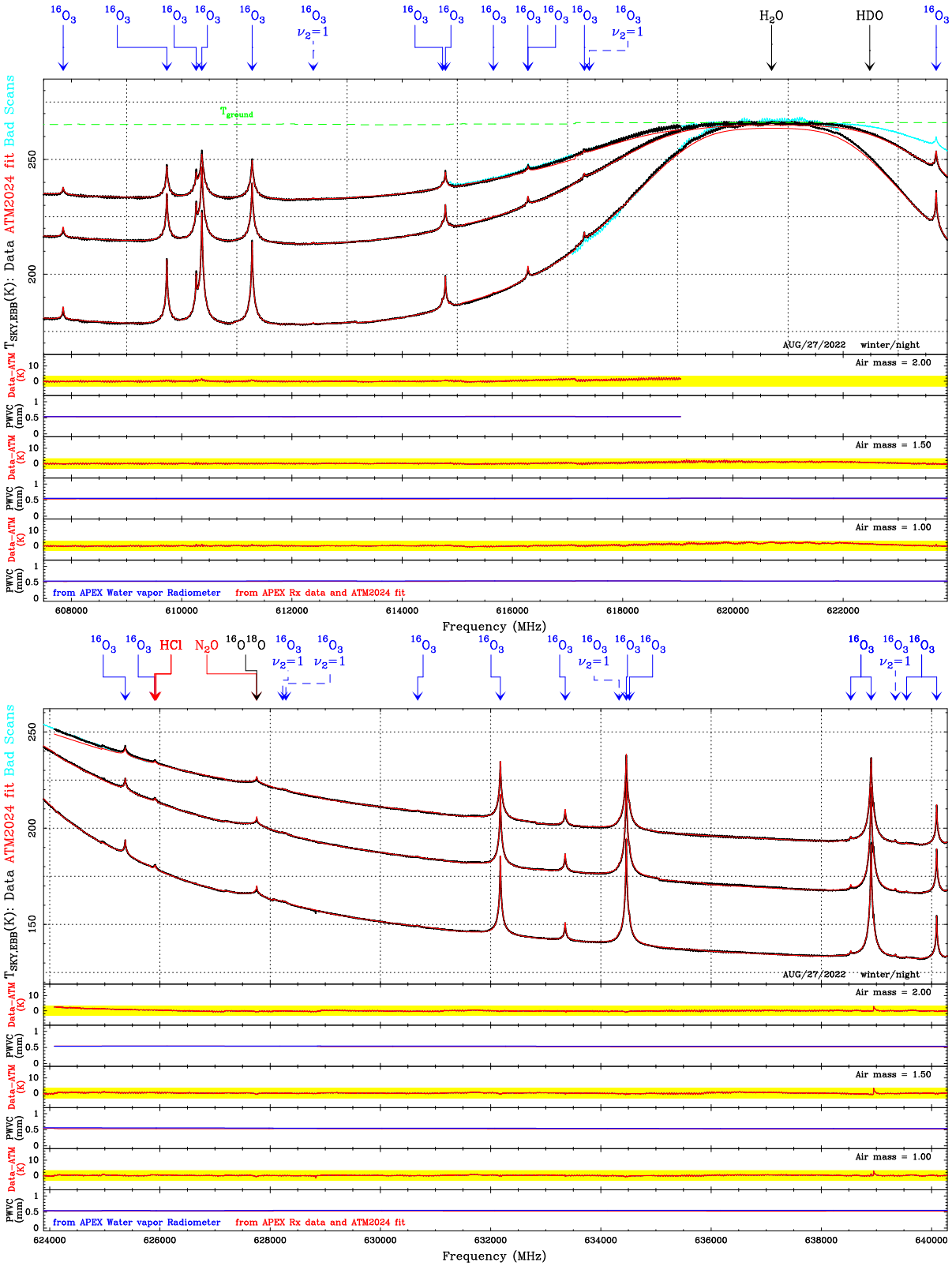

Figure 100: Zoom on Aug. 27^{nd} 2022 SEPIA660 3 air mass sky dip data and ATM2024 fit results (part 2).

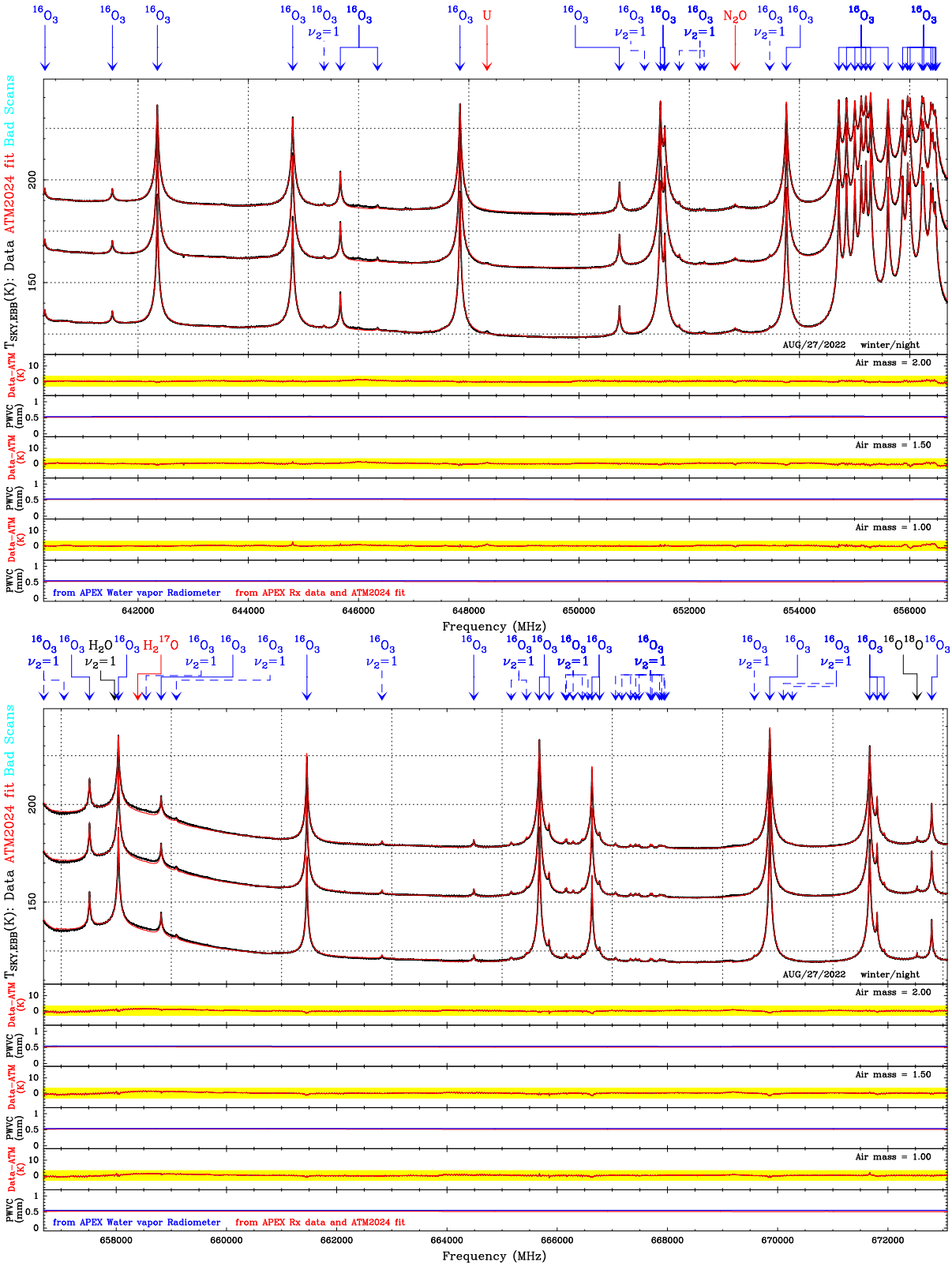

Figure 101: Zoom on Aug. 27^{nd} 2022 SEPIA660 3 air mass sky dip data and ATM2024 fit results (part 3).

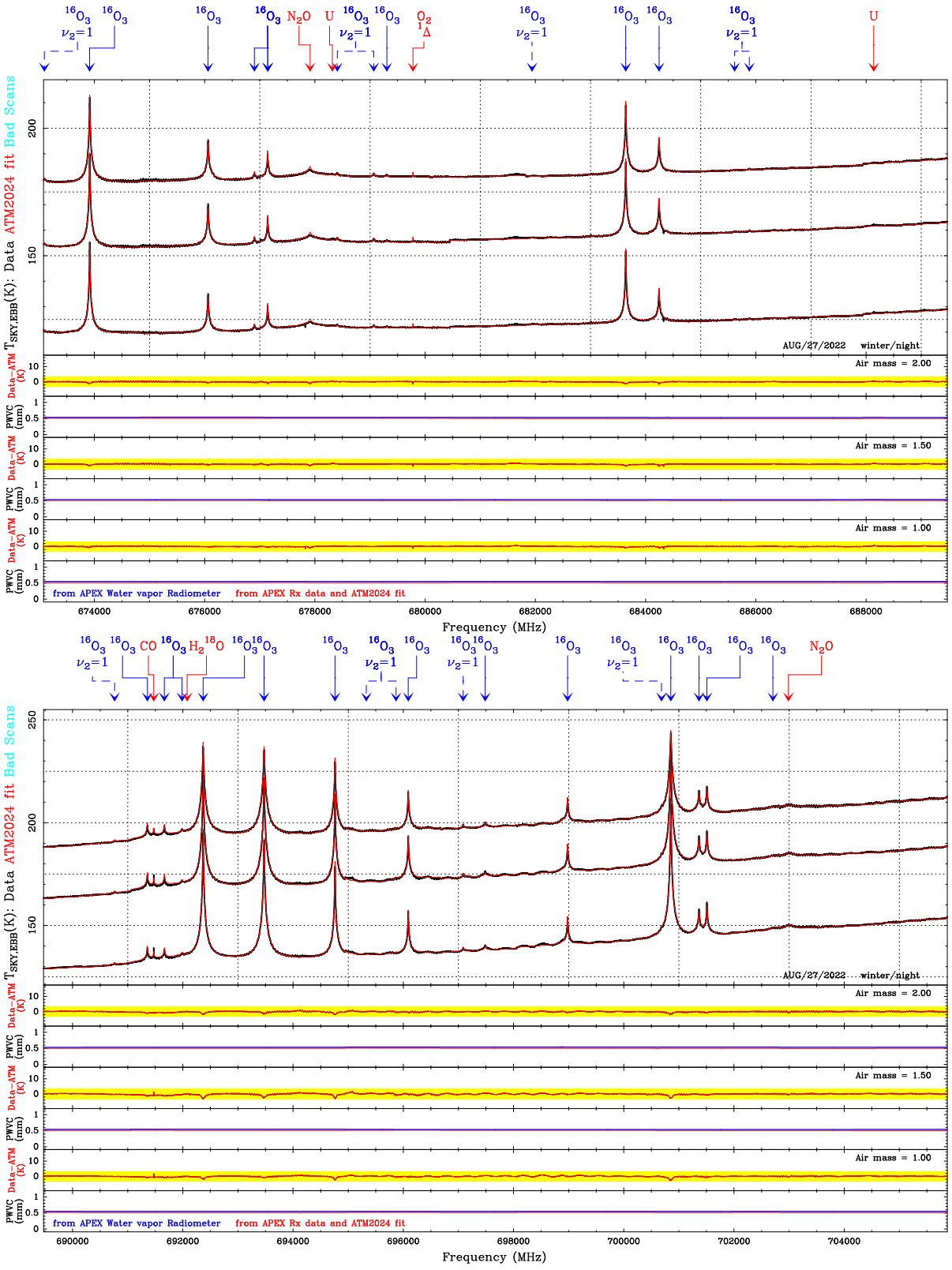

Figure 102: Zoom on Aug. 27^{nd} 2022 SEPIA660 3 air mass sky dip data and ATM2024 fit results (part 4).

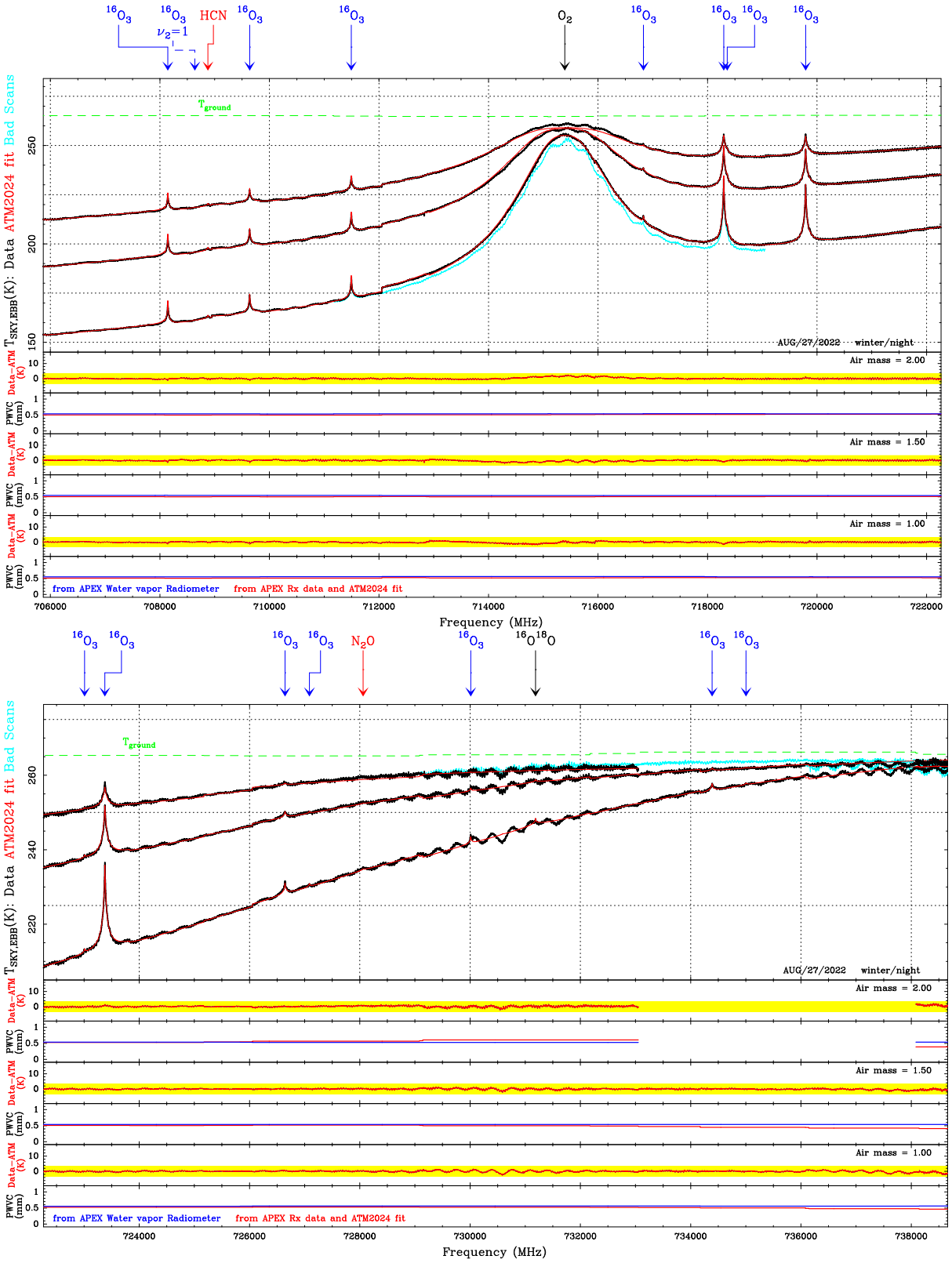

Figure 103: Zoom on Aug. 27^{nd} 2022 SEPIA660 3 air mass sky dip data and ATM2024 fit results (part 5).

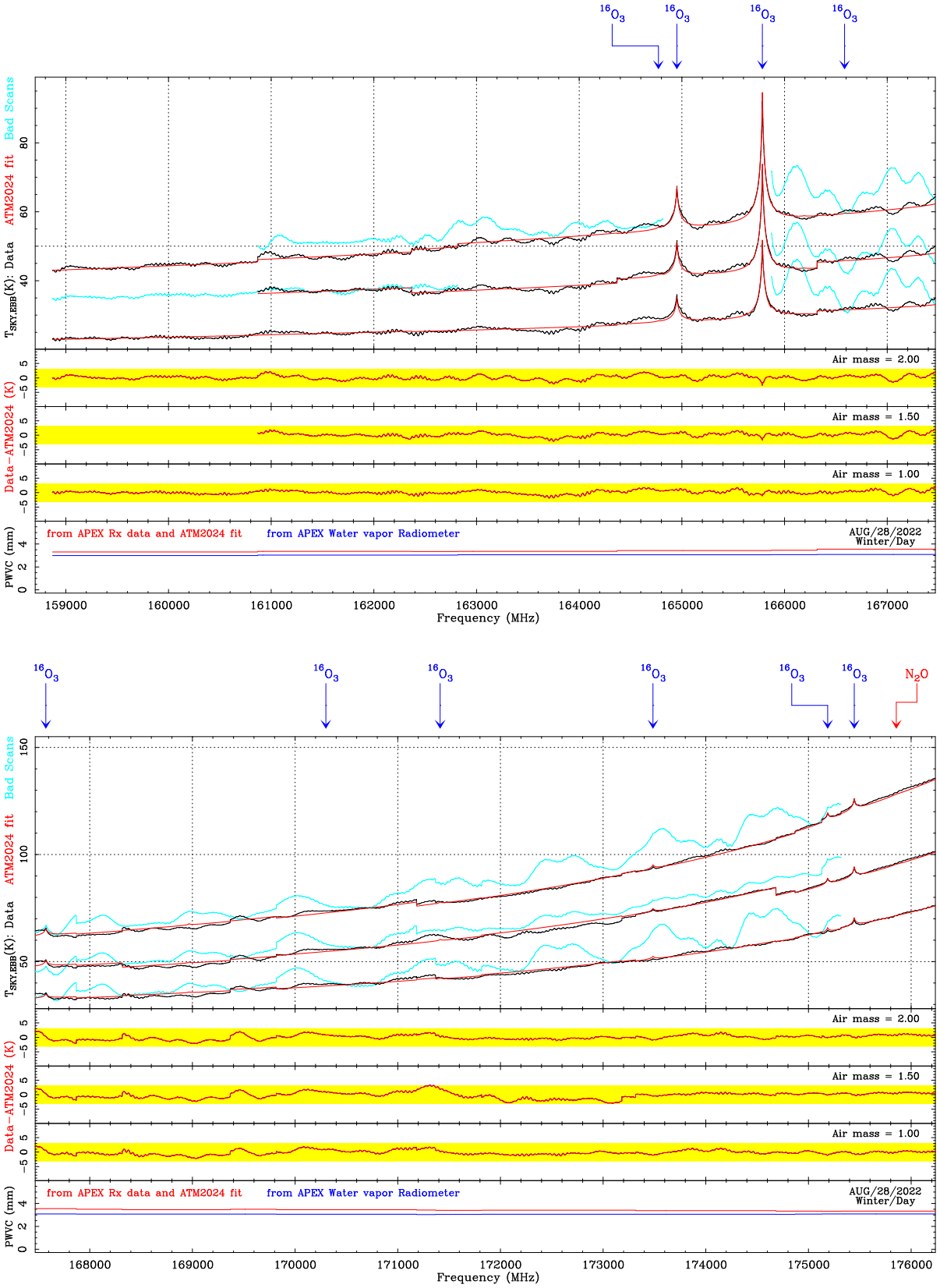

Figure 104: Zoom on Aug. 28^{th} 2020 SEPIA180 3 air mass sky dip data and ATM2024 fit results (part 1).

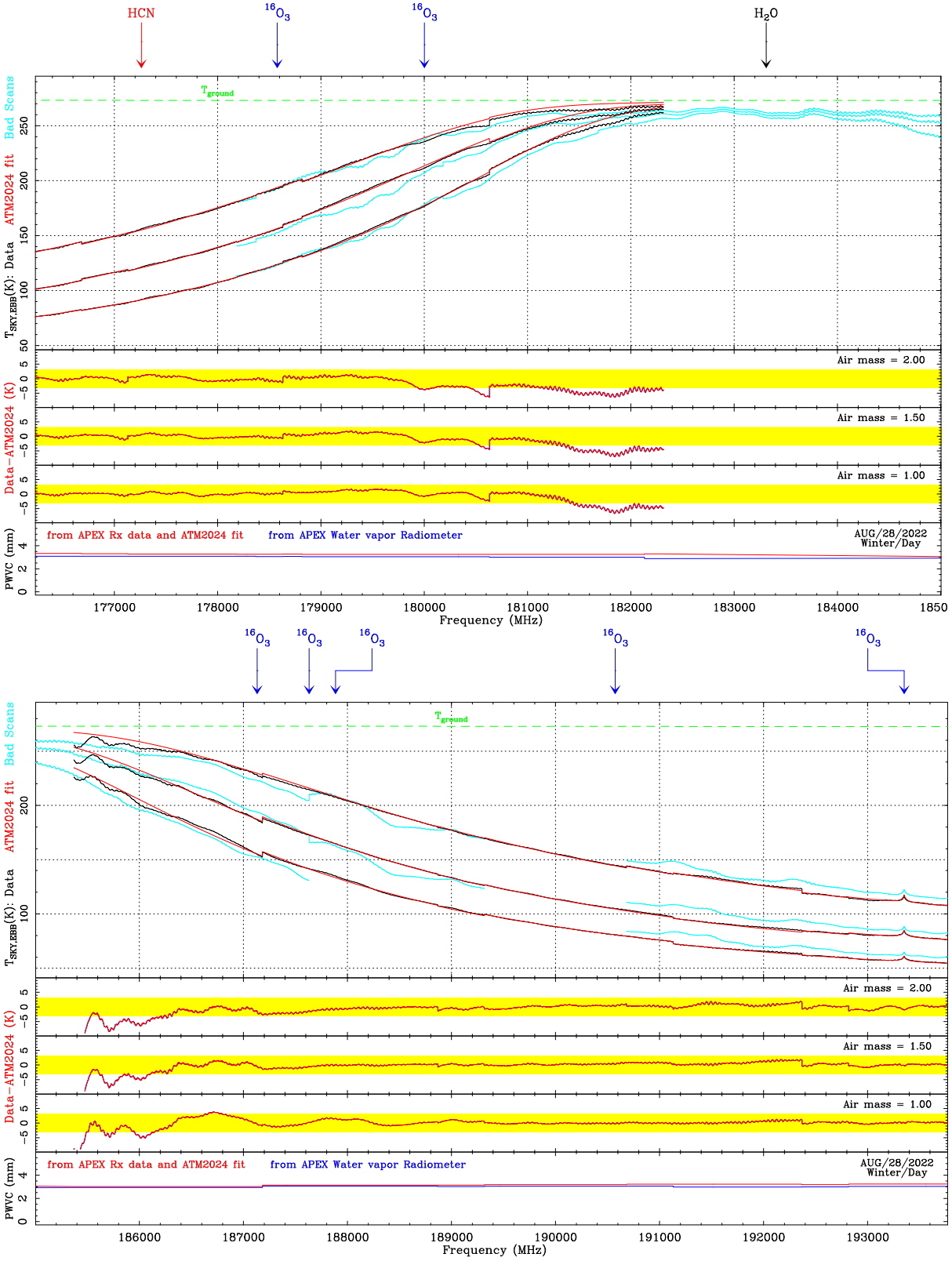

Figure 105: Zoom on Aug. 28^{th} 2020 SEPIA180 3 air mass sky dip data and ATM2024 fit results (part 2).

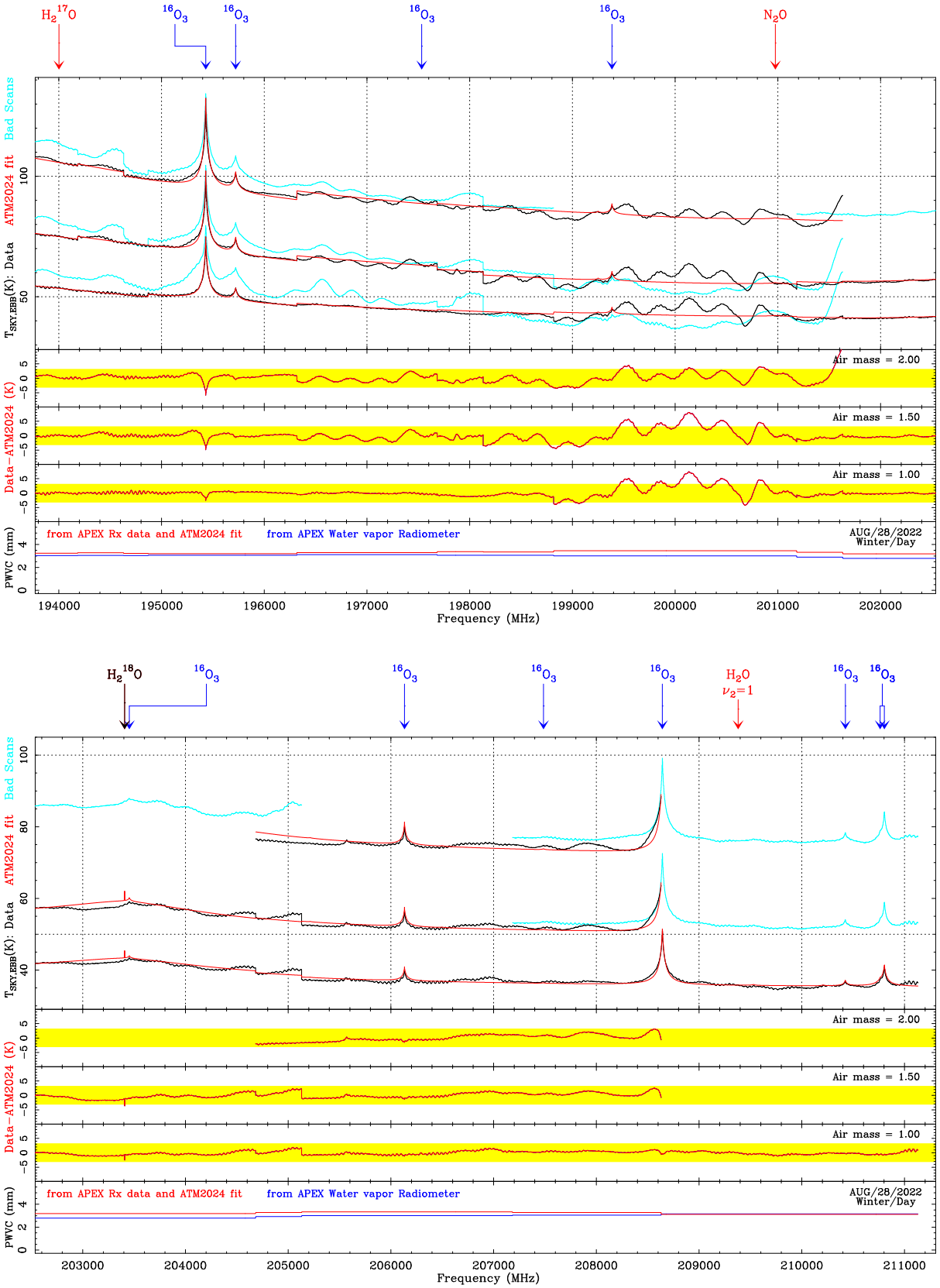

Figure 106: Zoom on Aug. 28^{th} 2020 SEPIA180 3 air mass sky dip data and ATM2024 fit results (part 3).

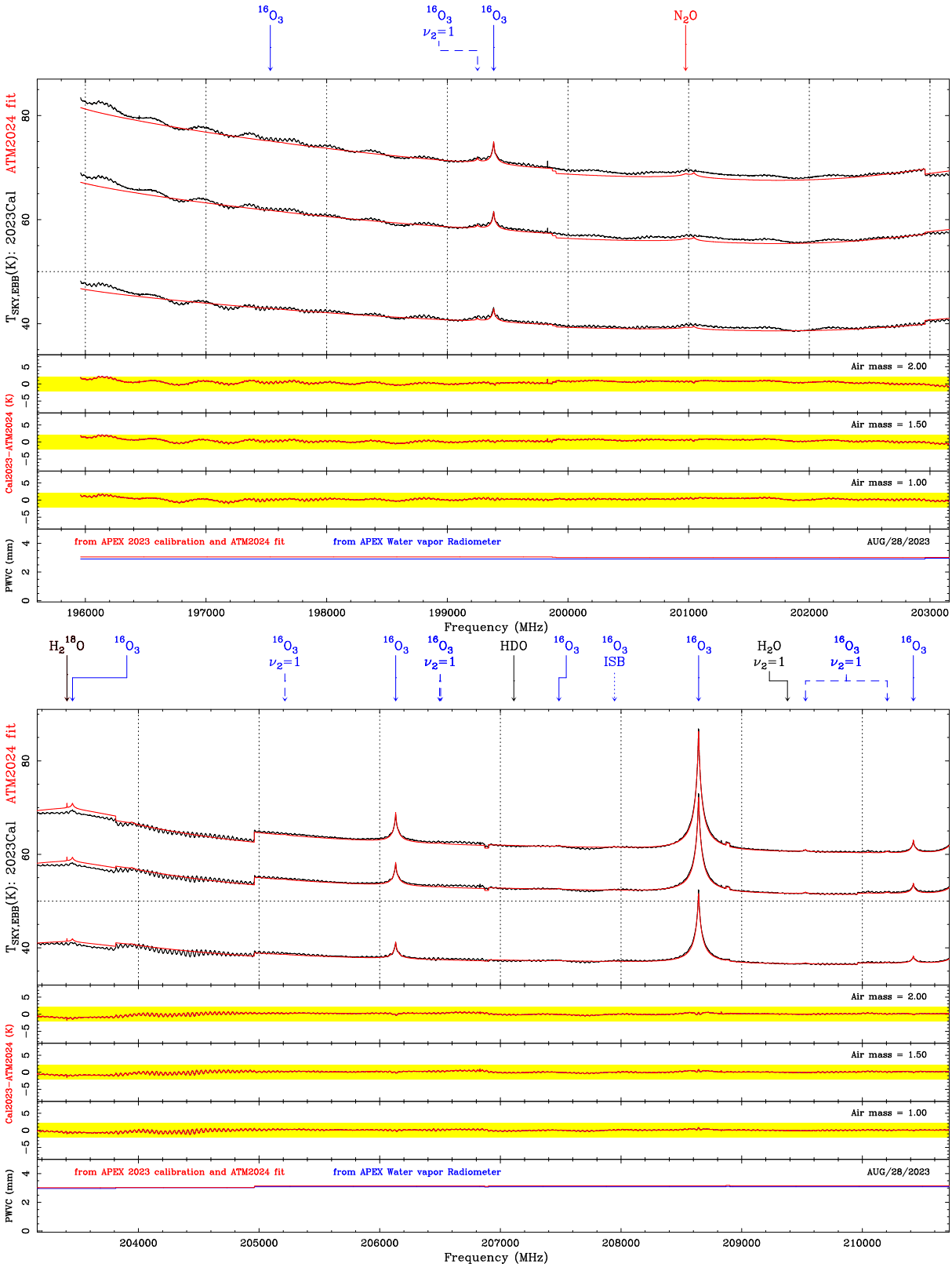

Figure 107: Zoom on Aug. 28^{th} 2020 nFLASH230 3 air mass sky dip data and ATM2024 fit results (part 1).

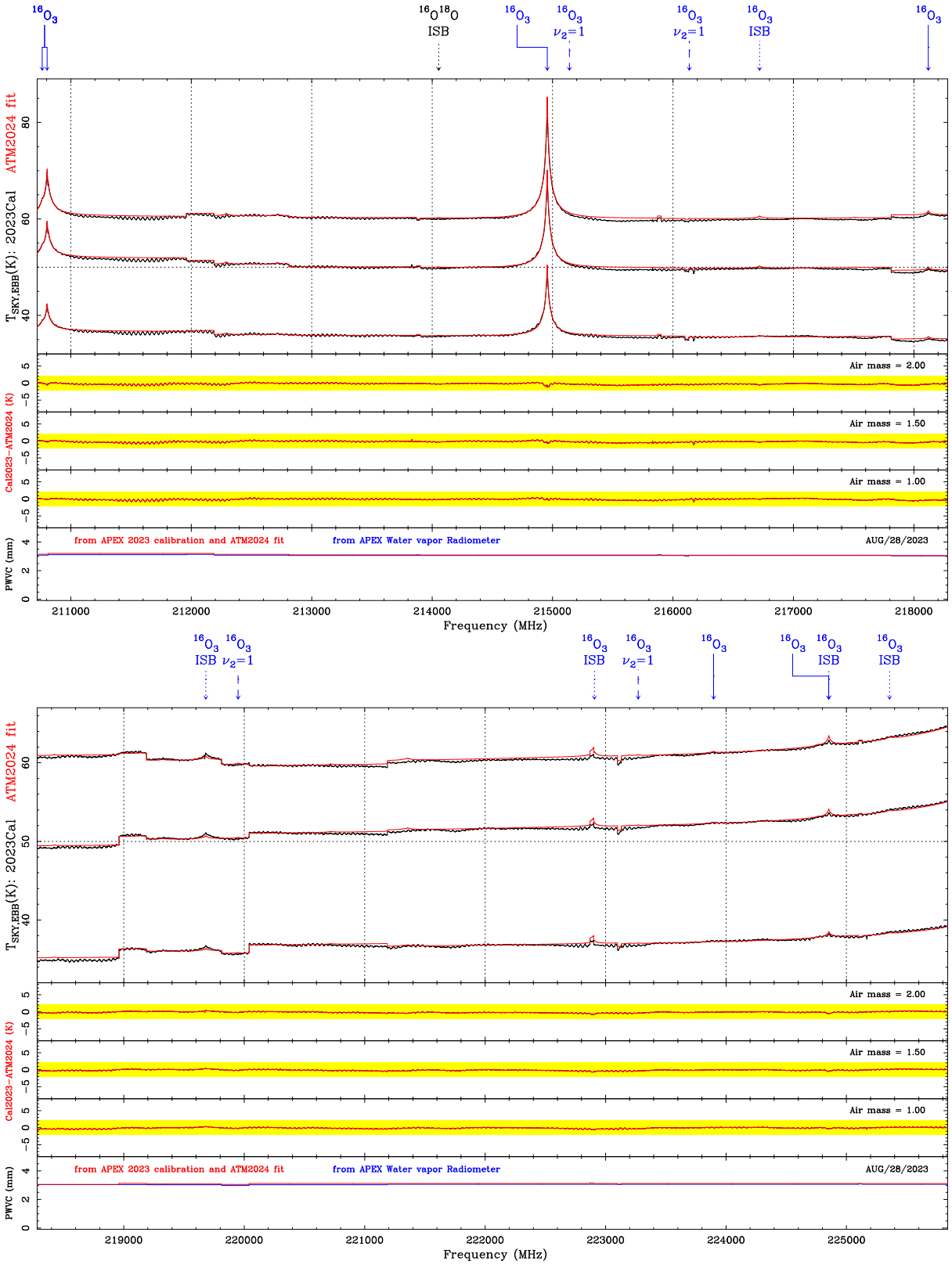

Figure 108: Zoom on Aug. 28^{th} 2020 nFLASH230 3 air mass sky dip data and ATM2024 fit results (part 2).

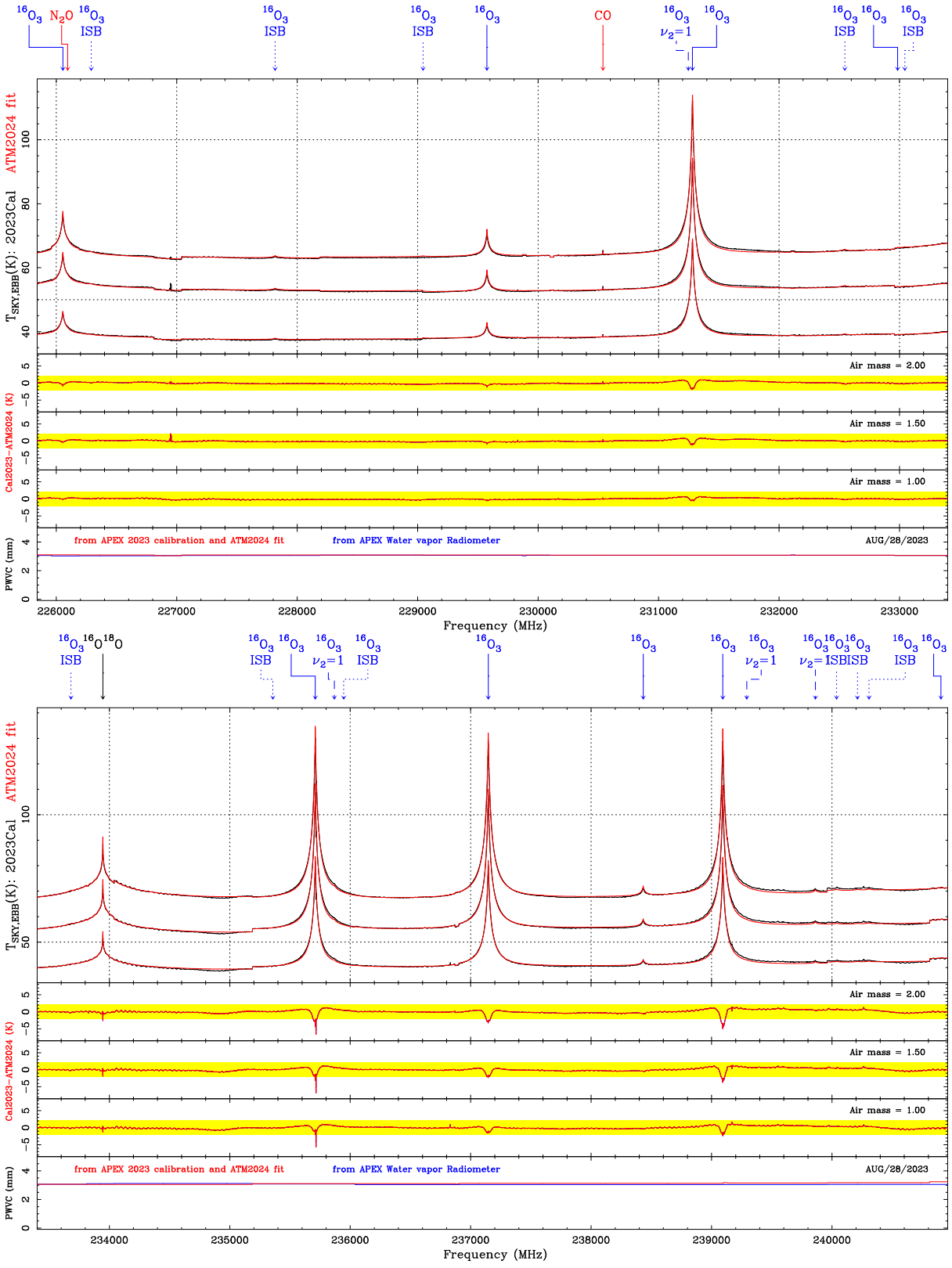

Figure 109: Zoom on Aug. 28^{th} 2020 nFLASH230 3 air mass sky dip data and ATM2024 fit results (part 3).

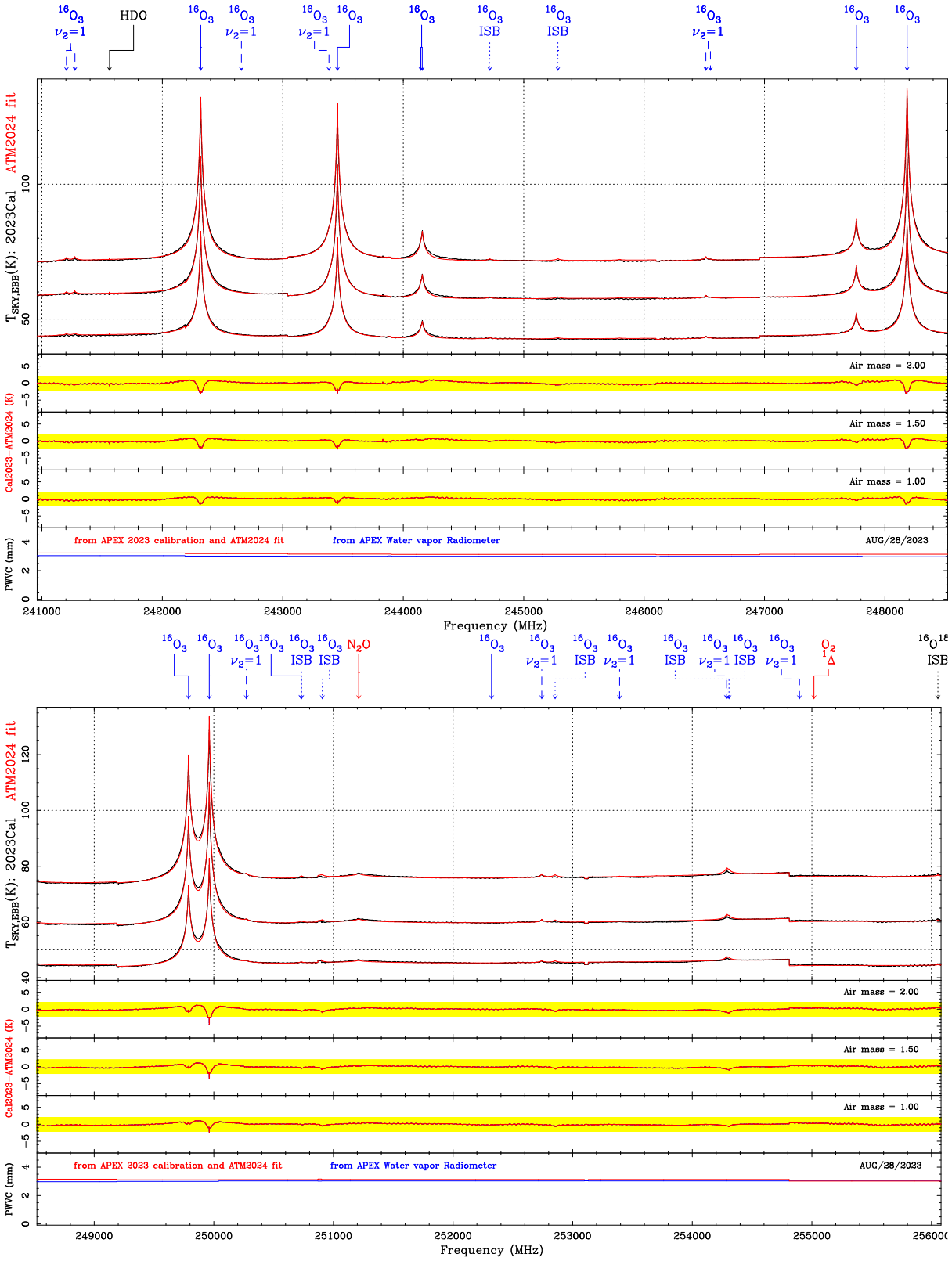

Figure 110: Zoom on Aug. 28^{th} 2020 nFLASH230 3 air mass sky dip data and ATM2024 fit results (part 4).

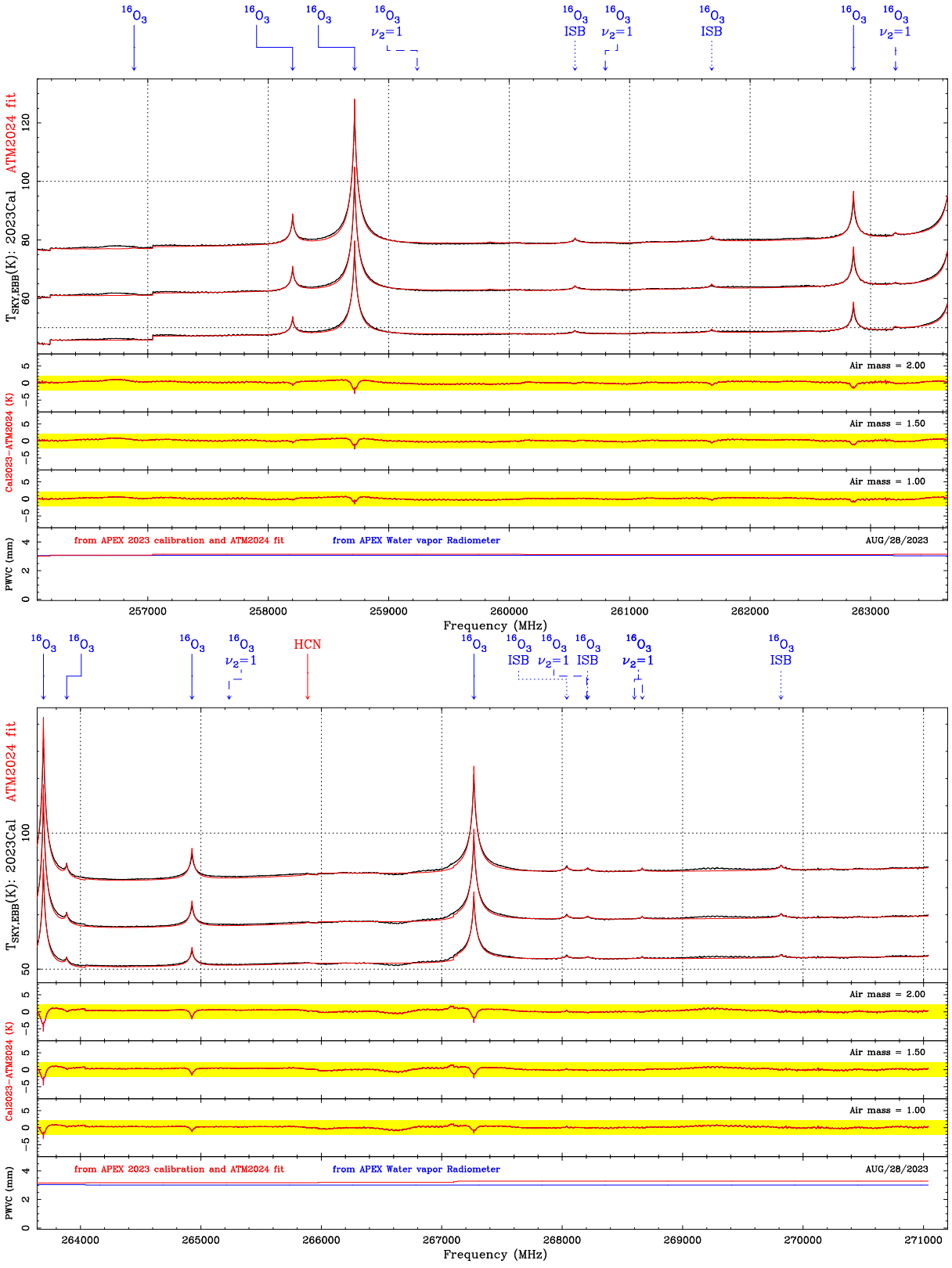

Figure 111: Zoom on Aug. 28^{th} 2020 nFLASH230 3 air mass sky dip data and ATM2024 fit results (part 5).

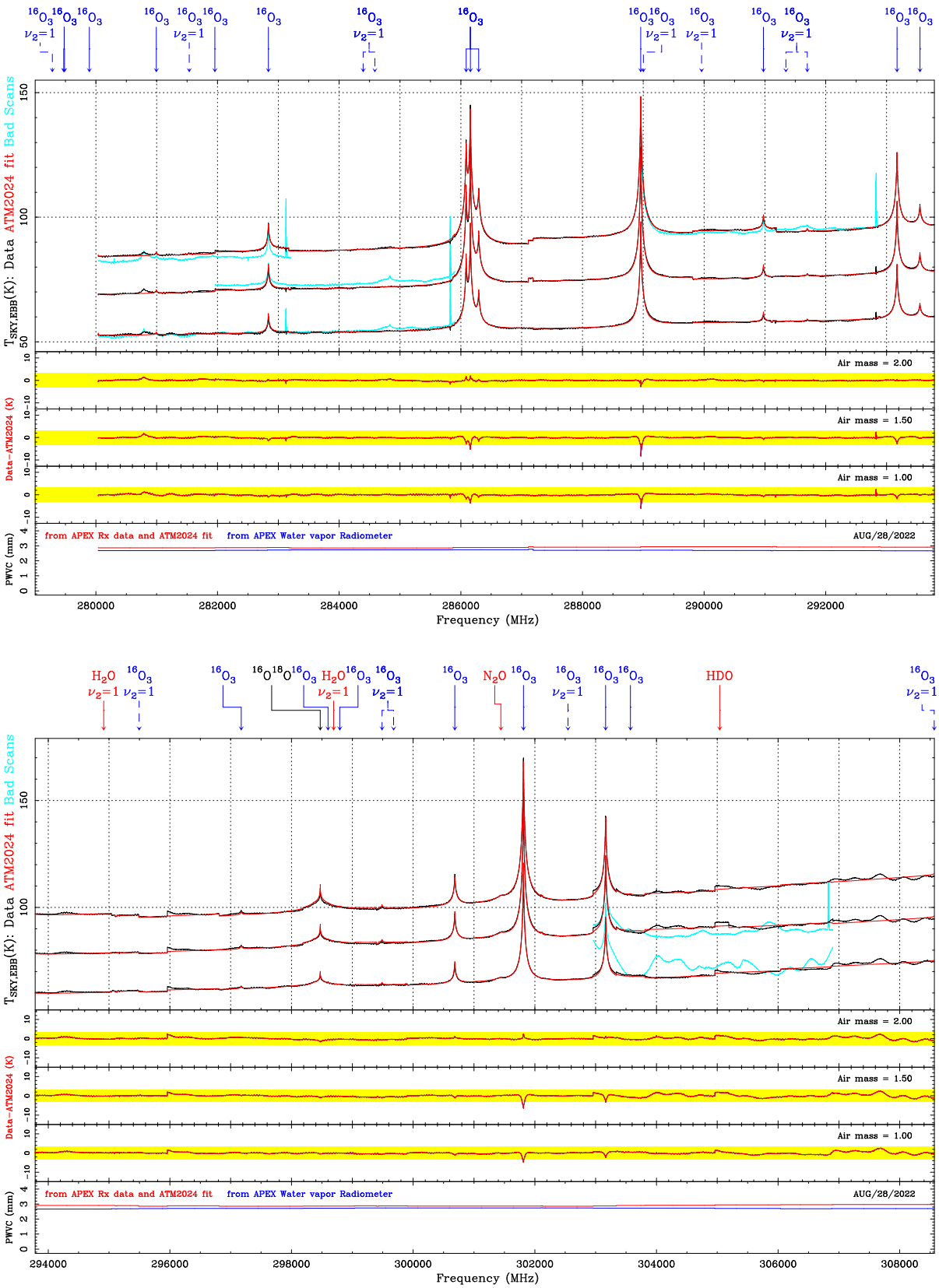

Figure 112: Zoom on Aug. 28^{th} 2022 three air mass skydip taken with SEPIA345, and ATM2024 fit results (part 1).

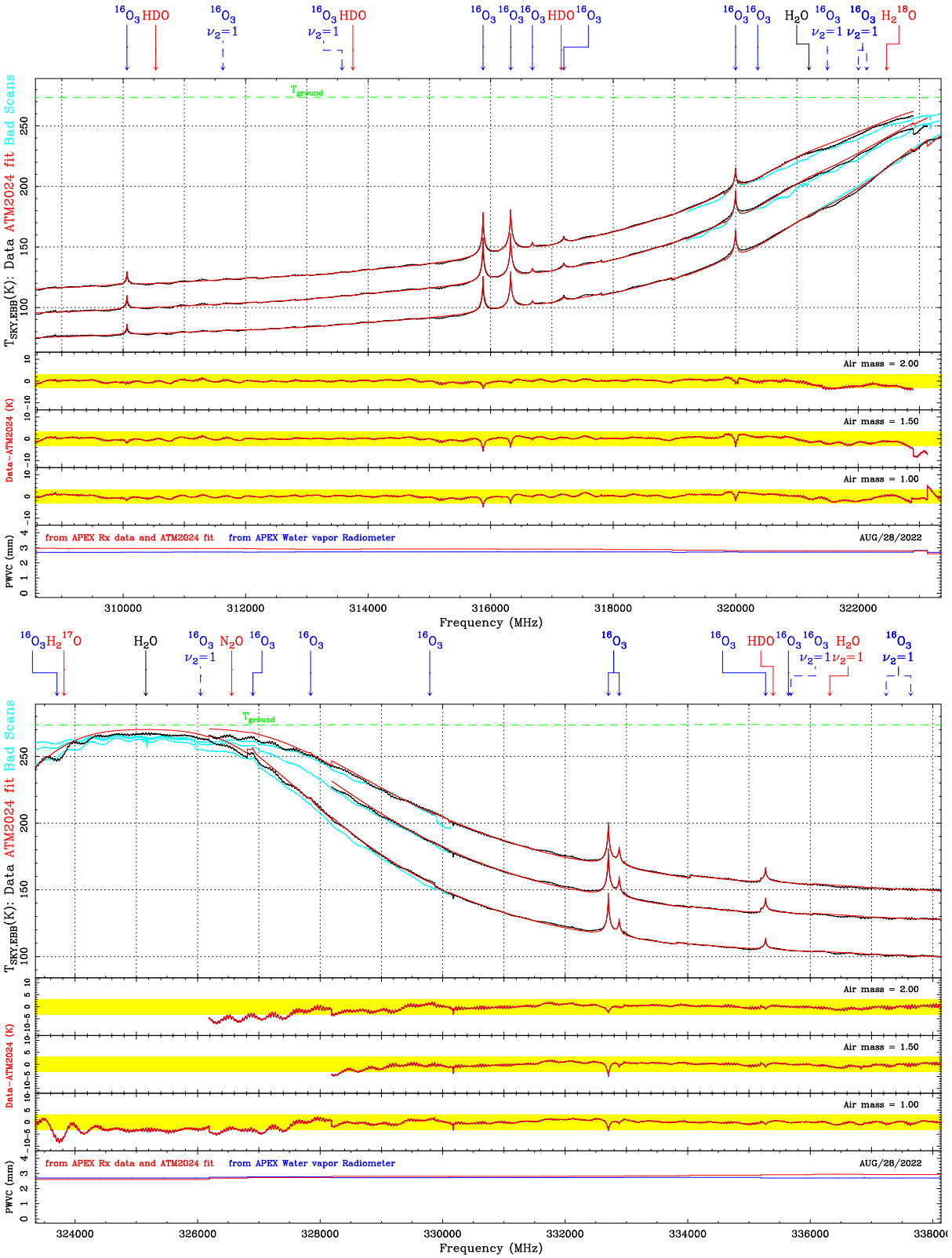

Figure 113: Zoom on Aug. 28^{th} 2022 three air mass skydip taken with SEPIA345, and ATM2024 fit results (part 2).

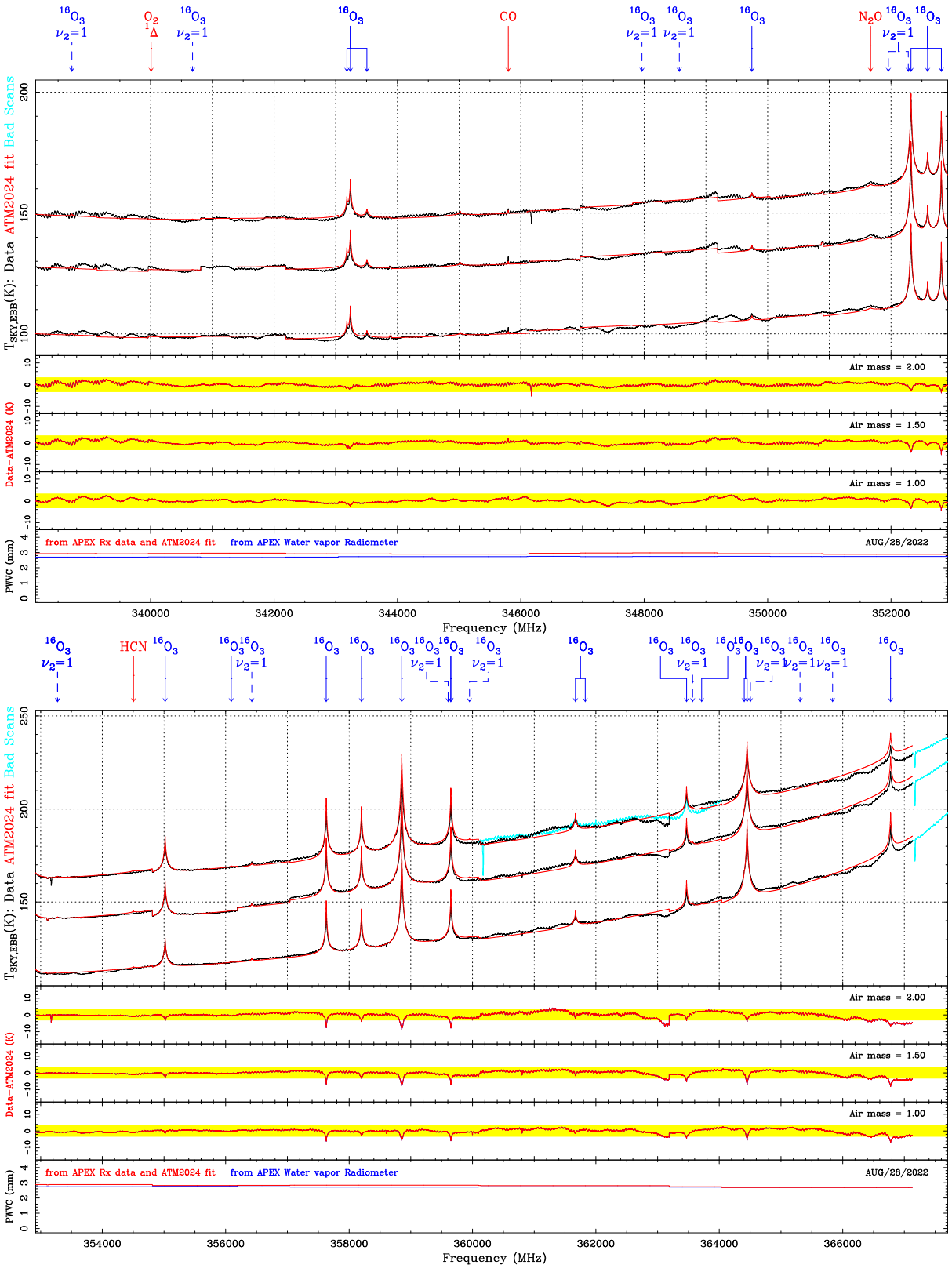

Figure 114: Zoom on Aug. 28^{th} 2022 three air mass skydip taken with SEPIA345, and ATM2024 fit results (part 3).

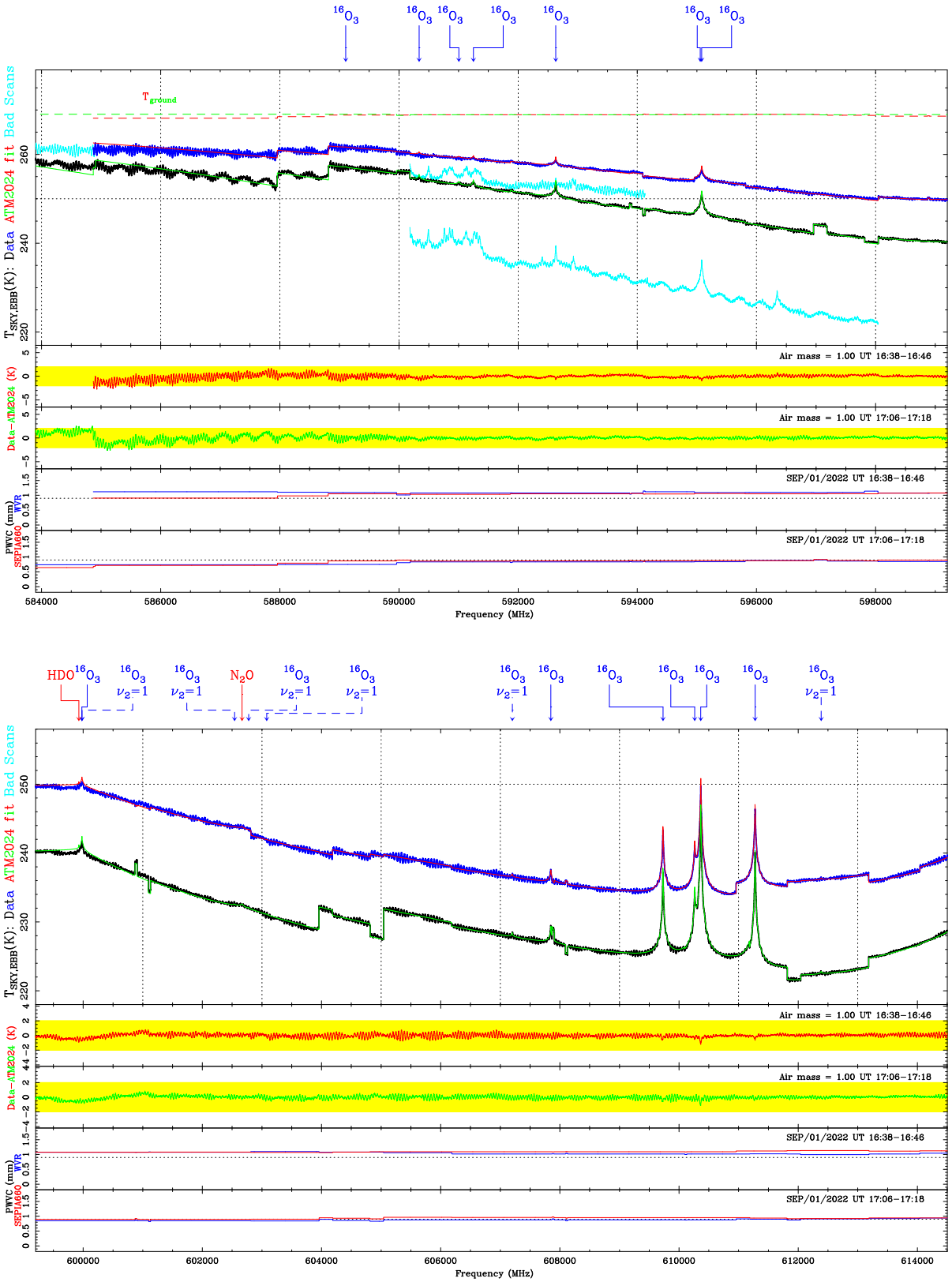

Figure 115: Zoom on Sept. 1^{st} 2022 two consecutive scans at air mass=1.0 taken with SEPIA660, and ATM2024 fit results (part 1).

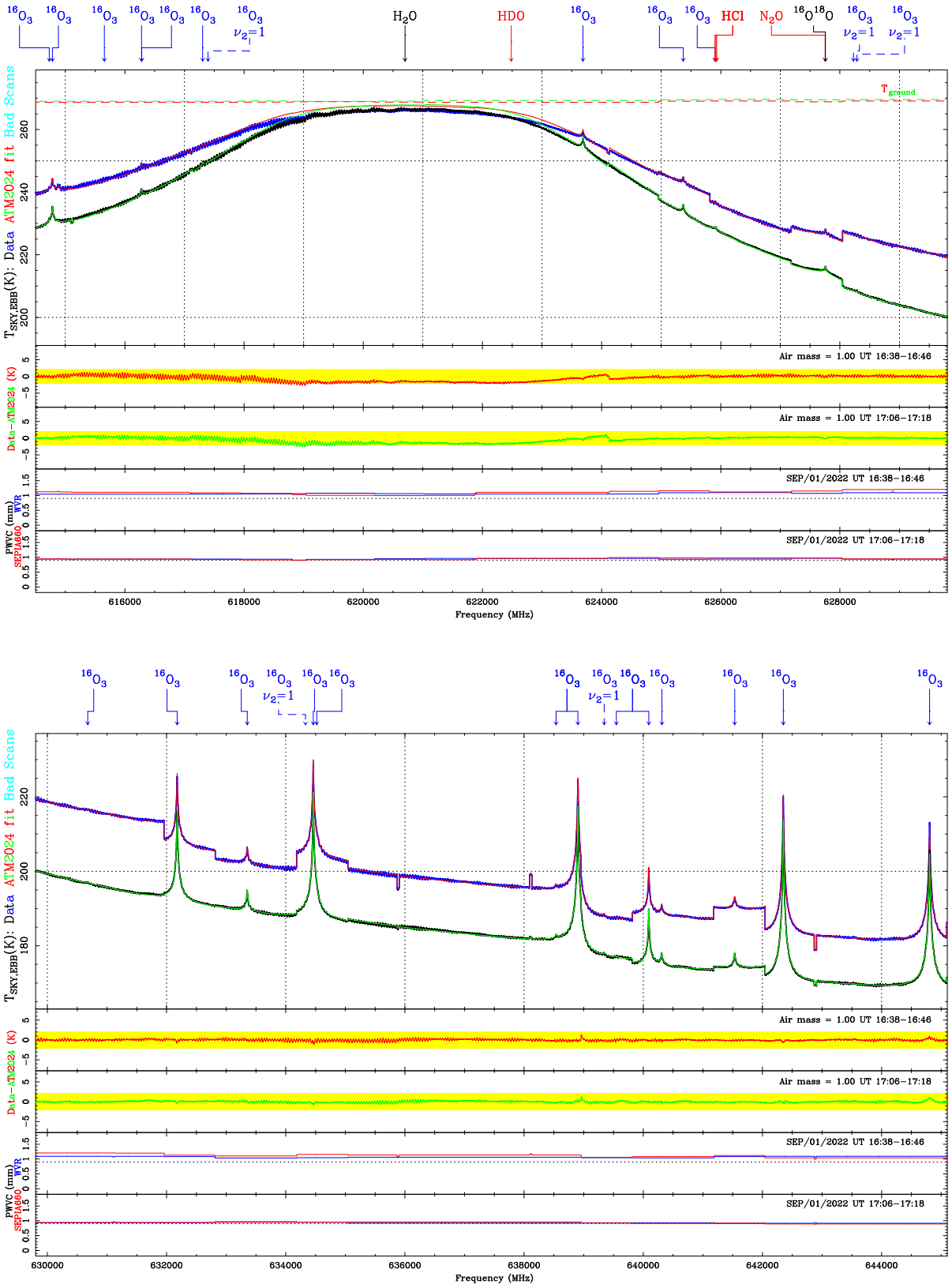

Figure 116: Zoom on Sept. 1^{st} 2022 two consecutive scans at air mass=1.0 taken with SEPIA660, and ATM2024 fit results (part 2).

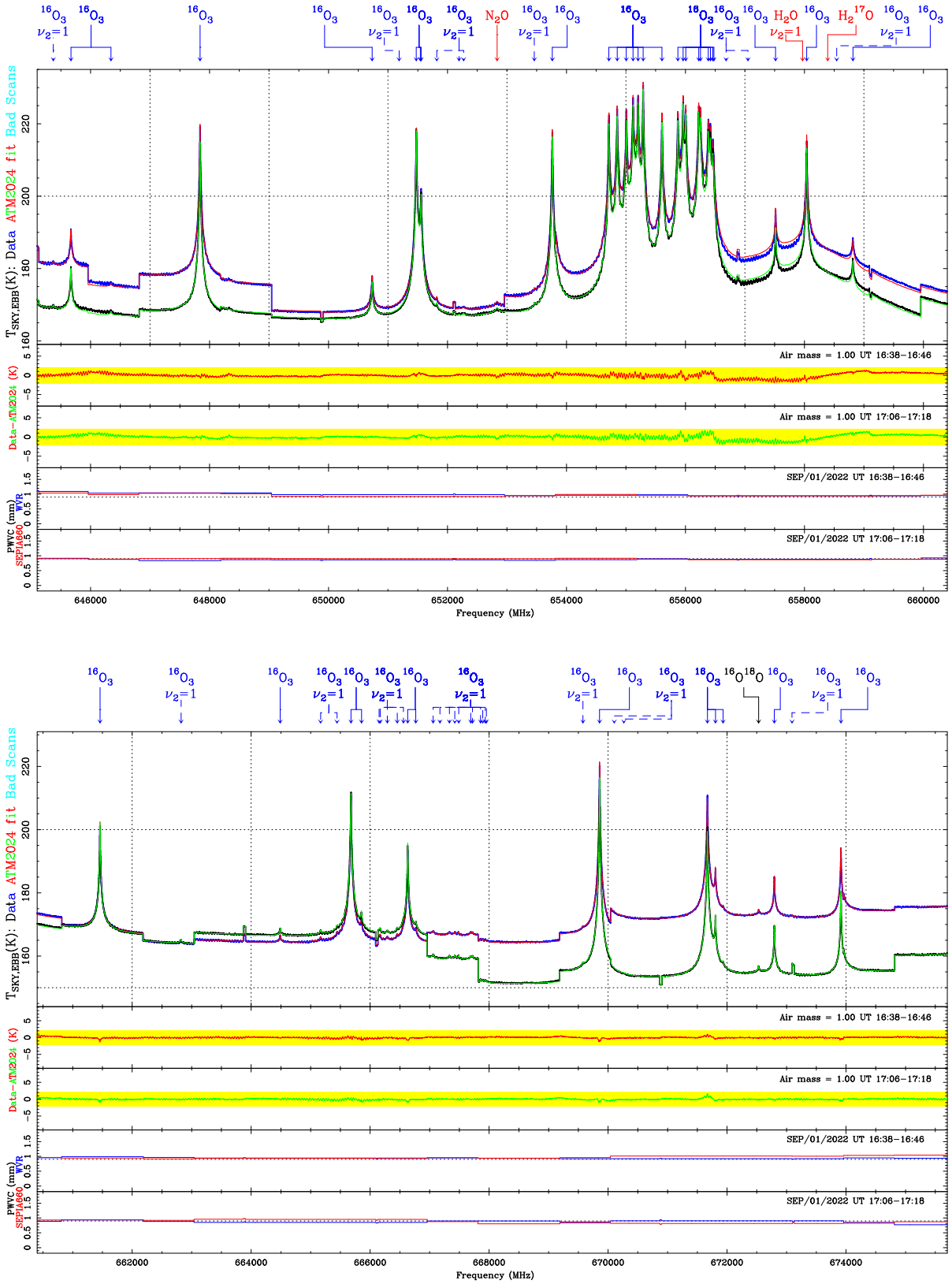

Figure 117: Zoom on Sept. 1^{st} 2022 two consecutive scans at air mass=1.0 taken with SEPIA660, and ATM2024 fit results (part 3).

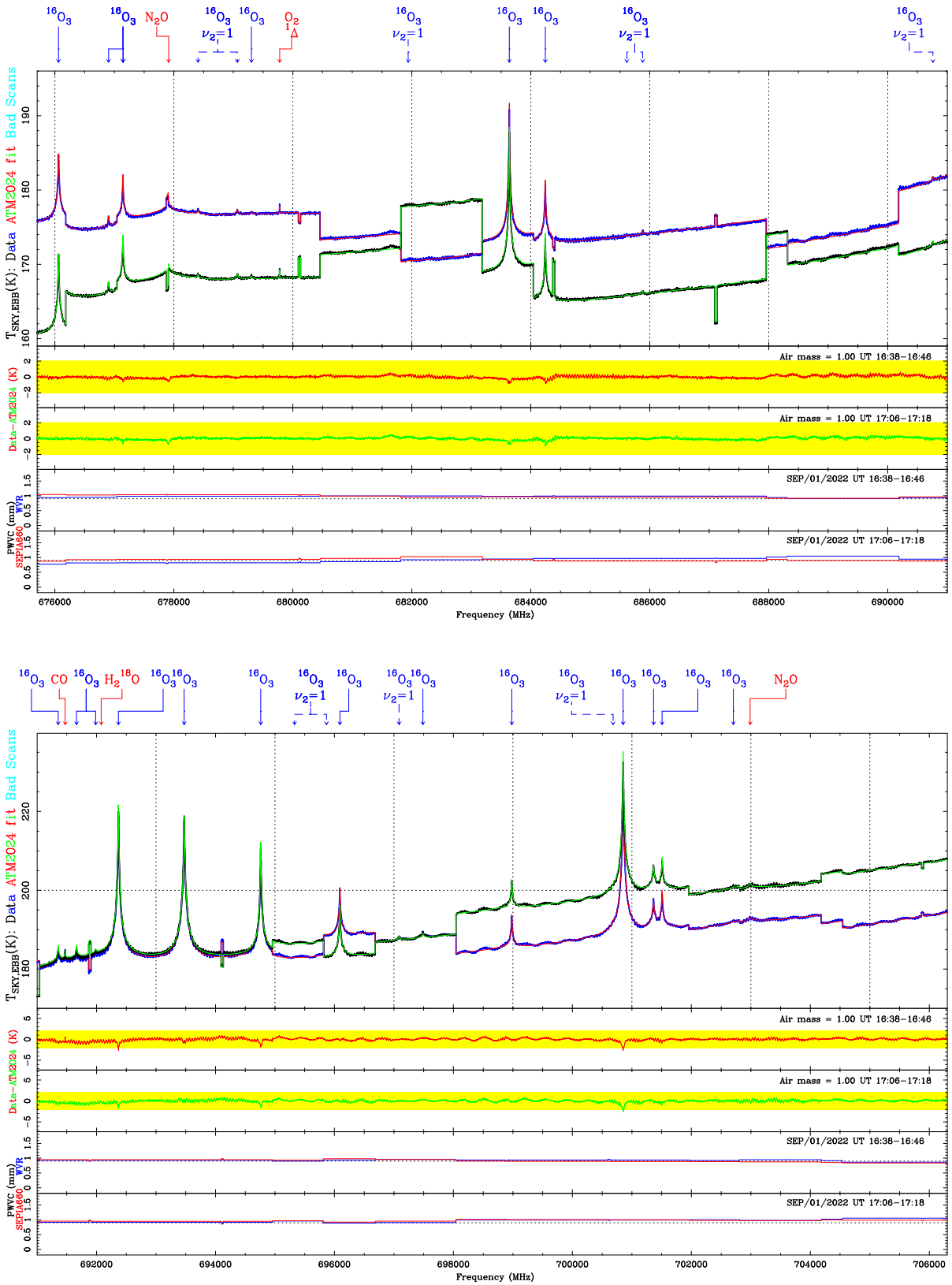

Figure 118: Zoom on Sept. 1^{st} 2022 two consecutive scans at air mass=1.0 taken with SEPIA660, and ATM2024 fit results (part 4).

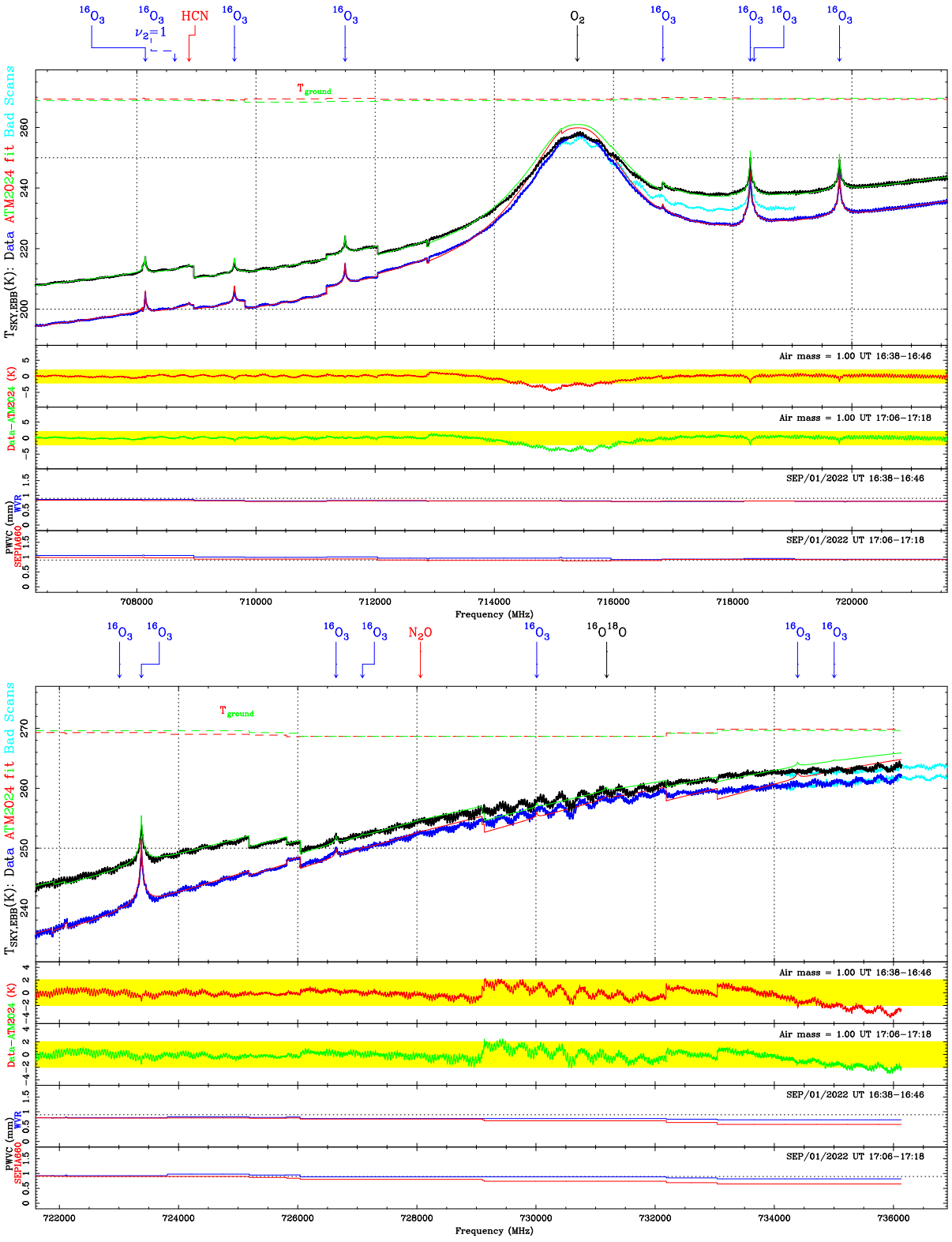

Figure 119: Zoom on Sept. 1^{st} 2022 two consecutive scans at air mass=1.0 taken with SEPIA660, and ATM2024 fit results (part 5).

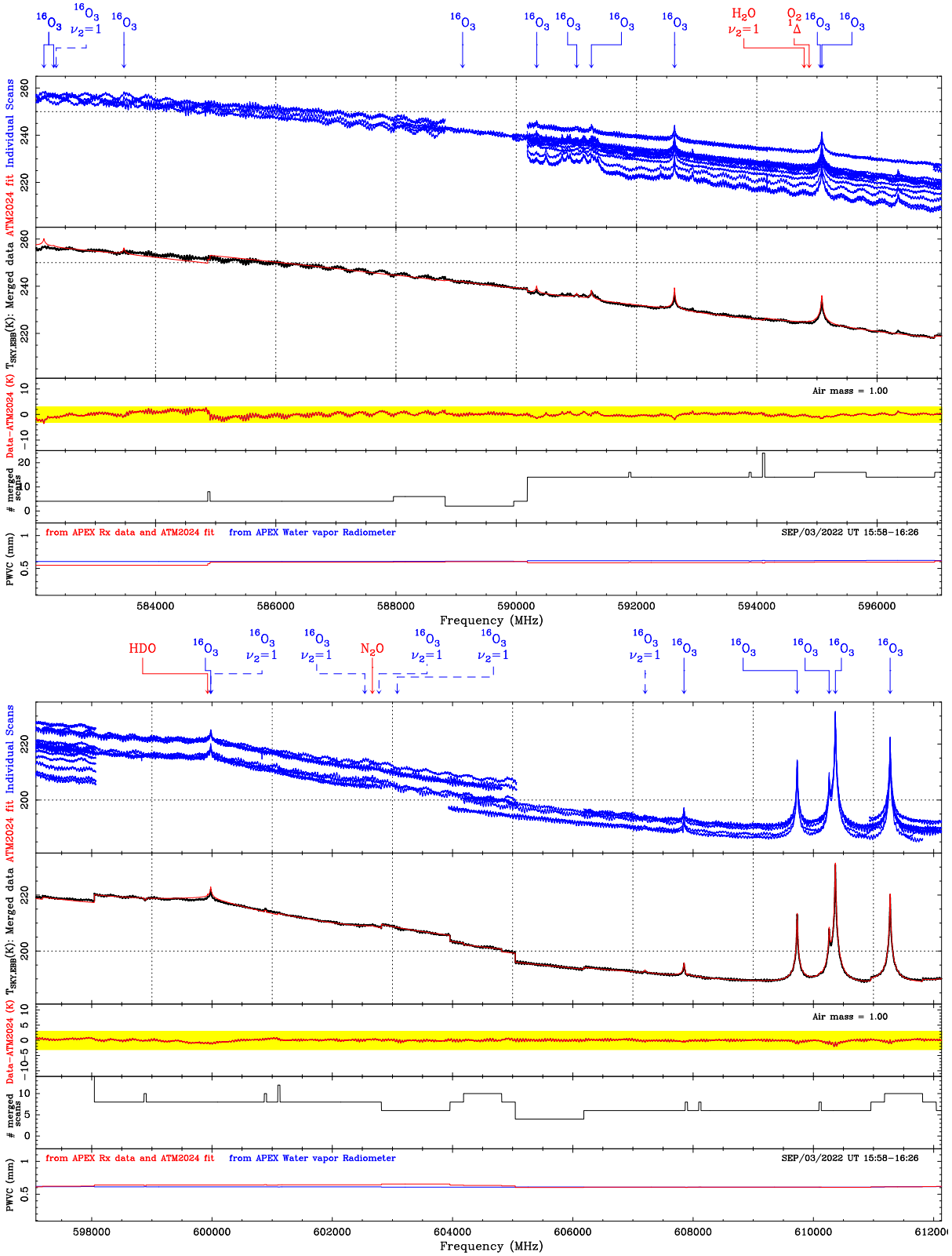

Figure 120: Zoom on Sept. 3^{rd} 2022 two scan at air mass=1.0 taken with SEPIA660, and ATM2024 fit results (part 1).

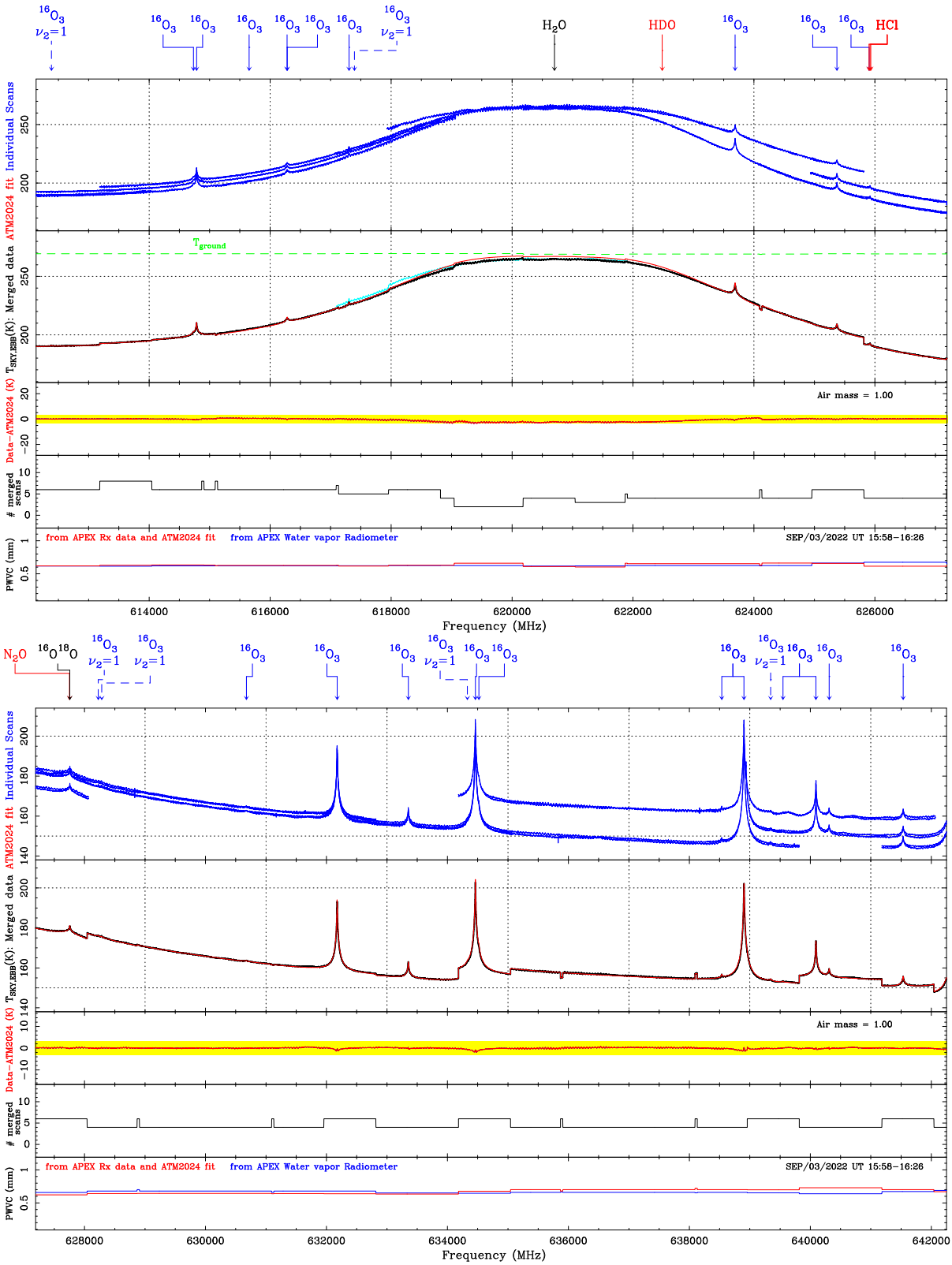

Figure 121: Zoom on Sept. 3^{rd} 2022 scan at air mass=1.0 taken with SEPIA660, and ATM2024 fit results (part 2).

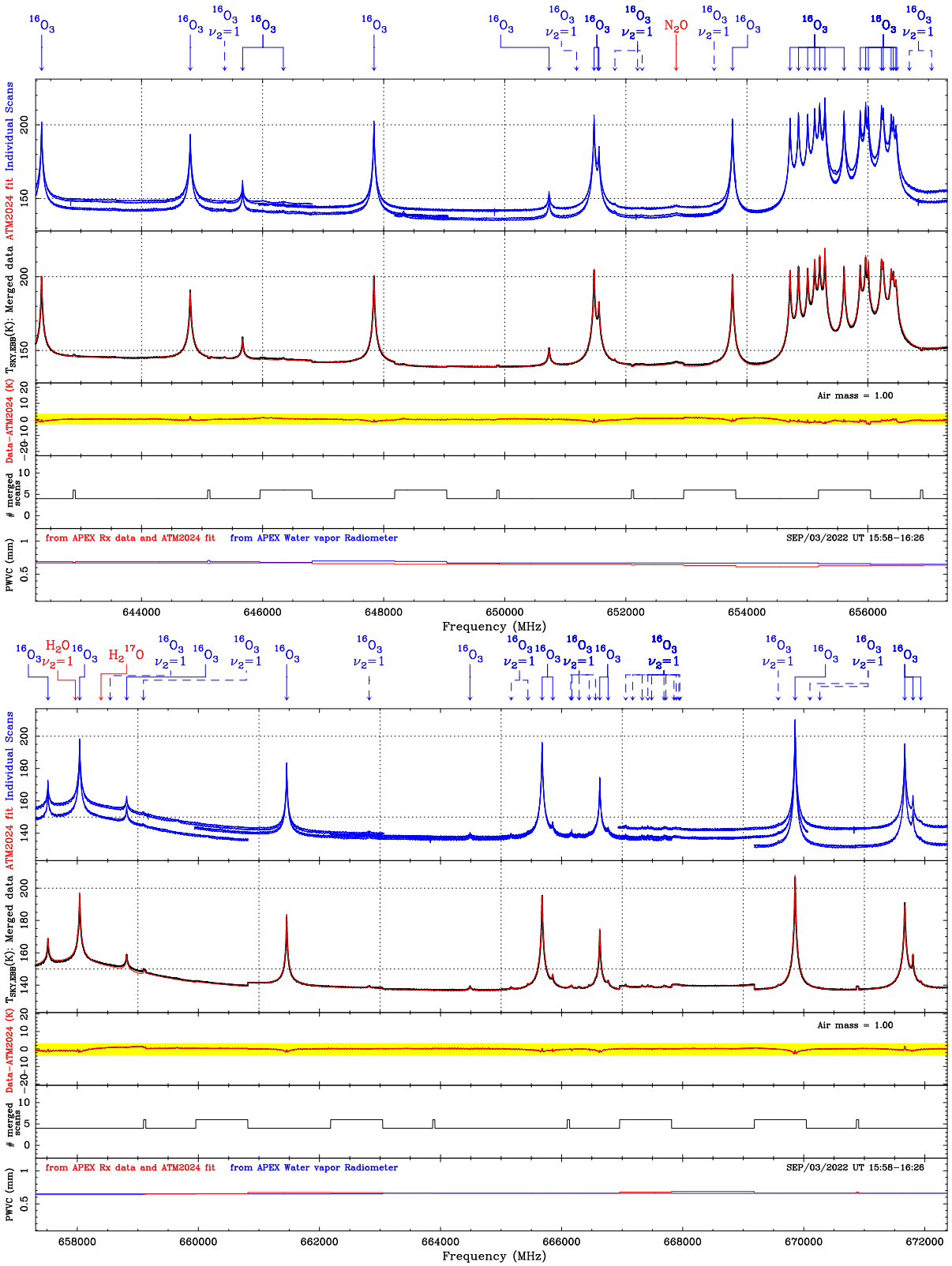

Figure 122: Zoom on Sept. 3^{rd} 2022 scan at air mass=1.0 taken with SEPIA660, and ATM2024 fit results (part 3).

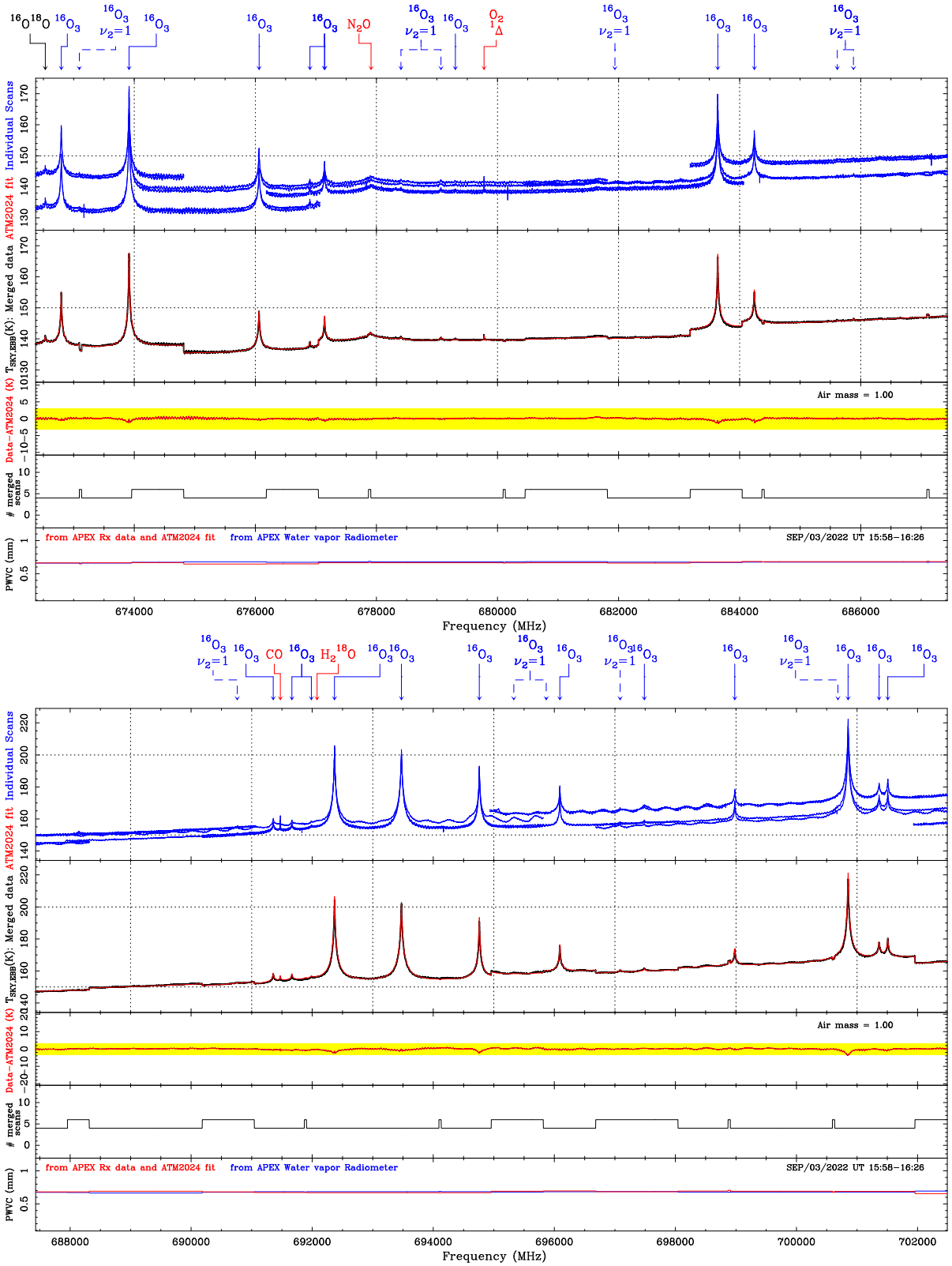

Figure 123: Zoom on Sept. 3^{rd} 2022 scan at air mass=1.0 taken with SEPIA660, and ATM2024 fit results (part 4).

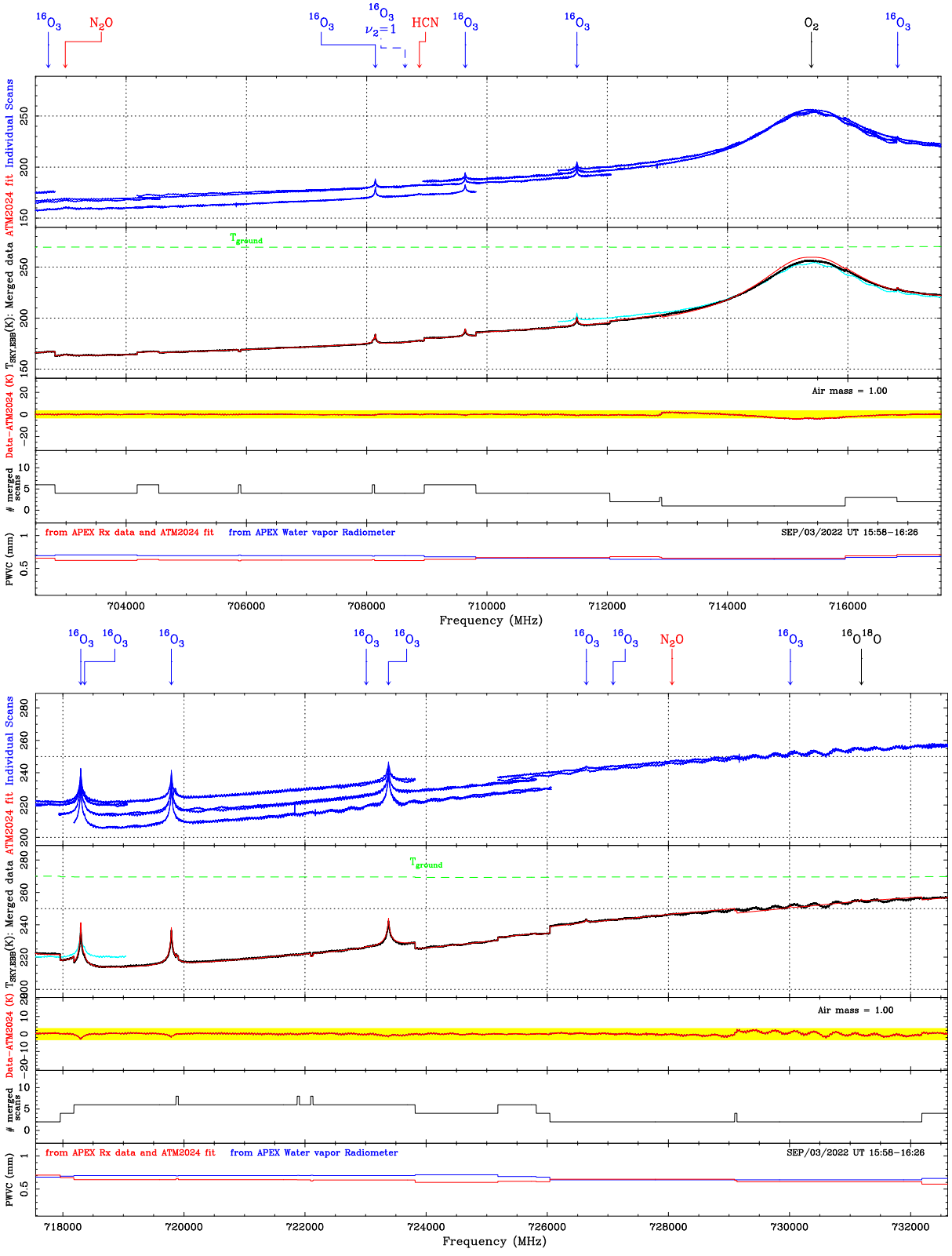

Figure 124: Zoom on Sept. 3^{rd} 2022 scan at air mass=1.0 taken with SEPIA660, and ATM2024 fit results (part 5).

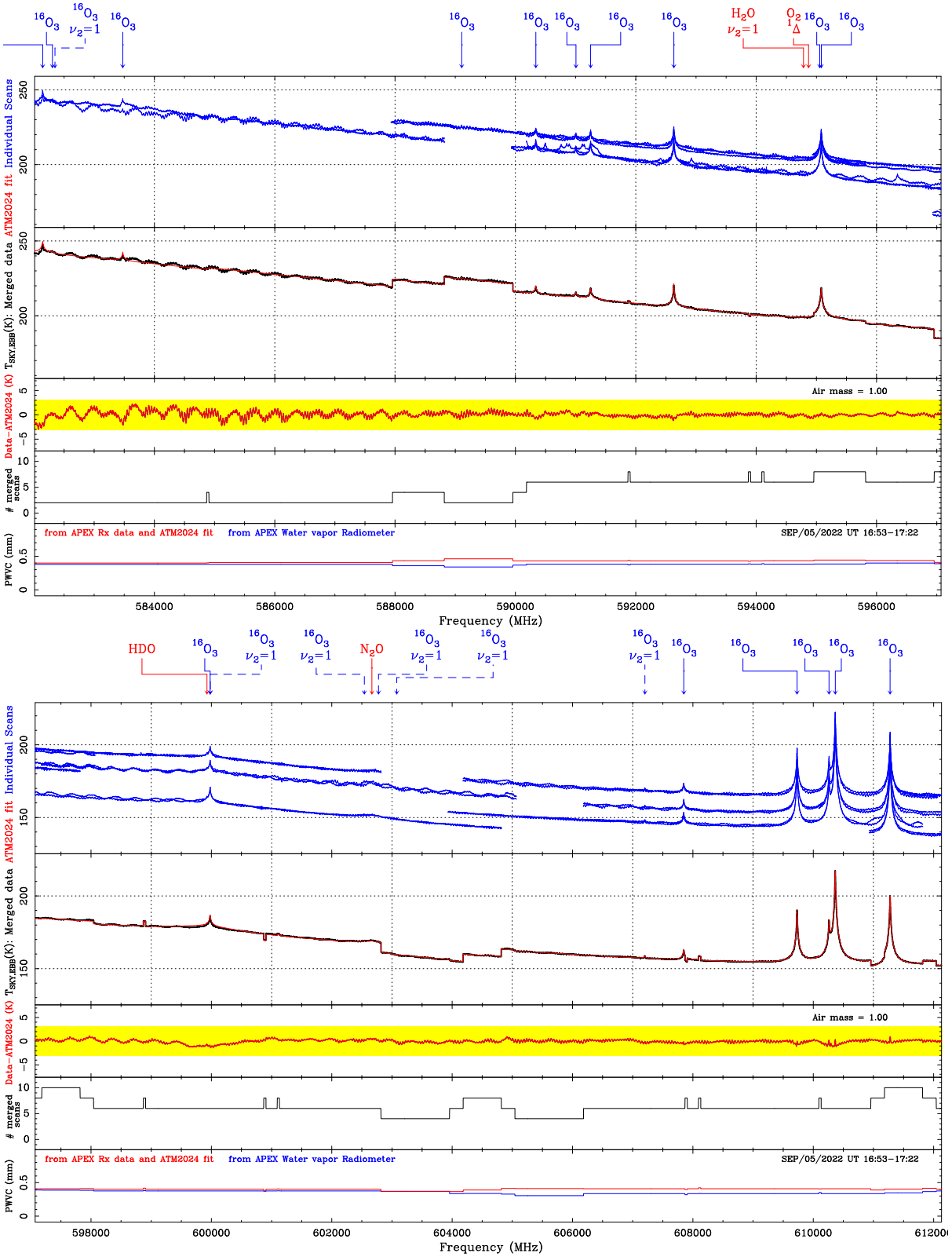

Figure 125: Zoom on Sept. 5^{rd} 2022 scan at air mass=1.0 taken with SEPIA660, and ATM2024 fit results (part 1).

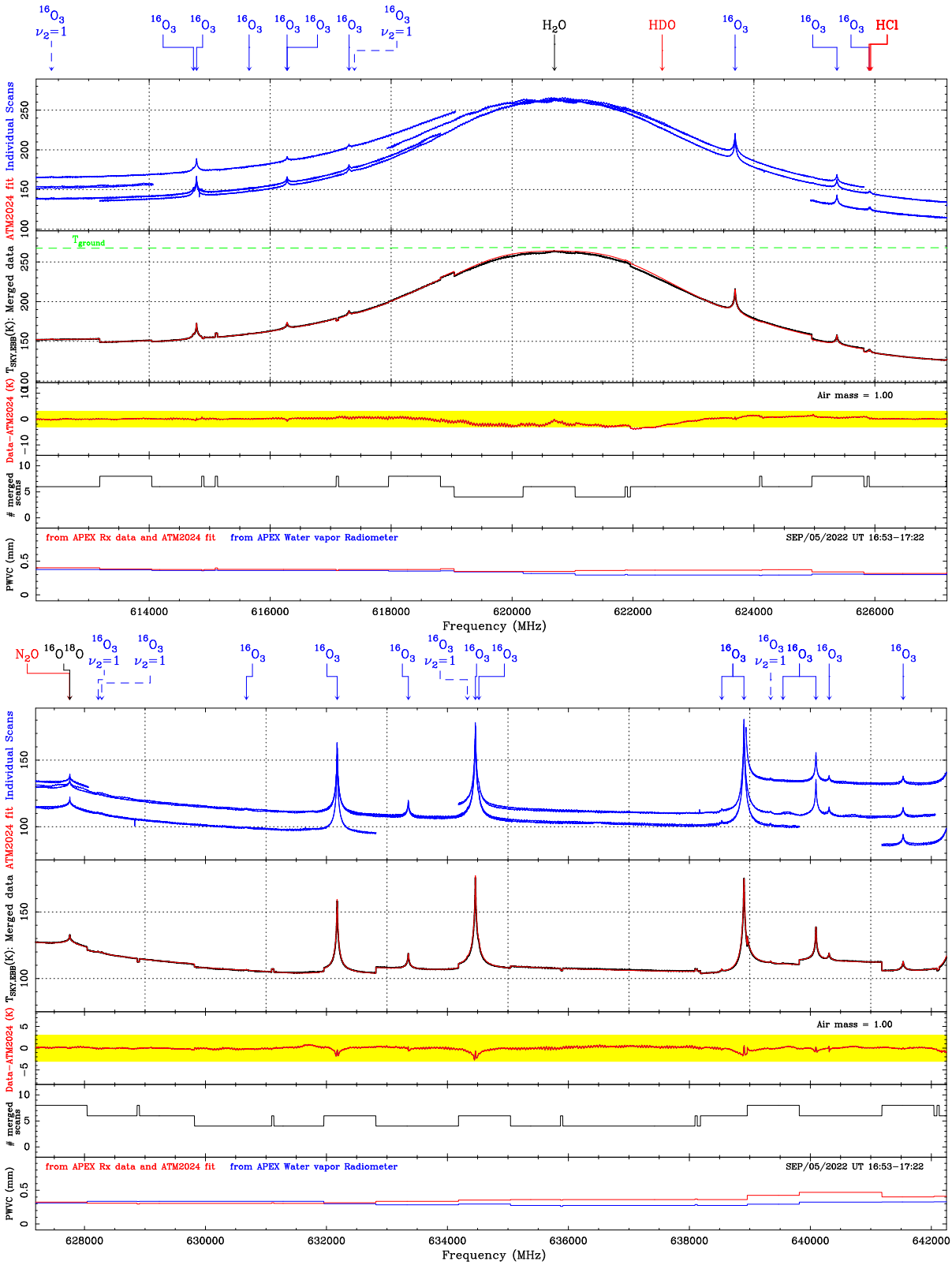

Figure 126: Zoom on Sept. 5^{rd} 2022 scan at air mass=1.0 taken with SEPIA660, and ATM2024 fit results (part 2).

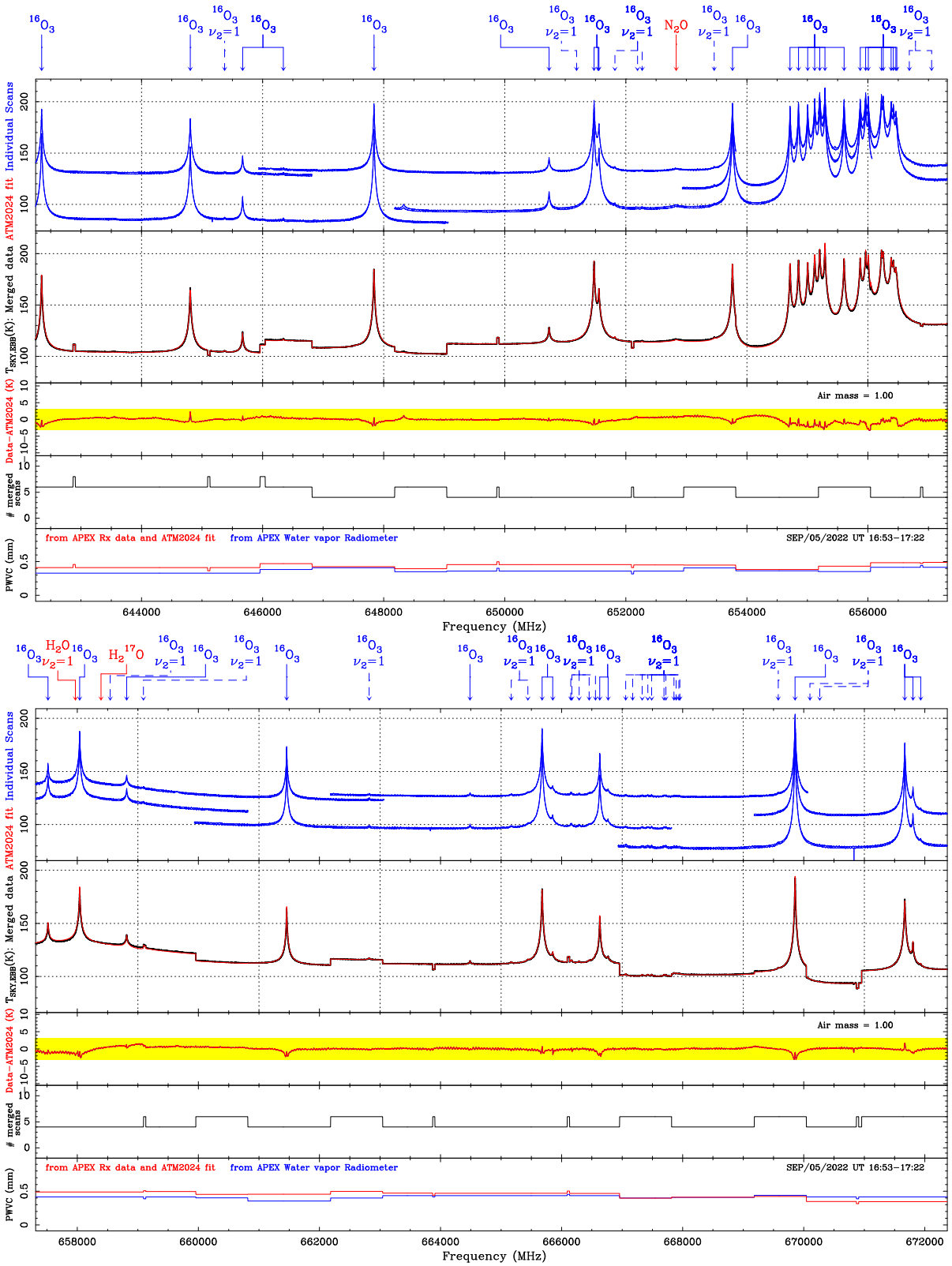

Figure 127: Zoom on Sept. 5^{rd} 2022 scan at air mass=1.0 taken with SEPIA660, and ATM2024 fit results (part 3).

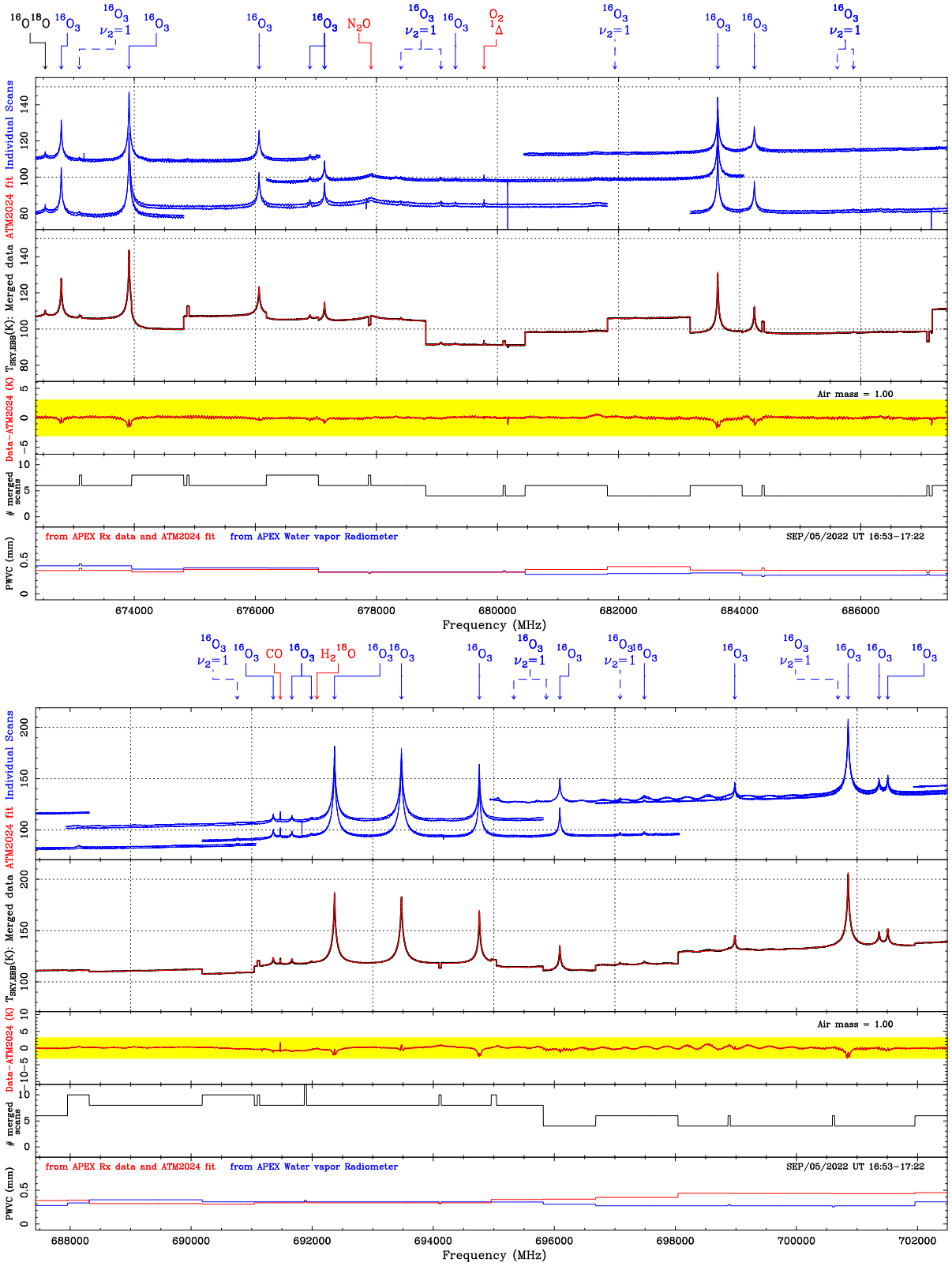

Figure 128: Zoom on Sept. 5^{rd} 2022 scan at air mass=1.0 taken with SEPIA660, and ATM2024 fit results (part 4).

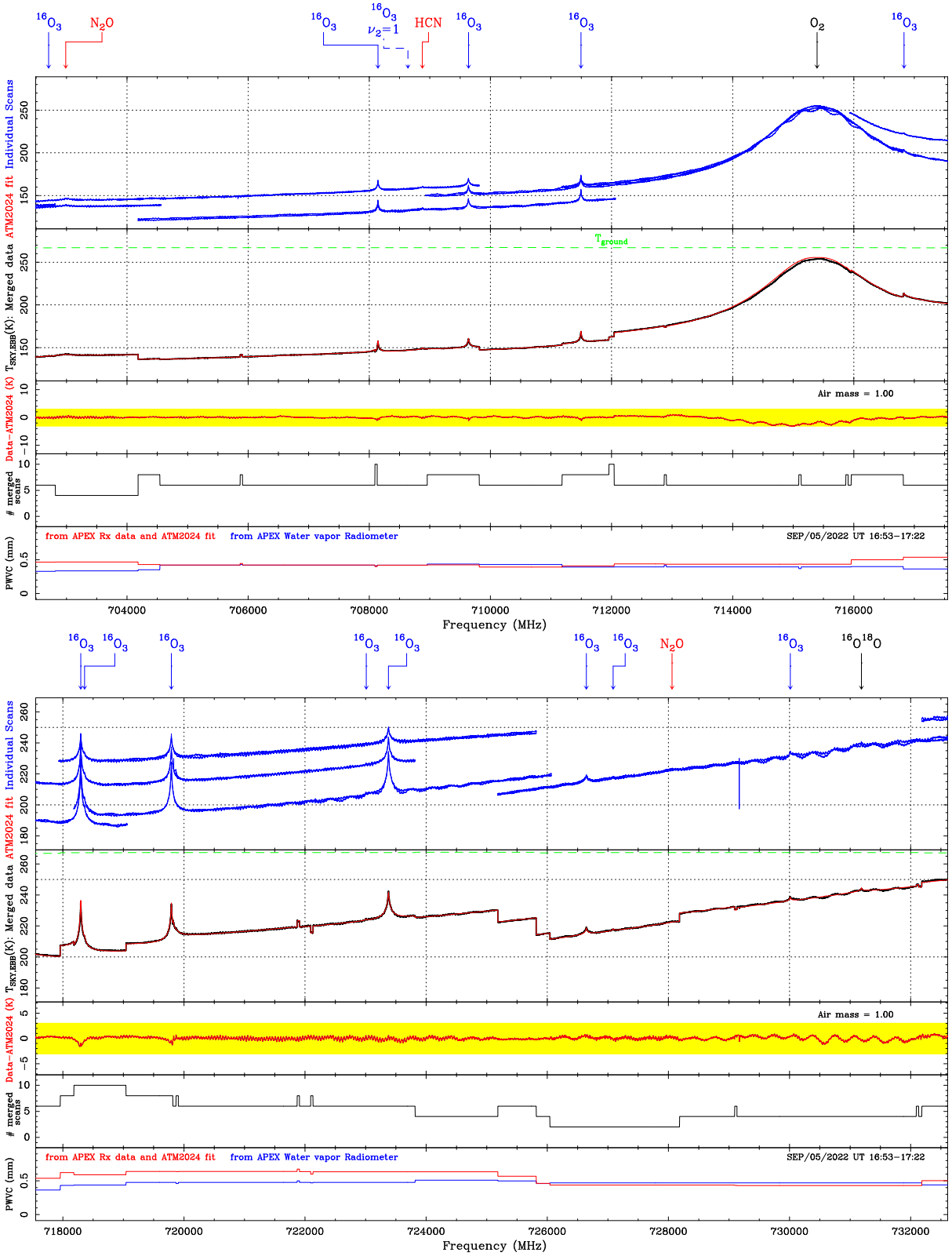

Figure 129: Zoom on Sept. 5^{rd} 2022 scan at air mass=1.0 taken with SEPIA660, and ATM2024 fit results (part 5).

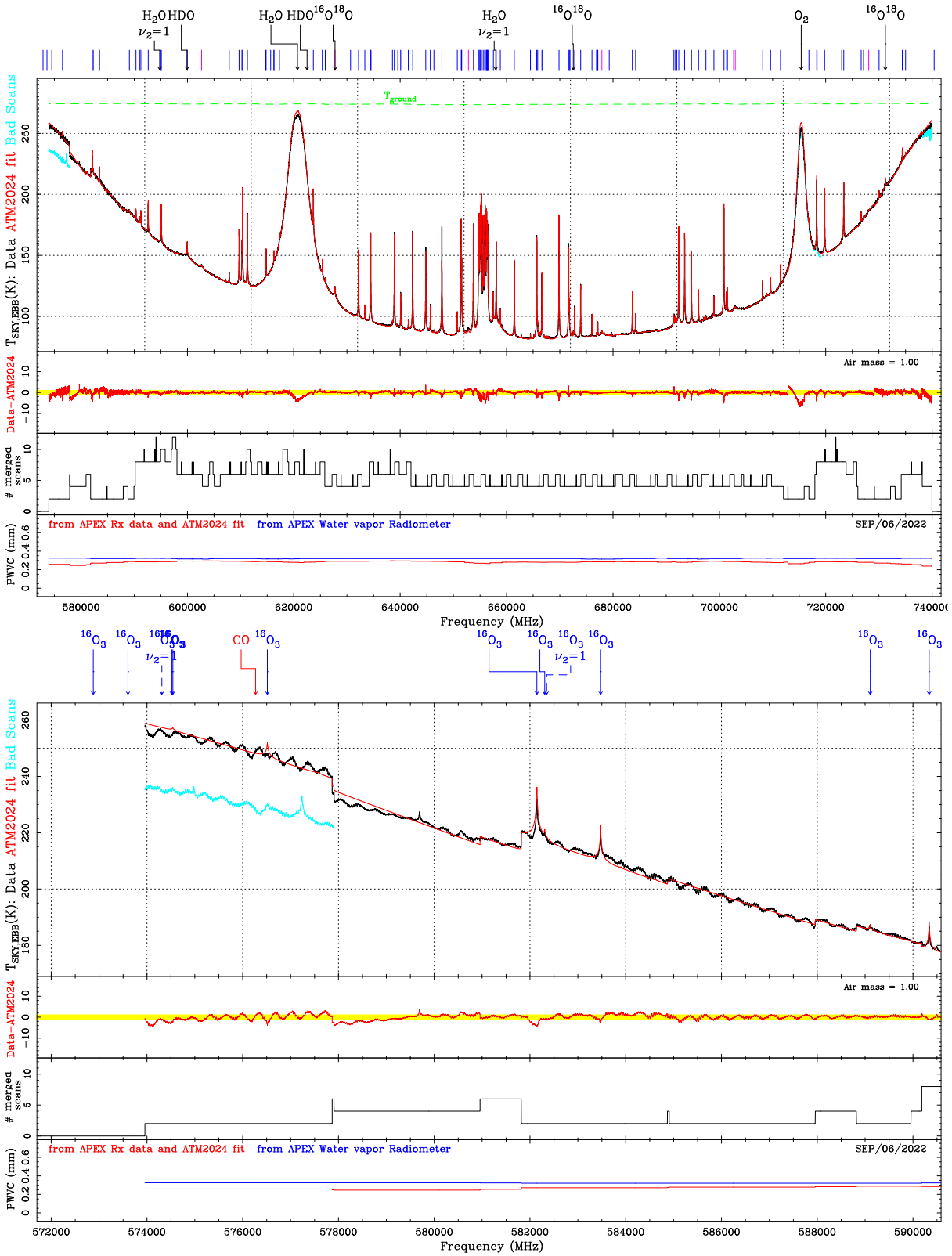

Figure 130: Sept. 6^{th} 2022 scan at air mass=1.0 taken with SEPIA660, and ATM2024 fit results (full and zoom part 1).

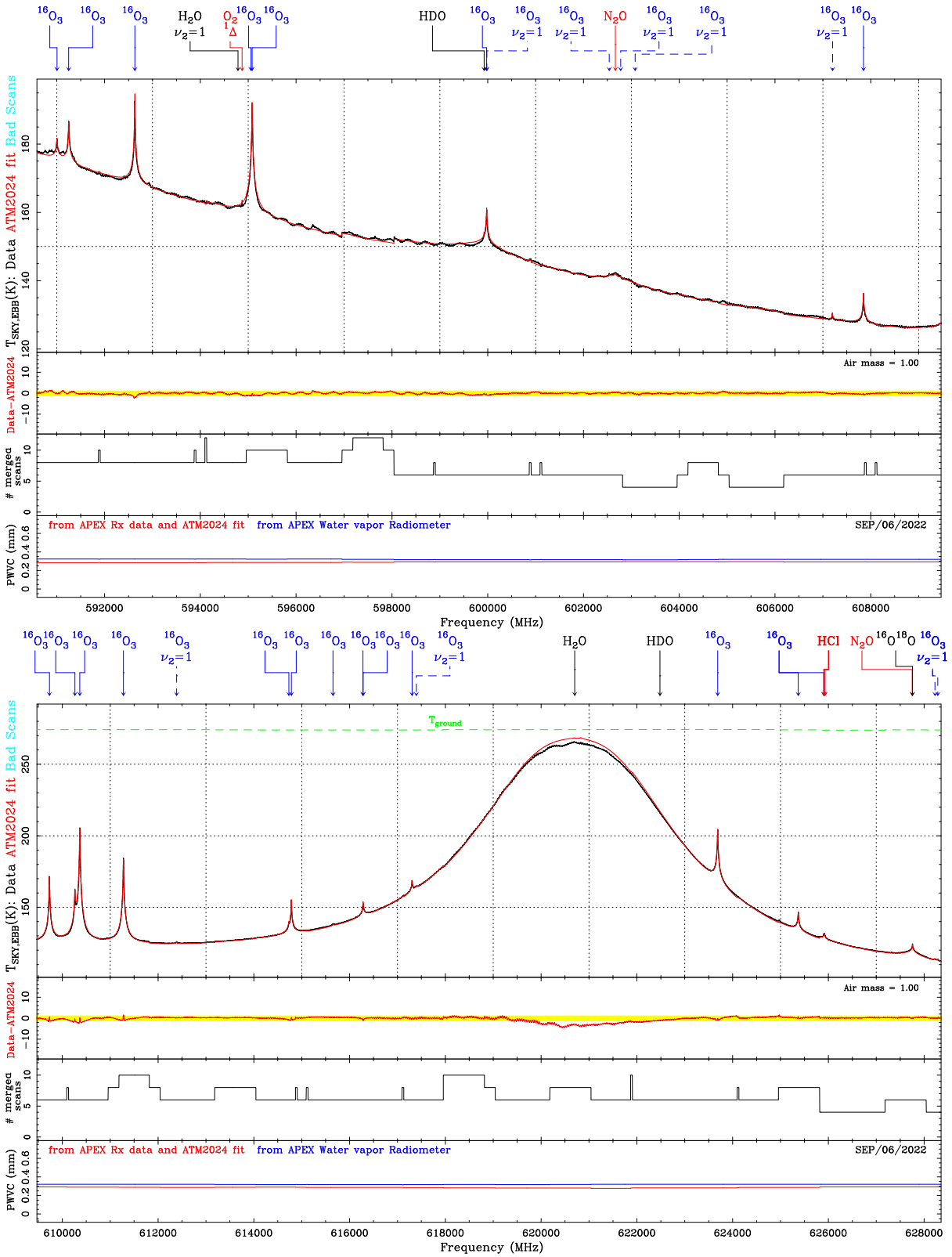

Figure 131: Zoom on Sept. 6^{th} 2022 scan at air mass=1.0 taken with SEPIA660, and ATM2024 fit results (parts 2 and 3).

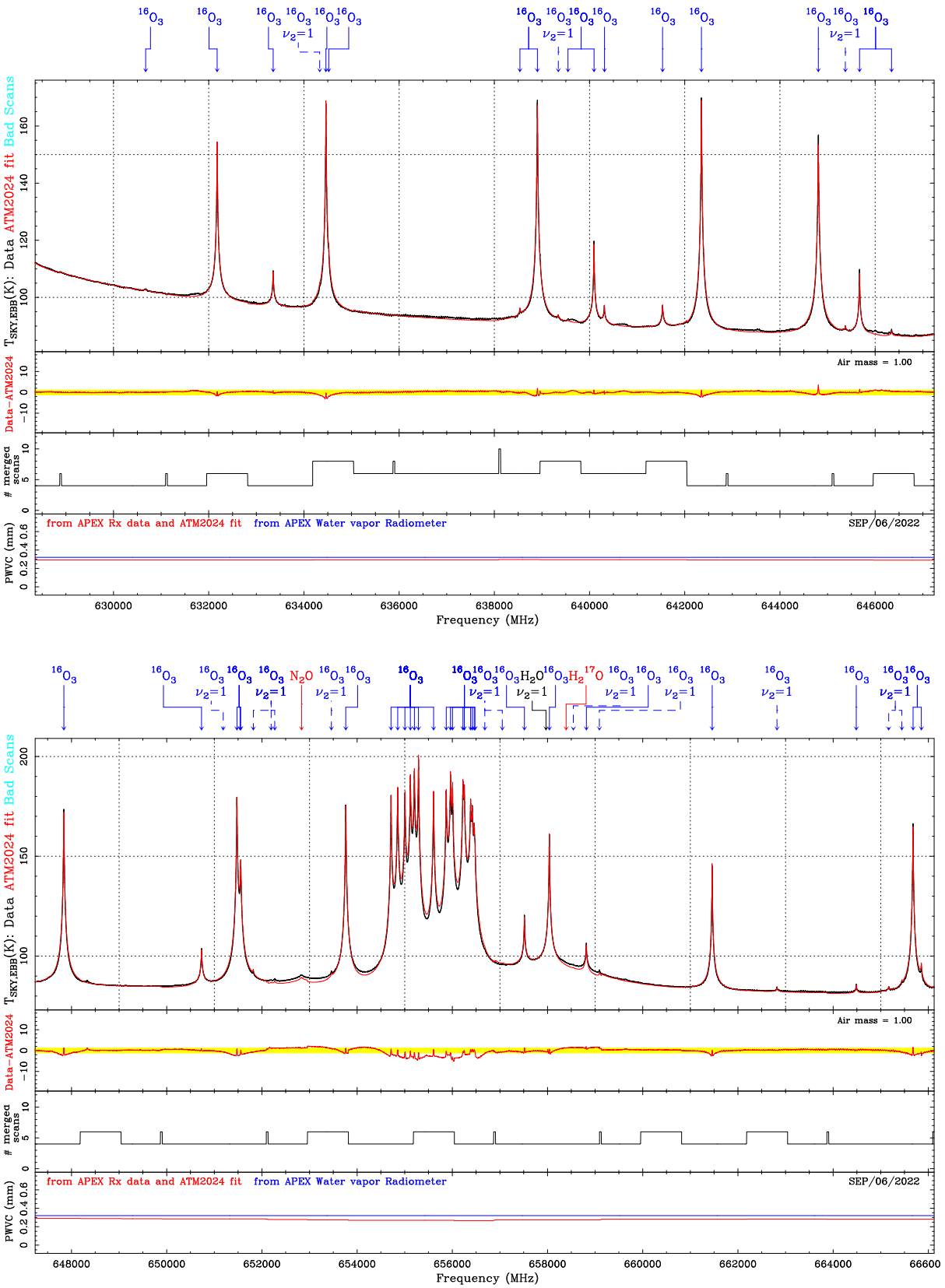

Figure 132: Zoom on Sept. 6^{th} 2022 scan at air mass=1.0 taken with SEPIA660, and ATM2024 fit results (parts 4 and 5).

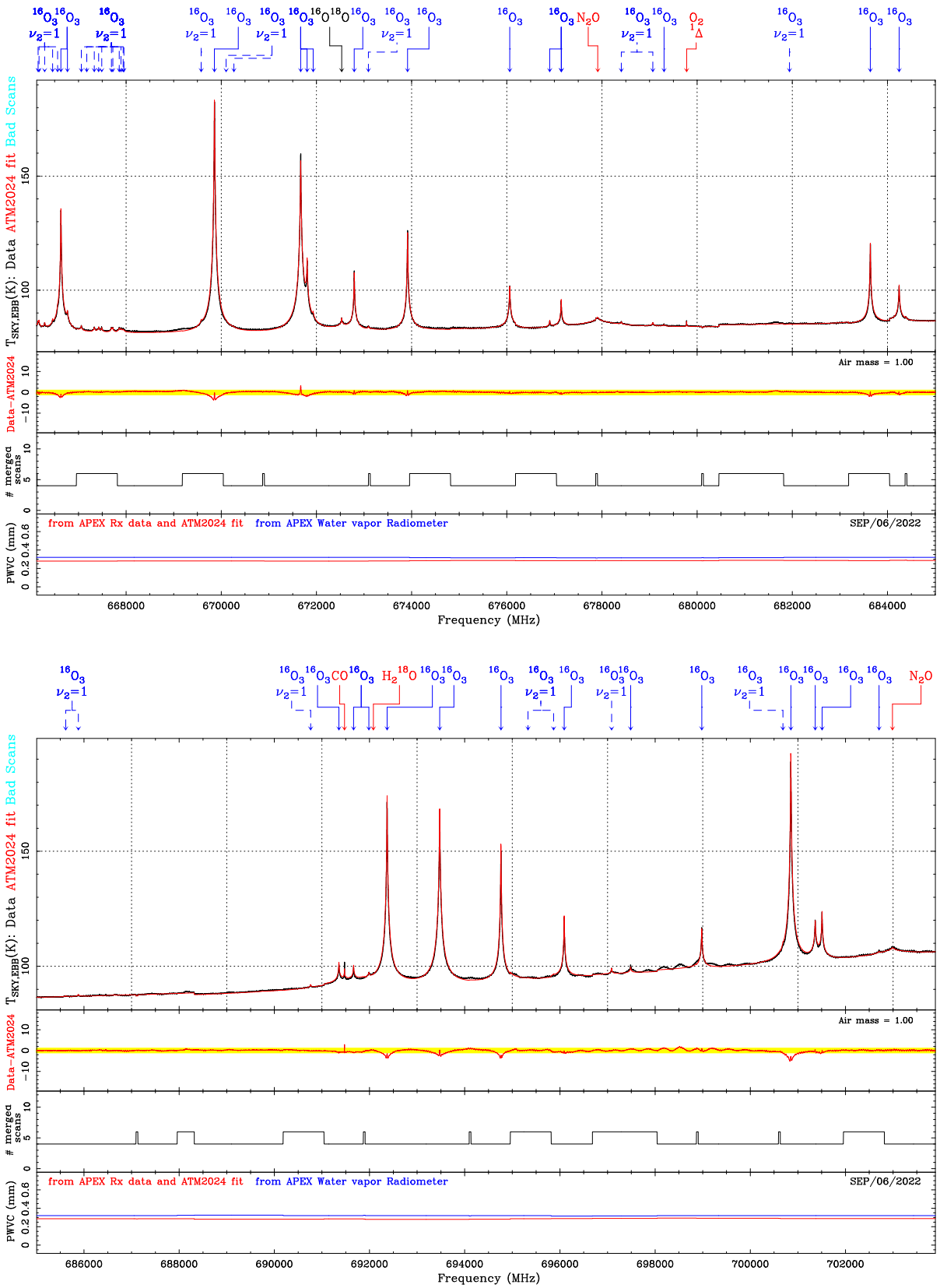

Figure 133: Zoom on Sept. 6^{th} 2022 scan at air mass=1.0 taken with SEPIA660, and ATM2024 fit results (parts 6 and 7).

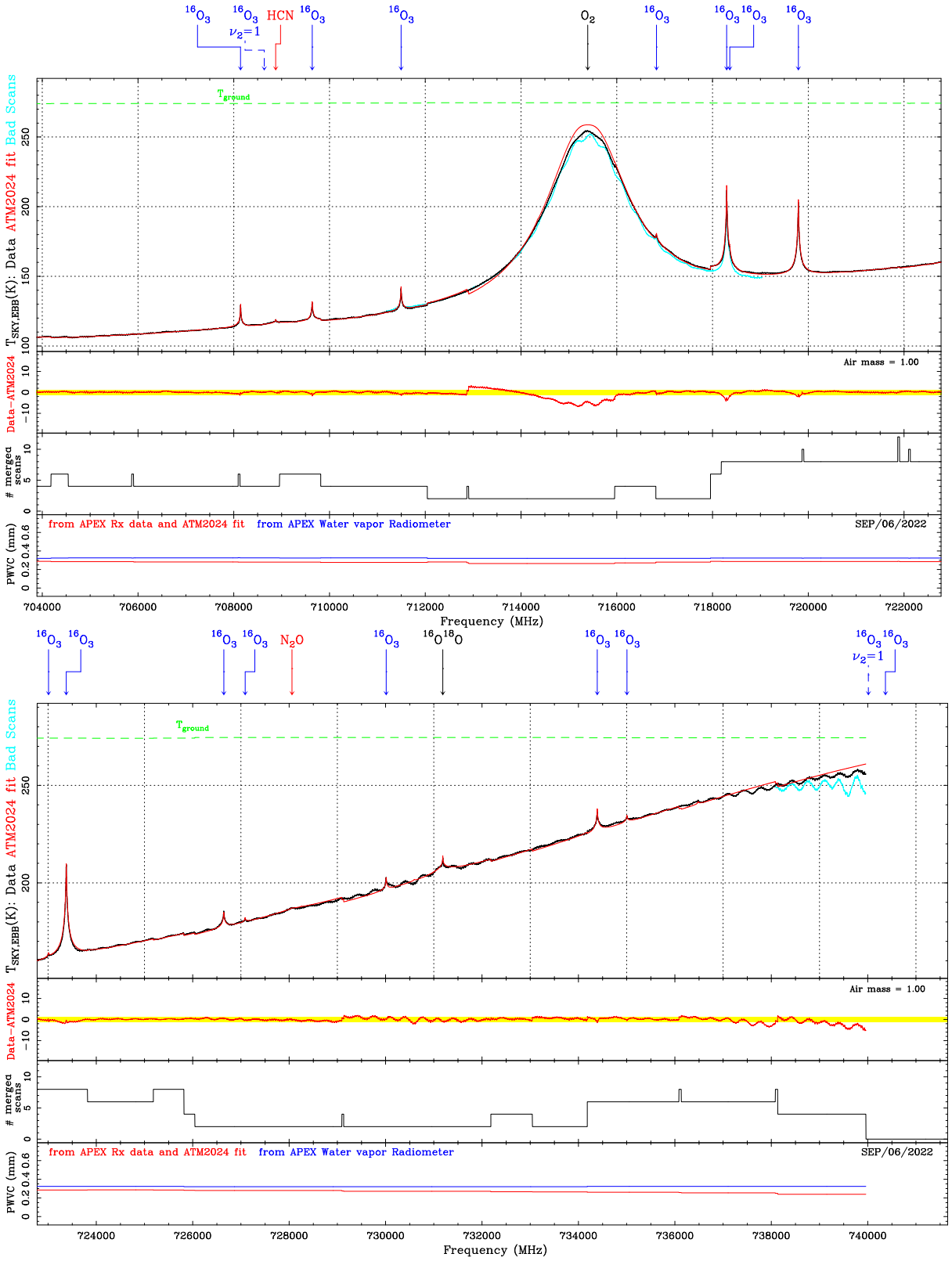

Figure 134: Zoom on Sept. 6^{th} 2022 scan at air mass=1.0 taken with SEPIA660, and ATM2024 fit results (parts 8 and 9).

Impact of the changes in the atmospheric model on the ALMA system temperature calibration

Justo Gonzalez

1. Introduction

This report describes the impact of the updates in the Atmospheric Transmission at Microwaves (ATM) model on the system temperature calibration performed by the ALMA Telescope Calibration Software (TelCal SW).

2. Definition of system temperature

In the first place, we have to consider the definition of system temperature, which is a measure of the overall noise of the system accounting for the receiver and sky contributions, converted to an equivalent temperature scale assuming that we can model the source and noise contributions with an equivalent Rayleigh-Jeans (RJ) temperature.

For an ideal antenna, ignoring spillover and efficiencies, the noise temperature (T_{noise}) is defined as the sum of the receiver temperature (T_{rx}) and sky temperature (T_{sky}), which in turn depends on the Rayleigh-Jeans equivalent physical temperature of the atmosphere averaged on the line of sight ($T_{atm} \cong 300K$), the cosmic microwave background (CMB) temperature ($T_{CMB} \cong 3K$), and the atmospheric opacity τ.

$$T_{noise} \cong T_{rx} + T_{sky} \text{ [1]}$$

$$T_{sky} = T_{atm}(1 - e^{-\tau}) + T_{CMB}e^{-\tau} \text{ [2]}$$

We can combine Equations [1] and [2] to obtain:

$$T_{noise} \cong T_{rx} + T_{atm}(1 - e^{-\tau}) + T_{CMB}e^{-\tau} \text{ [3]}$$

Now let's consider the signal from a source with an equivalent RJ temperature T_{source}, which would be attenuated to a signal of $S = T_{source}e^{-\tau}$ after passing through the atmosphere. The signal-to-noise ratio (SNR) would be given by:

$$SNR = \frac{Signal}{Noise} = \frac{T_{source}e^{-\tau}}{T_{noise}} = \frac{T_{source}}{T_{noise}e^{\tau}} = \frac{T_{source}}{T_{sys}} \text{ [4]}$$

As we can see, if we join the atmospheric attenuation term with the noise temperature in the denominator, we obtain a quantity that comprises the system noise and the source attenuation term. This quantity is what is defined as system temperature:

$$T_{sys} = T_{noise}e^{\tau} = T_{rx}e^{\tau} + T_{atm}(e^{\tau} - 1) + T_{CMB} \text{ [5]}$$

In what follows, we will study the various methods implemented in the ALMA Telescope Calibration Software (TelCal SW) to measure these quantities and how sensible they are to changes in the atmospheric model (ATM).

3. Methods to measure the system temperature

Now that we have established the basic definition for system temperature as a measure of the noise in the system, including the sky and receiver contributions, which is then combined with the atmospheric attenuation of the source signal, the next step is to determine how it is measured, which is key to understanding the role and impact of ATM in the system temperature calibration.

A commonality for all methods here presented is that the measurement of system temperatures is based on dual-load calibration. Assuming that we are in a linear regime, where the voltage measured V is proportional to the equivalent Rayleigh-Jeans temperature T, we can obtain the system gain G, which is assumed to be constant, with two voltage measurements V_1, V_2 of different signals with known temperatures T_1, T_2

$$V_1 = G(T_1 + T_{rx}) \text{ [6]}$$

$$V_2 = G(T_2 + T_{rx}) \text{ [7]}$$

Where for simplicity we are ignoring spillover and efficiencies. Now, since [6] and [7] define a system of two Equations with two variables G and T_{rx}, we can solve for the gain G and receiver temperature T_{rx}:

$$G = \frac{V_1 - V_2}{T_1 - T_2} \text{ [8]}$$

$$T_{rx} = V_1 \frac{T_1 - T_2}{V_1 - V_2} - T_1 \text{ [9]}$$

Once the gain G is calculated, we can obtain the noise temperature T_{noise} from the off source V_{sky} signal, as shown by Equation [11]:

$$V_{sky} = G\left(T_{rx} + T_{sky}\right) = GT_{noise} \text{ [10]}$$

$$T_{noise} = \frac{V_{sky}}{G} \text{ [11]}$$

However, for the system temperature, it is not enough to know the gain G and off source signal V_{sky}since the atmospheric opacity τ is also involved, as shown by Equation [12]:

$$T_{sys} = T_{noise} e^{\tau} = \frac{V_{sky}}{G} e^{\tau} \text{ [12]}$$

3.1 Classical method

The classical method to obtain the System Temperatures is based on a dual-load method to obtain the G term of Equation [12], whereas the atmospheric opacity τ is obtained directly from the atmospheric model (ATM).

3.2 Dual load Sky-Ambient

In this case the dual-load measurement is based on:

- An off-source measurement of the sky temperature T_{sky}, obtaining a signal V_{sky}
- A measurement using a load at the cabin ambient temperature of T_{amb} $300K$, placed in the receiver beam, obtaining a signal V_{amb}

In this case the G is given by Equation [13] and the corresponding system temperature by Equation [14].

$$G = \frac{V_{amb} - V_{sky}}{T_{amb} - T_{sky}} \text{ [13]}$$

$$T_{sys} = \frac{V_{sky}}{G} e^{\tau} = V_{sky} \left(\frac{T_{amb} - T_{sky}}{V_{amb} - V_{sky}} \right) e^{\tau} \text{ [14]}$$

We can further expand T_{sky} with Equation [2] to obtain a final expression for the system temperature

$$T_{sys} = [e^{\tau}(T_{amb} - T_{atm}) + T_{atm} - T_{CMB}] \left(\frac{V_{sky}}{V_{amb} - V_{sky}} \right) \text{ [15]}$$

As we can see this method depends significantly on the atmospheric model (ATM) via the atmospheric temperature T_{atm} and also via the opacity term e^{τ}.

3.3 Sky-Ambient-Hot

In this case the dual-load measurement is based on:

- A measurement using a load at the cabin ambient temperature of T_{amb} $300K$, placed in the receiver beam, obtaining a signal V_{amb}
- A measurement using a hot load at a temperature of T_{hot} $380K$, placed in the receiver beam, obtaining a signal V_{hot}

In this case the G is given by Equation [16] and the corresponding system temperature by Equation [17]:

$$G = \frac{V_{hot} - V_{amb}}{T_{hot} - T_{amb}} \text{ [16]}$$

$$T_{sys} = \frac{V_{sky}}{G} e^{\tau} = V_{sky} \left(\frac{T_{hot} - T_{amb}}{V_{hot} - V_{amb}} \right) e^{\tau} \text{ [17]}$$

As we can see this method still depends on the atmospheric model (ATM) via the opacity term e^{τ}, but we have removed the dependency on the atmospheric temperature T_{atm}.

3.4 Alpha method

As explained by R. Lucas, S. Corder in [1] the alpha method combines features of the dual load sky-ambient method (Section 3.1.1) and the dual load ambient-hot method (Section 3.1.2) to minimize the dependency on the atmospheric model, namely removing the opacity term e^{τ}, leaving only a dependency on the Rayleigh-Jeans equivalent physical temperature of the atmosphere averaged on the line of sight (T_{atm}).

This is done by resorting to the concept of a 'virtual load' at the same temperature as the atmosphere ($T_{load} = T_{atm} \cong 300K$), which would produce a signal V_{load}. In this setup, Equation [15] simplifies canceling the first term if we replace $T_{amb} = T_{atm}$ and $V_{amb} = V_{load}$, as shown by Equation [18]:

$$T_{sys} = [T_{atm} - T_{CMB}] \left(\frac{V_{sky}}{V_{load} - V_{sky}} \right) \text{ [18]}$$

On the other hand V_{load} can be calculated by assuming that the gain is constant over the range of atmospheric T_{atm}, ambient T_{amb}, and hot load T_{hot} temperatures as shown by Equation [19]:

$$G = \frac{V_{amb} - V_{load}}{T_{amb} - T_{atm}} = \frac{V_{hot} - V_{amb}}{T_{hot} - T_{amb}} \text{ [19]}$$

$$V_{load} = V_{amb} - G(T_{amb} - T_{load}) = \left(\frac{T_{atm} - T_{amb}}{T_{hot} - T_{amb}} \right) V_{hot} + \left(1 - \frac{T_{atm} - T_{amb}}{T_{hot} - T_{amb}} \right) V_{amb} \text{ [19]}$$

As we can see, a term with the ratio $T_{atm} - T_{amb}$ over $T_{hot} - T_{amb}$ appears, this is the so-called 'alpha factor' which gives name to this method:

$$\alpha = \frac{T_{atm} - T_{amb}}{T_{hot} - T_{amb}} \text{ [20]}$$

$$V_{load} = \alpha V_{hot} + (1 - \alpha) V_{amb} \text{ [21]}$$

Upon inspection of Equations [18], [20], and [21], we see that we have removed the dependency on the opacity term e^{τ} but introduced a dependency on the Raileigh-Jeans equivalent physical temperature of the atmosphere averaged on the line of sight (T_{atm}).

3.5 Summary of methods to measure the system temperature

In summary, we have seen in Sections 3.1.2 and 3.2 that the dependency on the atmospheric model cannot be completely removed. Although the alpha method manages to remove the dependency on the opacity term e^{τ} by adding an extra measurement based on the hot load, it still has a dependency on the Raileigh-Jeans equivalent physical temperature of the atmosphere averaged on the line of sight (T_{atm}).

Although both methods have a dependency on the atmospheric model, the current default used by ALMA is the alpha method to minimize the dependency on the atmospheric model and effectively measure the opacity term e^{τ}. However, the traditional method is still used for Band 1, due to the large beam size which couples poorly to the hot load.

Name	tsysmode	trecmode	Physical magnitudes directly measured / used	Magnitude calculated with atmospheric model	Method used for Bands
Traditional	'WVR'	'SA'	$T_{amb}, V_{amb}, V_{sky}$	e^{τ},T_{atm}	1
Alpha	'ALPHA'	'AH'	$T_{amb}, T_{hot}, V_{amb}, V_{hot}, V_{sky}$	T_{atm}	2-10

4. Test strategy

In order to assess the impact of the changes introduced in ATM and also evaluate how good AMT is in comparison with the observed atmospheric properties, we consider the following test comparison strategies.

4.1 System temperature comparison: new ATM 95km vs old ATM 48km

In this test, we directly compare the system temperatures obtained with the old ATM model from 2019, using the default alpha method, with the system temperatures obtained with the new ATM model from 2024, which incorporates the updated abundance profiles as shown in Juan Ramon Pardo et al. [2]. With test, we can see the first-hand direct impact of the changes in ATM on the system temperatures.

As we will see, the differences are quite small, but this is actually expected since the O3 abundance profile has been only slightly changed to fit the APEX Sepia 660 spectra, as shown in Juan Ramon Pardo et al. [2].

Also, notice that with the alpha method, we expect small changes in the system temperature spectra because it resorts to a hot load measurement to solve for the atmospheric opacity term (e^{τ}), leaving only a dependency on the Rayleigh-Jeans equivalent physical temperature of the atmosphere averaged on the line of sight (T_{atm}), which has a relatively narrow range even at the peak of strong atmospheric lines.

Additionally, we also test the impact of changing the maximum altitude used by ATM from 48km (the current default) to 95 km. With this test, we better capture the changes in the contribution of low-pressure ozone, which directly affect the peak intensity in the center of the ozone lines.

4.2 Impact on the pipeline calibration

In this test, we directly compare the corrected bandpass spectrum generated by the ALMA calibration pipeline after applying the system temperature calibration. In one case, we use the old ATM model from 2019 with a maximum altitude of 48 km, and in the other, we use the new ATM model with a maximum altitude of 95 km. With this test, we can see the final impact of the changes in ATM combined with increasing the maximum altitude used by ATM to 95km.

4.3 System temperature comparison: Alpha method vs traditional

In this test, we use in both cases the new ATM model from 2024 and a maximum altitude of 95km, but compare the method used to obtain the system temperatures, using in one case the alpha method which resorts to a hot load measurement to obtain the opacity term, with the traditional method based on an ambient-sky dual load measurement which resorts to ATM to provide the opacity term. Therefore with this test we can evaluate how good ATM is in terms of predicting opacity.

4.4 Receiver temperature comparison: ambient / hot load vs ambient / sky

In this test, we use in both cases the new ATM model from 2024 and a maximum altitude of 95km, but compare the methods used to obtain the receiver temperatures, using in one case the ambient-hot loads, which do not require any information from ATM or knowledge of forward efficiency, and in the other case the sky-ambient loads, which require the sky temperature from ATM (T_{sky} shown in Equation 2) and an assumed forward efficiency (set to a constant value of 98% in TelCal).

A known disadvantage of measuring receiver temperature using ALMA's ambient and hot loads, as opposed to a cryogenic load as used in a lab, is that it is very sensitive to gain compression as we will see in the results. Nevertheless, with this test, we can evaluate how good ATM is in terms of providing a stable reference for detected HW issues.

5. Test data set selection

5.1 Science observations

We are especially interested in spectral regions affected by strong ozone lines. The reason for this is that the ozone molecule is asymmetric and has a dipolar moment, resulting in a plethora of lines across the spectral range covered by the ALMA bands. The first clearly visible ozone lines appear in band 6 and keep increasing in strength up to bands 8, 9 and 10.

However, something to bear in mind regarding the impact of system temperature calibration in science observations is that the baseline correlator (BLC) suffers from a lack of quantization correction in the autocorrelation spectra for frequency division mode (FDM); therefore, the atmospheric calibration scans have to be carried out always at lower frequency resolution in time division mode (TDM), even if the science targets and bandpass/phase/amplitude calibrators are observed in high frequency resolution using FDM mode. This results in spectral residuals that are not caused by issues in the atmospheric model but just by the different resolutions used for science and atmospheric calibration scans, as pointed out by Todd Hunter et al. [1].

On the other hand, the Atacama Compact Array (ACA) correlator provides full quantization correction for any spectral resolution; therefore, the atmospheric calibration scans can be carried out at the same resolution as the rest of the science and calibration scans, and no systematic residuals are to be expected after applying the system temperature calibration. For these reasons, we decided to resort to 7-meter dish observations using the Atacama Compact Array (ACA) correlator to test the impact of the system temperature calibration on science observations.

Therefore, we select 7-meter ACA correlator observations with atmospheric calibration scans carried out at the same resolution as the bandpass calibration and science scans. And to cover both ends of the ALMA spectral range, we selected datasets in Band 6 (224.04-226.04 GHz with a strong ozone line at 239.094 GHz) and Band 9 (693.55-695.55 GHz with two strong ozone lines at 692.37 GHz and 693.47 GHz).

5.2 Engineering time data sets

Aside from science observations in high spectral resolution, we can also resort to lower spectral resolution data sets, covering a wide frequency range. For this, we can resort to spectral checks performed during engineering time that cover the entire band.

Following the bands used for science observations, we also select bands 6 and 9 for spectral checks. Moreover, we are also interested in exploring band 9 because it covers a similar range as the APEX SEPIA 660 receiver used in the first study by Juan Ramon Pardo et al. [2]. Therefore, we can do a cross-comparison of the residuals.

Additionally, we are interested in spectral checks from band 2, since this is a new band being commissioned, and we can evaluate how good ATM is in terms of providing a stable reference for detected HW issues.

5.3 Selected data sets

In summary, given all these criteria, we collected the following datasets for testing the impact of the atmospheric model:

Dataset uid	Type of observation	Band	Frequency range GHz	Channel width MHz	PWV mm
uid://A002/Xf0fd41/X12df	Science (NGC 7592E)	6	224.04-226.04 O3 @ 239.094	0.97656	0.44
uid://A002/Xdc946c/Xcc56	Science (NGC 253)	9	693.55-695.55 O3 @ 692.37 O3 @ 693.47	3.90	0.16-0.17
uid://A002/Xae17cd/X259a	Engineering (spectral check)	6	211-275	15.625	0.69-0.65
uid://A002/X81cc73/X1e0	Engineering (spectral check)	9	602-720	15.625	0.47-0.50
uid://A002/X10b5aab/X26b	Engineering (spectral check)	2	67.02-84.02	15.625	0.69

6. Test results

6.1 Band 6 science observation

6.2 System temperature comparison: new ATM vs old ATM

The system temperature spectra are shown in **Figure 1** where we see that there is very little difference between both versions and the system temperature spectra almost completely overlaps.

The percentual difference is shown in **Figure 2**, where we see that the difference barely reaches 0.006%. Moreover, if we increase the maximum altitude used by the new ATM model from 2024 up to 95 km, the difference only increases to 0.6% as we see in **Figure 3**.

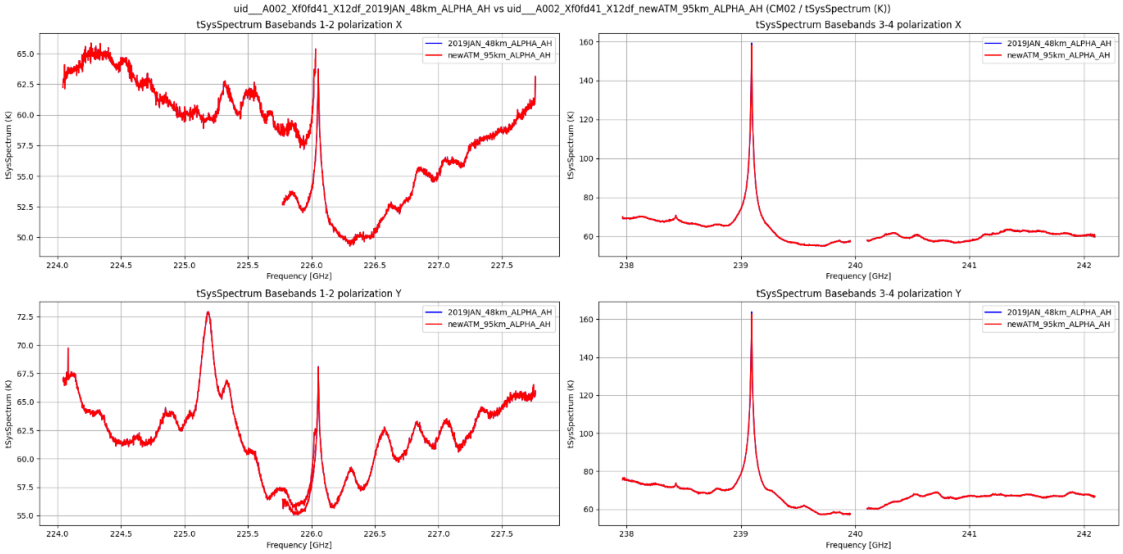

Figure 1 System temperature spectrum corresponding to the bandpass target of the Band 6 science observation. Blue corresponds to the ATM model from 2019 using a maximum altitude of 48 km, and red to the current model for 2024 after updating the abundance profiles and using a maximum altitude of 95 km. Top and bottom rows are polarisations X and Y, respectively. We see that both models are almost exactly coincident, to the point that they completely overlap, and only the 2024 model is visible.

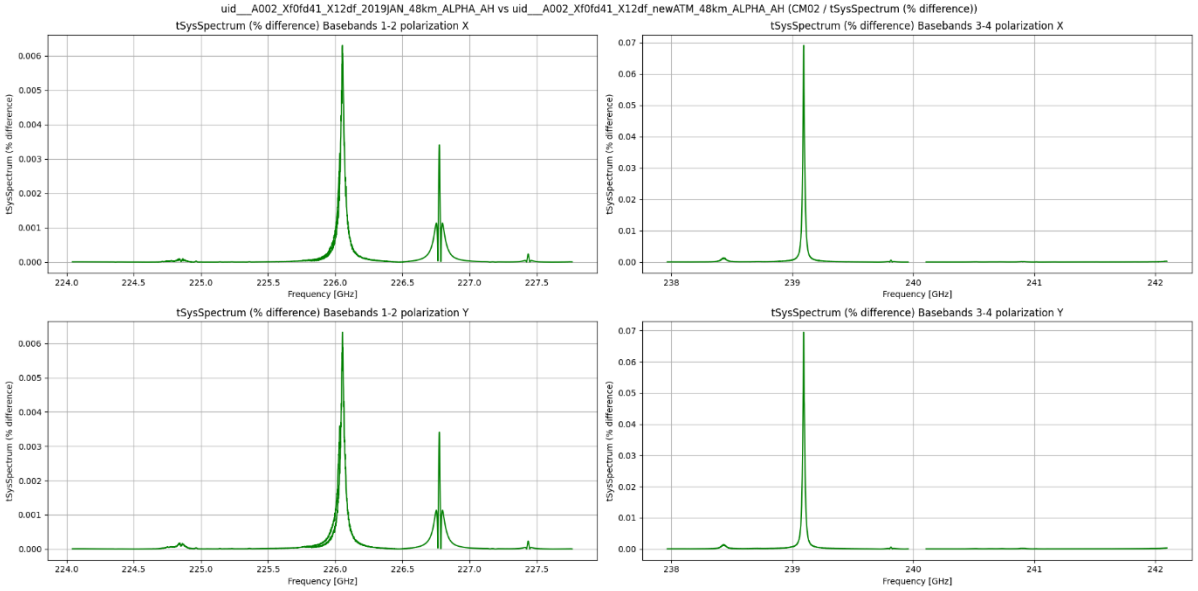

Figure 2 Percentage difference in the system temperature spectrum corresponding to the bandpass target of the Band 6 science observation comparing the ATM model from 2019 using a maximum altitude of 48 km with the current model for 2024 after updating the abundance profiles and using a maximum altitude of 48 km. Top and bottom rows are polarisations X and Y, respectively. We see that the maximum difference is almost negligible (0.006%).

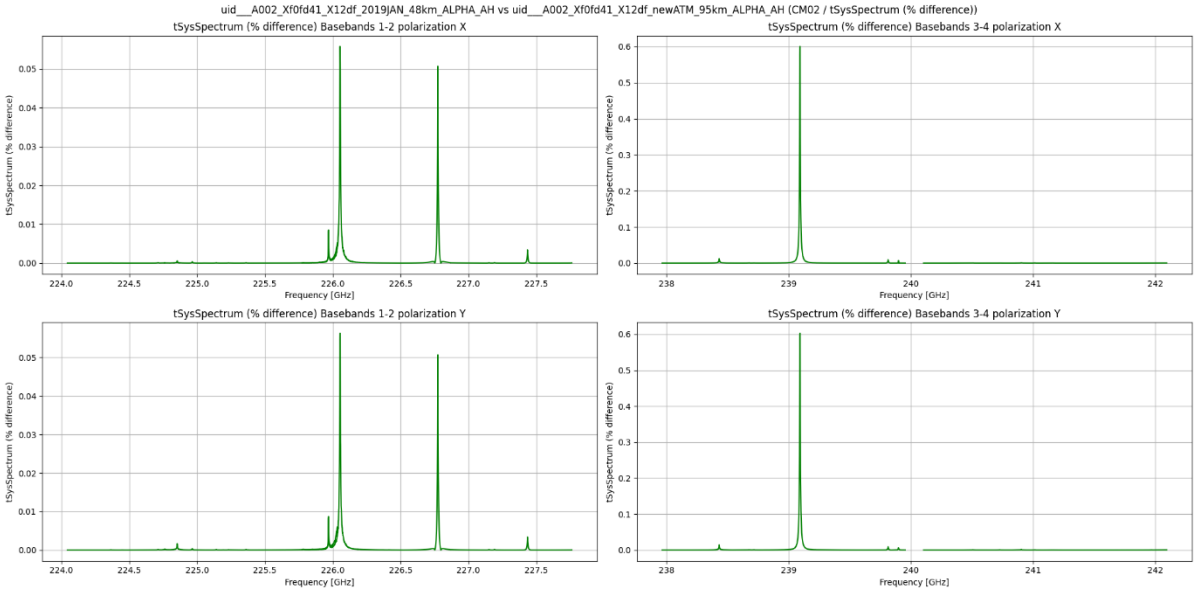

Figure 3 Percentage difference in the system temperature spectrum corresponding to the bandpass target of the Band 6 science observation comparing the ATM model from 2019 using a maximum altitude of 48 km with the current model for 2024 after updating the abundance profiles and using a maximum altitude of 95 km. Top and bottom rows are polarisations X and Y, respectively. We see that the maximum difference increases when changing the maximum altitude from 48km to 95km, but still, it is quite small (0.6% max).

6.3 Impact on the pipeline calibration

Figure 4 shows that there is also almost no difference in the corrected bandpass spectrum using system temperatures generated by the old ATM model from 2019 with a maximum altitude of 48km, or by new ATM model from 2024 using a maximum altitude of 95km.

Actually we see in both cases that the O3 line 239.094 GHz is completely corrected and what remains is just some noise which is expected given the lower transmission associated with atmospheric lines.

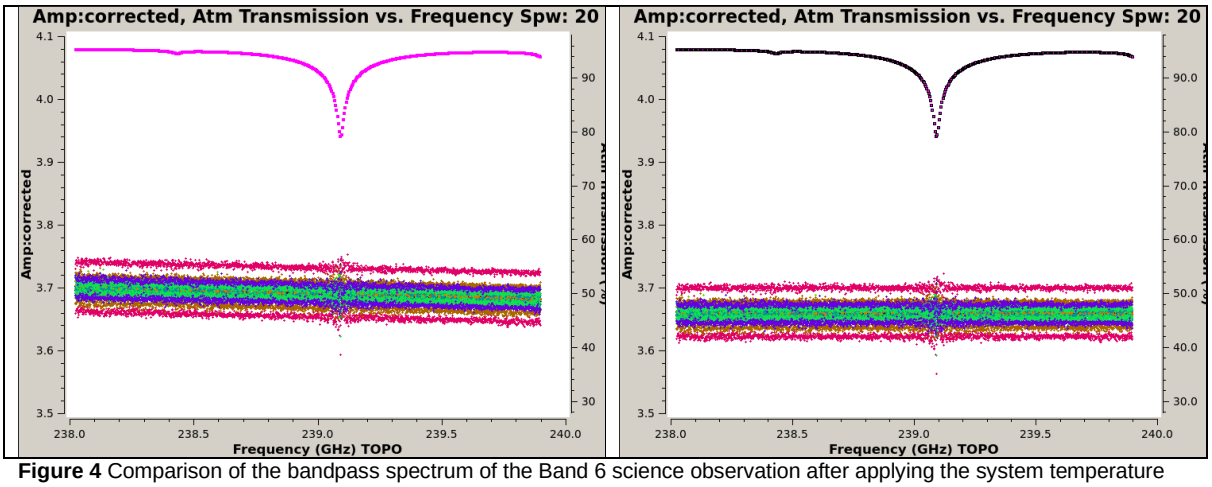

Figure 4 Comparison of the bandpass spectrum of the Band 6 science observation after applying the system temperature calibration. Left corresponds to the ATM model from 2019 using a maximum altitude of 48 km, and right corresponds to the current model for 2024 after updating the abundance profiles and using a maximum altitude of 95 km. We see that both are quite similar and do not show a systematic residual (dip) at the 239.094 GHz Ozone line, and what remains is just some scatter corresponding to the extra noise associated with lower transmission. Additionally the baseline slope seems to have change, but this is most likely associated with other changes in the ALMA calibration pipeline.

6.4 System temperature comparison: Alpha method vs traditional

The system temperature spectra for both cases is shown in **Figure 5** where we see that there is very little difference between both methods and the system temperature spectra almost completely overlaps.

We can then obtain the percentual difference between both methods, using 4 combinations: new / old ATM model, and a maximum altitude of 48km or 95km. The results are shown in **Figure 6**, where we see that both methods already agree to a very good degree using the old ATM model and a maximum altitude of 48km and only a residual of < 2% appears in the centre of the O3 line at 239.094 GHz. This residual is progressively reduced when using a maximum altitude of 95 km to 0.6% and finally disappears when using the new ATM model, where we see that the maximum difference between the 2 methods is reduced to 0.6% at the edge of the band.

These results show that ATM is actually quite good and produces reliable estimates of the opacity term e^{τ}in comparison with observations based on the alpha method.

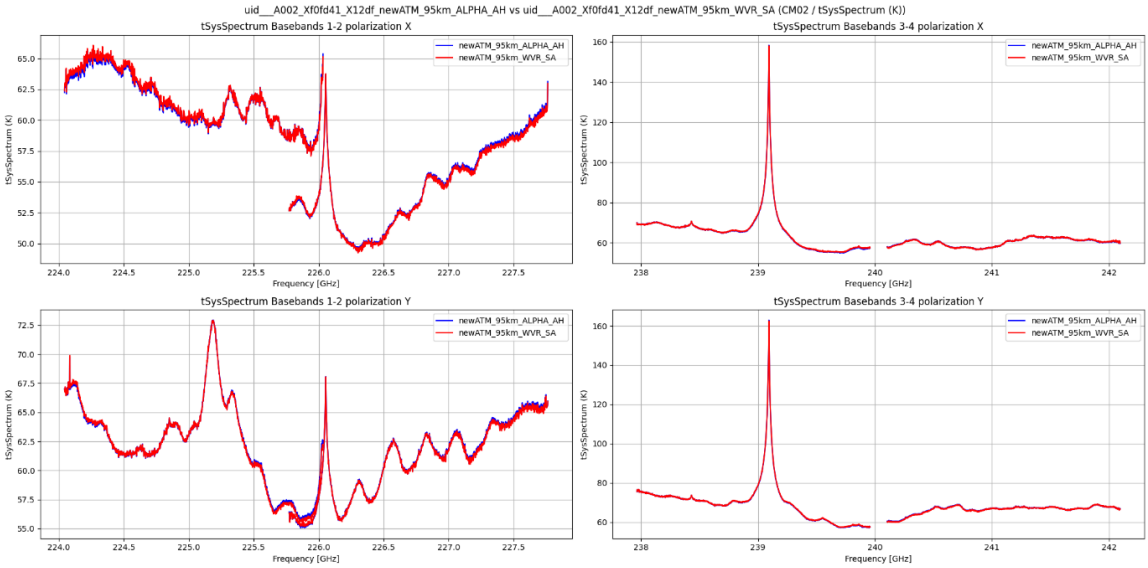

Figure 5 System temperature spectrum corresponding to the bandpass target of the Band 6 science observation using the current ATM model for 2024 and a maximum altitude of 95km. Blue corresponds to the ALPHA method resorting to a hot load measurement to obtain the opacity term, and blue to the traditional method based on an ambient-sky dual load measurement and resorting to ATM to obtain the opacity term. Top and bottom rows are polarisations X and Y, respectively.
We see that both models are quite similar, and only a slight difference is visible in the basebands 1–2.

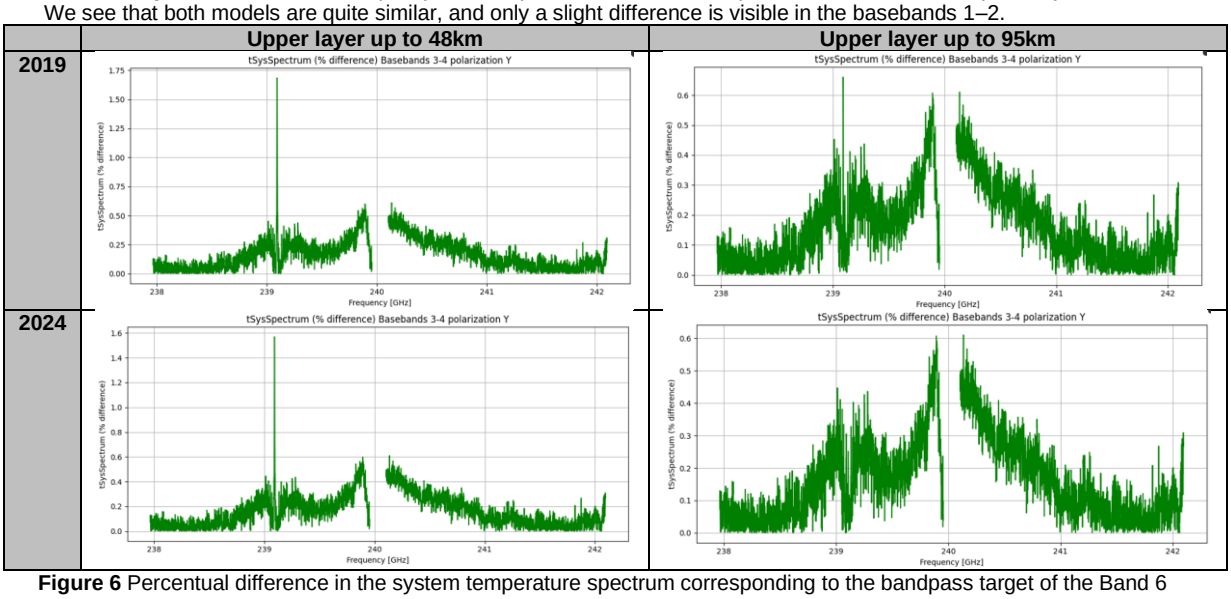

Figure 6 Percentual difference in the system temperature spectrum corresponding to the bandpass target of the Band 6 science observation comparing the ALPHA method resorting to a hot load measurement to obtain the opacity term versus the traditional method based on an ambient-sky dual load measurement and resorting to ATM to obtain the opacity term. We see that there is a 1.75% residual corresponding to the centre of the 239.094 GHz Ozone line using the ATM model from 2019 and a maximum altitude of 48km (top left panel). This residual is reduced only to 1.6% when using the current model for 2024 after updating the abundance profiles (bottom left panel). However, when using a maximum altitude of 95 km, it is reduced to 0.7% even using the ATM model from 2019 (top right panel) and finally disappears when using the current model for 2024 and also changing the maximum altitude to 95km (bottom right panel).

6.5 Receiver temperature comparison: ambient / hot load vs ambient / sky

We compare the absolute receiver temperatures obtained with both methods using four combinations: a new / old ATM model and a maximum altitude of 48km / 95km. The results are shown in **Figure 7**. We see that both methods deliver a receiver temperature with a similar trend but a bit of offset in between; however, the receiver temperatures obtained with the old ATM model and a maximum altitude of 48km present a spike of ~20K in the centre of the O3 line at 239.094 GHz. This spike is progressively reduced when using a maximum altitude of 95 km to ~7K and finally almost disappears when using the new ATM model.

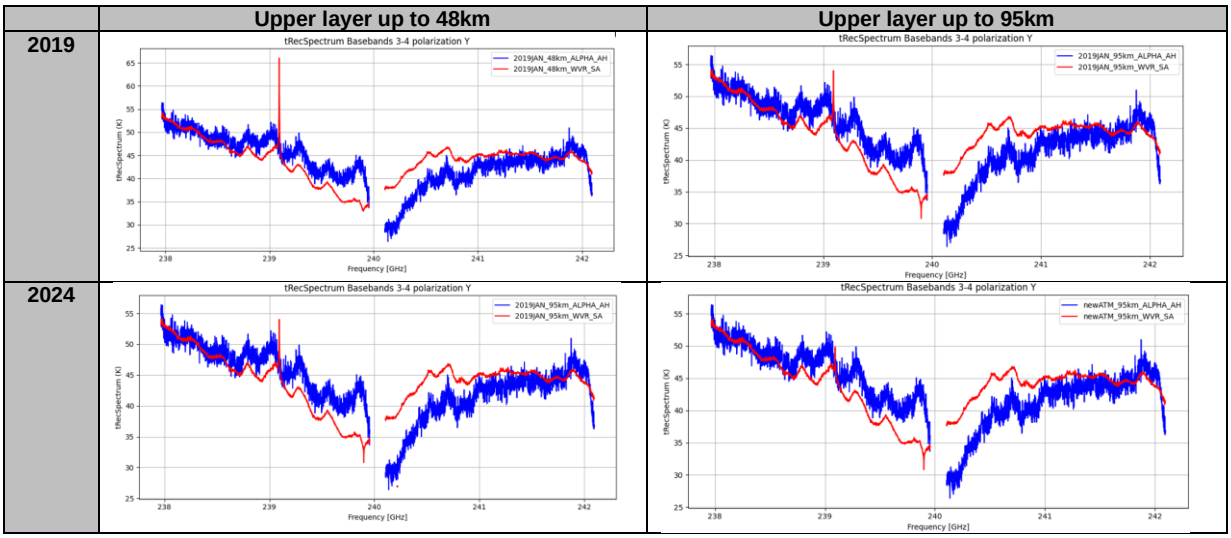

Figure 7 Receiver temperature spectrum of the Band 6 science observation comparing the ambient-hot load measurement (in blue) with the ambient-sky measurement (in red). Top and bottom rows are polarisations X and Y, respectively. We see that there is a spike of (~20K) corresponding to the centre of the 239.094 GHz Ozone line in the receiver temperatures obtained with the ambient-hot load measurement using the ATM model from 2019 and a maximum altitude of 48km (top left panel). This spike is reduced to ~7K when using the current model for 2024 after updating the abundance profiles (bottom left panel). Also, when using a maximum altitude of 95 km, it is reduced to 7 K even using the ATM model from 2019 (top right panel), and finally, it is reduced to ~3 K when using the current model for 2024 and also changing the maximum altitude to 95km (bottom right panel).

Apart from the spike associated with the O3 line at 239.094 GHz, we notice that the discrepancy between the two methods increases towards the inner edge of the basebands but does not seem to be a monotonic function of the frequency since the lower frequency and higher frequency edges properly match. Therefore, it looks likely a HW issue (non-linearity that is a function of frequency) needs to be investigated, although the receiver temperatures calculated with the sky-ambient loads could incorporate better modelling of the forward efficiency (sky coupling) rather than a constant 98%.

6.6 Band 9 science observation

6.7 System temperature comparison: new ATM vs old ATM

The system temperature spectra are shown in **Figure 8**, where we see that there is very little difference between both versions and the system temperature spectra almost completely overlaps.

The percentual difference is shown in **Figure 9**, where we see that the difference is small and reaches a maximum of 1%. However, as opposed to the Band 6 case, if we increase the maximum altitude used by the new ATM model from 2024 up to 95 km, the difference increases up to 4-6% at the peak of the strongest lines as we see in **Figure 10**.

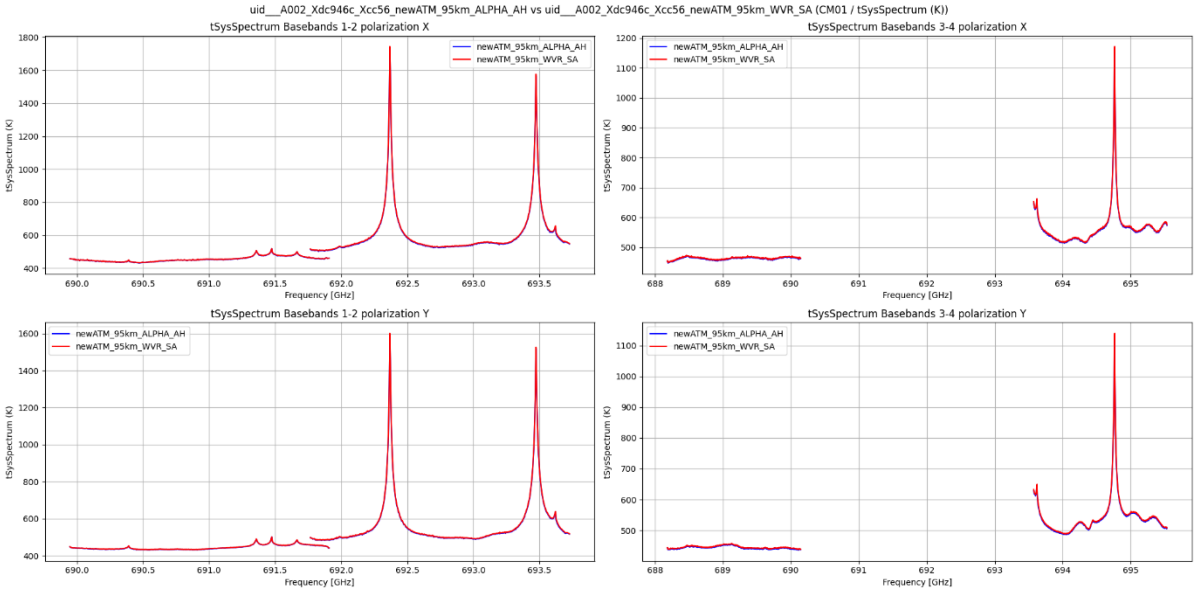

Figure 8 System temperature spectrum corresponding to the bandpass target of the Band 9 science observation. Blue corresponds to the ATM model from 2019 using a maximum altitude of 48 km, and red to the current model for 2024 after updating the abundance profiles and using a maximum altitude of 95 km. Top and bottom rows are polarisations X and Y, respectively. We see that both models are almost exactly coincident, to the point that they completely overlap, and only the 2024 model is visible.

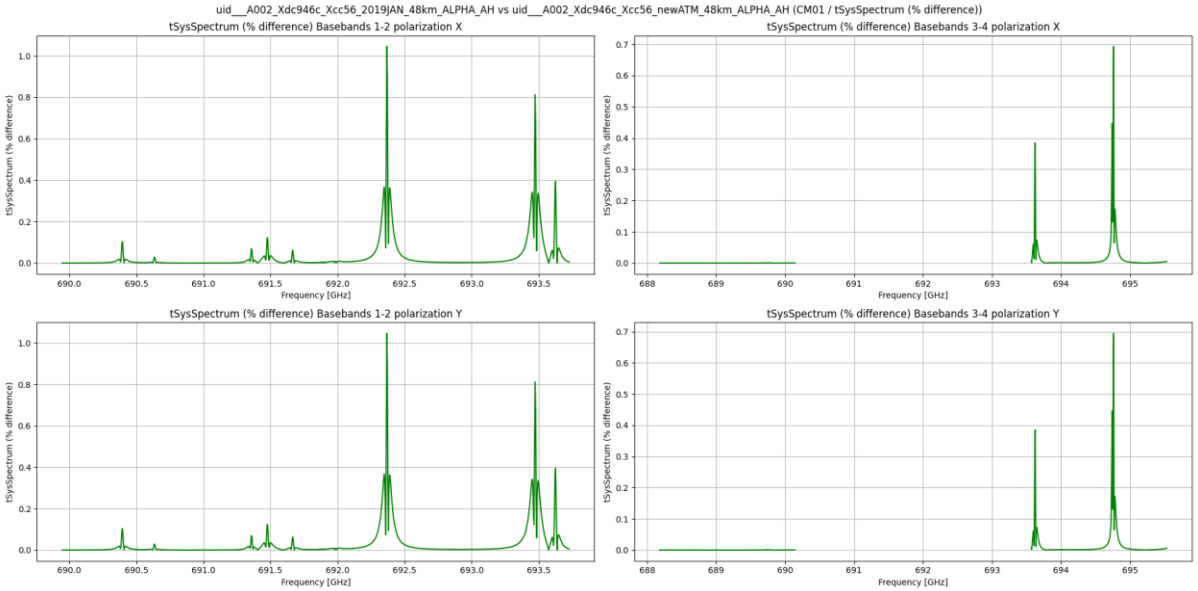

Figure 9 Percentage difference in the system temperature spectrum corresponding to the bandpass target of the Band 9 science observation comparing the ATM model from 2019 using a maximum altitude of 48 km with the current model for 2024 after updating the abundance profiles and using a maximum altitude of 48 km. Top and bottom rows are polarisations X and Y, respectively. We see that the maximum difference is still small (1%).

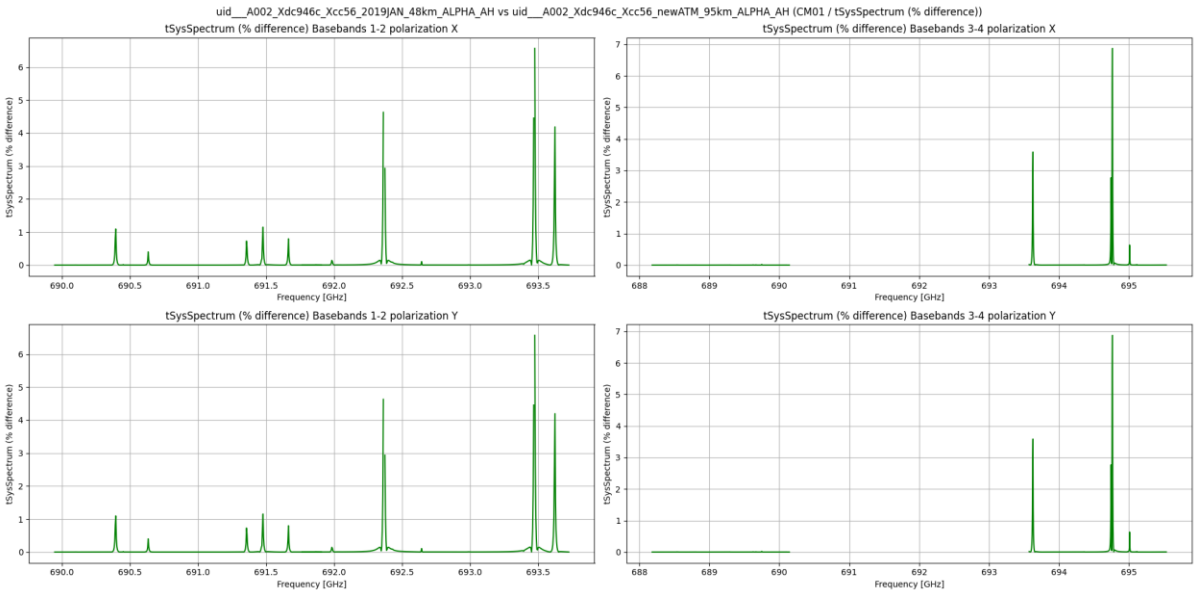

Figure 10 Percentage difference in the system temperature spectrum corresponding to the bandpass target of the Band 9 science observation comparing the ATM model from 2019 using a maximum altitude of 48 km with the current model for 2024 after updating the abundance profiles and using a maximum altitude of 95 km. Top and bottom rows are polarisations X and Y, respectively. We see that the maximum difference increases significantly when changing the maximum altitude from 48km to 95km, but still, and reaches 4-6 % at the peak of the strongest lines.

6.8 Impact on the pipeline calibration

Figure 11 shows that there also for the case of band 9 there is also almost no difference in the corrected bandpass spectrum using system temperatures generated by the old ATM model from 2019 with a maximum altitude of 48km, or by new ATM model from 2024 using a maximum altitude of 95km. Actually we see in both cases that the O3 lines 692.37 GHz and 693.47 GHz are completely corrected and what remains is just some noise which is expected given the lower transmission associated with atmospheric lines.

This result is less expected that the case of Band 6, since the change in system temperatures can be up to 4-6% different using the new ATM model from 2024 and a maximum altitude of 95km, as shown by **Figure 10**. However, this level of difference is only reached at the line centres, and for the wings, it is clearly below 0.5%.

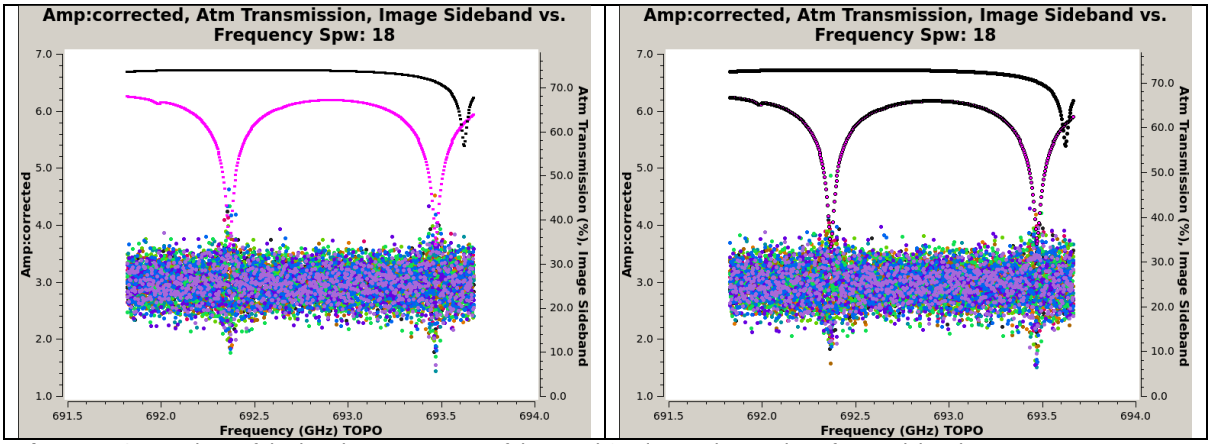

Figure 11 Comparison of the bandpass spectrum of the Band 9 science observation after applying the system temperature calibration. Left corresponds to the ATM model from 2019 using a maximum altitude of 48 km, and right corresponds to the current model for 2024 after updating the abundance profiles and using a maximum altitude of 95 km. We see that both are quite similar and do not show a systematic residual (dip) at the 692.37 GHz and 693.47 GHz Ozone lines, and what remains is just some scatter corresponding to the extra noise associated with lower transmission. Additionally the baseline slope seems to have change, but this is most likely associated with other changes in the ALMA calibration pipeline.

6.9 Receiver temperature comparison: ambient / hot load vs ambient / sky

We compare the absolute receiver temperatures obtained with both methods using four combinations: a new / old ATM model and a maximum altitude of 48km / 95km. The results are shown in **Figure 12**. We see that both methods deliver a receiver temperature with a similar trend but a bit of offset in between; however, the receiver temperatures obtained with the old ATM model and a maximum altitude of 48km present a spike of ~10-15K in the centre of the O3 lines at 692.37 GHz and 693.47 GHz. These spikes are progressively reduced when using a maximum altitude of 95 km to ~5K and finally almost disappears when using the new ATM model.

Apart from the spikes associated with the O3 lines at 692.37 GHz and 693.47 GHz, we notice an almost constant offset independent of the frequency which could be corrected with a constant forward efficiency (sky coupling) value higher than the one currently used (98%). This is different from the band 6 case in which a frequency-dependent offset is observed as shown by **Figure 7**.

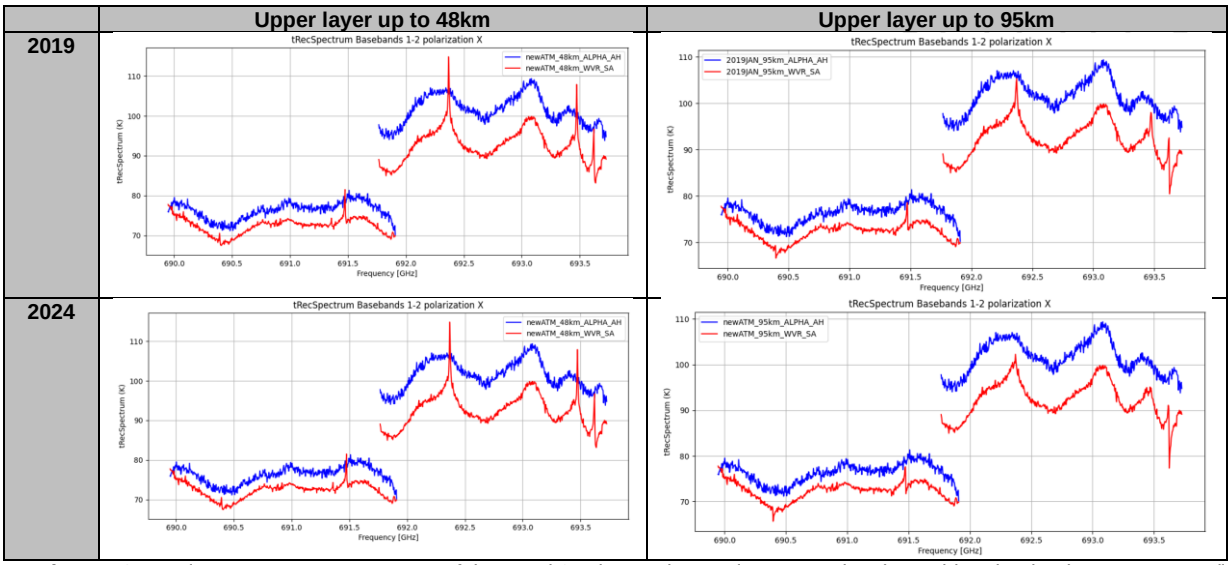

Figure 12 Receiver temperature spectrum of the Band 9 science observation comparing the ambient-hot load measurement (in blue) with the ambient-sky measurement (in red). Top and bottom rows are polarisations X and Y, respectively. We see that there are spikes of (~10-15K) corresponding to the centre of the 692.37 GHz and 693.47 GHz Ozone lines in the receiver temperatures obtained with the ambient-hot load measurement using the ATM model from 2019 and a maximum altitude of 48km (top left panel). These spikes are reduced to ~5K when using a maximum altitude of 95 km (top right panel), and finally, they are reduced to ~3 K when using the current model for 2024 and also changing the maximum altitude to 95km (bottom right panel).

6.10 Band 6 spectral check

6.11 System temperature comparison: new ATM vs old ATM

The system temperature spectra are shown in **Figure 13Figure 1** where we see that there is very little difference between both versions and the system temperature spectra almost completely overlaps.

The percentual difference is shown in **Figure 14**, where we see that the difference barely reaches 0.05%. Moreover, if we increase the maximum altitude used by the new ATM model from 2024 up to 95 km, the difference only increases to 0.35% as we see in **Figure 15**.

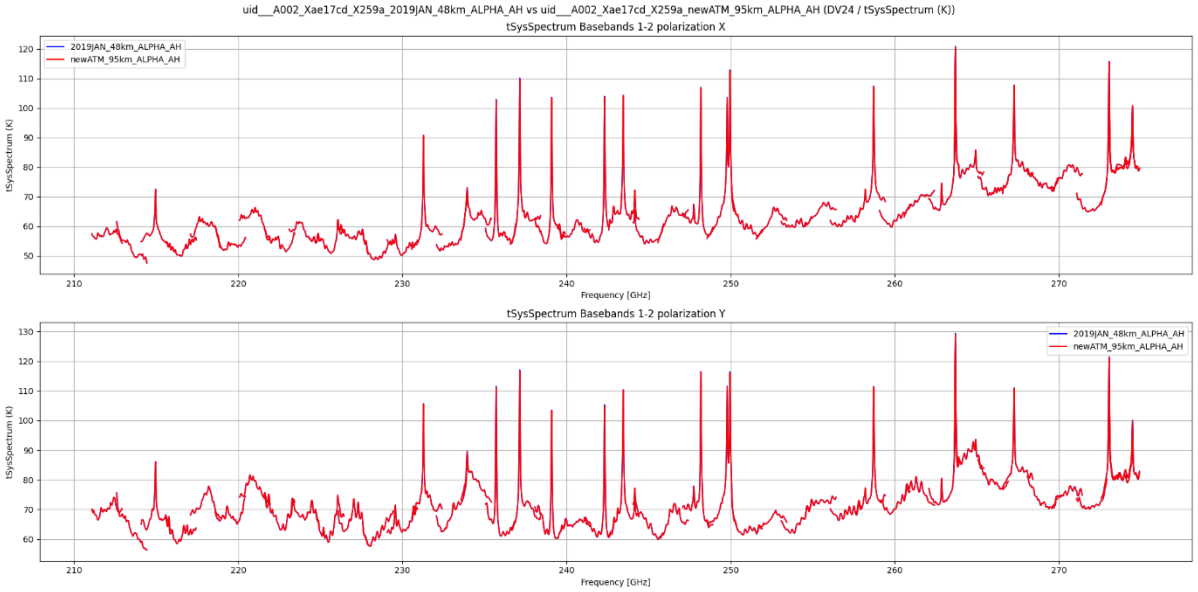

Figure 13 System temperature spectrum corresponds to the Band 6 spectral check. Blue corresponds to the ATM model from 2019 using a maximum altitude of 48 km, and red to the current model for 2024 after updating the abundance profiles and using a maximum altitude of 95 km. Top and bottom rows are polarisations X and Y, respectively We see that both models are almost exactly coincident, to the point that they completely overlap, and only the 2024 model is visible.

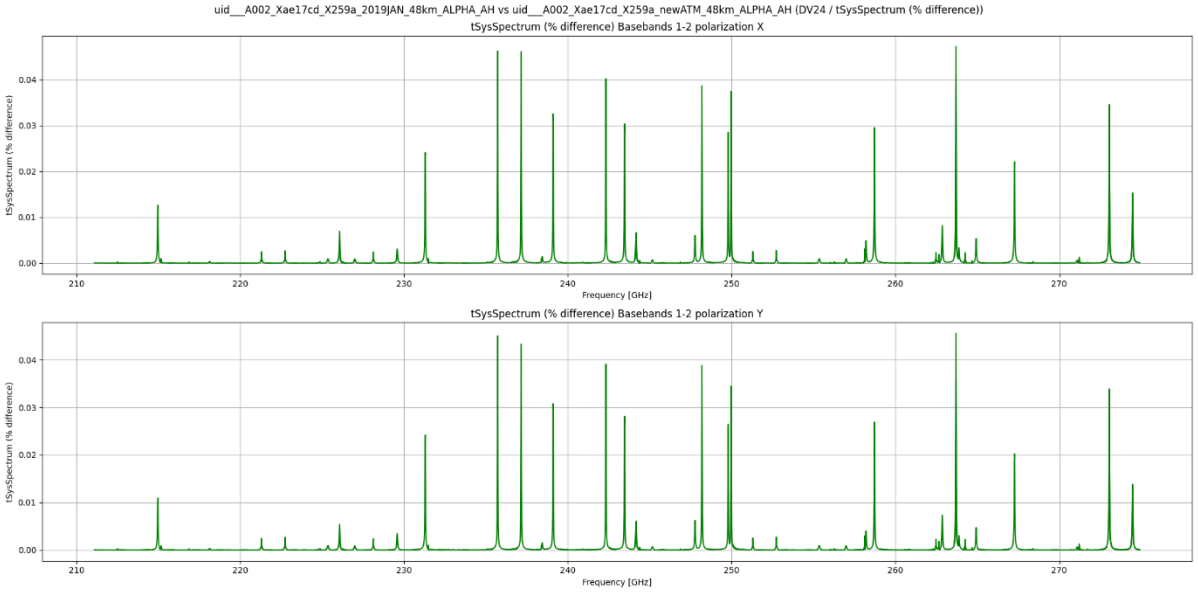

Figure 14 Percentage difference in the system temperature spectrum corresponding to the Band 6 spectral check comparing the ATM model from 2019 using a maximum altitude of 48 km with the current model for 2024 after updating the abundance profiles and using a maximum altitude of 48 km. Top and bottom rows are polarisations X and Y, respectively. We see that the maximum difference is almost negligible (0.05%).

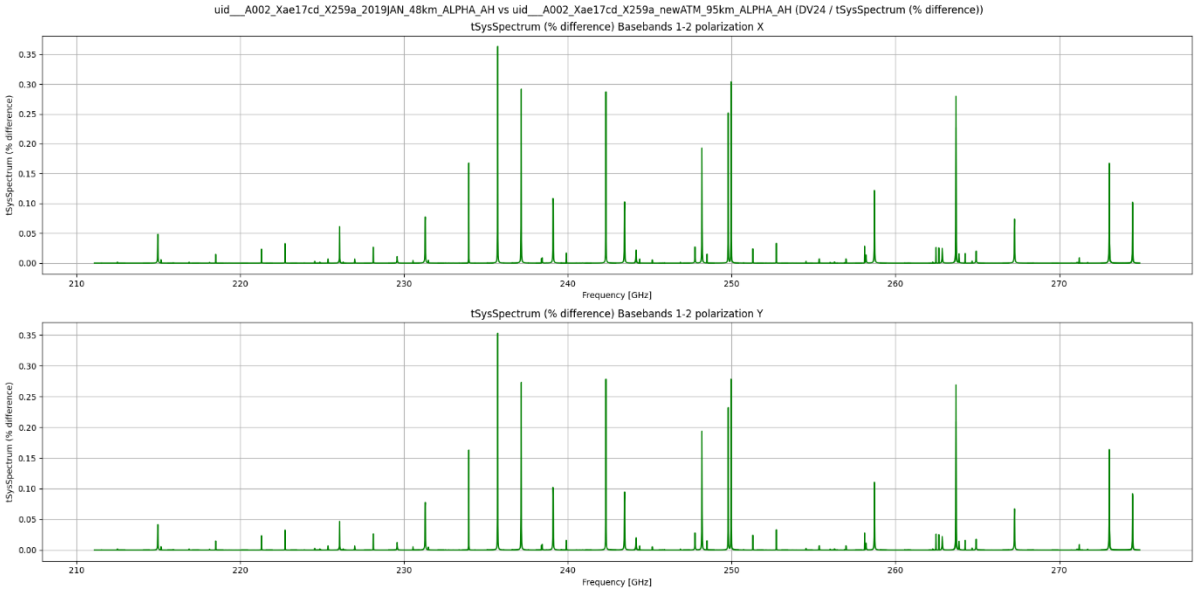

Figure 15 Percentual difference in the system temperature spectrum corresponding to the Band 6 spectral check comparing the ATM model from 2019 using a maximum altitude of 48 km with the current model for 2024 after updating the abundance profiles and using a maximum altitude of 95 km. Top and bottom rows are polarisations X and Y, respectively. We see that the maximum difference increases when changing the maximum altitude from 48km to 95km, but still, it is quite small (0.35% max).

6.12 System temperature comparison: Alpha method vs traditional

The system temperature spectra for both cases are shown in **Figure 16**, where we see that again, there is very little difference between both methods, and the system temperature spectra almost completely overlap.

We can then obtain the percentual difference between both methods, as shown in **Figure 17**, where we see that the maximum percentual difference is about 1.75%. However, a pattern emerges, as it appears that apart from the higher differences associated with the centre of atmospheric lines, there are also strong spectral slopes associated with each scan, with a mirror point at around 228 GHz, which apparently corresponds to switching sideband.

These results show again that ATM is actually quite good and produces reliable estimates of the opacity term in comparison with observations based on the alpha method. However, there are clearly underlying systematic HW issues that become dominant given the existing good agreement between ATM and actual atmospheric emissions.

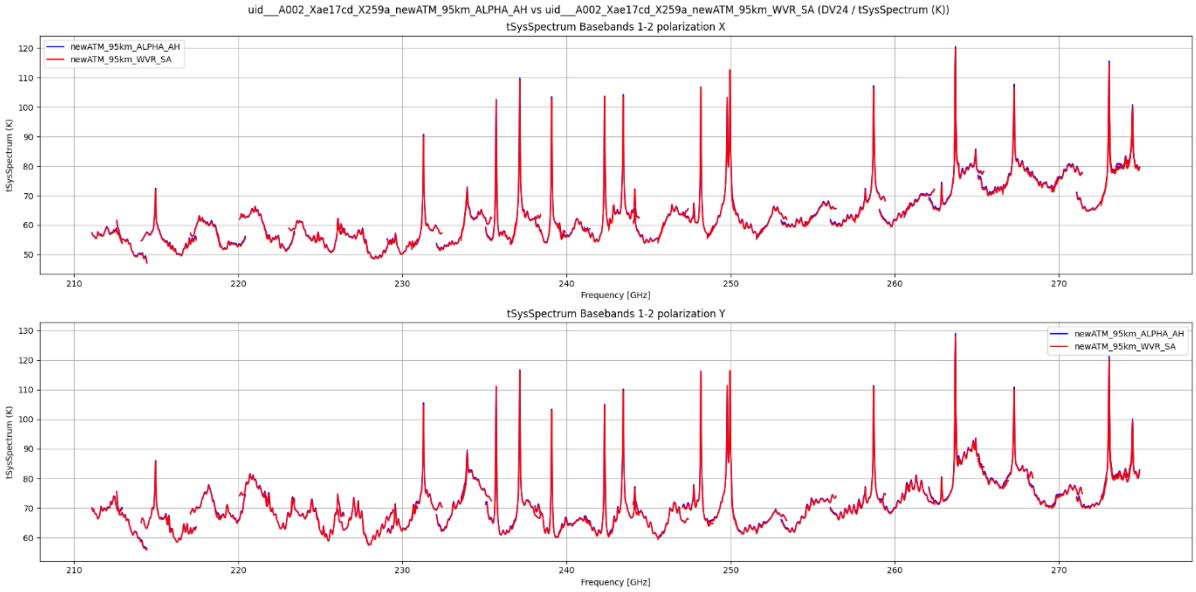

Figure 16 System temperature spectrum corresponding to Band 6 spectral check using the current ATM model for 2024 and a maximum altitude of 95km. Blue corresponds to the ALPHA method resorting to a hot load measurement to obtain the opacity term, and blue to the traditional method based on an ambient-sky dual load measurement and resorting to ATM to obtain the opacity term. Top and bottom rows are polarisations X and Y, respectively. We see that both models are quite similar overall.

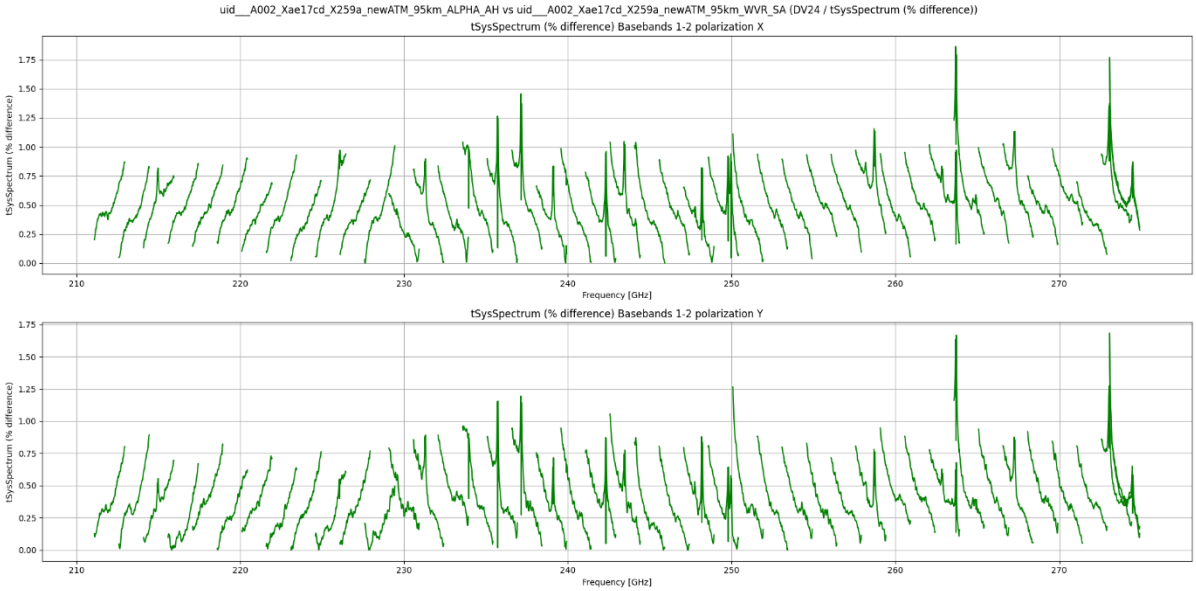

Figure 17 Percentual difference in the system temperature spectrum corresponding to the Band 6 spectral check comparing the ALPHA method resorting to a hot load measurement to obtain the opacity term versus the traditional method based on an ambient-sky dual load measurement and resorting to ATM to obtain the opacity term. Top and bottom rows are polarisations X and Y, respectively. We see a maximum difference of 1.75 % corresponding to the strongest Ozone line, but also many strong spectral slopes corresponding to each scan, separated by a gap.

6.13 Receiver temperature comparison: ambient / hot load vs ambient / sky

The results are shown in **Figure 18**, where we see that the sky-ambient load method relying on ATM to provide the sky temperature produces relative stable estimates of the receiver temperatures, whereas the method based on ambient-hot loads suffers from strong spectral slopes and gaps in between scans and a mirror point at around 228 GHz, which apparently corresponds to switching sideband.

This behaviour matches the percentual differences seen in the comparison of the methods used to obtain system temperatures and is actually associated with known HW issues, namely the non-linearity of the receivers, which are saturated by the hot load, and also the spectral-dependent non-linearity of the current back-end or digitizers.

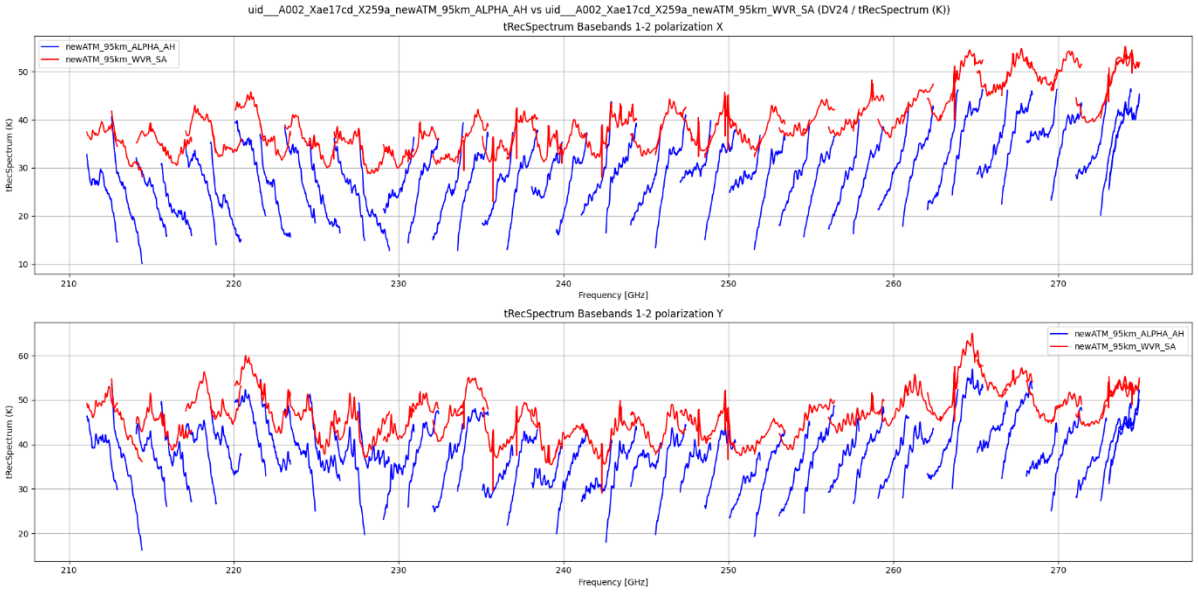

Figure 18 Receiver temperature spectrum of the Band 6 spectral check comparing the ambient-hot load measurement (in blue) with the ambient-sky measurement (in red). Top and bottom rows are polarisations X and Y, respectively. We see that ambient-sky measurements are more stable, whereas the ambient-hot load measurement present strong spectral slopes corresponding to each scan, separated by a gap. However, the SA (red) measurements are likely over-estimated due to an overly optimistic assumption of 98% forward efficiency.

6.14 Band 9 spectral check

6.15 System temperature comparison: new ATM vs old ATM

The system temperature spectra are shown in **Figure 19**, where we see that there is very little difference between both versions and the system temperature spectra almost completely overlaps.

The percentual difference is shown in **Figure 20**, where we see that the difference is small and reaches a maximum of 2%. However, as opposed to the Band 6 case, if we increase the maximum altitude used by the new ATM model from 2024 up to 95 km, the difference increases up to 7% at the peak of the strongest lines as we see in **Figure 21**.

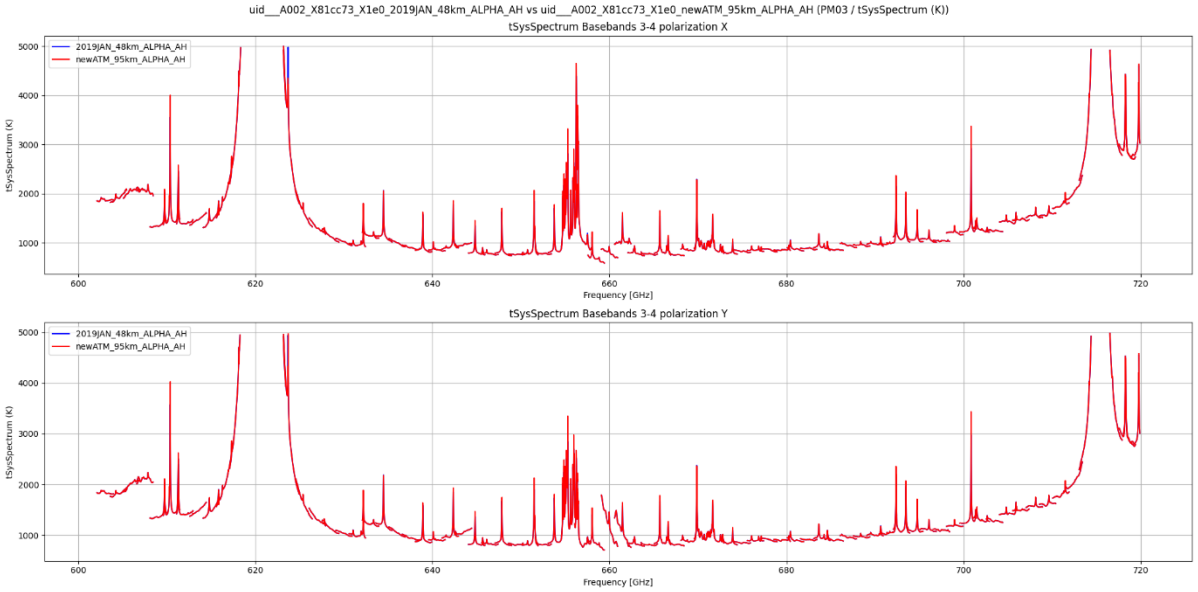

Figure 19 System temperature spectrum corresponds to the Band 9 spectral check. Blue corresponds to the ATM model from 2019 using a maximum altitude of 48 km, and red to the current model for 2024 after updating the abundance profiles and using a maximum altitude of 95 km. Top and bottom rows are polarisations X and Y, respectively. We see that both models are almost exactly coincident, to the point that they completely overlap, and only the 2024 model is visible.

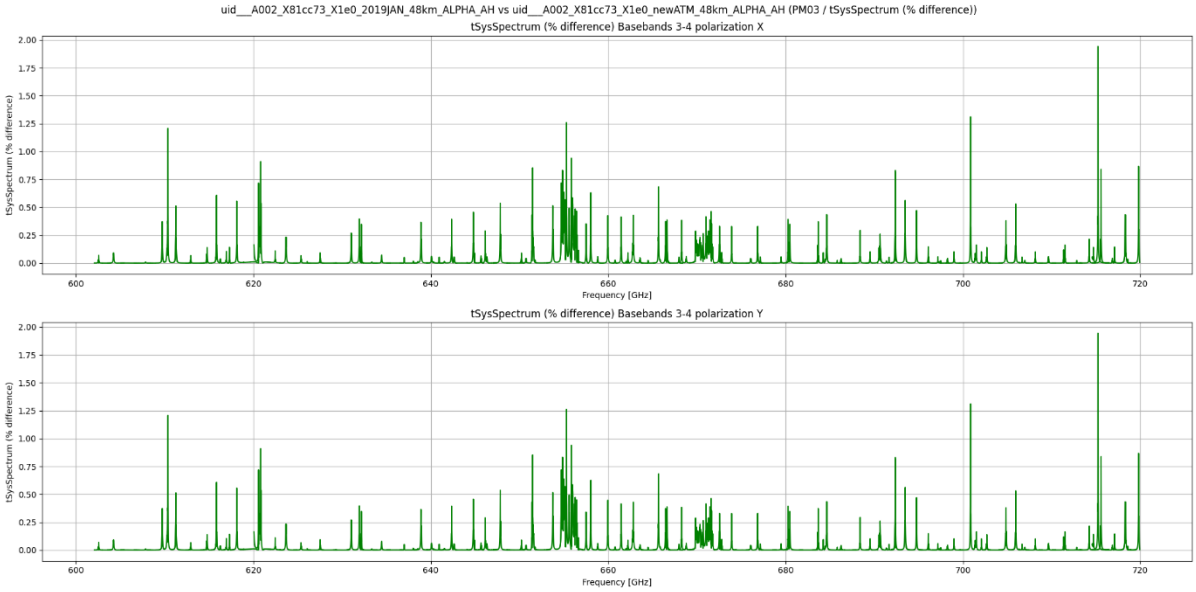

Figure 20 Percentage difference in the system temperature spectrum corresponding to the Band 9 spectral check comparing the ATM model from 2019 using a maximum altitude of 48 km with the current model for 2024 after updating the abundance profiles and using a maximum altitude of 48 km. Top and bottom rows are polarisations X and Y, respectively. We see that the maximum difference is still small (2%).

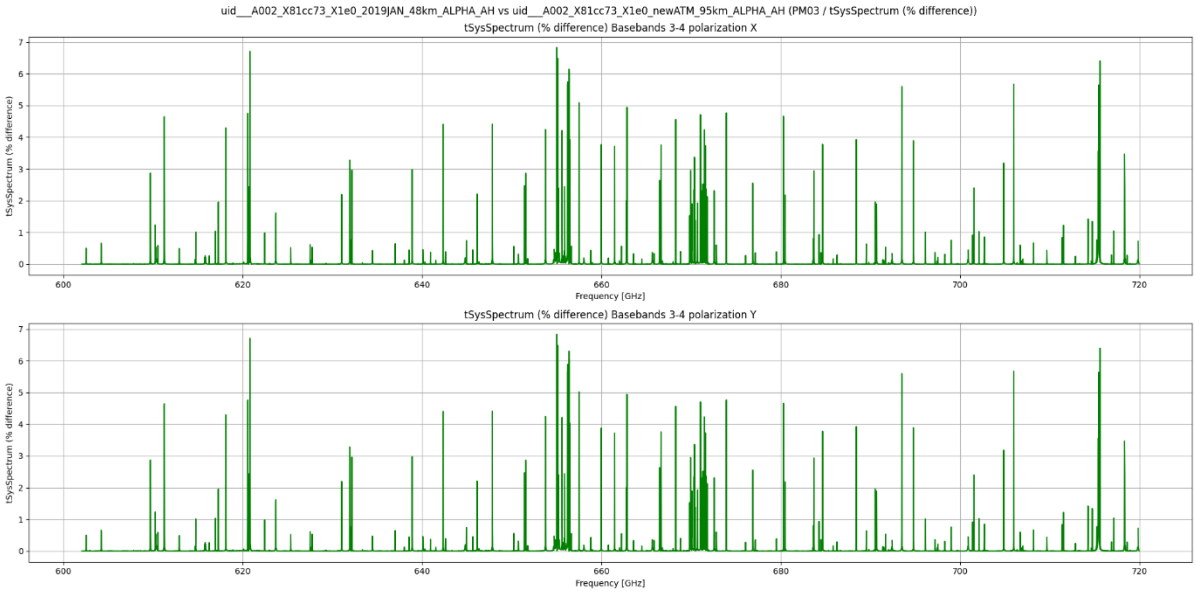

Figure 21 Percentual difference in the system temperature spectrum corresponding to the Band 9 spectral check comparing the ATM model from 2019 using a maximum altitude of 48 km with the current model for 2024 after updating the abundance profiles and using a maximum altitude of 95 km. Top and bottom rows are polarisations X and Y, respectively. We see that the maximum difference increases when changing the maximum altitude from 48km to 95km, but still, and reaches up to 7%.

6.16 System temperature comparison: Alpha method vs traditional

The system temperature spectra for both cases are shown in **Figure 22**, where we see that again, there is very little difference between both methods, and the system temperature spectra almost completely overlaps.

We can then obtain the percentual difference between both methods, as shown in **Figure 23**, where we see that the maximum percentual difference is about 7% in the centre of the O3 cluster at 656–658 GHz. This is definitely higher than the band 6 case (2%) but compatible with the maximum differences found for the APEX Sepia 660 case, which are at the level of 4-5% as reported by Juan Ramon Pardo et al. [2].

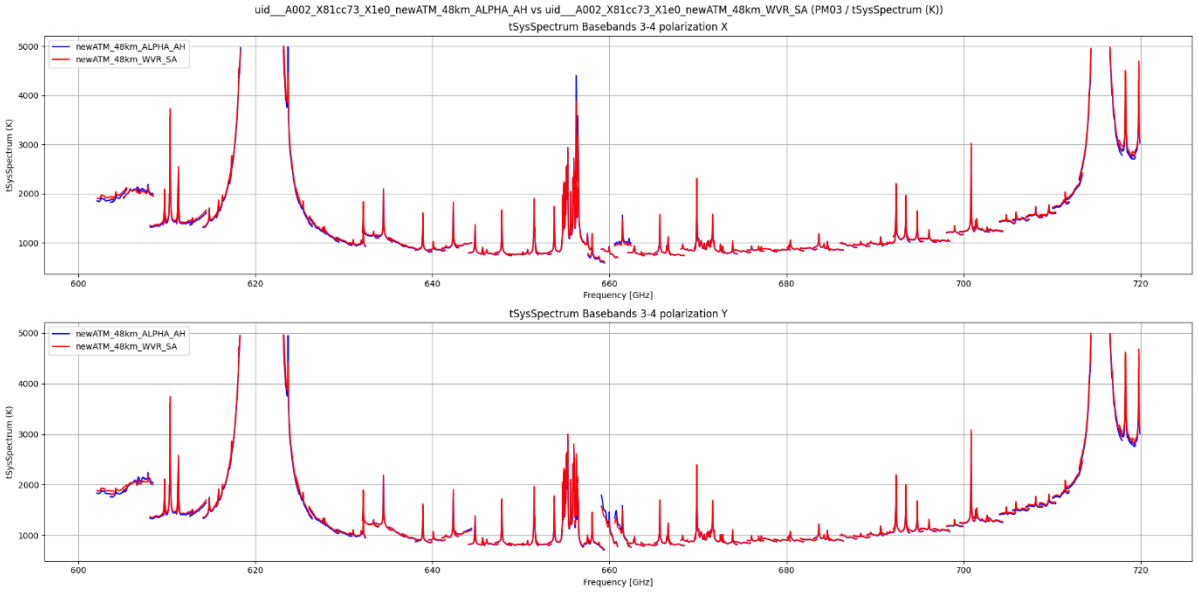

Figure 22 System temperature spectrum corresponding to Band 9 spectral check using the current ATM model for 2024 and a maximum altitude of 95km. Blue corresponds to the ALPHA method resorting to a hot load measurement to obtain the opacity term, and blue to the traditional method based on an ambient-sky dual load measurement and resorting to ATM to obtain the opacity term. Top and bottom rows are polarisations X and Y, respectively. We see that both models are quite similar overall.

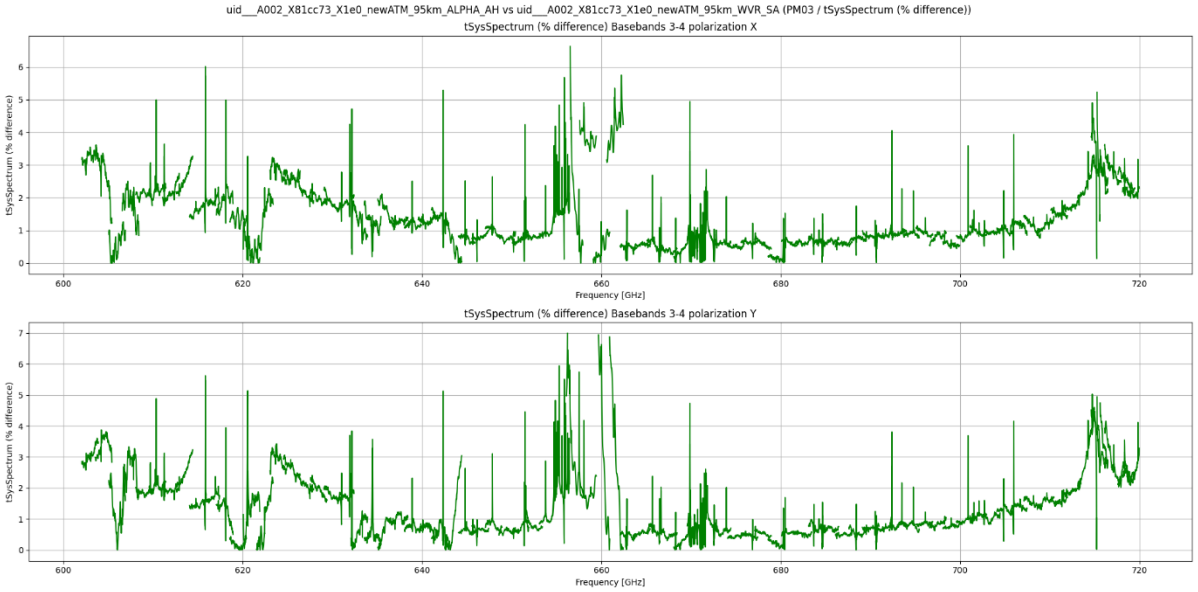

Figure 23 Percentual difference in the system temperature spectrum corresponding to the Band 9 spectral check comparing the ALPHA method resorting to a hot load measurement to obtain the opacity term versus the traditional method based on an ambient-sky dual load measurement and resorting to ATM to obtain the opacity term. Top and bottom rows are polarisations X and Y, respectively. We see a maximum difference of 7 % corresponding to the cluster of Ozone lines around 656GHz.

6.17 Receiver temperature comparison: ambient / hot load vs ambient / sky

The results are shown in **Figure 24**, where we see that both methods provide similar estimates of the receiver temperatures, separated by an offset. However, the receiver temperatures from the sky-ambient loads method present a number of strong spikes and extra noise in the centre of the O3 cluster at 656–658 GHz. Moreover, the spectral slopes and mirroring points, which in the case of band 6 were only visible in the receiver temperatures obtained with ambient-hot loads, are now present in the case of the sky-ambient-loads method.

These results can be explained if the non-linearity of the receivers and the and the spectral-dependent non-linearity of the current back-end or digitizers, which is only triggered by the hot load in the case of lower frequency bands < 6, is triggered directly by the strong atmospheric emission in high frequency bands.

Also, note that Band 9 is a DSB receiver band, and therefore the SA measurements are affected by any deviation of the sideband gains from their assumed equality (the same also applies for deviation of the image suppression of 2SB bands from the assumed -20dB, but the magnitude of the error is generally much less).

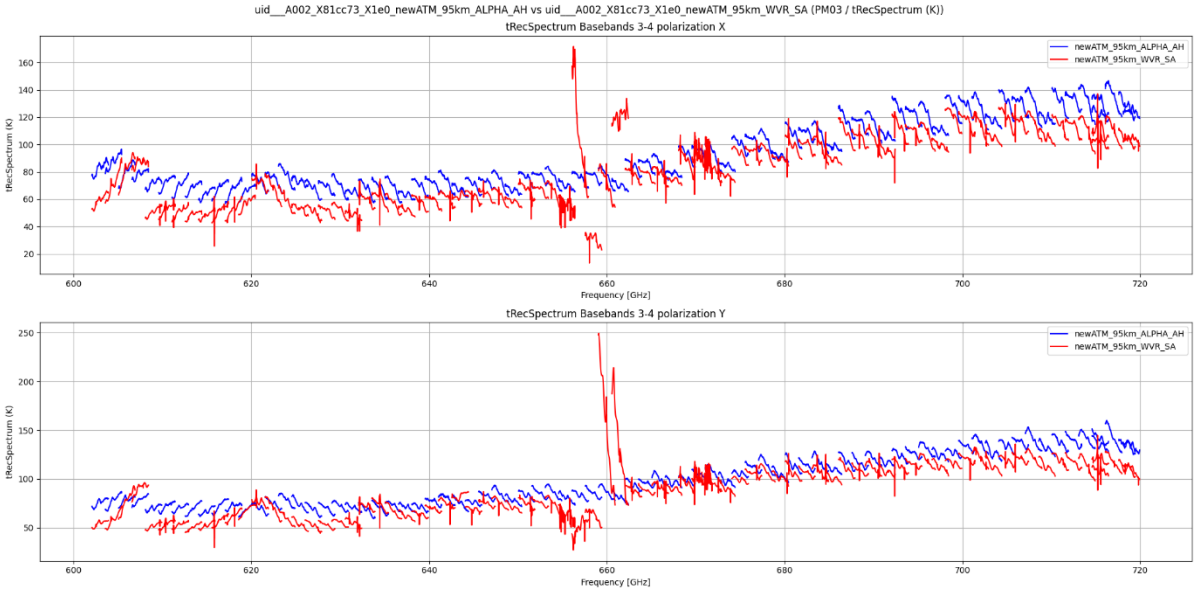

Figure 24 Receiver temperature spectrum of the Band 9 spectral check comparing the ambient-hot load measurement (in blue) with the ambient-sky measurement (in red). Top and bottom rows are polarisations X and Y, respectively. We see both measurements follow the same trend, separated by an offset, and present spectral slopes corresponding to each scan, separated by a gap. Moreover, the ambient-sky measurements present quite strong spikes associated with some baseline gaps in the system temperature spectra.

6.18 Band 2 spectral check

6.19 System temperature comparison: new ATM vs old ATM

The system temperature spectra are shown in **Figure 25**, and the percentual difference is shown in **Figure 26**, where we see that the difference barely reaches 0.0012%.

Moreover, if we increase the maximum altitude used by the new ATM model from 2024 up to 95 km, the difference only increases to 0.05% as we see in **Figure 27**.

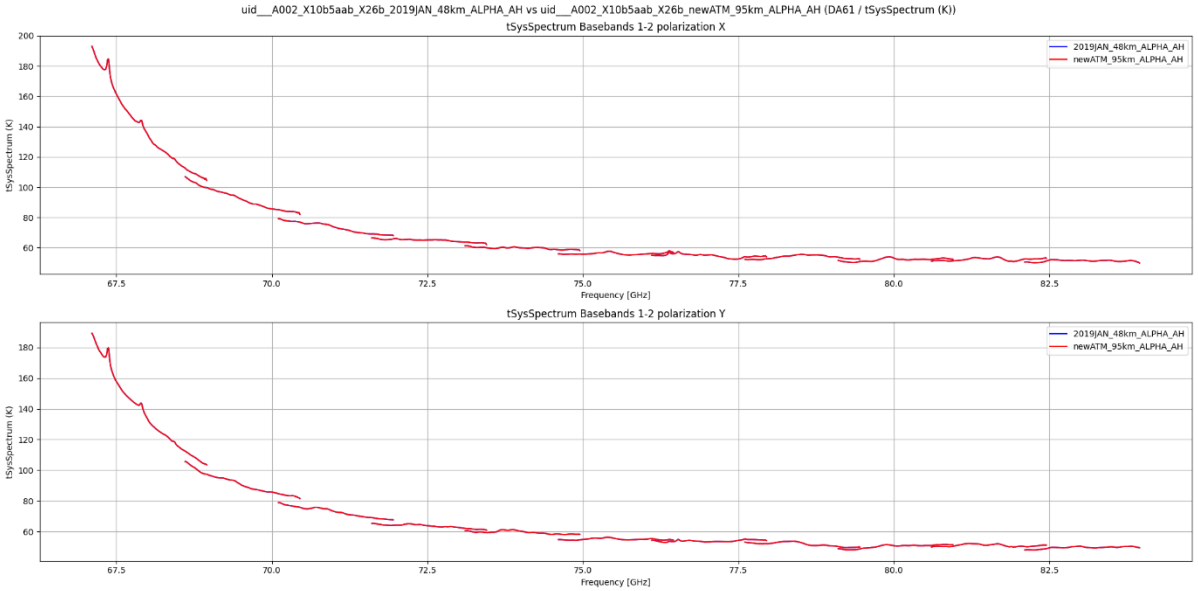

Figure 25 System temperature spectrum corresponds to the Band 2 spectral check. Blue corresponds to the ATM model from 2019 using a maximum altitude of 48 km, and red to the current model for 2024 after updating the abundance profiles and using a maximum altitude of 95 km. Top and bottom rows are polarisations X and Y, respectively. We see that both models are almost exactly coincident, to the point that they completely overlap, and only the 2024 model is visible.

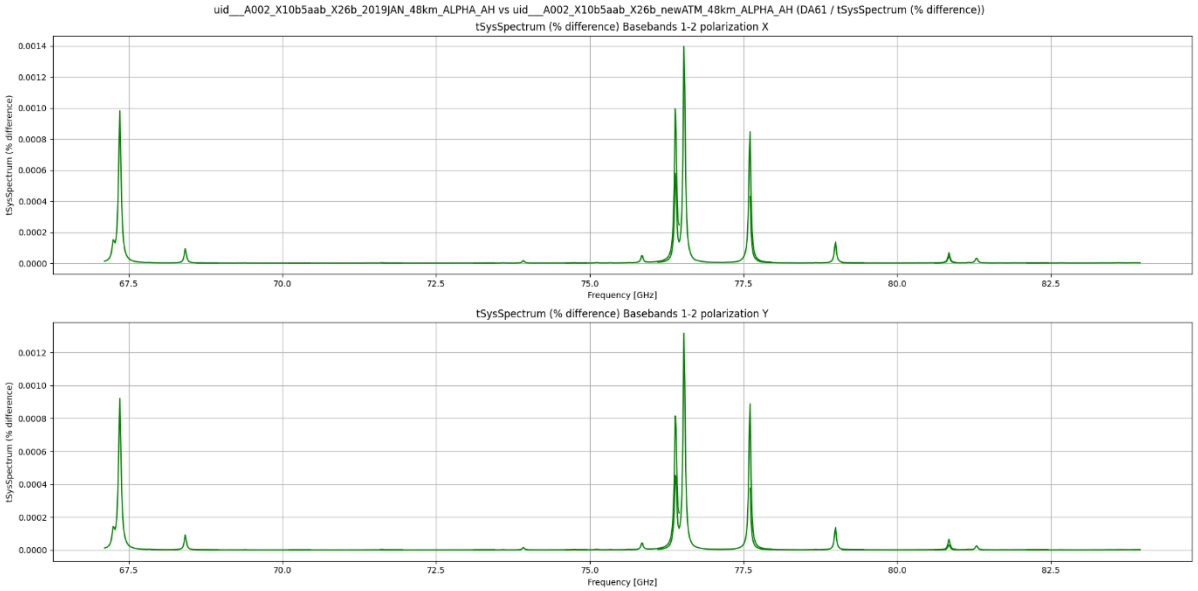

Figure 26 Percentage difference in the system temperature spectrum corresponding to the Band 2 spectral check comparing the ATM model from 2019 using a maximum altitude of 48 km with the current model for 2024 after updating the abundance profiles and using a maximum altitude of 48 km. Top and bottom rows are polarisations X and Y, respectively. We see that the maximum difference is almost negligible (0.0012%).

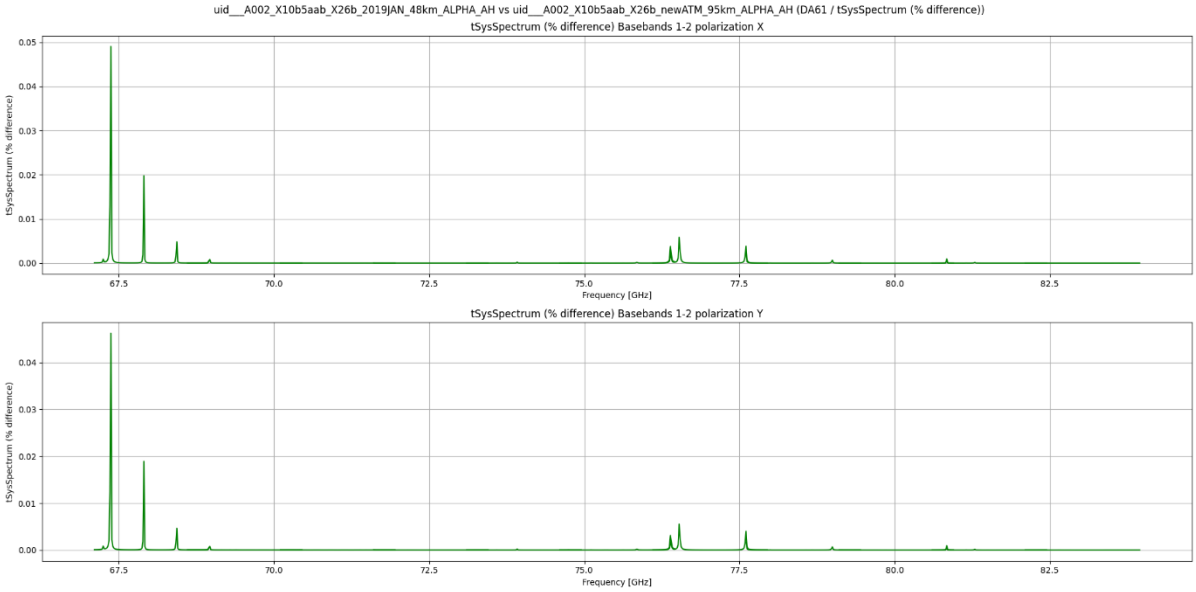

Figure 27 Percentual difference in the system temperature spectrum corresponding to the Band 2 spectral check comparing the ATM model from 2019 using a maximum altitude of 48 km with the current model for 2024 after updating the abundance profiles and using a maximum altitude of 95 km. Top and bottom rows are polarisations X and Y, respectively. We see that the maximum difference increases when changing the maximum altitude from 48km to 95km, but still, it is quite small (0.05% max).

6.20 System temperature comparison: Alpha method vs traditional

The system temperature spectra for both cases are shown in **Figure 28**, where we see that again, there is very little difference between both methods, and the system temperature spectra almost completely overlaps.

We can then obtain the percentual difference between both methods, as shown in **Figure 29**, where we see that the maximum percentual difference is about 1.2%. However, the same pattern seen in the band 6 spectral scan emerges again, with strong spectral slopes associated with each scan, which is actually associated with known HW issues, particularly the spectral-dependent non-linearity of the current back-end or digitizers.

These results show again that ATM is actually quite good and produces reliable estimates of the opacity term in comparison with observations based on the alpha method. However, there are clearly underlying systematic HW issues that become dominant given the existing good agreement between ATM and actual atmospheric emissions.

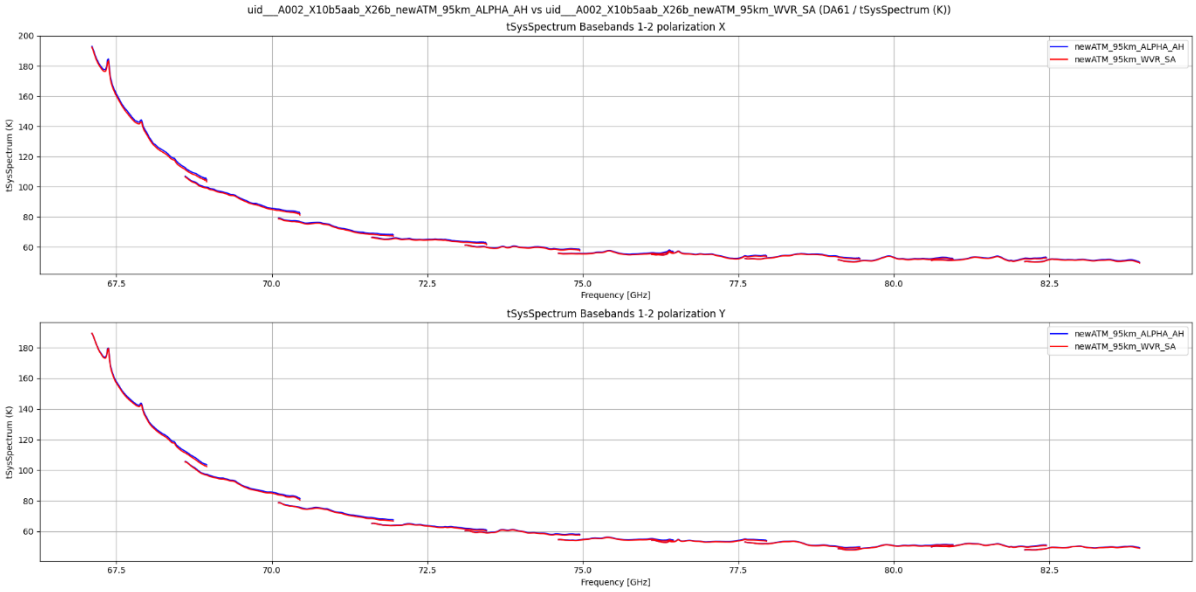

Figure 28 System temperature spectrum corresponding to Band 2 spectral check using the current ATM model for 2024 and a maximum altitude of 95km. Blue corresponds to the ALPHA method resorting to a hot load measurement to obtain the opacity term, and blue to the traditional method based on an ambient-sky dual load measurement and resorting to ATM to obtain the opacity term. Top and bottom rows are polarisations X and Y, respectively. We see that both models is quite similar overall.

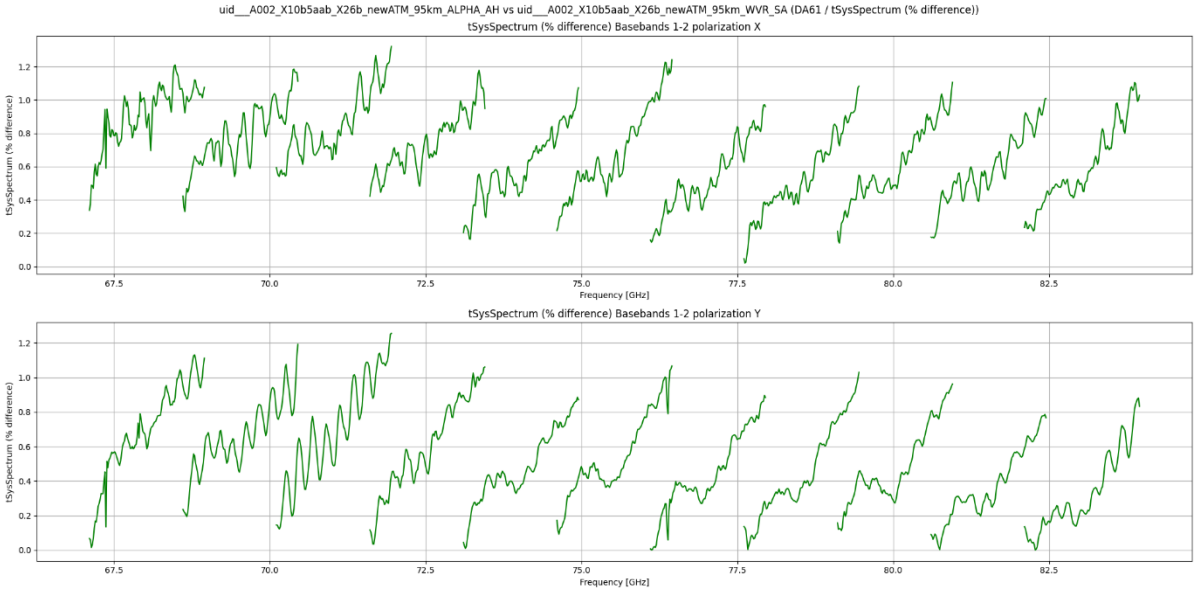

Figure 29 Percentual difference in the system temperature spectrum corresponding to the Band 2 spectral check comparing the ALPHA method resorting to a hot load measurement to obtain the opacity term versus the traditional method based on an ambient-sky dual load measurement and resorting to ATM to obtain the opacity term. Top and bottom rows are polarisations X and Y, respectively. We see a maximum difference of 1.2 % and many strong spectral slopes corresponding to each scan, separated by a gap.

6.21 Receiver temperature comparison: ambient / hot load vs ambient / sky

In the case of band 2 we study two different antennas: DA60, which has not been optimized for low compression (**Figure 30**), and DA61, which has been optimized (**Figure 31**). We see that receiver temperatures of the unoptimized antenna obtained with the ambient-hot dual load method have wide amplitude ripples (**Figure 30**), which are minimized for the optimized antenna (**Figure 31**); however, the optimized antenna still has strong spectral slopes in comparison with the receiver temperatures obtained with the sky-ambient dual load method, which relies on ATM to provide the sky temperature. (T_{sky} shown in Equation 2).

The effect of worse compression clearly shows as higher receiver noise measured with the AH method (blue curves) for DA60 (both receivers have very similar real receiver noise as measured in the lab). The elevated values measured by the SA method (red curves) are due to the error in the assumed forward efficiency, which is really closer to 96% than the assumed 98%, and is frequency dependent.

These results show that ATM can provide reliable reference information to measure the receiver temperatures using the Sky-ambient dual load method, which otherwise shows a lot of non-linearities and fine-tuning dependencies when measured with the ambient-hot dual load method. However, improved estimates of forward efficiency for each receiver band and possibly as a function of frequency will be needed in TelCal to obtain correct absolute receiver noise.

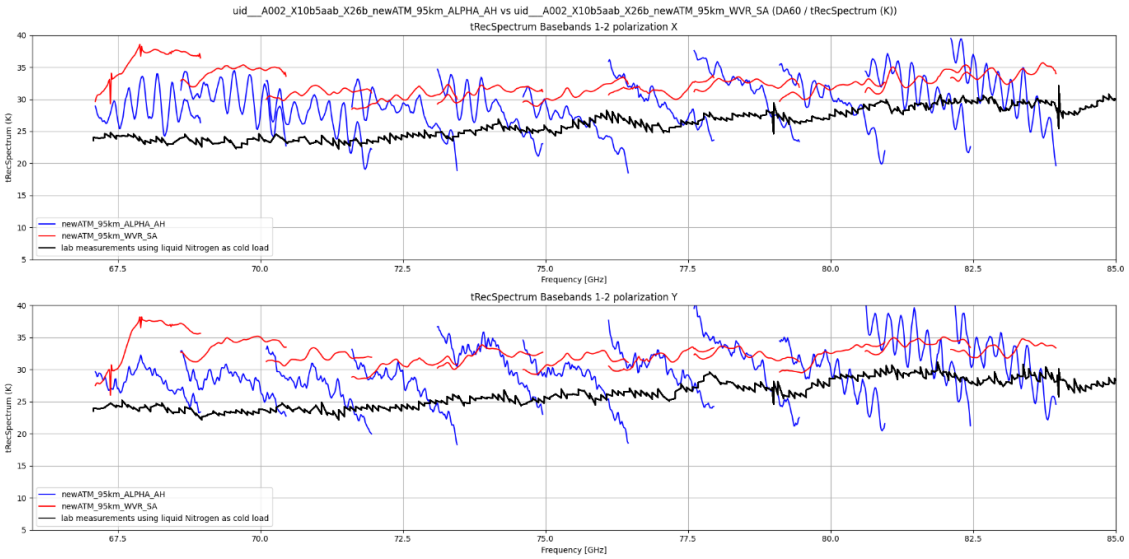

Figure 30 Receiver temperature spectrum of the Band 2 spectral check of an antenna not optimized for low compression (DA60; CLNA bias is as originally delivered, which results in significant compression on the ambient and hot loads), comparing the ambient-hot load measurement (in blue), the ambient-sky measurement (in red), and the lab measurements using liquid nitrogen as a cold load (in black). The top and bottom rows are polarizations X and Y, respectively. We see that ambient-sky measurements are more stable, although separated by an offset from the lab measurements, probably due to the relatively higher forward efficiency value assumed by TelCal (0.98). On the other hand, the ambient-hot load measurements present strong ripples and spectral slopes corresponding to each scan, separated by a gap.

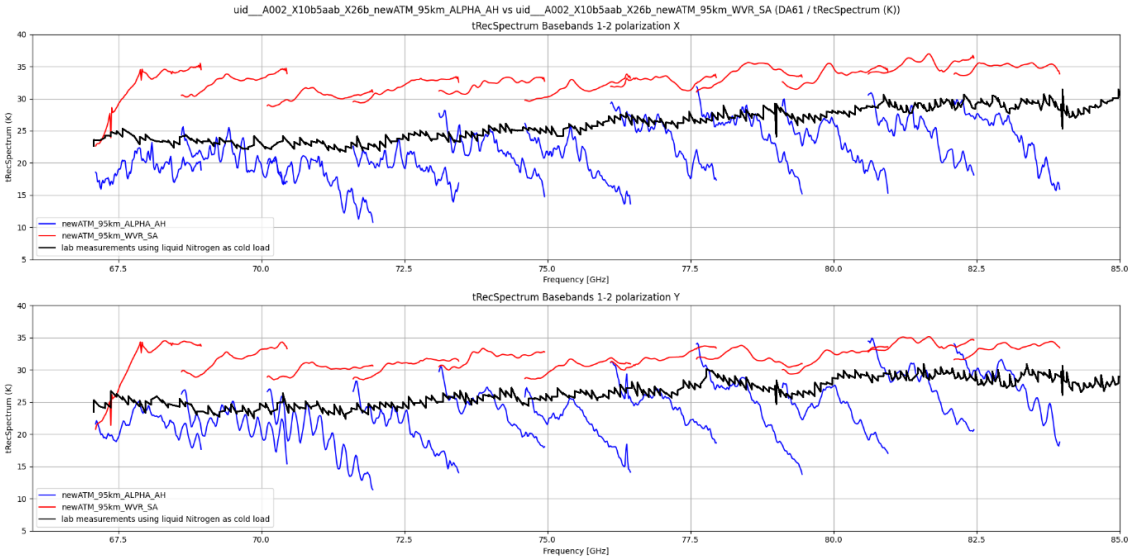

Figure 31 Receiver temperature spectrum of the Band 2 spectral check of an antenna with CLNA bias optimized for low compression (DA61), comparing the ambient-hot load measurement (in blue) with the ambient-sky measurement (in red), and the lab measurements using liquid nitrogen as a cold load (in black). We see that ambient-sky measurements are more stable, although separated by an offset from the lab measurements, probably due to the relatively higher forward efficiency value assumed by TelCal (0.98). On the other hand, the ambient-hot load measurements still present strong spectral slopes corresponding to each scan, separated by a gap, although the amplitude of the ripples has been minimized.

7. Conclusions

In conclusion, we see that the previous version of ATM (from 2019) was already quite good, and the system temperature calibration was already able to completely remove the atmospheric features from the bandpass scan as long as the frequency resolution of the atmospheric calibration scan matches that of the bandpass calibrator. In this case, only some extra noise (scatter) is left in the affected spectral regions, as seen in the corrected bandpass spectrum from the ALMA calibration pipeline (as seen on the left panel in figures **Figure 4** and **Figure 11**).

The new ATM model from 2024 has updated abundance profiles, but the differences are rather minor in the case of ozone, which is the molecule providing most of the atmospheric features due to its dipolar momentum. Moreover, the alpha method resorts to a hot load measurement to solve for the atmospheric opacity term (e^{τ}), leaving only a dependency on the Rayleigh-Jeans equivalent physical temperature of the atmosphere averaged on the line of sight (T_{atm}), which has a relatively narrow range even at the peak of strong atmospheric lines.

Consequently, the system temperature spectra using the new ATM model changes only by 0.35% for the case of ALMA band 6 (211–275 GHz), as seen in **Figure 15**, although it can change by up to 7% in the case ALMA band 9 (602-720 GHz), as seen in **Figure 21**.

These differences have almost no impact on the results of the system temperature calibration performed by the pipeline (as seen on the right panel in figures **Figure 4** and **Figure 11**). We expected a bigger impact on the case of band 9 since the difference in system temperatures can be up to 7%; however, this level of difference is only reached in the very centres of the lines, affected by the low pressure ozone included when increasing the maximum altitude to 95km, whereas the wings have barely changed.

Additionally, we have done a comparative study of the system temperature spectrum obtained with the alpha method, which requires only T_{atm} from the atmospheric model, and that obtained with the traditional method, which requires both e^{τ} and T_{atm}. The results obtained are good, with a difference of up to 1.2% for ALMA band 2 (67–116 GHz), 1.75% for ALMA band 6 (211–275 GHz), and 7% for ALMA band 9 (602–720 GHz). The difference obtained for ALMA band 9 is consistent with the results obtained by Juan Ramon Pardo et al. [2] with the APEX Sepia 660 receiver, who obtained a similar difference of 4-5% at the centre of the O3 cluster at 656–658 GHz.

Given that the comparative results are quite good for the lower frequency ALMA bands (< 6), an interesting possibility opens to skip the hot load calibration sub-scans and use the traditional method for obtaining the system temperatures for the lower bands to increase the observation time or perform some other atmospheric calibration sub-scan.

Moreover, given the good confidence of the atmospheric model, it can be used as a tool to diagnose systematic HW issues in ALMA during the commissioning of the Wide Sensitivity Upgrade, which will bring new correlators, receivers, digitizers, etc. in a similar way as it has helped to find calibration issues in the case of the APEX Sepia 660 receiver. Another recent example of this is measuring the forward efficiency of Band 2 pre-production receivers by comparing the receiver temperatures obtained with the sky-ambient dual load method, and with the ambient-hot dual load method (Neil Phillps).

In this sense, we have also compared the receiver temperature spectrum obtained with the ambient-hot load method with that obtained with the sky-ambient load method, relying on ATM to provide the sky temperature T_{sky}. As shown in **Figure 18**, the sky-ambient load method provides stable measurements of the receiver temperatures, whereas the ambient-hot load method exbibits strong spectral slopes, actually associated with known HW issues, namely the non-linearity of the receivers, which are saturated by the hot load, and also the spectral-dependent non-linearity of the current back-end or digitizers. Furthermore, the receiver temperatures obtained with the ambient-hot load method depend on the low compression optimization as shown in **Figure 30** and **Figure 31**.Therefore, it can be of good use to always consider the receiver temperature spectrum obtained with the sky-ambient load method relying on ATM, which provides a stable reference.

However, systematic and frequency-dependent errors in receiver temperature computed using the sky rather than instrumental loads due to uncertainty in forward efficiency and image rejection will need to be addressed to obtain accurate absolute results. Moreover, to fully rely on the atmospheric model to obtain system and receiver temperatures, it will be necessary to assess the impact of clouds on the sky temperature and opacity.

8. Future work

As explained in the conclusions, in order to fully utilize the receiver temperatures based on the sky-ambient dual load method, we need to better model the forward efficiency used in TelCal, which is currently set to a constant value of 0.98 for all bands. One possibility is to actually measure the forward efficiency by comparing the receiver temperatures from the ambient-hot and sky-ambient dual load methods (Neil Phillps). In this sense, two options are possible:

- Measure the forward efficiency using full-spectra resolution autocorrelations for each channel and an equivalent high-resolution ATM run, then average every 2 GHz to obtain mean values not affected by the non-linear behaviour of digitizers and receiver compression.

- Measure the forward efficiency of 2GHz channel average total power data based on square-law detectors that are not affected by the non-linearity of the digitisers and a high-resolution ATM run averaged every 2GHz.

Additionally, we need to assess the impact of clouds on the sky temperature and opacity; for this, we can resort to datasets exhibiting problems fitting the WVR data, which require the 'remove cloud' algorithm by Bill Dent as suggested by Andy Lipnicky.

9. Acknowledgements

I would like to thank Juan Ramon Pardo, Neil Phillips and Andy Lipnicky for the many interesting discussions and suggestions. Also a big thank you to Federico Montesino Pouzols and Andy Lipnicky for their help reprocessing the data.

10. References

[1] Dual Load Amplitude Calibration in ALMA, R. Lucas, S. Corder, ALMA Memo series

[2] Improving the calibration of atmospheric spectral features in ALMA data, TR Hunter, N Phillips, D Broguiere, J Gonzalez - ALMA Development Study (Cycle 3) Final Report, 2018

[3] Extremely high spectral resolution measurements of the 450 μm atmospheric window at Chajnantor with APEX, JR Pardo, C De Breuck, D Muders, J González… - Astronomy & Astrophysics, 2022

Status of the dry path correction for ALMA

Justo Gonzalez

1. Introduction

A known issue with the antenna position calibration in ALMA is that the correction offsets seem to fluctuate several millimeters in the zenith direction, even if they are measured by consecutive all-sky delay observations separated by less than ~2 hours.

A complete analysis of the problem was performed during the 2015 long baseline campaign, when six additional remote weather stations were incorporated into the ALMA pad network close to the most remote pads used for long baselines. As [Ref. Doc. 1] reports, incorporating more accurate weather data did not alleviate the problem, even if WVR correction was already in place.

Although [Ref. Doc. 1] suggests that the root cause of the problem may originate in non-modelled aspects of the WVR correction obtained from ATM, further investigation by the TelCal team showed that the fluctuation also happens in dry conditions (e.g., PWV 0.20-0.58 mm) as shown by Figure 1, with a comparable amplitude to that of mildly wet conditions (e.g., PWV 1.19-1.32 mm) as shown by Figure 2, or highly wet conditions (e.g., PWV 3.33-3.53 mm) as shown by Figure 3.

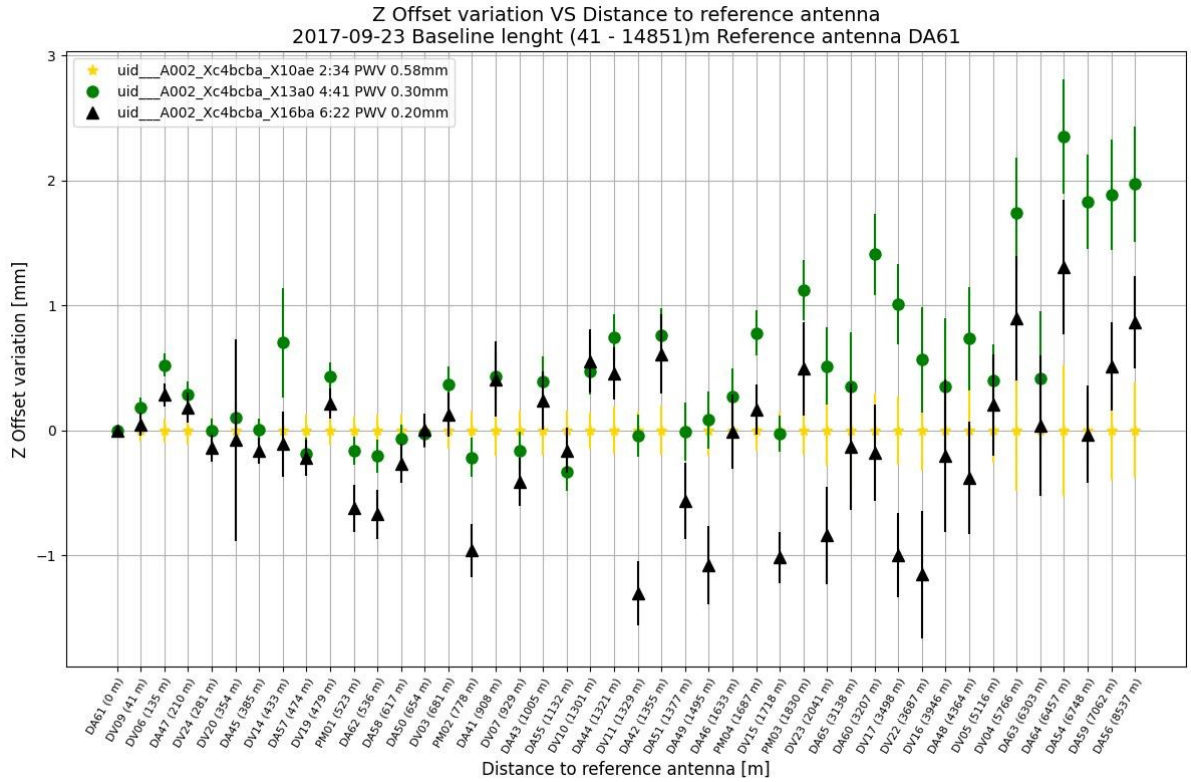

Figure 1 Fluctuation of the antenna position offset (Z component) in dry conditions as a function of distance w.r.t. the reference antenna

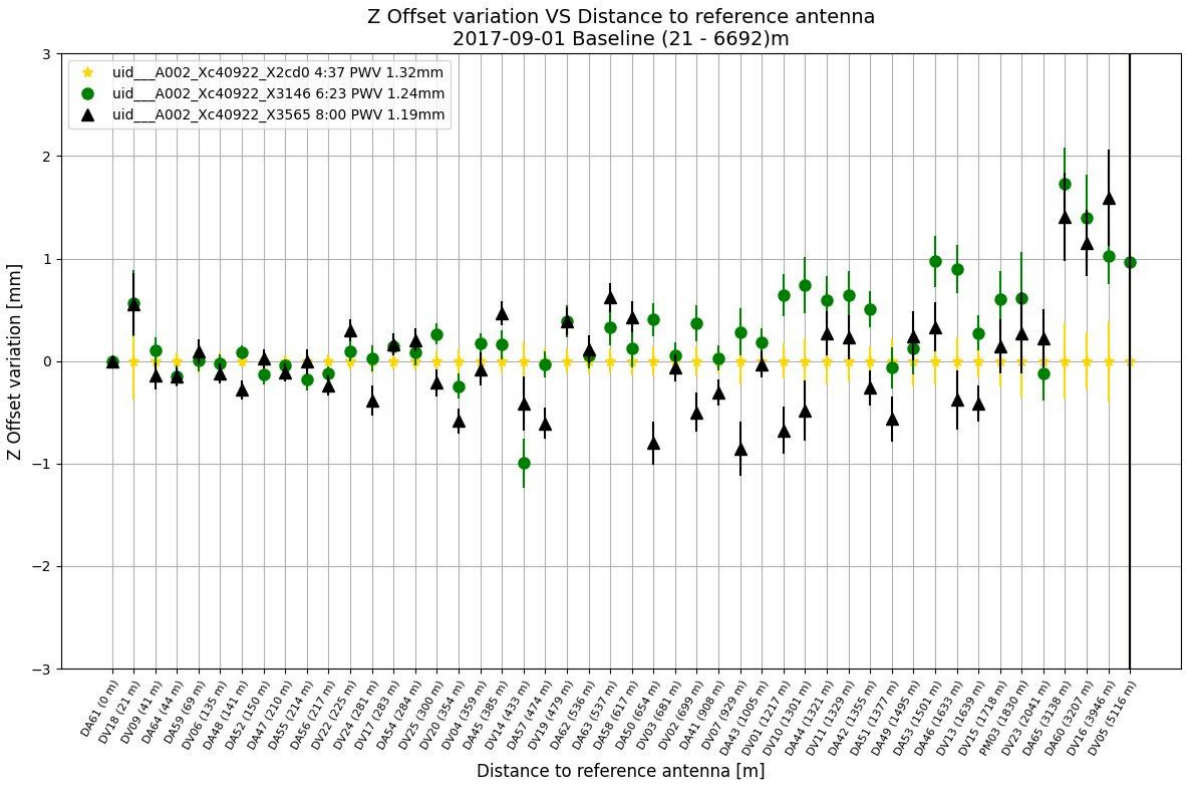

Figure 2 Fluctuation of the antenna position offset (Z component) in mildly wet conditions as a function of distance w.r.t. the reference antenna

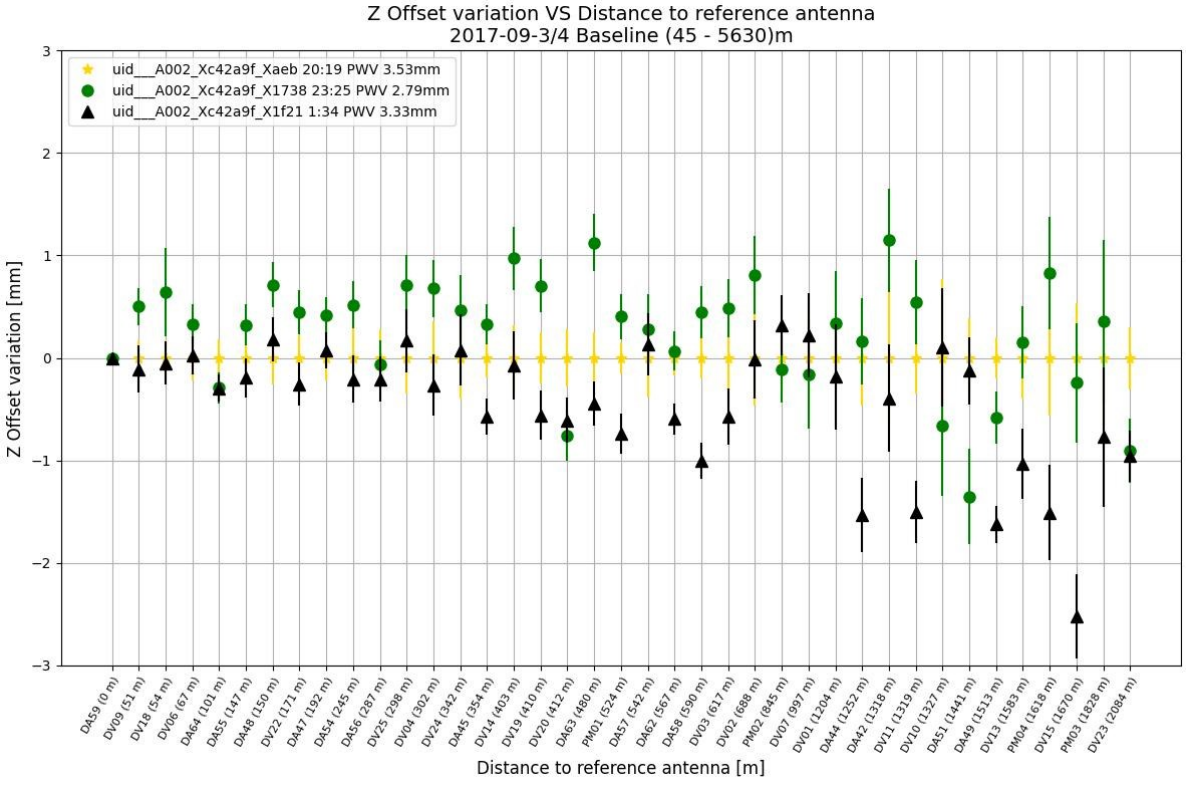

Figure 3 Fluctuation of the antenna position offset (Z component) in highly wet conditions as a function of distance w.r.t. the reference antenna

2. The Saastamoinen model

Given that the fluctuation in antenna position offsets is also present in very dry conditions, the TelCal team decided to conduct a study of the dry path correction, which is not calculated by ATM but by the delay server SW, which in turn is based on the Calc SW historically used for VLA/VLB [Ref. Doc. 2], implementing the Saastamoinen model (see [Eq.1], [Ref. Doc. 3] and [Ref. Doc. 4]), where ZHD is the zenith hydrostatic delay, φ is the ellipsoidal latitude, h is the surface height above the ellipsoid in [km], and P is the total surface pressure in [hPa].

$$ZHD = \frac{0.0022767 \cdot P}{1-0.00266\cdot\cos(2\varphi)-0.00028\cdot h} \text{ [Eq.1]}$$

Saastamoinen derived [Eq.1] assuming that the atmosphere is in hydrostatic equilibrium and that the corrections due to the presence of water vapor in the air (i.e., pressure from water vapor) can be omitted and represent less than 10% of the total refractivity. In these conditions, the refractivity integral is given by [Eq. 2], where g is the gravitational acceleration at the centroid of the atmospheric column, n_0 and T_0 are the ground refractivity, and R is the corresponding gas constant. Additionally, the refraction index of dry air is modeled with [Eq. 3], where P and T are the pressure in [mbar] and temperature in [K], respectively; therefore, it is proportional to the average density.

$$\int_{r_0}^{r_{ion}}(n-1)dr \cong \frac{R}{g}(n_0-1)T_0 \text{ [Eq. 2]}$$

$$(n-1)10^6 = 77.624\left(\frac{P}{T}\right) \text{ [Eq. 3]}$$

We can see that by combining [Eq. 2] and [Eq. 3], that the temperature dependency is cancelled, and the refractivity integral simply depends on the ground pressure P over the gravitational acceleration at the centroid of the atmospheric column g. Therefore, the denominator shown in [Eq.1] represents the variation of the gravitational acceleration depending on the altitude and latitude to account for the changes in surface gravity due to the Earth's elliptical shape.

The Saastamoinen model is widely accepted and has been shown to provide accurate measurements of the zenith hydrostatic delay, and as a matter of fact is still in use for satellite navigation systems such as Galileo (see [Ref. Doc. 5]). However a recent study by Feng, Peng, et al (see [Ref. Doc. 8]) has shown that the ZHD provided by the Saastamoinen model does not model seasonal biases in the order of several mm, which are specially present at high altitudes as measured by radiosonde ray-tracing delays.

3. ATM Dry path model

For the dry delay, ATM implements the model by Liebe 93 (see [Ref. Doc. 9]), and in particular, the non-dispersive term is given by [Eq. 4], where P_d is the partial pressure of dry air in [mbar] and T is the temperature in [K]. Similarly, according to the derivation by Saastamoinen, the refraction index depends on the ratio of pressure to temperature, that is, density.

$$N_d = 0.2588 P_d \left(\frac{300}{T}\right) \text{ [Eq. 4]}$$

The phase shift depends on the frequency ϑ and is given per unit of length ([m/rad]), as shown by [Eq. 5]. This allows ATM to numerically integrate the phase shift induced by each layer to obtain the total phase shift as shown by [Eq. 6], where Δh is the layer thickness.

$$\beta_d = \left(\frac{1.2008 \cdot 10^{-3}}{57.29578}\right) \vartheta N_d \text{ [Eq. 5]}$$

$$\beta_{d,total} = \sum_{layers} \beta_{d,layer} \, \Delta h \text{ [Eq. 6]}$$

Finally, the path length is obtained by multiplying by the wavelength, as shown by [Eq. 8], thus effectively eliminating the frequency dependence from the dry path length.

$$\lambda = \frac{c}{\vartheta} \text{ [Eq. 7]}$$

$$dryPath = \lambda \left(\frac{\beta_{d,total}}{2\pi}\right) \text{ [Eq. 8]}$$

In summary, neither ATM nor the Saastamoinen model include a frequency dependency for the dry path, and in both cases, the refraction index depends on the ratio pressure over temperature, that is, density, as expected from the first principles, assuming that the phase shift is proportional to the amount of material.

However, ATM resorts to a numerical integration and properly accounts for the water vapor pressure, whereas the Saastamoinen model resorts to an approximated analytical result by neglecting the water vapor pressure, which ultimately removes the temperature dependence. On the other hand, the Saastamoinen model incorporates the Earth's ellipsoid into the gravity calculation, whereas ATM assumes spherical symmetry.

4. Comparison of ATM vs Saastamoinen model dry path

Provided that we have clarified the theoretical differences between ATM and the Saastamoinen model in the treatment of the dry path, our goal is to numerically compare both models to establish if the difference between them could be compatible with the fluctuations in the antenna position calibration reported in the introduction section.

To perform the comparison between the dry path provided by ATM and the Saamstamoinen model we have resorted to the CASA interface for ATM (atmosphere tool). The common settings are as follows:

```
# Define common parameters for ATM profile
max_altitude=qa.quantity(95,'km')
temperature_gradient=qa.quantity(-6.5,'K/km')
scale_heigh_water=qa.quantity(2.0,'km')

# Define spectral grid
freqCenter = qa.quantity(97.500,'GHz')
freqWidth = qa.quantity(0.006,'GHz')
freqStep = qa.quantity(0.002,'GHz')
```

In particular the frequency used 97.5 GHz corresponds to the Band 3 representative frequency of the all-sky delay observations used to derive the antenna position correction.

The altitude used to initialize ATM corresponds to that of the meteorological stations used for this study, namely Meteo201, placed on one of the long baseline pads at 4646 meters, and MeteoCentral, placed in the center of the array at 5084 meters. The idea is that the altitude difference between these two meteorological stations would be enough to study significant variations in the differential dry path, which is what matters for phasing purposes between baselines. The latitudes are also relevant, since they are used by the Saastamoinen model, although not by ATM.

```
# Define date and meteo stations
date = "2015-10-22"

station1_id = "Meteo5"
station1_name = "Meteo201"
station1_filename = "%s_%s.dat.txt" % (station1_id,date)
station1_altitude = 4646.0373
station1_latitude = -23.0240591

station2_id = "Meteo6"
station2_name = "MeteoCentral"
station2_filename = "%s_%s.dat.txt" % (station2_id,date)
station2_altitude = 5084.4050
station2_latitude = -23.0268718
```

Finally, one key aspect of the issues reported in this study is the initial pressure step used to initialize the ATM profile. We have experimented with 5 cases with increasing granularity to determine the numerical convergence: 12.5 mbar, 10 mbar, 7.5 mbar, 6 mbar, and 5 mbar. Although previous versions of ATM allowed you to change the pressure multiplicative factor, this option has been removed in the latest version of ATM to guarantee numerical convergence, and now ATM uses a fixed value of 1.075. Also, the initial pressure step has been constrained to the range [5, 12.5] mbar.

4.1 Comparison prior to the development study

Before the development study, we detected that ATM exhibited some ‘jumps’ in the dry path when the initial pressure step was in the lower range (< 7.5 mbar). This prevented us from decreasing the initial pressure step further to study the numerical convergence of ATM and how it compares with the Saastamoinen model. One of the goals of the development study was to precisely address this numerical issue of ATM. Nevertheless, notice that although the dry path calculation exhibits numerical instabilities, the wet path is numerically stable and independent of the initial pressure step.

- First panel: Dry path (antenna 1 – antenna 2) using ATM
- Second panel: Dry path (antenna 1 – antenna 2) using Saastamoinen model
- Third panel: Dry path (antenna 1 – antenna 2) difference Saastamoinen model - ATM
- Fourth panel: Wet path (antenna 1 – antenna 2) using ATM

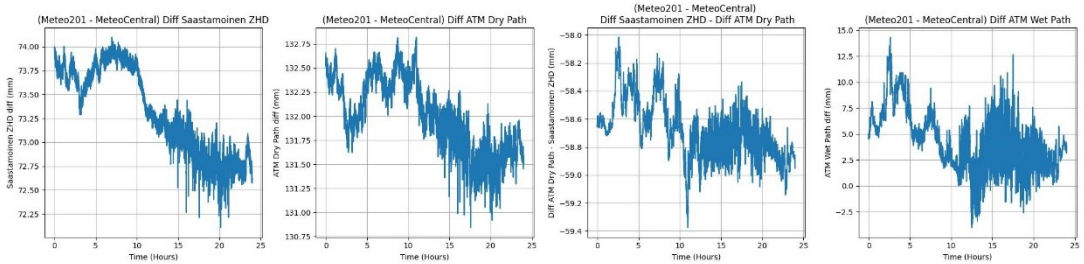

Figure 4: ATM initial pressure step 12.5 mbar

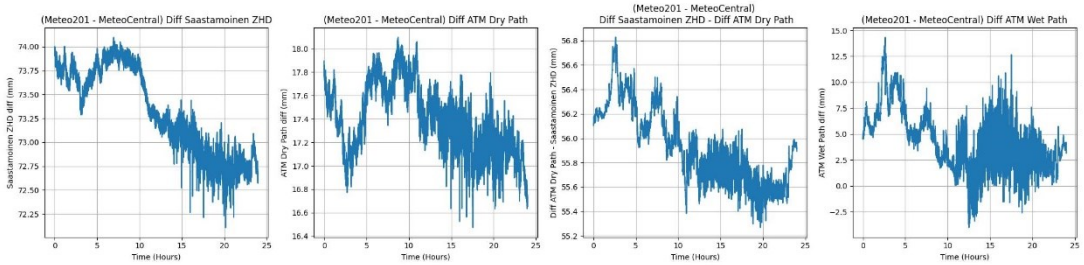

Figure 5 ATM initial pressure step 10 mbar

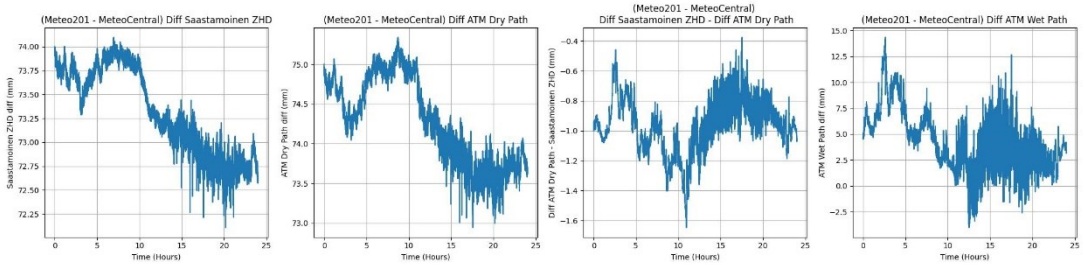

Figure 6 ATM initial pressure step 7.5 mbar

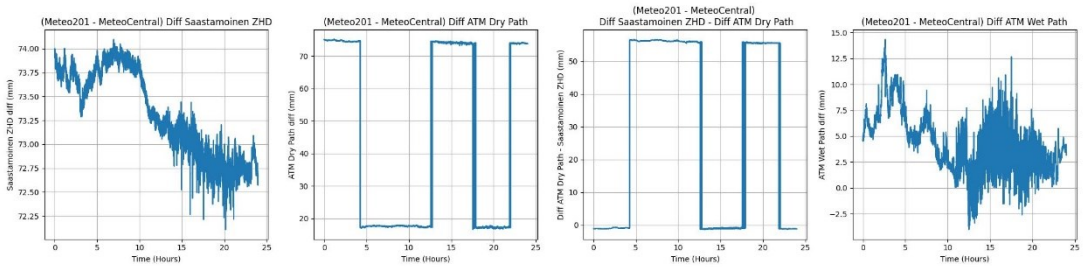

Figure 7 ATM initial pressure step 6 mbar

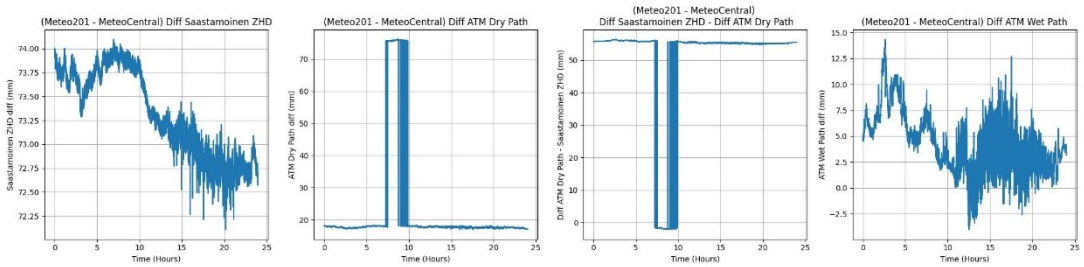

Figure 8 ATM initial pressure step 5 mbar

4.2 Comparison after the development study

Upon investigation of the numerical instabilities reported in the previous section, Juan Ramon established that the issue was caused by a boundary condition between the stratosphere and troposphere. After fixing this problem, we re-ran the tests and were able to reduce the initial pressure step down to 6-5 mbar. At this level of refinement ATM converges numerically and this can be seen comparing Figure 12 with Figure 13 corresponding to an initial pressure step of 6mbar and 5mbar respectively.

Moreover the two models converge, as shown by the first and second panels of Figure 13 corresponding to ATM and the Saastamoinen model respectively. The difference between the two models is shown in the third panel, which represents a fluctuation of ~1mm over 73.5 mm (1.3%). This difference could explain partly the apparent fluctuation in the antenna position calibration offset but not remove it entirely since it has an amplitude of 2-3 mm as shown by Figure 1.

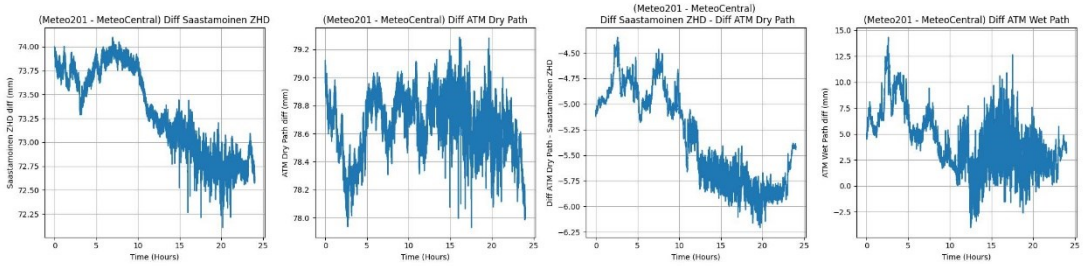

Figure 9: ATM initial pressure step 12.5 mbar

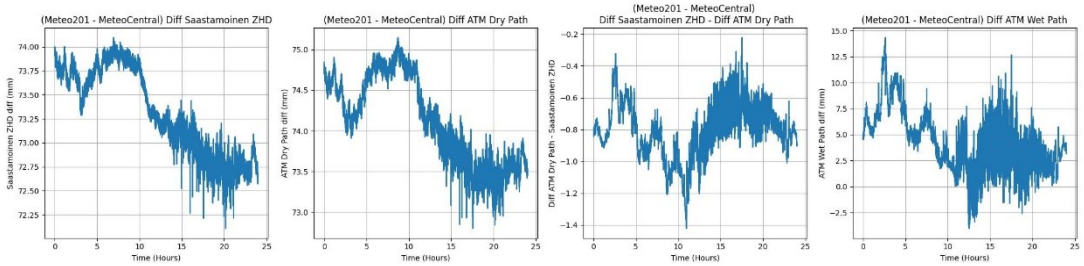

Figure 10 ATM initial pressure step 10 mbar

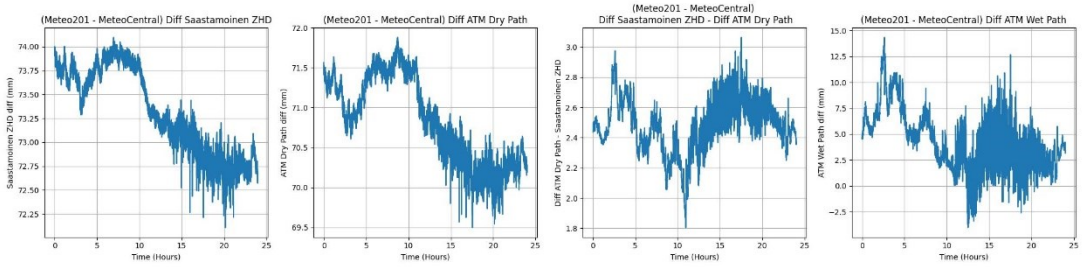

Figure 11 ATM initial pressure step 7.5 mbar

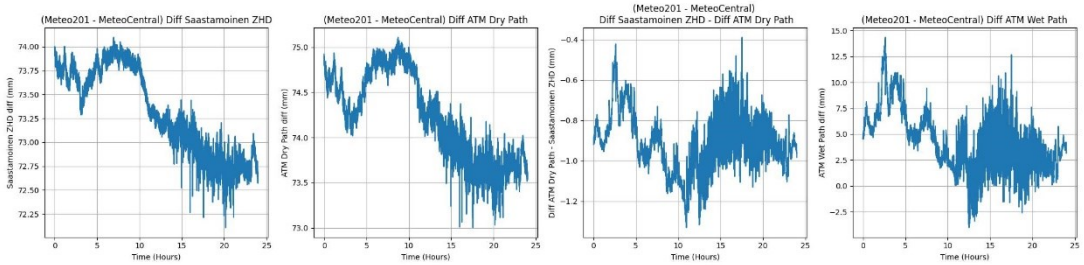

Figure 12 ATM initial pressure step 6 mbar

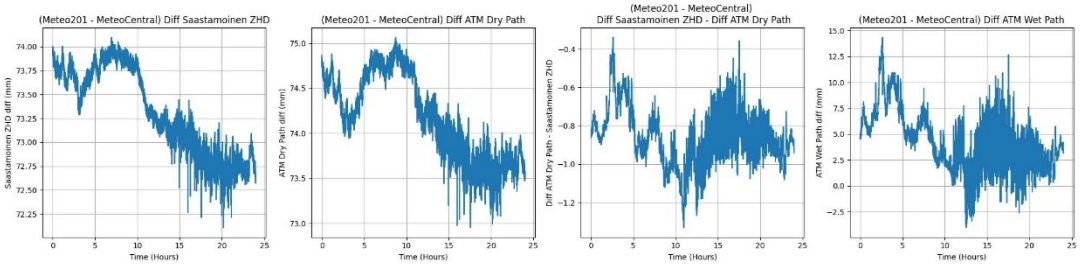

Figure 13 ATM initial pressure step 5 mbar

5. Discussion and conclusions

In summary we have obtained the following results:

1. Neither ATM nor the Saastamoinen model include a frequency dependency for the dry path, and in both cases, the refraction index for a given layer depends on the ratio of pressure over temperature, that is, density, as expected from the first principles, assuming that the phase shift is proportional to the amount of material.
2. However, to obtain the total refraction index ATM resorts to a numerical integration and properly accounts for the water vapor pressure following Liebe 93 ([Ref. Doc. 9]), whereas the Saastamoinen model ([Ref. Doc. 3]) resorts to an approximated analytical result by neglecting the water vapor pressure, which ultimately removes the temperature dependence.
3. Despite of the difference between ATM and the Saastamoinen model described in point 2 the two models provide a quite similar differential dry path when considering two stations at 4646 meters and 5084 meters. Specifically, a ~1mm fluctuation over 73.5 mm (1.3%) as shown by the third panel of Figure 13. This difference could explain partly the apparent fluctuation in the antenna position calibration offset but not remove it entirely since it has an amplitude of ~2mm as shown by Figure 1.
4. As a part of this comparison exercise, we have detected a numerical instability affecting the dry path calculation by ATM caused by a boundary condition between the stratosphere and troposphere. This numerical issue has been fixed by Juan Ramon, allowing to lower the initial pressure step down to 6–5 mbar. At this level of refinement, ATM converges numerically, and this can be seen by comparing Figure 12 with Figure 13.
5. On the other hand, the numerical issue affecting the dry path calculation by ATM was not affecting the wet part calculation, as shown by the right-hand panels of Figures 7 and 8. Actually, the wet path calculation in ATM is mostly independent of the atmospheric layering schema since the amount of water vapor is determined directly by the precipitable water vapor (PWV), which is constrained by the water vapor radiometer measurements. This can be seen by comparing the wet path obtained with ATM, shown on the right panel of Figures 4, 5, 6, 7, and 8, which does not change despite the different initial pressure steps of [12.5, 10.0, 7.5, 6.0, 5.0] mbar, respectively.

6. Reference documents

[Ref. Doc. 1] Analysis of antenna position measurements and weather station network data during the ALMA Long Baseline Campaign of 2015 (https://arxiv.org/abs/1610.04140)

[Ref. Doc. 2] Refractive Bending and Delay Calculations: Background Information and ALMA Implementation (https://safe.nrao.edu/wiki/bin/view/Main/RefBendDelayCalc#CALC)

[Ref. Doc. 3] Saastamoinen, J. "The Use of Artificial Satellites for Geodesy", Geophys. Monograph Series, vol. 15, ed. by S.W.Henriksen et al, AGU, Wash., D.C., pp 247-251, 1972.

[Ref. Doc. 4] Davis, J.L., et al., "Geodesy by Radio Interferometry: Effects of Atmospheric Modeling Errors On Estimates Of Baseline Length", Radio Science, 20, 1593-1607, 1985.

[Ref. Doc. 5] Galileo Tropospheric Correction Model (https://gssc.esa.int/navipedia/index.php/Galileo_Tropospheric_Correction_Model#cite_note-BEVIS-6)

[Ref. Doc. 6] Pardo, Juan R., José Cernicharo, and Eugene Serabyn. "Atmospheric transmission at microwaves (ATM): an improved model for millimeter/submillimeter applications." *IEEE Transactions on Antennas and Propagation* 49.12 (2001): 1683-1694.

[Ref. Doc. 7] J.R.Pardo,E.Serabyn,andJ.Cernicharo,“Submillimeter atmospheric transmission measurements on Mauna Kea during extremely dry El Nino conditions: Implications for broadband opacity contributions” J. QuantumSpectrosc.Radiat.Transfer,vol.68/4,pp.419–433,2001.

[Ref. Doc. 8] Feng, Peng, et al. "Assessment of the accuracy of the Saastamoinen model and VMF1/VMF3 mapping functions with respect to ray-tracing from radiosonde data in the framework of GNSS meteorology." *Remote Sensing* 12.20 (2020): 3337.

[Ref. Doc. 9] Liebe, Hans J., George A. Hufford, and M. G. Cotton. "Propagation modeling of moist air and suspended water/ice particles at frequencies below 1000 GHz." *In AGARD* (1993).